PhD Course in
Models and Methods for Material and Environmental Sciences

Department of Chemical and Geological Sciences
University of Modena and Reggio Emilia

The Glacial History of a high catchment in the Dolomites: New insights on climate-related geomorphological processes during the Late Pleistocene

PhD candidate, cycle XXXII:
Vittoria Vandelli

Tutor:
Prof. Mauro Soldati
Co-Tutor:
Prof. Mauro Marchetti
Coordinator of the PhD Course:
Prof. Maria Giovanna Vezzalini

Academic year 2018/2019

List of contents

Abstract *1*

Riassunto *3*

1. Introduction **5**

1.1 The last glacial cycle in the Italian Alps 5

1.2 Aim and objectives 15

1.3 Outline 16

2. Study area **17**

2.1 Geographical and climatic setting 17

2.2 Geological and structural setting 20

2.3 Geomorphology 27

2.3.1 Structural landforms 29

2.3.2 Glacial landforms 30

2.3.3 Periglacial landforms 32

2.3.4 Gravity-induced landforms 33

2.4 State of the art on glacial studies within the Alta Badia valley 35

3. Materials and methods **41**

3.1 Investigation on subsurface deposits 43

3.2 Investigation on glacial landforms 44

3.2.1 Reconstruction of glacial surfaces 46

3.2.2 Geomorphological surveys and sampling campaigns 47

3.2.3 Deriving exposure ages from in situ cosmogenic ^{36}Cl 50

4. Results **59**

4.1 Results on the investigation of subsurface deposits 59

4.1.1 Sedimentary and radiocarbon dating evidence on Pre-LGM deposits 59

4.2 Results on the investigation of glacial landforms 64

4.2.1 Cosmic Ray Exposure dating results 64

4.2.2 Reconstruction of glacier surfaces 75

5. Discussion **86**

5.1 Pre-LGM period and emplacement of supraglacial gravity-induced deposits on the Pralongià plateau 86

5.1.1 Correlation of Pre-LGM ^{14}C ages with local and global paleoenvironmental and paleoclimatic data 89

5.2 The glacial history of the Alta Badia valley during the LGM and the Lateglacial 92

6. Conclusions **97**

References *100*

Acknowledgements *114*

Appendix 1 115
Appendix 2 117
Appendix 3 127
Appendix 4 161

Abstract

In the high Dolomites catchments, as the southernmost margin of the Eastern Alps, the chronological and spatial characterization of glacial fluctuations occurred during the Late Pleistocene remains still today not well constrained. This occurs despite the recent improvement in investigation methods offered by the development of new dating techniques and by the current possibility to integrate field surveys with high resolution remote sensing data.

The present work illustrates new data that allow the reconstruction of paleogeographic and paleoenvironmental conditions occurred during the Late Pleistocene – a period characterized by global millennial and sub-millennial climate changes – in an area of the Eastern Dolomites, the Alta Badia valley. Despite the intense slope dynamics which characterizes the valley, well preserved glacial deposits have been identified and mapped. They have been attributed, on the basis of geomorphological evidence, to the Last Glacial Maximum (LGM) and to the Lateglacial periods. The research took advantage of the study of these glacial deposits to reconstruct the extent and volumes of the icefield that during the LGM occupied the valley, as well as the advance phases of the local glaciers occurred during the Lateglacial. The dating of these deposits by means of the ^{36}Cl Cosmic Ray Exposure (CRE) technique, applied for the first time in Alta Badia and neighbouring valleys, was fundamental to constrain in space and time paleoglaciers fluctuations within the valley. The geometry of the glaciers (areal extensions, paleotopography, volumes) were reconstructed by means of the analysis of aerial photographs and Digital Terrain Models, as well as through geomorphological field surveys and management and processing of data using Geographic Information Systems.

The Lateglacial Equilibrium Line Altitudes (ELAs) were estimated in relation to different phases of glacial advance. The ELAs have been calculated for every single glacier, providing the opportunity to carry out paleoclimatic correlations on a regional scale for the period considered. The geomorphological evidence and the results of CRE dating on superficial deposits allowed to constrain the minimum age for the withdrawal of the LGM icefield that was at ca. 18-17 ka. In addition, several phases of glacial advance occurring between ca. 16-13 ka were recognized. These results allowed to improve the Alpine chronological dataset relevant to the period ranging from the LGM to the end of the Lateglacial.

The research took also advantage of the study of subsurface deposits exposed owing to eight continuous coring boreholes and an excavation wall on a former glaciated plateau, Pralongià, at ca. 2000 m a.s.l.. Radiocarbon dating performed on organic sediment – collected from the boreholes and from the excavation wall at different depths – provided ages ranging between 45 and 38 ka BP (MIS3), which are unique within the framework of the paleogeographic and paleoclimate reconstructions in high Alpine catchments. Stratigraphic evidence and radiocarbon dating results allowed to conclude that the Pralongià plateau was ice free during most of the MIS3. From a paleoclimatic viewpoint, it is then confirmed the difficulty, during MIS3, of ground ice persistence, which was probably even more amplified by the peculiar orographic conditions of the Alta Badia valley. The study revealed also that between 38 ka and the onset of full glacial conditions (~ 27 ka) gravitational clastic deposits, originating from the Dolomites massifs surrounding the valley, were emplaced on the plateau. This interpretation is supported by many examples of large landslides that occurred during and after the LGM in the Italian Alps which are reported in literature.

Key words: *geomorphology, paleoclimate, paleoglaciers, LGM, Lateglacial*

Riassunto

Le Dolomiti rappresentano il margine più meridionale della catena Alpina orientale. Nelle alte valli dolomitiche la caratterizzazione cronologica e spaziale delle fluttuazioni glaciali precedenti l'Olocene rimane ancora oggi poco documentata, nonostante le molteplici possibilità di indagine offerte dallo sviluppo di nuove tecniche di datazione assoluta e alla recente possibilità di integrare le indagini sul terreno con l'analisi di immagini telerilevate ad alta risoluzione. Il presente lavoro illustra nuovi dati che permettono la ricostruzione paleogeografica e paleoambientale del Tardo Pleistocene (periodo caratterizzato da variazioni climatiche millenarie e sub-millenarie a scala globale) di un'area delle Dolomiti Orientali, l'Alta Val Badia. Qui, nonostante l'intensa dinamica di versante, sono stati identificati e cartografati depositi glaciali ancora ben preservati e attribuiti, sulla base delle evidenze geomorfologiche, all'Ultimo Massimo Glaciale (UMG) e al Tardoglaciale. La presente ricerca si è avvalsa dello studio di questi depositi per ricostruire l'estensione e i volumi dell'*icefield* che durante l'UMG occupava la valle e le fasi di avanzata dei ghiacciai locali durante il Tardoglaciale. La datazione di questi depositi mediante la tecnica delle superfici esposte (^{36}Cl *Surface Exposure Dating*), applicata per la prima volta in Alta Badia e valli limitrofe, è risultata fondamentale per vincolare temporalmente e spazialmente le fluttuazioni dei paleoghiacciai della valle. Le geometrie dei ghiacciai (estensioni areali, paleotopografie, volumi) sono state ricostruite sulla base dell'analisi di fotografie aeree e Modelli Digitali del Terreno, di rilievi geomorfologici e della gestione ed elaborazione di dati tramite Sistemi Informativi Geografici. Le stime delle Linee di Equilibrio tardoglaciali, relative a diverse fasi di avanzata, sono state calcolate per ogni singolo ghiacciaio, fornendo così l'opportunità di effettuare correlazioni paleoclimatiche su scala regionale per il periodo considerato. Le evidenze geomorfologiche e le età di esposizione superficiale hanno permesso di vincolare l'età minima del ritiro dell'*icefield* in corrispondenza dell'UGM, intorno a ca. 18-17 ka. Inoltre, sono state riconosciute diverse fasi tardoglaciali di riavanzata occorse tra ca. 16 e 13 ka, permettendo così di ampliare il dataset cronologico alpino per il periodo che si estende dall'UGM fino alla fine del Tardoglaciale.

La ricerca si è avvalsa inoltre dello studio di depositi sub-superficiali portati alla luce grazie a carotaggi effettuati a 2000 metri di quota sull'altopiano del Pralongià, coperto dall'*icefield* durante l'UMG. Datazioni radiometriche su materiale organico, prelevato

dai carotaggi a diverse profondità, hanno fornito età comprese tra 45 e 38 ka (MIS3), uniche nel quadro delle ricostruzioni paleogeografiche e paleoclimatiche alle alte quote alpine. Lo studio di questi depositi ha permesso di concludere che durante il MIS3 il Pralongià era libero dai ghiacci. Dal punto di vista paleoclimatico è confermata la difficoltà, durante questo periodo, di una persistenza del ghiaccio al suolo, che in Val Badia, vista la peculiare conformazione orografica, è stata probabilmente ancor più amplificata. Lo studio ha inoltre rivelato che tra 38 ka e l'instaurarsi delle condizioni pleniglaciali (~27 ka) depositi clastici gravitativi, provenienti dai massicci dolomitici che orlano la valle, sono stati messi in posto sull'altopiano. Questa interpretazione trova riscontro in analoghi esempi di grandi frane occorse durante e dopo l'UMG nelle Alpi italiane riportate dalla letteratura.

Parole chiave: *geomorfologia*, *paleoclima*, *paleoghiacciai*, *UGM*, *Tardoglaciale*

1. Introduction

1.1 The last glacial cycle in the Italian Alps

The landscape of the Italian Alps bears witnesses of past glacial fluctuations occurred during the last glacial cycle. The theory of past glaciation in the lowland (Ice Age theory) was developed during the first half of the 19th century (Venetz, 1833; Agassiz, 1840; de Charpentier, 1841). The study of the Alps played a key role in the development of the Ice Age theory (Ivy-Ochs, 2015 and references therein). A great merit for the development of this theory is given to Jean-Pierre Perraudin, hiker and hunter from Lourtier (canton Valais, Switzerland) who observed giant granite boulders perched high in the Val de Bagnes (close to Lourtier) as well as long scratches marking the exposed rocks that lined the narrow valley which he intuitively attributed to the action of glaciers. In 1815, he discussed his ideas with the naturalist Venetz who shared Perraudin's theories with de Charpentier and Agassiz. The latter was one of the most influent scientists of the time and contributed to popularise such issues among the scientific community.

Later in the 1880s, the German geographer Penck, studying river valleys of the Northern Alps, noticed that the bottom of each valley was a flat surface incised by river action depositing gravels. At higher elevations with respect to the valley bottom, on both side of the valleys, he found three different level of terraces built up of gravel which he supposed to be originated during a cold climate when frost action and lack of vegetation increased the erosion rate. He discovered four levels of terraced gravelly deposits that he referred to four ice ages occurred in the Pleistocene (Fig. 1.1). Penck, together with his colleague Brückner, named each age with names coming from the Alpine valleys ordering them alphabetically, from the older to the youngest: Günz, Mindel, Riss and Würm (Penck and Brückner, 1909; Imbre and Imbre, 1986).

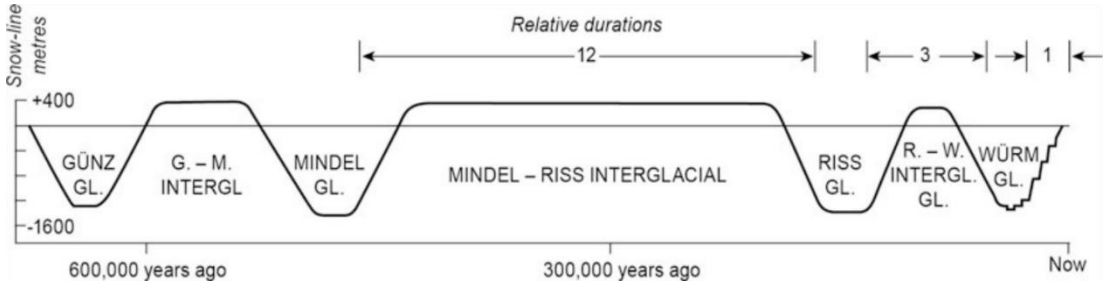

Fig. 1.1 The four-fold model of Alpine Glaciation as proposed by Penck and Brückner (1909); after Murray-Wallace (2018).

With the popularization of palynology (1920s), pollen studies have revealed the complexity of Pleistocene climate fluctuations. With the introduction of radiocarbon dating (Libby, 1951), it became possible to determine the radiometric age (<50,000 yr BP) of organic-bearing deposits emplaced by former glaciers. Thanks to the introduction of surface exposure dating (e.g. Phillips et al., 1986) it became possible to date glacial deposit with poor/absent organic matter and also the bedrock shaped by glacier action (Fig. 1.2).

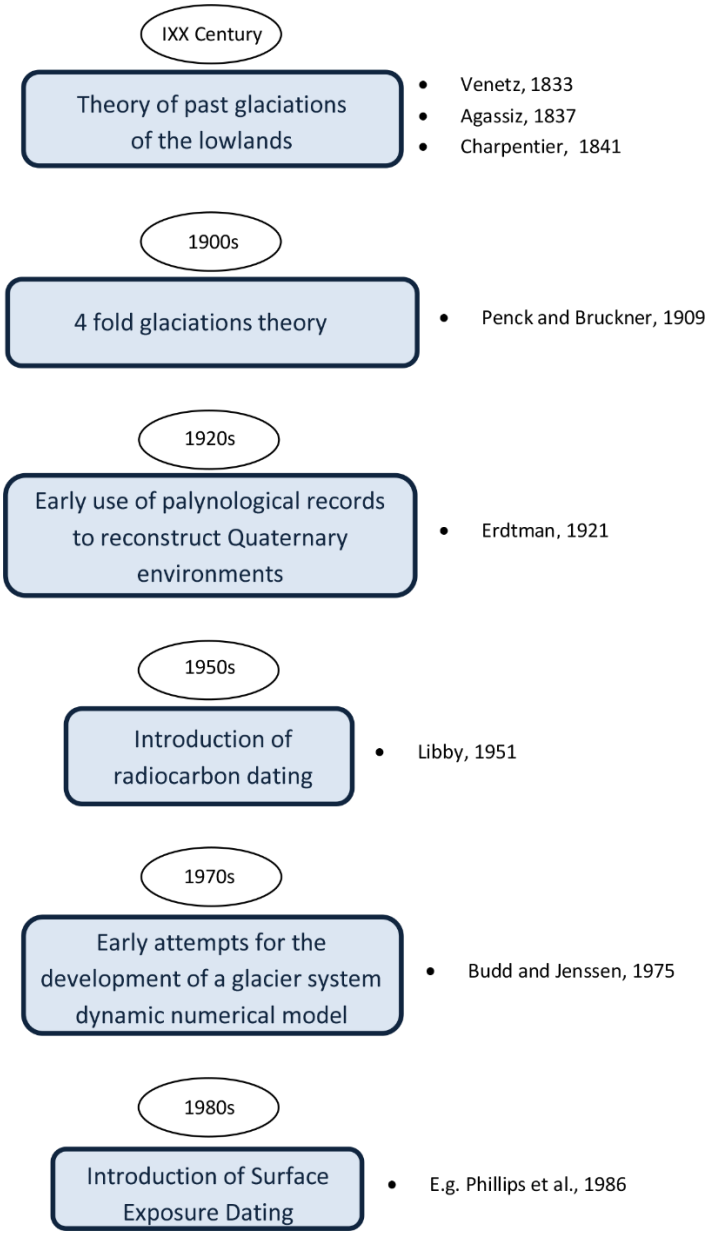

Fig. 1.2 Development in the study of paleoenvironment and paleoglaciers.

At present-day, the last glacial cycle is understood as the period between the penultimate and current interglacial or generally between Termination II and Termination I (Fischer et al., 1999). More precisely, it encompasses the last cold stage between 110.8 and 11.7 ka (lower boundary based on Martinson et al., 1987 and upper boundary based on Lowe et al., 2008).

In the Alps the last glacial cycle (Würmian) is understood as the time interval between the end of the Last Interglacial (Eemian) and the beginning of the Holocene. The Eemian correspond to the Marine Isotope stage (MIS) 5e which is best recorded by steep decline oxygen isotope values around 118 ka (Fig. 1.3), indicating a major atmospheric cooling. The Eemian around the Alps is reflected by interglacial conditions with widespread broadleaf deciduous forests. Pollen data record an increase in precipitation for the period (Ivy-Ochs et al., 2008).

The Würmian glaciation has been subdivided, according to the definition of the Subcommission on European Quaternary Stratigraphy (Chaline and Jerz, 1984) into Early, Middle and Late Würmian.

The Early Würmian environmental and climate history of the southern Alpine foreland is well constrained by pollen records from Pini et al. (2010). This period is characterized by climate instability. Around 110 ka ago the first dry and cold stadial phase after Eemian occurred followed by the reduction of forest and the increase in herbs and shrubby xerophytes. After this period warm-temperate conditions returned (1st post-Eemian Interstadial). Around 113 ka ago a minor and sudden episode of increase of herbs and xerophyte has been recorded as witness of colder and arid conditions. The first post-Eemian Interstadial ended around 90 ka ago with the onset of the 2nd post-Eemian stadial recorded by the prevalence of xerophytes and Pinus in pollen sequences. Glacier extension during the Early Würmian is poorly constrained in the southern Alps and foreland. Interstadial conditions were recorded during MIS5c from biostratigraphic data and dating of peat bog layers at the Ivrea-Verbano amphitheatre (Gianotti et al., 2015 and references therein). A substage of the Lake Garda moraine amphitheater was presumably attributed to the MIS4 (Cremaschi, 1987). Further data are available for the Northern Alpine foreland but whether a large advance of Alpine glaciers occurred during the Early Würmian stadials is still a matter of debate (Ivy-Ochs et al., 2008). In particular, some data suggest a major advance in the Western Alps (Preusser and Schlüchter, 2004; Preusser et al., 2003, 2007), whilst

evidence from the Eastern Alps show that the main valleys were ice-free at that time (Reitner, 2005, 2007; Spotl and Mangini, 2006; Starnberger et al., 2013).

The end of the 2nd post-Eemian Interstadial marks the transition from the Early to the Middle Würmian commonly set at the boundary MIS5-MIS4 (Chaline and Jerz, 1984). The Middle Würmian largely corresponds to MIS3 and the period of the most pronounced Dansgaard-Oeschger (DO) climatic events as known e.g. from Greenland (Dansgaard et al., 1993). Available proxy records from the Alps indicate an Arctic tundra vegetation even in the lowlands interrupted by larger intervals of milder conditions (interstadials). In accordance with the global sea level curves (oxygen isotope data), this period was characterized by distinctly larger amounts of global ice (i.e. generally there had been more water in the form of ice than today). With a conforming climate progression on the poles and in the Alps, glaciated areas in high mountain regions should have been more extensive than today. The considerable climate variability of MIS3 is recorded by e.g. speleothems and lacustrine and loess deposits in the Northern Alps and their foreland (Starnberger et al., 2013 and references therein). Less is known about the southern side. Only a few papers providing Late Pleistocene paleoenvironmental and paleoclimate information on the southern Alpine foreland are available in literature (e.g. Pini et al., 2010; Carrera et al., 2018) and suggest a long-term climatic deterioration toward the end of MIS3 leading eventually to maximum ice extent during the Last Glacial Maximum (LGM, MIS2).

During MIS2, Alpine glaciers reached their maximum advance (Fig. 1.4) in synchronous with the global Last Glacial Maximum between 26 and 19 ka BP (Clark et al., 2009; Shakun and Clarson 2010; Hughes et al., 2013). A steep drop in sea level reflecting an increase in global ice volume was recorded at around 30 ka, with a more gradual lowering until 20 ka which was followed by a rise during the Lateglacial and early to middle Holocene (Fig. 1.3; Lambeck et al., 2014 and references therein).

The LGM moraines in the Alpine forelands are generally well developed. Records and chronological evidence from both Northern and Southern Alps suggest that glaciers reached the forelands at around 30 ka BP (Figs. 1.4 and 1.5 and Tab. 1.1). In Fig. 1.5 the location of some of the most significant chronological records relevant to the glacial history of the Alps is shown, they are mainly relevant to the southern side of the chain; the explanation of such records is provided in Tab. 1.1.

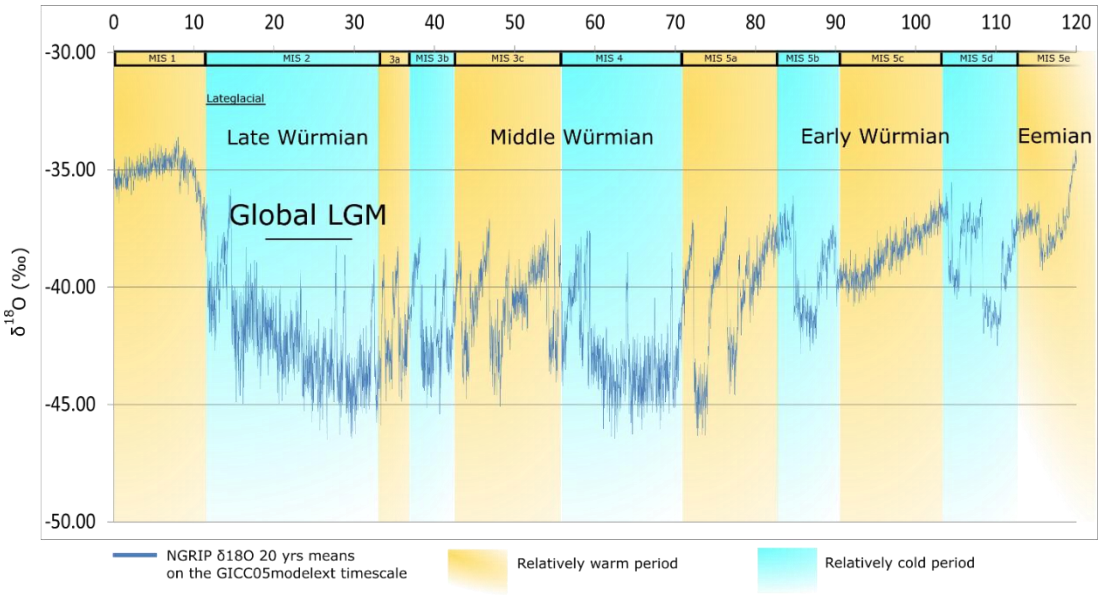

Fig. 1.3 Greenland ice core record (GCC05, Svensson et al., 2005) and subdivision of the Last Glacial cycle according to Chaline and Jerz (1984). Glacial chronology subdivision of MIS2 refers to Ivy-Ochs, 2015.

During the LGM period almost the whole Italian Alps were covered by extensive icefields which fed a network of interconnected outlet glaciers confined in the main Alpine valleys and piedmont glaciers spill out into the Alpine Italian foreland. For example, in the western sector, Dora Riparia glacier flowed for a distance around 50 km in the Susa Valley and Dora Baltea watershed was occupied by a large valley glacier developing on the south-eastern side of the Mt. Blanc and terminated in the Ivrea amphitheatre (Giardino et al., 2017). At the Ivrea amphitheatre, four LGM retreat stadials – the latter understood as re-advances occurred during the LGM stepwise retreat – were recognized by Gianotti et al. (2008, 2015). The ^{10}Be dates from two erratic boulders on the Ivrea amphitheatre provided a minimum age for LGM final retreat of 23.8 ± 1.7 ka and 20.1 ± 3.0 ka.

The central sector of the Italian Alps hosted some of the main glacier systems of the chain. From Toce, Ticino, Adda and Oglio catchments, valley glaciers flowed forming a network of transection glaciers connecting trough the main Alpine passes (Antonioli and Vai, 2004). Based on compilation and re-evaluation of existent radiocarbon dates relevant to the southern Swiss Alps, Scapozza et al. (2014) set the LGM advance of the Ticino glacier at 27.4-22.7 ka cal BP. Stratigraphic, radiocarbon and palynological record from an end-moraine system of the Oglio valley glacier revealed that the glacier culminated in the end moraine shortly after 25.8 ± 0.8 ka cal BP (Ravazzi et al., 2012)

and glacier retreat was underway no later than 18.6 to 17.9 ka cal BP (Ravazzi et al., 2012; Lauterback et al., 2012).

The Dolomites region during the LGM was bounded to the east by the Tagliamento glacier forming a piedmont lobe in the Friulian Plain and to the west by Adige glacier. The latter was the largest (40 km long, 20 km wide) Italian glacier and it was fed by Isarco, Avisio, Brenta and Sarca watersheds. Down valley this glacier split into two glacial lobes: the less extensive laid along the present Garda Lake and the other crossed the Adige Valley. During the LGM the Dolomites corresponded to the feeding area of the Piave glacier (G.B. Castiglioni, 1964), whose deglaciation history is well-defined for its central and distal sectors (see Pellegrini et al., 2005; Carton et al., 2009) while only few data are available for its upper part (see Poto et al., 2013). In particular, according to Pellegrini et al. (2005), during the LGM, the lower part of the Piave catchment (Belluno valley) hosted a valley glacier about 800 m thick. The retreat of the Piave glacier was marked by different phases of readvance (three at least) as documented by lateral moraines, kame terraces and small marginal moraines (Carton et al., 2009). The lower part of the Piave catchment was already ice-free 15 ka BP, this is confirmed also by Pellegrini (2000) and Poto et al. (2013).

Two phases of glacier culmination were recorded at the Garda amphitheater, the major at some 26-23 ka BP and the minor at 23-17 ka BP (Monegato et al., 2017). Similarly, the Tagliamento glacier reached its amphitheater through two phases of glacier culmination, the major at 26.5-23 ka BP (Santa Margherita advance) and the minor at 24-21 ka BP (Canodusso advance). The recessional moraines (Remanzacco recessional phase) were built up between 21 and 19 ka BP (Monegato et al., 2007). Dating the end of sediment supply provision to distal outwash plain at the Cormor megafan confirmed that the withdrawal of the Tagliamento glacier from the LGM moraine complex was underway between 22 and 19.5 ka BP (Fontana et al., 2014).

LGM frontal moraines in the Maritime Alps were dated to 24 ka BP by ^{10}Be exposure dating (Federici et al., 2017). In the Mt. Blanc Massif, Wirsig et al. (2016) found exposure ages of ~18.5 ka from ^{10}Be dating of boulder and bedrock surfaces, which is indicative of the initiation of lowering of the LGM ice surface.

Following the peak of the LGM, the most of valley glaciers worldwide underwent a general decline, decreasing in volume and slowly retreating to the upper cirques. The Alpine Lateglacial (Fig. 1.6) started when glaciers retreated from the mountain fronts

leading to a collapse of piedmont lobes in the north and withdrawal from the amphitheatres in the south (Ivy Ochs, 2015).

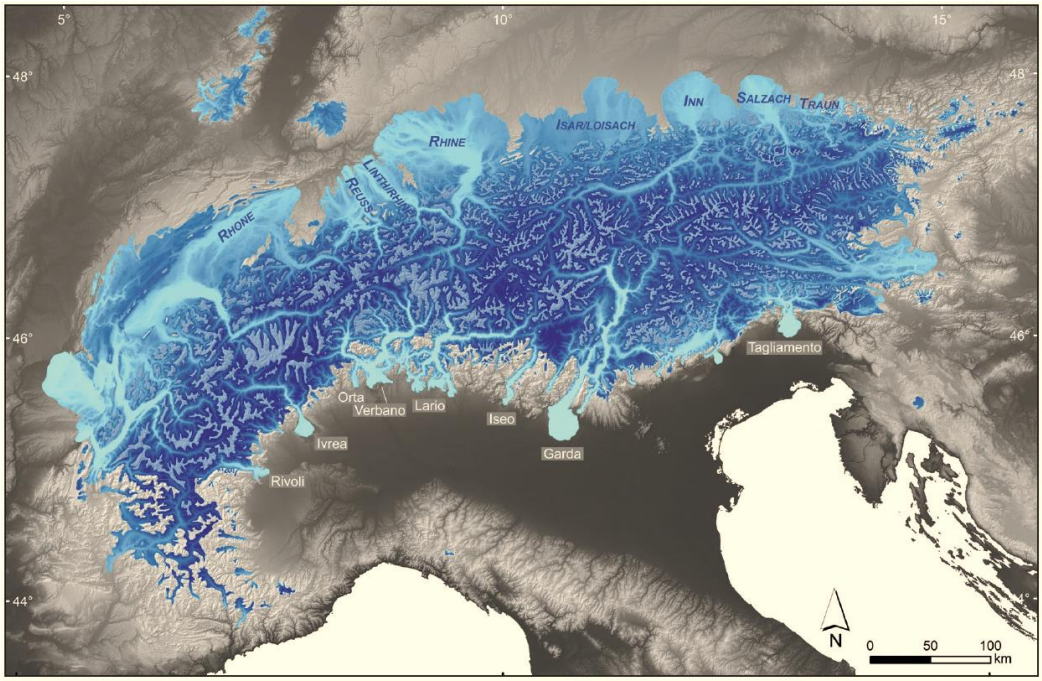

Fig. 1.4 The Alps during the Last Glacial Maximum (Late Würm) after Ivy-Ochs (2015).

Penck and Brückner (1909) proposed a three-fold division of the Lateglacial: Buhl, Gschnitz and Daun stadials. This chronology has been revised by several authors and the most recent and commonly accepted subdivision for the Lateglacial in the Alpine region (Ivy-Ochs et al., 2008; Heiri et al., 2014) and in Italian Alpine valleys (Federici et al., 2008, 2012; Monegato, 2012; Colucci et al., 2014) includes, from the oldest to youngest, the following stadials: Buhl, Gschnitz, Clavadel/Sender, Daun, Egesen (Fig. 1.6). The Buhl was replaced by the "Sciliar stadial" (or "Schlernstadium") in von Klebelsberg (1948) and in Masini (1998). Von Klebelsberg (1950) added the "Steinach stadial" (still used by van Husen, 2000) between the Sciliar and the Gschnitz ones (Ghinoi and Soldati, 2017).

Moraines are assigned to stadials according to their relative position in a valley sequence, their morphology and their Equilibrium Line Altitude (ELA) depression relative to the Little Ice Age (Ivy-Ochs et al., 2008) or alternatively to the present ELA. This assumes that moraines with similar morphostratigraphic position, morphology and ELA depression and located in homogeneous climatic regions were deposited almost synchronously during the same phase of glacier advance.

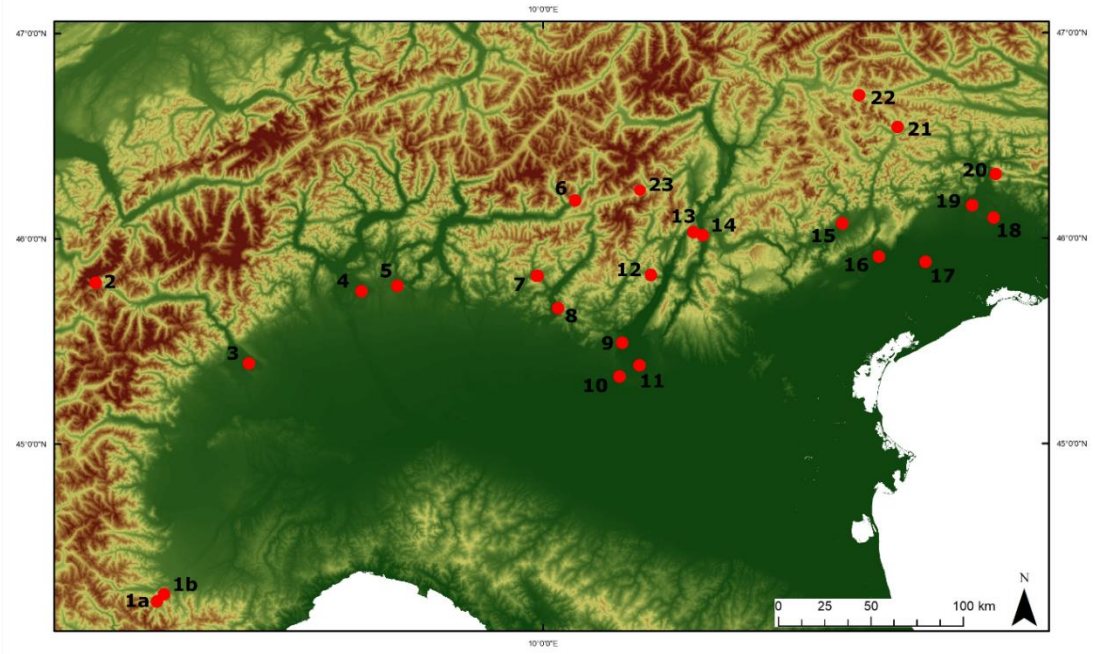

Fig. 1.5 Location of significant radiocarbon dates and ^{10}Be surface exposure ages relevant to the glacial history of the Alps with a deeper focus on the southern part. For number legend and explanation see Tab. 1.1.

During the earliest Lateglacial, the former LGM glaciers were stagnant and downwasting within the main valleys. This phase is constrained by luminescence dating of proglacial sediments from the Eastern Alps at 17 ± 2 ka BP (Klasen et al., 2007).

The Gschnitz stadial was the most significant one and is witnessed by well-developed blocky end moraines located in the main Alpine valleys. ^{10}Be exposure dating of stadial moraine in the Gschnitz type locality (Austria) revealed ages between 17-16 ka BP (Ivy-Ochs et al., 2006a). ELA depression during the Gschnitz stadial was 600-700 m lower than the LIA ELA. The Clavadel/Sender and Daun stadials lie between the Gschnitz and the Egesen stadials. Gschnitz stadial can be correlated to the Heinrich event 1 (H1) or to the Greenland-Stadial 2a (GS-2a) (cf. Sanchez Goñi and Harrison, 2010).

Daun stadial moraines generally lie downstream of Egesen stadial moraines. They differ from the latter in having broad, smoothed ridges that are poor in boulders, thus difficult to date with exposure dating techniques (Ivy-Ochs, 2015). Daun moraines were related to an advance prior to the beginning of the Bolling warm period (Maisch, 1987) or to a cold period occurring between Bolling-Allerod warm periods.

Tab.1.1 Radiocarbon and surface exposure dating (see Fig. 1.5 for site location).

#	Author/s	Dates	Dating Method	Interpretation
1a	Federici et al. (2012)	16,590 ± 440 years BP	^{10}Be	Gschnitz stadial at Ponte Murato (Maritime Alps)
1b	Federici et al. (2017)	24.0 ka BP	^{10}Be	LGM maximum advance at Tetti del Bandito (Maritime Alps)
2	Wirsig et al. (2016)	18.5 ±1.1 ka BP	^{10}Be	First signs of ice surface lowering in the Mt. Blanc (Western Alps) and Zillertal Alps (Eastern Alps)
3	Gianotti et al. (2008)	20.8 ± 1.5 ka BP	^{10}Be	Oldest age for the last glacial deglaciation at Ivrea amphitheatre (Western Alps)
4	Scapozza et al. (2014)	28.5-22.9 ka cal BP	^{14}C	LGM Advance for the Ticino Glacier (Central Alps)
5	Scapozza et al. (2014)	22.5-21 ka cal BP	^{14}C	First recessional phase (withdrawal) for the Ticino Glacier (Central Alps)
6	Hormes et al. (2008)	11,480 ± 670 and 10,850 ± 820 years BP	^{10}Be	Egesen moraines in Val Viola (Central Alps)
7	Ravazzi et al. (2012)	18.3-17.2 ka cal BP	^{14}C	Maximum age and minimum age for deglaciation in the foreland
7	Ravazzi et al. (2012)	25.8 ± 0.8 ka cal BP	^{14}C	Oglio valley glacier culminated in end moraine
8	Lauterbach et al. (2012)	17,859-18,567 yr cal BP	^{14}C	Minimum age for retreat of LGM glaciers
9	Ravazzi et al. (2014)	17.46 ± 0.2 ka cal BP	^{14}C	Manerba (Lake Garda, Lombardy) advance culmination followed by glacier retreat
10	Monegato et al. (2017)	26-23 and 23-17 ka BP	^{14}C	Two LGM stadials at Garda amphitheatre
11	Baroni et al. (2006)	16,880-16,470 yr cal BP	^{14}C	Withdrawal of glaciers in Southern Alps
12	Magny et al. (2012)	13,104-12,732 yr cal BP	^{14}C	Younger Dryas deposit
13	Baroni et al. (2001)	11,829 ± 90 yr BP (uncalibrated)	^{14}C	Minimum age for glacial withdrawal
14	Fuganti et al. (1998)	10,312-9,997 and 10,488-10,311 yr cal BP	^{14}C	The Adige valley (Eastern Alps) was ice-free
15	Pellegrini (2000)	13,160 ± 110 yr cal BP	^{14}C	Vallone Bellunese in ice-free condition
16	Bondesan (1999)	17,670 ± 320 yr cal BP	^{14}C	Age of maximum LGM Piave glacier expansion
17	Monegato et al. (2007)	between 30.8-29.9 and 28.7-27.8 ka cal BP	^{14}C	Tagliamento glacier reached the amphitheatres
18	Monegato et al. (2007)	26.5-23 ka cal BP	^{14}C	St. Margherita (Udine Province, Eastern Alps) maximum advance
19	Monegato et al. (2007)	20.3-18.8 ka cal BP	^{14}C	Deglaciation of Ragogna Lake (Udine Province, Eastern Alps)
20	Monegato et al. (2007)	22.2-21.4 ka cal BP	^{14}C	Conodusso maximum advance (Udine Province, Eastern Alps)
21	Poto et al. (2013)	13.11-13.33 ka cal BP	^{14}C	Upper part of Piave catchment in ice-free condition
22	Pellegrini et al. (2005)	16,210 ± 50 yr cal BP	^{14}C	First phase of glacier retreat in Val Piana (Trento Province, Eastern Alps)
23	Cavallin et al. (1997)	12,275 ± 115 yr BP (uncalibrated)	^{14}C	Minimum age of Lateglacial deposit at the Tonale Pass (Central Alps)

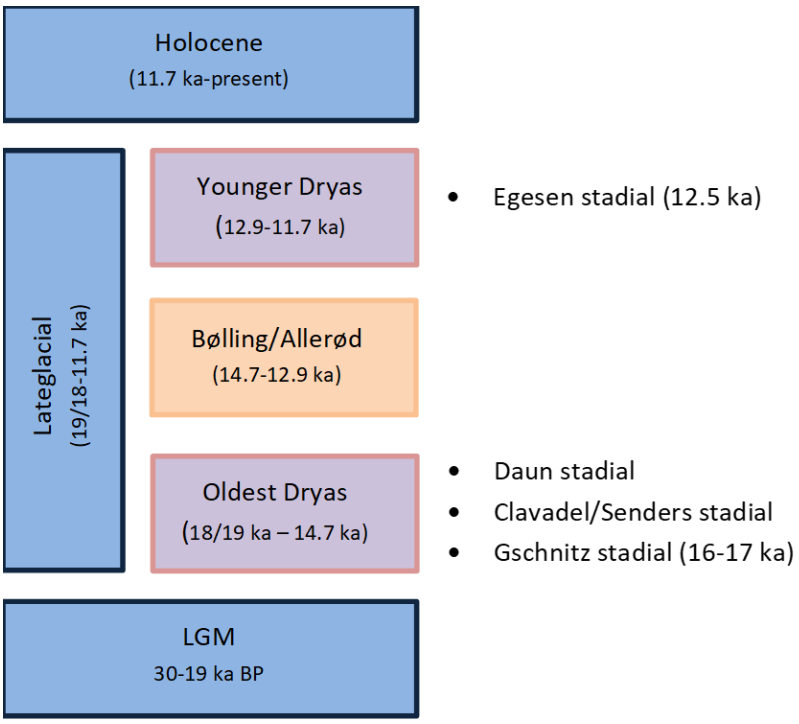

Fig. 1.6 Schematic summary of Lateglacial stadials in relation to major climatic events modified from Ivy-Ochs et al. (2008) and references therein.

The Egesen stadial moraines are generally characterized by steep-sloping blocky moraines sets located several kilometres downstream from Little Ice Age (LIA) moraines (Ivy-Ochs, 2015). ELA depression with respect to the LIA ELA is between 250-350 m. Federici et al. (2008) in the Maritime Alps found an ELA depression with respect to the LIA of 260-320 m, and 520-530 m with respect to the present-day one. In Austrian and Swiss Alps, Kerschner et al. (2000) reported a difference in elevation between the Egesen ELA and the present-day ELA of 450 m at the northern and western margins, and of 300 m in the central valleys. Exposure ages for Egesen moraines in the Maritime Alps (Piano del Praiet moraine) also revealed a mean of 11,340 ± 870 years BP which is consistent with other exposure ages obtained from other sites in the Alps, e.g. in Switzerland at Julier Pass (Ivy-Ochs et al. 1996, 2006b) and at the Great Aletsch glacier (Kelly et al., 2004); in Austria at the Schönferwall site (Ivy-Ochs et al. 2006b). This confirms the connection between Egesen and the Younger Dryas cold period (Fig. 1.7).

Minor glacier advances occurred during the early Holocene in the Alps which were locally dated at around 10.8 ka BP and 8.4 ka BP by means of surface exposure dating techniques applied to boulders in moraine deposits (Ivy-Ochs et al., 2009 and reference

therein). These two periods of glacier readvances have been respectively named Kartell and Kromer stadials. Another minor glacier advance has been recorded at around 3.3 ka BP preceding the Little Ice Age (1300-1850 AD). During this latter a series of significant historical expansions of the ice-surface took place.

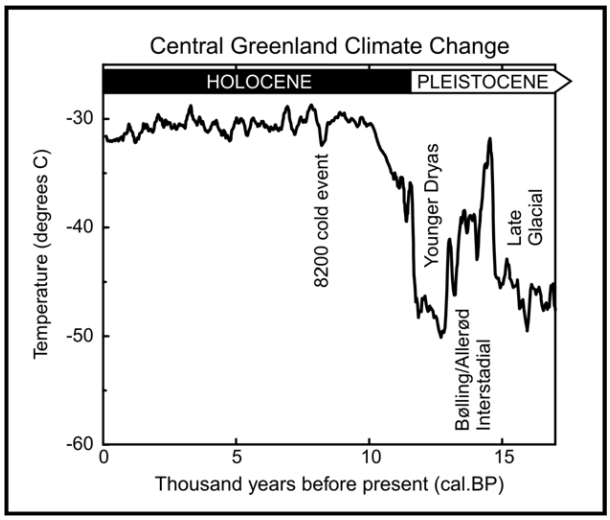

Fig. 1.7 Late glacial and Holocene climatic curve, showing temperature changes over the past 18,000 calendar years as reconstructed from Central Greenland snow accumulation rates; after Englemark and Buckland (2005).

1.2 Aim and objectives

Since 1970s the former glacier fluctuations has been used as proxy data to examine past climate changes by means of empirical relationships between glacier physical parameters (e.g. ELA) and past climate conditions (e.g. paleoprecipitation and paleotemperature). Thus, the reconstruction of former glacier extensions provides insights on climatic conditions occurred in the 'recent' geological history. Additionally, the significant millennial and sub-millennial climate instability, globally documented for the Late Pleistocene, suggests how fast and abruptly climate can change. Characterizing in both space and time Late Pleistocene climate changes and defining their effects on the landscape are crucial to understand the effects of the ongoing climate change on present landscape and to predict future scenarios.

Starting from these premises, this PhD research aimed at extending the dataset on the glacial geochronology of the Alps and at providing further insights and to contribute in the characterization, from a high-Alpine perspective, of paleoenvironmental and paleoclimate conditions occurred during Late Pleistocene in the Eastern Dolomites

(Southern Alps, Italy), as the southernmost distal part of the Alpine chain. In particular, the work was focused on the key area of the Alta Badia valley (Province of Bolzano, Italy) and was based on: i) collecting paleoenvironmental record by studying subsurface deposits, possibly attributable to the Pre-LGM period, retrieved from direct surveys on a former glaciated plateau, and ii) constraining in space and time the Late Pleistocene glacial history of the Alta Badia valley by investigating glacial landforms possibly attributable to the LGM and to the Lateglacial.

1.3 Outline

The research carried out within the PhD project had a two-fold structure including, from one hand, the study of the previously mentioned subsurface deposits, and from the other hand, the study of the glacial landforms, both carried out within the same study area, the Alta Badia valley. From the integration of both studies, the reconstruction of the glacial history of the Alta Badia valley during the Late Pleistocene was provided. The organisation of this thesis reflects the two-fold structure of the research; in fact, the materials and methods as well as the results of each of the two studies are described and discussed within separate and dedicated sections. In particular, the thesis is organised into six chapters plus four additional appendixes. After an introductory paragraph concerning the state of the art of the last glacial cycle in the Alps with particular reference to the southern side (section 1.1), the aim and the objectives of the thesis are presented (section 1.2). The study area is then presented in section 2 by focusing on its geographical (section 2.1), geological (section 2.2) and geomorphological (section 2.3) features referring also to the regional framework of the Dolomites. In section 3, materials and methods used for the investigations on subsurface deposits (section 3.1) and on glacial landforms (section 3.2) are presented. The outputs of the investigations are presented and discussed in section 4 (Results) and 5 (Discussion) respectively. In particular, the outputs of the investigations on subsurface deposits are presented and discussed in section 4.1 and 5.1 respectively, whilts the outputs of the investigations on glacial landforms are presented and discussed in section 4.2 and 5.2 respectively. The integrated outputs resulting from the investigation of both subsurface deposits and glacial landforms are presented in the sixth section, which is dedicated to the conclusions. In the latter the Late Pleistocene glacial history of the Alta Badia valley, based on the found geomorphological and geochronological evidence, is described.

Moreover, the reader can find: i) in Appendix 1, a detailed description of the laboratory procedures carried out for the preparation of the samples for cosmogenic dating (cf. also section 3.2.3); ii) in Appendix 2, the photographic documents relative to the direct surveys carried out on the Pralongià plateau; iii) in Appendix 3, the tables used for the calculation of the cosmogenic (exposure) ages; iv) in Appendix 4, the probability density function calculated for the obtained cosmogenic ages.

The outputs of the research on the subsurface deposits retrieved on the Pralongià plateau were published in Vandelli et al. (2019); whilst the outputs of the research on the glacial landforms within the Alta Badia valley are part of a paper in preparation.

2. Study area

2.1 Geographical and climatic setting

The study area is included within the Dolomites (Dolomiti) which are located in the eastern sector of the Alpine chain (Fig. 2.1). They are bounded by the following water courses (Fig. 2.2): i) Rienza River, to the north; ii) Piave River, to the east; iii) Brenta River and the terminal section of the Fresina Torrent, to the south; iv) Isarco River for a limited extension (between Bressanone and Bolzano) and the Adige River, to the west. These boundaries correspond to the Pusteria, Piave, Val Sugana and Adige valleys respectively.

The main mountain groups of the Dolomites (Fig. 2.2) are Croda Rossa (3139 m a.s.l.), Tofàne (3243 m), Cristallo (3216 m), Antelào-Sorapìs (3263-3205 m), Catinaccio (3004 m), Sassolungo (3181 m), Sella (3151 m), Marmolada (3342 m) – this latter being the highest – Civetta (3218 m) and Pale di San Martino (3193 m).

The study area corresponds to the Alta Badia valley which is located in the north-central sector of the Dolomites, mainly within the Province of Bolzano and partially within the Belluno Province (Veneto Region). The Alta Badia, as the whole Dolomites, has a peculiar position with respect to the Alpine chain, being located in its southernmost distal part, and shows a complex morphology as well as a wide altitude range (ca. 1300-3000 m). The area is bounded by towering Dolomite mountain groups: to the west, Gardenaccia (Gherdenacia) Group with its highest peaks Ciampani (2668 m) and the Sassongher (2665 m); to the east, Conturines Group including Piz Lavarela (3055 m) and Piz dles Conturines (3064 m) peaks; to the south-west, Sella Group including Piz Boè (3152 m), the highest peak. Finally, Setsas (2138 m) and Lagazuoi (2752 m) mountains bound the valley to the south-east.

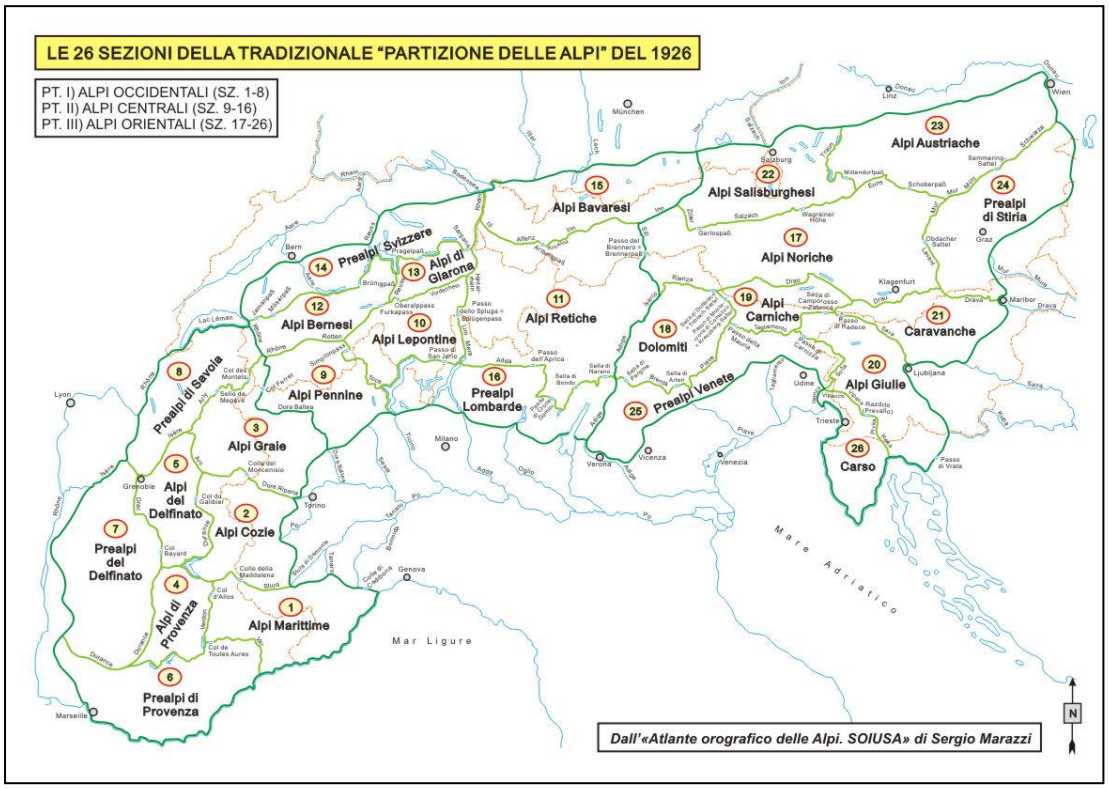

Fig. 2.1 Subdivision of the Alpine system according to the Orographic Atlas of the Alps (Atlante orografico delle Alpi): SOIUSA (Suddivisione Orografica Internazionale Unificata del Sistema Alpino); after Marazzi (2005). The Dolomites correspond to the sector number 18.

Concerning the hydrography, the Alta Badia valley is included within the River Adige catchment, next to River Piave one. The main permanent water courses are Rio Torto flowing from south-west to north-east and Rio San Cassiano flowing from south-east to north-west. Rio Torto is named Rio Gadera once overpasses the village of Corvara and continues toward the north after the confluence with Rio San Cassiano. They receive inputs from many ephemeral streams fed by rainfall and snowmelt waters and springs. The latter are mainly located at the contact between deeply fractured dolomite rocks and the underlying marly and clayey rocks, at a mean altitude of 2000 m. The main villages of the valley are located along the main water courses, they are: Colfosco/Kolfuschg (1640 m) and Corvara (1560 m) to the south-west, La Villa/Stern (1416 m) in the middle of the valley, San Cassiano/Sankt Kassian (1563 m) to the south-east and S. Leonardo/Sankt Leonhard (1365 m) to the north.

The climate can be classified as humid continental climate with warm summer (class "Dfb" according to Köppen, 1931) through the series of mean monthly air temperatures and precipitations recorded from 2008 to 2018 at the meteorological station of La Villa (1390 m). In particular, the mean annual precipitation recorded

between the period 2008-2018 is 970 mm and the mean annual temperature is 5.9°C, that is 1°C more with respect to the period 1990-2008 (cf. Panizza et al., 2011). The coldest month is usually January (mean temperature of -4.1°C), the warmest is July (mean temperature of 15.6°C). Winter months have the lowest values of mean precipitations, around 25 mm, and they coincide with the period of snow cover. The station of La Villa can be assumed as representative for the climate of the whole Alta Badia valley except for the high Dolomite groups ranging between 2600 m up to over 3000 m.

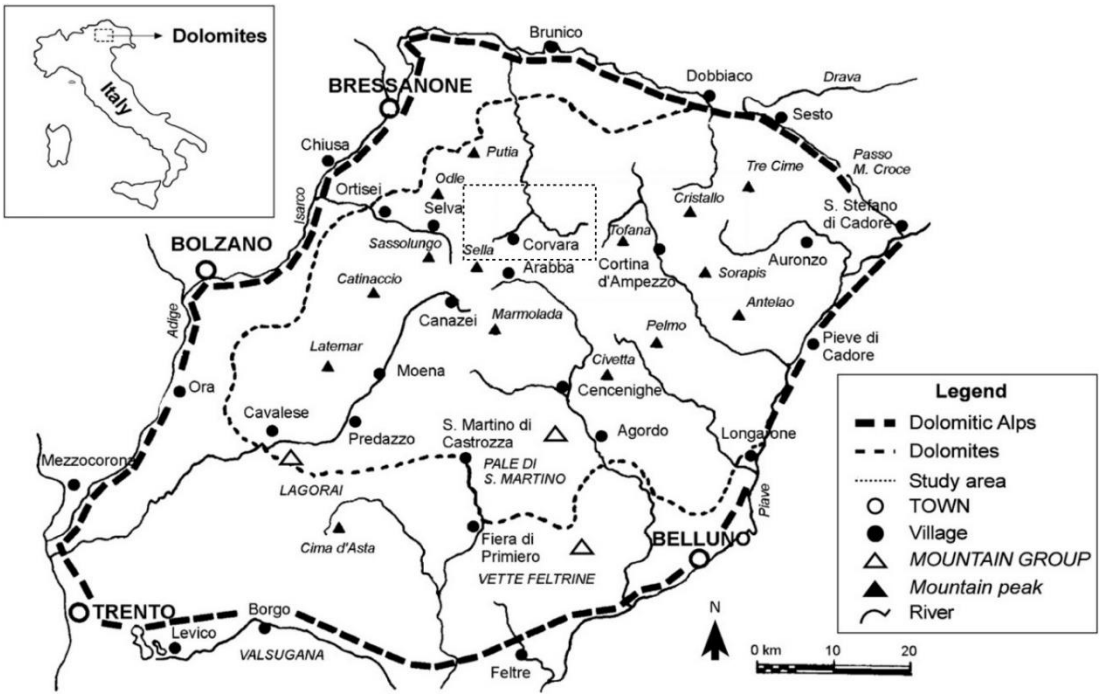

Fig. 2.2 Geographic setting of the Alta Badia valley (Dolomites) (after Bertoglio and De Simoni, 1979; modified by Borgatti and Soldati, 2010).

The Pisciadù peak weather station is representative of the climate in the latter areas; in fact, it is located at the south-eastern border of the valley at 2985 m and it records the air temperatures since July 2017. It revealed that the mean temperature of hottest months (June, July and August) ranges between 5.5 and 7.5°C. At that altitudes, the climate can be then classified as humid continental with cold summer (class "Dfb" according to Köppen, 1931).

Regarding snow precipitation, the weather station of Piz la Ila at 2050 m (http://meteobrowser.eurac.edu/app_direct/meteobrowser/) recorded a mean snow thickness of 70 cm during winter season 2016/2017.

2.2 Geological and structural setting

From a geological viewpoint, the Dolomites are included in the eastern sector of the Southern Alps, the latter understood as a segment of the continental African margin which underwent to deformation from the Late Cretaceous to the Quaternary, firstly with European vergence and later, during the Cenozoic, with African vergence. To the west the Dolomites are bounded by the Giudicarie Line and to the north by the Pusteria Line (Fig. 2.3) which are Periadriatic Neogene lineaments; whilst to the south and to the south-west they are enclosed by the Valsugana and Pieve di Cadore thrusts respectively. From the structural viewpoint, these tectonic lineaments separate the Dolomites from the main Alpine chain to the north and from the Prealps to the south. The stratigraphic sequence (Fig. 2.4) includes a Permo-mesozoic sedimentary succession that covers the Hercynian crystalline basement through an unconformity.

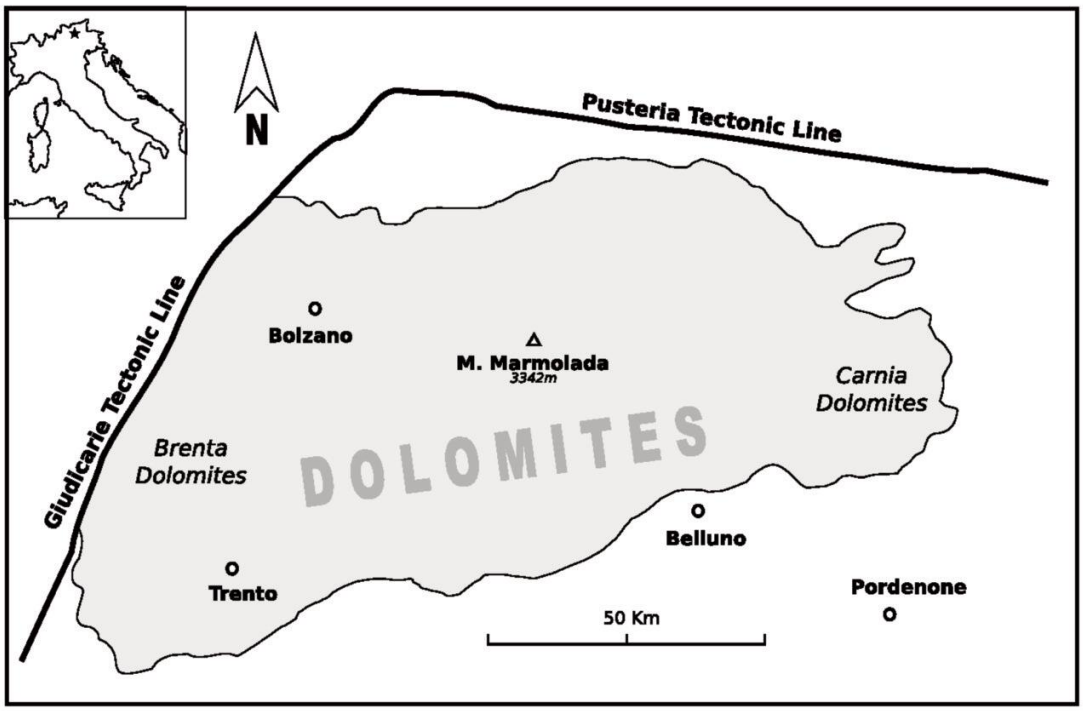

Fig. 2.3 Location of the Dolomites (after Panizza, 2009).

The geological history of the Dolomites started in the Permian. At that time the western Dolomites were affected by a volcanic event responsible for the emplacement of rhyolites, rhyodacites and dacites ("porphyries") on the Hercynian crystalline basement (Figs. 2.4 and 2.5) – constituted by metamorphic rocks (e.g. grey schists, phyllites and paragneiss) and underlay by a post-volcanic sedimentary succession of Permian terrigenous deposits (*Val Gardena Sandstone*, *Bellerophon Formation*). The

Mesozoic was marked by the development of carbonate platforms (e.g. *Werfen Formation, Contrin Formation, Marmolada Limestone, Sciliar Formation, Dolomia Cassiana, Dolomia Principale*) which were controlled by a series of subsidence and uplift events. The carbonate platforms were surrounded by deep marine basins occasionally filled by volcanic, volcaniclastic and terrigenous sediments (*Moena Formation, Livinallongo Formation, Wengen Formation, San Cassiano Formation*) (Figs. 2.4 and 2.5). During the Cenozoic the Alpine orogenesis occurred and during the Quaternary the exogenous processes shaped the landscape till present-day.

The geological history of the Alta Badia valley, as well as its geological features generally resemble those of the whole Dolomite region. The Alta Badia valley is included in the Geological Sheet n°28 "La Marmolada" (1:50,000 scale) of the Geological Map of Italy (Servizio Geologico d'Italia, 1977) and in the "Geologische Karte der Westlichen Dolomiten – Carta Geologica delle Dolomiti Occidentali" (scale 1:25,000) of the Bolzano Province (Brandner et al., 2007). Hereafter the geological formations are named and described by referring to the latter map which is the most recent and updated one.

In Alta Badia the base of the stratigraphic sequence is constituted by limestones, dolomites, sandstones, breccias and marls from the Upper Permian-Middle Triassic, affected by a dense network of fractures: *Bellerophon*, *Werfen*, *Morbiac*, *Moena*, *Contrin*, *Buchenstein*, *Zoppé* formations (Bosellini et al., 2003; Brandner et al., 2007). They outcrop on the southern foothills of the Gardenaccia plateau and on the north-west facing slope of the Piz la Ila – Col Alt mountain ridge. The base of these Permo-Triassic formations (*Bellerophon Formation*) was formed during the Upper Permian under shallow tropical waters often subject to strong evaporation and to the mechanic action of waves.

During the Upper Permian-Lower Triassic repeated transgressions and regressions originated the heterogeneous sequence of the *Werfen Formation* constituted by alternation of fossiliferous limestones, marls and shales. During the Upper-Anisian (Middle Triassic) an important transgression phase occurred. At that time, in the area, there was a shallow sea environment where the first growth of calcareous platform (*Contrin Formation*) occurred (Bosellini, 1996) contemporaneously to the deposition of bituminous-micritic limestones with intercalations of terrigenous clasts (*Morbiac Formation*) and fine-grained breccias (*Moena Formation*).

The transgression continued to the Ladinian, leading to the deposition of bituminous limestones with radiolarians and flint layers and nodules (*Buchenstein Formation*) and to deep-sea turbidites (*Zoppè Formation*).

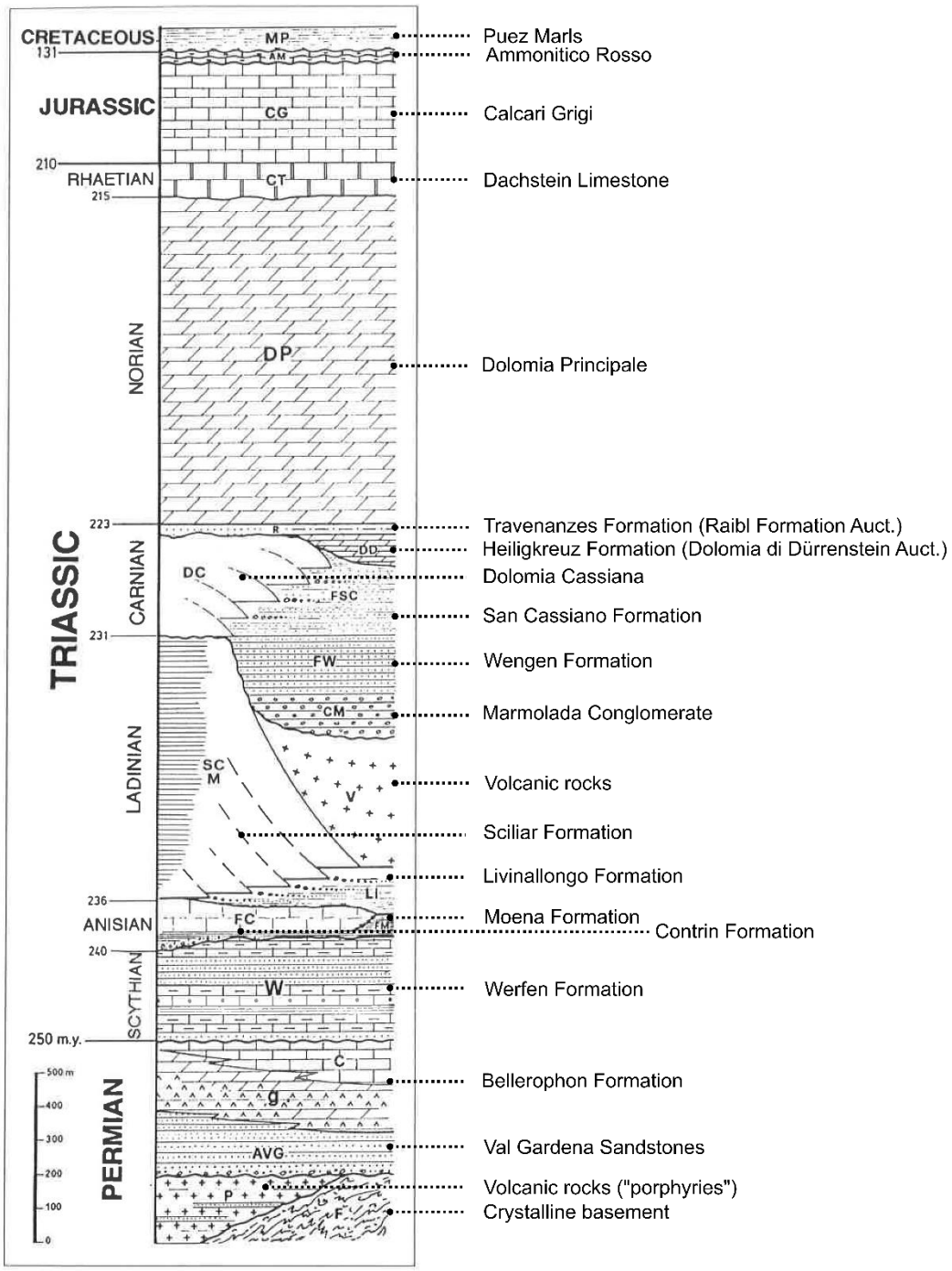

Fig. 2.4 Schematic stratigraphic sequence of the Dolomites (modified after Carton and Soldati, 1993).

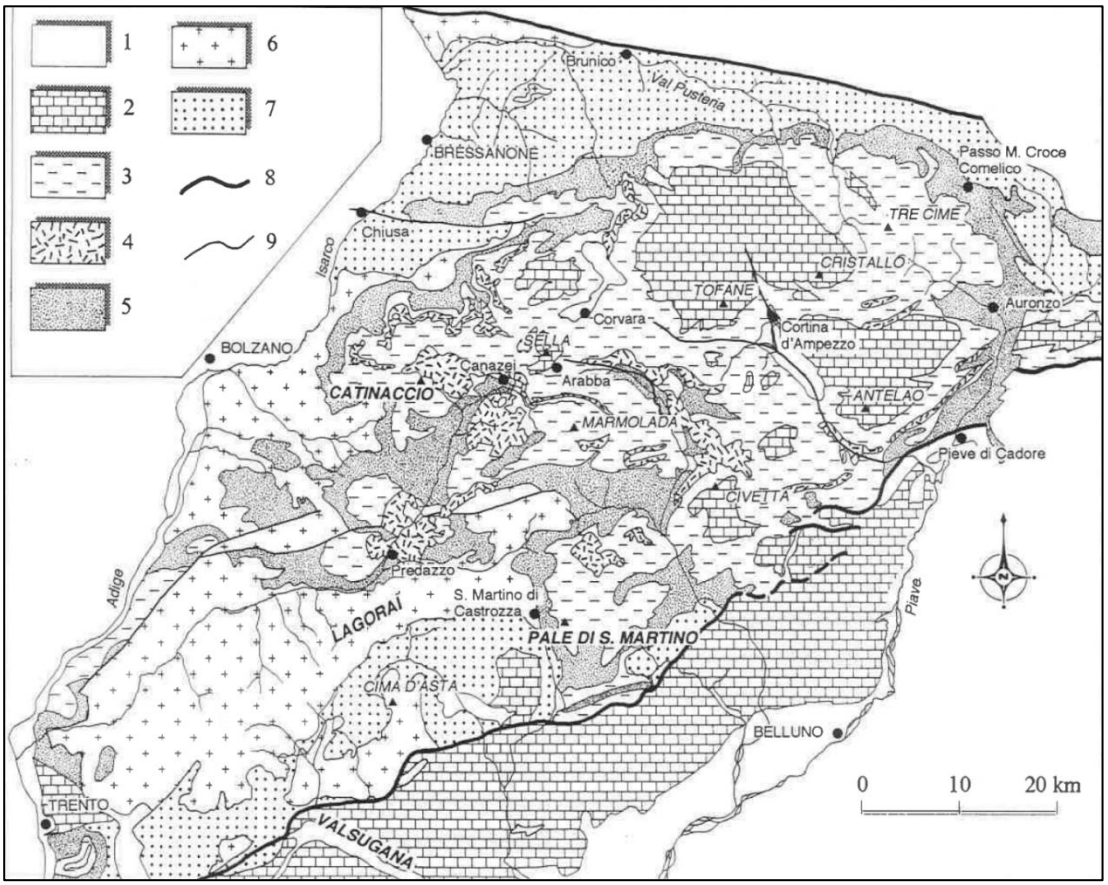

Fig. 2.5 Geological schematic map of the Dolomites. Legend: 1) Plio-Quaternary deposits; 2) dolomitic and carbonatic rocks, Norian-Cretaceous (*Dolomia Principale*, *Dachstein Limestone*, *Calcari Grigi*, *Ammonitico Rosso*); 3) dolomitic and clastic rocks, Carnian (*Dolomia Cassiana*, *San Cassiano Formation*, *Heiligkreuz*, *Travenanzes Formation*); 4) dolomitic and clastic rocks, Ladinian (*Sciliar Formation*, *Livinallongo Formation*, volcano-clastic deposits); 5) clastic rocks, Permian Lower Anisian (*Val Gardena Sandstones*, *Bellerophon Formation*, *Wengen Formation*); 6) volcanic rocks, Permian (rhyolites, rhyodacites and dacites); 7) Crystalline Basement, Carboniferous (phyllites, micaschists and paragneiss); 8) main tectonic lineaments; 9) secondary tectonic lineaments (after Carton and Soldati, 1993).

In the south-central part of the valley – along Piz la Ila-Col Alt mountain ridge and east of Campolongo Pass – the *Fernazza Group* and the *Caotico Eterogeneo* outcrop. *Caotico Eterogeneo* is constituted by megabreccias in volcanic matrix resulting from deep-sea mega-slumps possibly triggered by earthquakes and volcanic activity preceding the major volcanic eruption phase which occurred in Upper Ladinian (Middle Triassic). During the latter, pillow lavas, tuffs and volcanoclastic sandstones of the *Fernazza Group* were originated.

On the Pralongià plateau and at the foothills of the Sella Group, a thick volcanoclastic sequence crops out (*Wengen Formation*). It is constituted by the debris produced by

the dismantle of the Upper Ladinian volcanic apparatuses (located to the west) and deposited on a subsiding deep sea-floor between the Ladinian coral reefs (Viel, 1979). At the end of the Ladinian to the Lower Carnian, subsidence and volcanic activity stopped, allowing the development of a tropical shallow-sea where carbonate sediments, that today making up the rocks of the *Sciliar Group*, were deposited. The latter group includes: the *Sciliar Subgroup* composed by post-volcanic platform limestones and well stratified dolomite (lagoon facies), outcropping along the basal portion of the Sella and Gardenaccia Group; the *Denti di Terra Rossa Formation* constituted by post-volcanic dolomites, outcropping on the north and western slopes of the Sella Group; the *Dolomia Cassiana* constituted by different dolomite facies – platform, platform margin and platform scarp – outcropping with its platform facies on the Setsas. At the same time, the basins surrounding the carbonate platforms were filled by marine sediments, constituting alternation of marls, marly limestones and calcareous marls (*San Cassiano Formation*) whose outcrops are visible on the upper part of the Pralongià and Piz de Surega.

At the end of the Carnian, subsidence and sedimentation started again, allowing for the deposition of carbonate and terrigenous sediments, originating alternation of green and red marls, argillaceous schists, oolitic limestones with dolostone layers and constituting the *Pordoi Formation*, *Heiligkreuz Formation* (*Dürrenstein Formation* auct.; Pisa et al., 1980; Bosellini, 1984; De Zanche et al., 1993; Preto and Hinnov, 2003) and *Travenanzes Formation (Raibl Formation* auct.; Assereto et al., 1968; Pisa et al., 1980; De Zanche et al., 1993; Bosellini et al., 1996). They outcrop locally in the valley at the foothills of the Setsas mountain and Sella and Conturines groups.

The upper portion of the Sella and Gherdenacia groups and the basal portion of the western slope of the Conturines are constituted by the *Dolomia Principale* a cyclic sequence of meter-thick dolomites (Fig. 2.6). The *Dolomia Principale* was formed during the Upper Carnian and Norian in a tidal flat environment; thanks to the continuous subsidence it reached remarkable thickness, up to 500 m.

At the end of the Triassic there was a sensible change of the depositional environment due to a sea deepening followed by the deposition of limestones during the Jurassic. The more extensive outcrops of this upper part of the sequence can be found on the top of the Conturines (*Dachstein Limestone* and *Calcari Grigi*, Rhaetian-Pliensbachian), while more restricted outcrops occur at the top of the Sella and Gardenaccia mountain groups (*Gardenaccia Formation*, *Ammonitico Rosso*,

Pliensbachian-Tithonian). They outcrop together with pelagic-hemipelagic sediments of the Lower Cretaceous (*Puez Formation*, Valanginian-Aptian) which close the depositional sequence of the area and show, in their upper part, terrigenous inputs preluding the Alpine orogeny (Lukeneder, 2010).

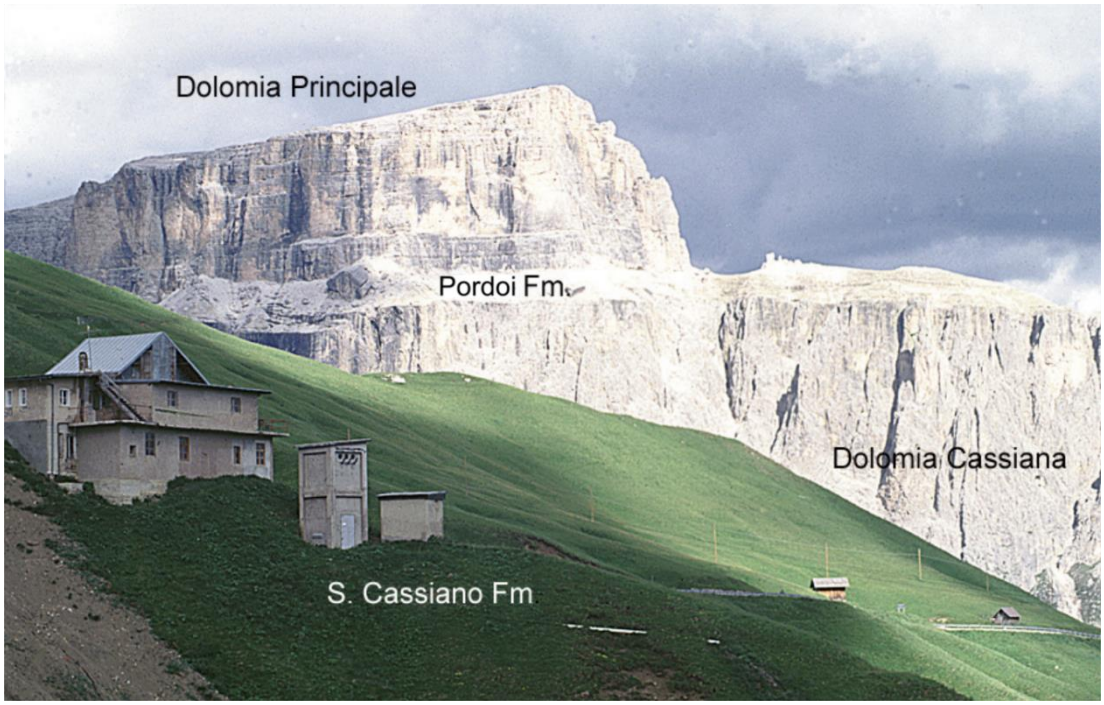

Fig. 2.6 Geological formations building up the Sella Group, view from the Sella Pass (after Bruschi et al., 2009).

From the tectonic viewpoint, the Alta Badia valley (Fig. 2.7) derived from four major deformational phases. The first one occurred during the Upper Permian leading to subsidence and fragmentation of the sedimentary basin. The other three phases, that are the eoalpine, meso-alpine and neo-alpine compression phases, are related to Alpine orogeny and in particular to the Cenozoic shortening of a Mesozoic passive continental margin of the Tethys Ocean (Doglioni 1987; Doglioni and Carminati 2008). The eoalpine and mesoalpine compression phases (Upper Cretaceous – Lower Eocene) were responsible for the origin of overthrusts and folds with north to south and north-northeast to south-southeast axes direction. During the Miocene the dolomitic region emerged from the sea. The neo-alpine orogenetic phase, the most important one, took place during the Neogene and caused overthrusts and folds with an east-west axis direction and right and left conjugate strike faults (Doglioni, 1987).

During the Pliocene and the Lower Pleistocene, uplifts and minor tilts affected the Dolomite region. From the Upper Pleistocene to the Holocene, the uplift of the area

included an isostatic component due to glacier retreat. Geomorphological evidence of neotectonics activity have been recognized in the Alta Badia valley (Corsini and Panizza, 2003).

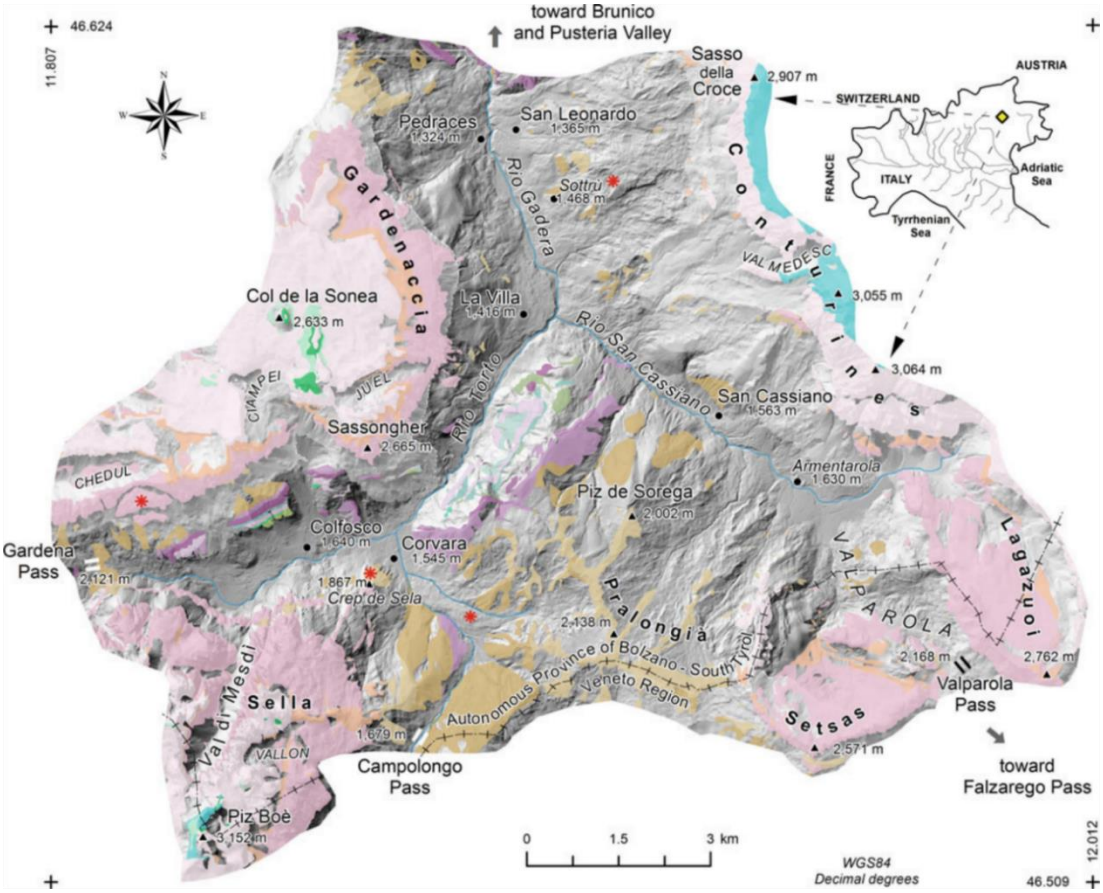

Fig. 2.7 Geological setting of the Alta Badia valley. Colours correspond to those used in the stratigraphic scheme of Fig. 2.8. Red marks refer to the landslides shown in Fig. 2.14 (after Marchetti et al., 2017).

In particular, two tectonic lineaments, which have been reactivated during the Pliocene and the Quaternary, were recognized: i) the north-south trending fault along the Val di Mesdì (Sella Group); the right strike fault with north-northwest to south-southeast trend along the Col Alt-Pralongià – Passo Incisa alignment. Jointing and faulting related to tectonic and neotectonic compressive stresses have played an important role in determining slope instability in the Alta Badia valley (Corsini et al., 2005).

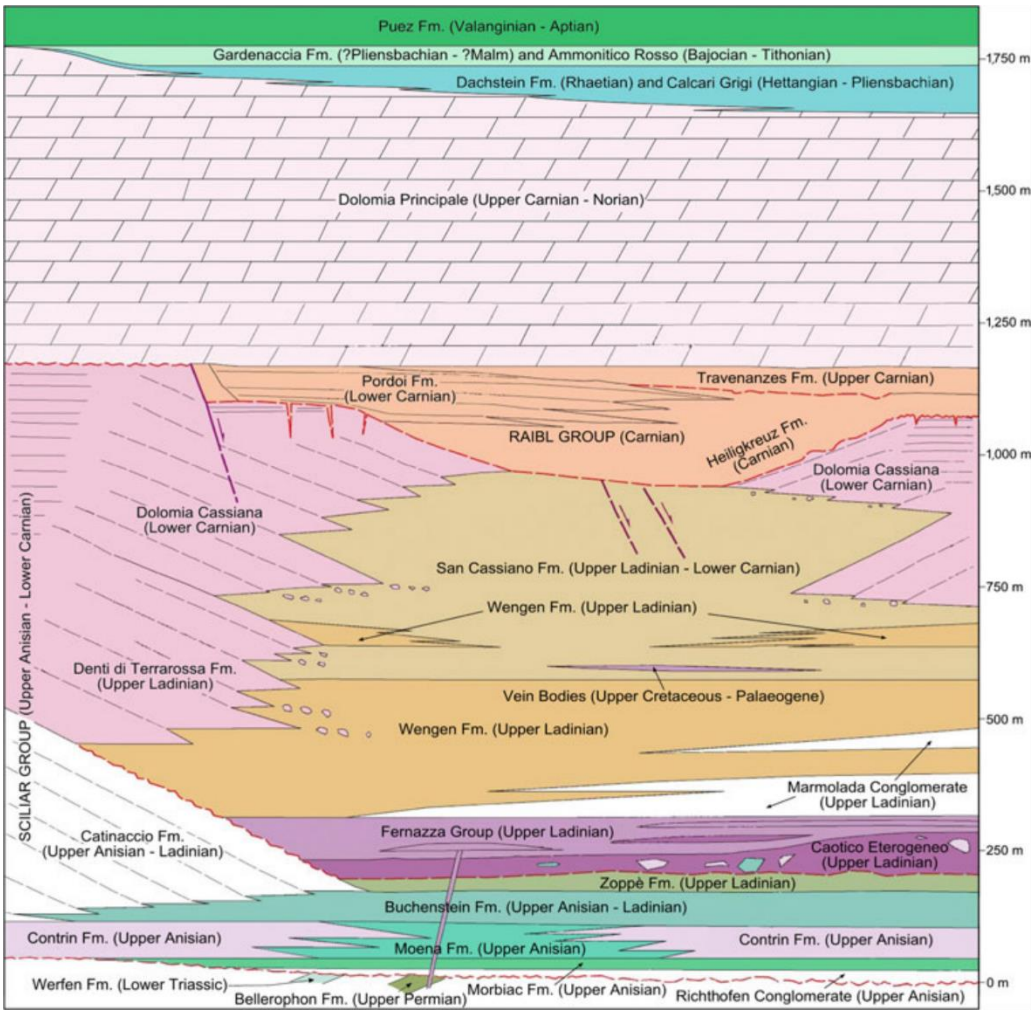

Fig. 2.8 Stratigraphic scheme of the geological sequence characterizing the Alta Badia and surrounding areas (Triassic-Lower Cretaceous). The dolomite formations are rose-coloured. The formations depicted in white are not outcropping in the Alta Badia (after Marchetti et al., 2017).

2.3 Geomorphology

The morphological features of the Dolomites are the result of complex geomorphological processes acting during the Quaternary, that were particularly effective since the end of the LGM. The effects of Pleistocene glaciations as well as the climate changes occurring during the Holocene modelled the Dolomite landscape (Fig. 2.9). At the same time the morphology of the region is strictly connected with its complex tectonic history. Varied (in space and time) morphostructural and morphoclimatic conditions have determined a significant variety of landforms (Carton and Soldati 1993; Gianolla et al., 2008).

As for the whole Dolomites, landforms and processes in the Alta Badia valley are deeply controlled by lithological and tectonic features as well as by the succession of different morphoclimatic phases during the Quaternary. The morphology of the Alta

Badia is characterized by high mountain groups with deeply fractured vertical cliffs, separated by wide valleys with gentler and undulated slopes (Fig. 2.10). The traces left by glaciers during the LGM are the witnesses of the oldest geomorphic process recognizable in the valley. More widespread and better preserved are the traces left by glaciers during the Lateglacial including till deposits and moraine ridges whose position and elevation is fundamental for the reconstruction of glacial fluctuations.

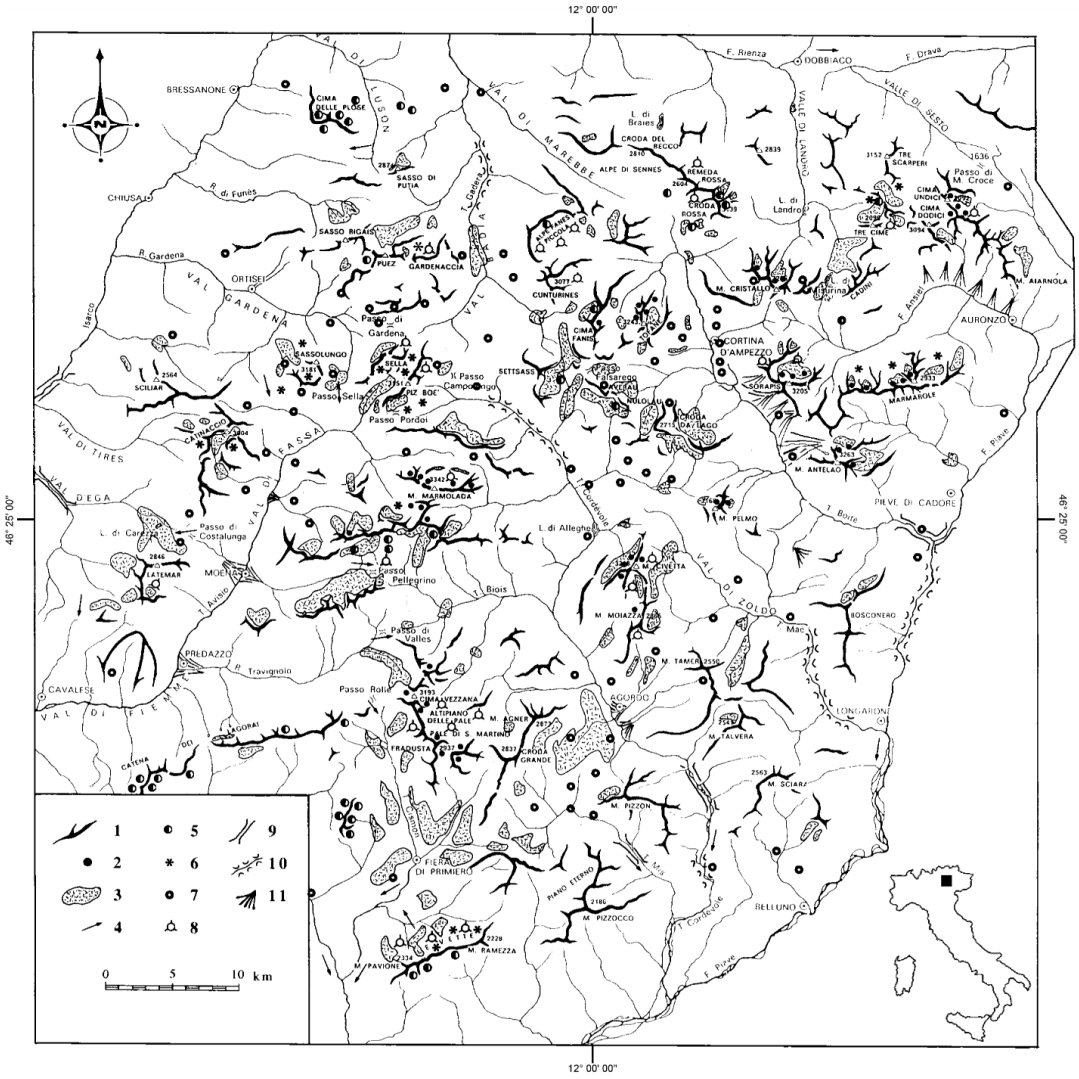

Fig. 2.9 Geomorphological schematic map of the Dolomites. Legend: 1) mountain crests; 2) glaciers; 3) main areas of glacial deposition; 4) movement direction of Pleistocene glaciers; 5) relict rock glaciers; 6) significant cryonival landforms (e.g. protalus ramparts, patterned grounds); 7) main landslides; 8) areas intensely affected by karst processes; 9) troughs; 10) deeply eroded fluvial valleys; 11) talus cones and alluvial fans (after Soldati, 2010).

The intense jointing of the dolomite massifs, glacial debuttressing as a consequence of the retreat of Pleistocene glaciers, as well as permafrost melting, and the high relief energy have favoured the onset of rock falls and rock slides. The water availability

from rainfall and snow melt together with the poor geomechanical features of the terrains outcropping at the foothills of the dolomite massifs and within the valleys has favoured the occurrence of landslides mainly constituted by earth flows and slides. Short and intense rainfall caused slope incision and debris flows on debris cones and valley bottoms respectively.

Landscape modifications induced by human activity have increased during the last fifty years and are mainly relevant to tourism (especially ski-related one) on which the local economy is based.

In the Alta Badia valley detailed geomorphological investigations have been carried out by Panizza et al. (1973), Carton et al. (1978, 1980), Corsini et al. (1998, 1999, 2001), Corsini and Panizza (2003), Soldati et al. (2006).

The landforms originated by processes which are and were active in the study area are described below with reference to the geomorphological map implemented by Panizza et al. (2011) and the synthesis by Marchetti et al. (2017).

2.3.1 Structural landforms

As mentioned above, the morphology of the Alta Badia valley is influenced by lithology, stratigraphy and tectonics resulting in the differential erosion of the outcropping formations (Figs. 2.10 and 2.11). Dolostone build vertical to subvertical cliffs while gentler slopes characterize the lower elevations where rock formations with diffuse intercalations of pelitic layers outcrop. Structural terraces, often covered by debris cones, characterize the area. They are typically due to differential erosion and can be found where terrains with a high percentage of pelite are in alternation with dolostone strata. Worthy of notice are the structural terraces located on the northern slope of the Sella Group and on the southern slope of Piz dles Conturines where the terrigenous evaporitic sequence crop-out (Pordoi and Travenanzes formations respectively).

The direction of valleys, as well as the occurrence of saddles, are generally controlled by the presence of thrusts, faults and folds, as is the case of the northern stretch of the Alta Badia valley, the San Cassiano valley, the Val di Mesdì and of the Gardena and Valparola passes.

Fig. 2.10 Southwestern view of the Alta Badia valley. The morphology of the area is characterized by high mountain groups with deeply fractured vertical cliffs, separated by wide valleys with gentler and undulated slopes. Extensive debris cones due to gravity-induced slope processes characterise the foot of the Sassongher massif (on the left) and of the Conturines southern cliff (in the background). The Pralongià plateau stands in the central part of the picture, to the right of the Sassonger massif and opposite the Conturines southern cliff (photo by F. Planinschek, courtesy of Tourist Board Alta Badia).

2.3.2 Glacial landforms

The former presence of glaciers in the Alta Badia valley is proved by a series of erosional and depositional landforms. They correspond to frontal and lateral moraine ridges and till (Fig. 2.12), often remodelled by gravitational processes or masked by soil and vegetation. Further evidence is offered by glacial cirques, hanging valleys and superficial erosional features.

Quite remarkable glacial cirques occur on Lagazuoi and Setsas, and within the Val de Chedul (Gardenaccia Group). Less extensive glacial cirques can be found on the eastern summit surfaces of the Sella and Gardenaccia groups, they occur in step-like sequences possibly related to the occurrence of the edges of the structural scarps.

The major cirques of the study area are also in connection with hanging valleys formed during the LGM at the confluence of tributary glacier tongues into the main valleys.

Worthy of notice is the Val de Mesdì hanging valley, within the Sella Group, where the difference between the tributary and the main valley bottoms is of some 200 m.

Fig. 2.11 Vertical dolomite strata at Crep de Munt (Sella Group); photo from Bruschi et al. (2009).

Rock masses modelled by glacial erosion characterize the summit surfaces of Gardenaccia and Sella mountain groups and Lagazuoi mount. In some cases, striation can be found as indicators of glacier flow direction. For example, on the eastern side of the Sella Group striations mainly show an eastern direction following the slope dip. Similar erosional features were identified on the Setsas whose smooth surface and rounded crest can be seen as an indicator of the transflucence of an ice mass from north-west to south-east, towards the Cordevole Valley.

Glacial deposits mainly occur on the right side of the Gadera stream and along the valley of S. Cassiano. They generally include accumulations of dolomite blocks and pebbles, and secondarily arenitic and calcarenitic ones, enveloped by a silty-clayey matrix. The glacial deposits were preliminary attributed to the Lateglacial or to the LGM period on the basis of their elevation within the valley. Generally, those deposits located over the elevation of 1800 m a.s.l. were referred to the LGM period while those located at a lower elevation were considered Lateglacial in age, being 1800 m the

lowest elevation at which glacially transported allochtonous/exotic clasts were found in the area.

Remnants of Lateglacial moraine ridges are still preserved, especially in the south-eastern sector of the area, e.g. at Pedraces and upstream La Villa, within the valley of San Cassiano, at Armentarola, as well as at Valparola pass and on the Setsas and Lagazuoi mounts.

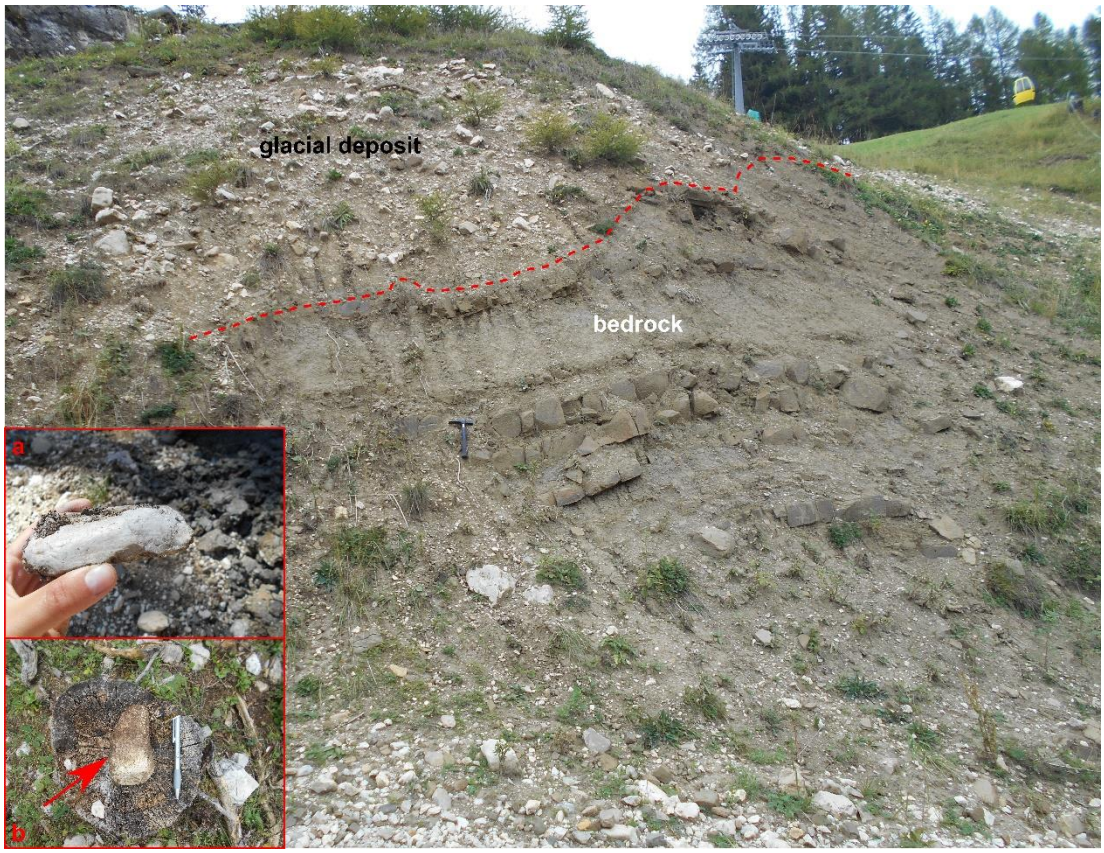

Fig. 2.12. Glacial deposit located along the slopes of the Pralongià plateau, possibly reworked by slope processes and overlying the bedrock (Wengen Formation). Within the glacial deposits observed in the Alta Badia valley was possible to retrieved levigated and striated clasts (a) and iron-shaped cobbles (b) witnessing a glacial origin for the deposits.

2.3.3 Periglacial landforms

Since the Lateglacial, periglacial processes became increasingly important, especially at high altitudes, at the base of the dolomite cliffs and on the top of the mountain groups. In particular, frost weathering processes caused detachment of debris from the dolomite cliffs, which contributed to the emplacement of extensive talus cones and scree slopes. The debris was mobilized by gravitational, torrential and secondarily by cryogenic processes. The size and distribution of the debris cones depend principally

on the jointing of the rock masses and secondarily on slope aspect (Panizza et al., 2011).

According to the rock glacier inventory implemented by the Autonomous Province of Bolzano (Mair et al., 2012), two main active rock glaciers can be found in Alta Badia. One is located northwest of Piz Boè at an elevation of 2900-3000 m, and another one on the northern part of the Sella Group summit, at La Masores de Murfreit, at some 2700 m (Fig. 2.13). In turn, two inactive tongue-like shaped rock glaciers can be observed in the vicinity of the Valparola Pass. One is departing from the Valparola Pass toward north-west between 2100-2250 m and the other one toward south-west between 2000-2250 m; they consist of large dolomite blocks which are likely to have been detached from the southwestern side of Lagazuoi and accumulated on an ancient glacier or icefield (Ghinoi and Soldati, 2017).

Fig. 2.13 Active rock glacier front located along the northern side of the Sella Group; photo from Mair et al. (2015).

2.3.4 Gravity-induced landforms

Landslides of different type and size characterize the landscape of the Alta Badia being the most common and widespread Quaternary deposits in the area (Fig. 2.14). Studies on landslides and climate change (Soldati et al., 2004; Borgatti et al., 2006; Borgatti and Soldati, 2010) demonstrated that the first phase of marked high slope instability occurred during the Preboreal and Boreal (some 11,500-8500 years BP) following the withdrawal of the LGM ice mass from the valley. At that time the dolomite slopes were affected by large-scale translational rock slides (e.g. Passo Gardena landslide) while rotational slides and flows (e.g. Corvara landslide) occurred in correspondence

of the underlying pelitic formations. The latter are likely to have been favoured by high groundwater levels due to an increase in precipitation and/or permafrost melting. Another phase of intensification of landslide events was recorded during the Sub-Boreal (about 5800-2000 years BP), mainly rotational slides and/or flows occurred during that period. Many of the events dated can be considered as reactivations of older movements possibly due to an increase in precipitation in the whole Alpine region.

Landslide activity has been also influenced by structural features. In particular, landslides have been favoured by (i) the presence of brittle and deeply jointed rocks (e.g. dolomite) which are generally affected by rock slides and rock falls in correspondence of the sub-vertical cliffs, and (ii) the occurrence of ductile lithologies (e.g. San Cassiano and Wengen formations) which favour the development of earth slides and flows on the middle and lower parts of the slopes.

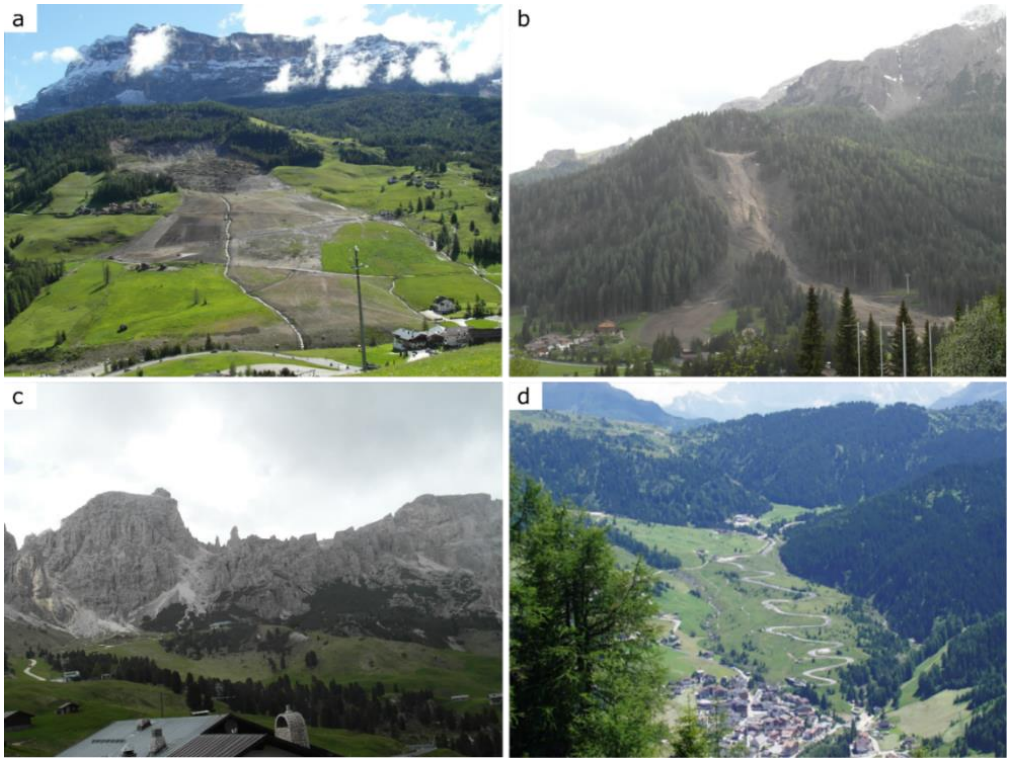

Fig. 2.14 Landslides in the Alta Badia: a) Sottrù landslide (cf. Ghinoi et al., 2014), a sudden reactivation of a historical earth slide/earth flow occurred in December 2012 on the right flank of Rio Gadera at the foot of the Conturines group (photo June 2016); b) Crep de Sela landslide, a rock/debris slide evolving into a muddy debris flow detached in April 2014 from the lower slopes of the Sella group in the vicinity of Corvara (photo June 2016); c) Passo Gardena landslide, rock slide which affected the dolomite cliffs of the northernmost part of the Gardenaccia mountain group in the early post-glacial (photo June 2016); d) Corvara landslide (cf. Corsini et al., 1999), an active earth slide/earth flow which reaches the homonymous village determining damages to the winding road leading to Campolongo Pass (photo from Marchetti et al., 2017).

2.4 State of the art on glacial studies within the Alta Badia valley

In the Alta Badia valley, evidence of past glacier fluctuations is found in the widespread glacial deposits, which have been attributed, by previous authors, to the LGM and to the Lateglacial periods. According to literature, during the LGM the Alta Badia valley was covered by an extensive glacial tongue, coming from the north, which gave way to local valley glaciers during the Lateglacial.

In their topical book, Penck and Brückner (1909) inferred that the primary feeding area of the main glacial tongue was from the Pusteria valley (Fig. 2.15). The glacier might have had an upward and upstream movement within the valley, reaching some 2300 m in altitude. The glacier provenience was inferred from the finding of exotic boulders of phyllites in correspondence of the locality Prati di Armentara (east of the village of S. Leonardo) and granite boulders in correspondence of S. Cassiano at an altitude of 1600 m a.s.l.; their provenance was identified from the Pusteria valley, where crystalline rocks do crop out (Penck, 1909).

Von Klebelsberg in 1927 described moraine deposits extending on both side of the Gadera stream, north of the village of La Villa (von Klebelsberg, 1927). He also described two moraine ridges located at ca. 1 km respectively south-west and south-east of La Villa which were supposed to have been deposited during a retreating phase of the LGM glacial tongue. The same author described in correspondence of Colfosco at ca. 1645 m a glacial deposit which he attributed to the Gschnitz stadial. He also supposed the presence of two paleoglaciers located respectively north of Colfosco and in Val di Mesdì (south of Colfosco) both attributed to the Daun stadial.

The hypothesis of a northern provenance of the main glacial tongue was resumed also by Mutschlechner (1932, 1933) (Figs. 2.16 and 2.17) who retrieved quartz phyllites south of Alting locality at 1580 m (at Freina-Berg in Fig. 2.17) and in the surroundings of the Valparola Pass. In addition, according to this author, in the Badia valley, during the LGM, local glaciers likely reached remarkable dimensions, partly joining the main glacier tongue. This was confirmed by the Mutschlechner's finding of glacial deposits located on the right side of the Rio Torto and including polished clasts attributed by the author to the *Calacari Grigi* formation outcropping few kilometers further south on the Sella Group and likely transported toward the valley by a local glacier. The LGM glaciers covered the main mountain passes (e.g. Campolongo and Falzarego) as well as the Pralongià plateau. For what concern the Lateglacial deposits,

Mutschlechner found very difficult to identify well preserve moraine ridges in the area which could have eventually been attributed to one of the Lateglacial stadials. He basically shared and confirmed the findings of von Klebelsberg (1927) and additionally identified a small moraine ridge which he attributed to the Daun stadial, north of the Setsas at 2300 m.

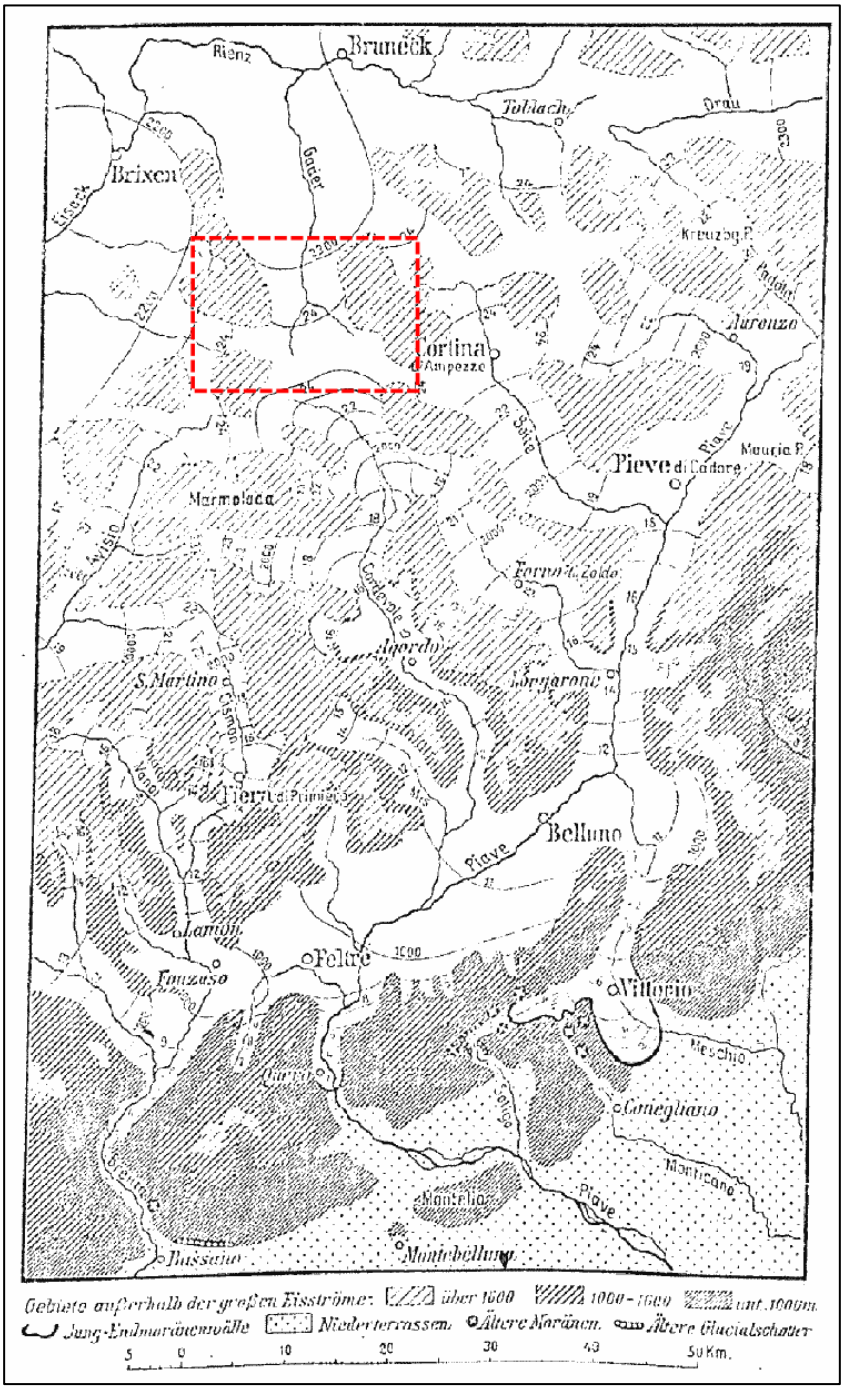

Fig. 2.15 Piave and Brenta glaciers during the LGM (from Brückner, 1909). Red square indicates the location of the Alta Badia valley.

In correspondence of the locality Piz de Sorega, Mutschlechner (1933) mapped widespread glacial till as well as a muddy deposit of glacial origin, the latter was probably exposed due to the activity of the near Corvara landslide. Moreover, he identified the presence on the Pralongià of dolomite boulders from Sciliar Formation and Dachstein Limestone formation (Sciliar Dolomite and Dachstein Dolomite auct.) for which he assumed they came from the Settsass massif, since the latter is of the same lithological nature.

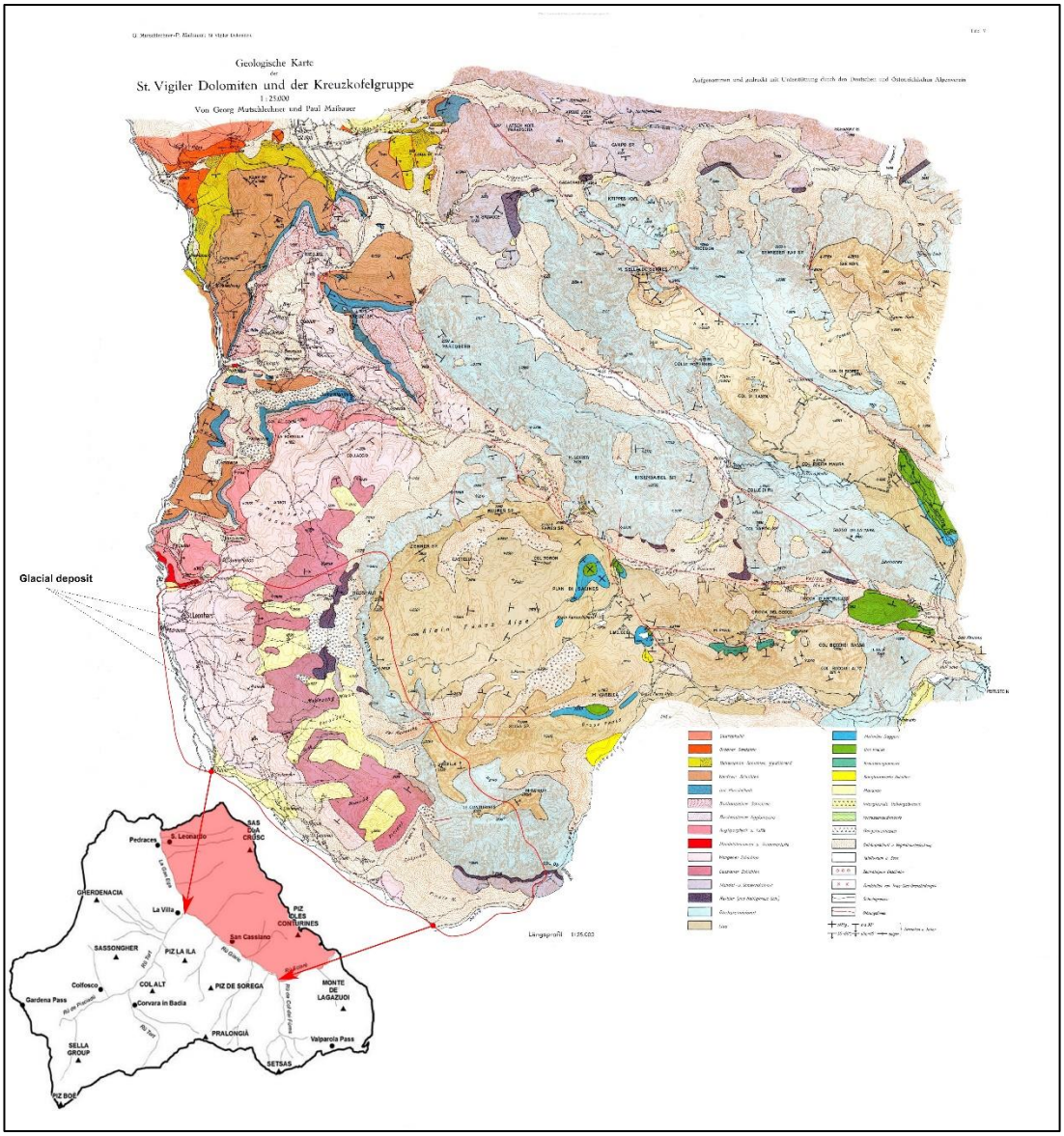

Fig. 2.16 Geological map, retrieved from Mutschlechner (1932), relevant to the area on the right side of the Gadera stream (highlighted in red in the sketch map on the left corner) including the Conturines and Fanes mountain groups. Glacial deposits are represented in light yellow.

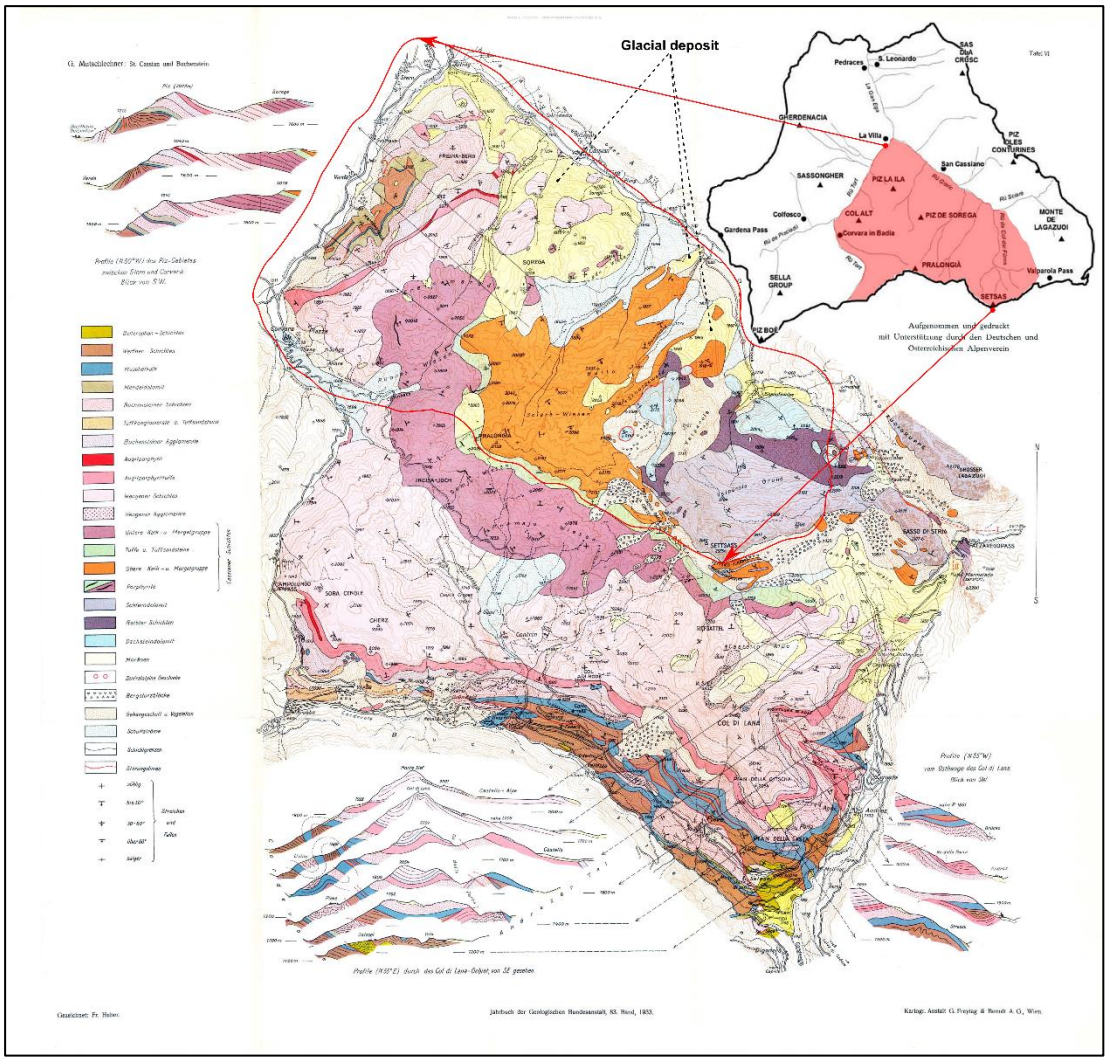

Fig. 2.17 Geological map, retrieved from Mutschlechner (1933), relevant to the south-central part of the Alta Badia valley (highlighted in red in the sketch map on the upper right corner). Glacial deposits are represented in light yellow.

The Lateglacial is characterized by the relatively quick disappearance of the LGM icefield replaced by local valley glaciers departing from the highest Dolomites groups surrounding the valley (Marchetti et al., 2017). Valley glaciers were responsible for the deposition of frontal and lateral moraines. This moraine remains are witnesses of the presence in the area of large local valley glaciers moving toward the north. As found by G.B. Castiglioni (1964) who mapped frontal moraine cordons in the Alta Badia valley and assigned them, on the basis of morphostratigraphic evidence, alternatively to the Lateglacial stadials of Bühl (Sciliar), and Gschnitz. In particular, G.B. Castiglioni mapped three moraine ridges attributed to the Bühl (Sciliar) within the Gadera stream valley – whose presence was not confirmed by present-day field surveys (cf. Panizza et al., 2011) – as well as one moraine ridge in Valparola attributed to the same stadial (Fig. 2.18). Moreover, several moraine ridges of the Gschnitz

stadial were mapped east of the mount Setsas. No Daun moraines were mapped by G.B. Castiglioni within the valley.

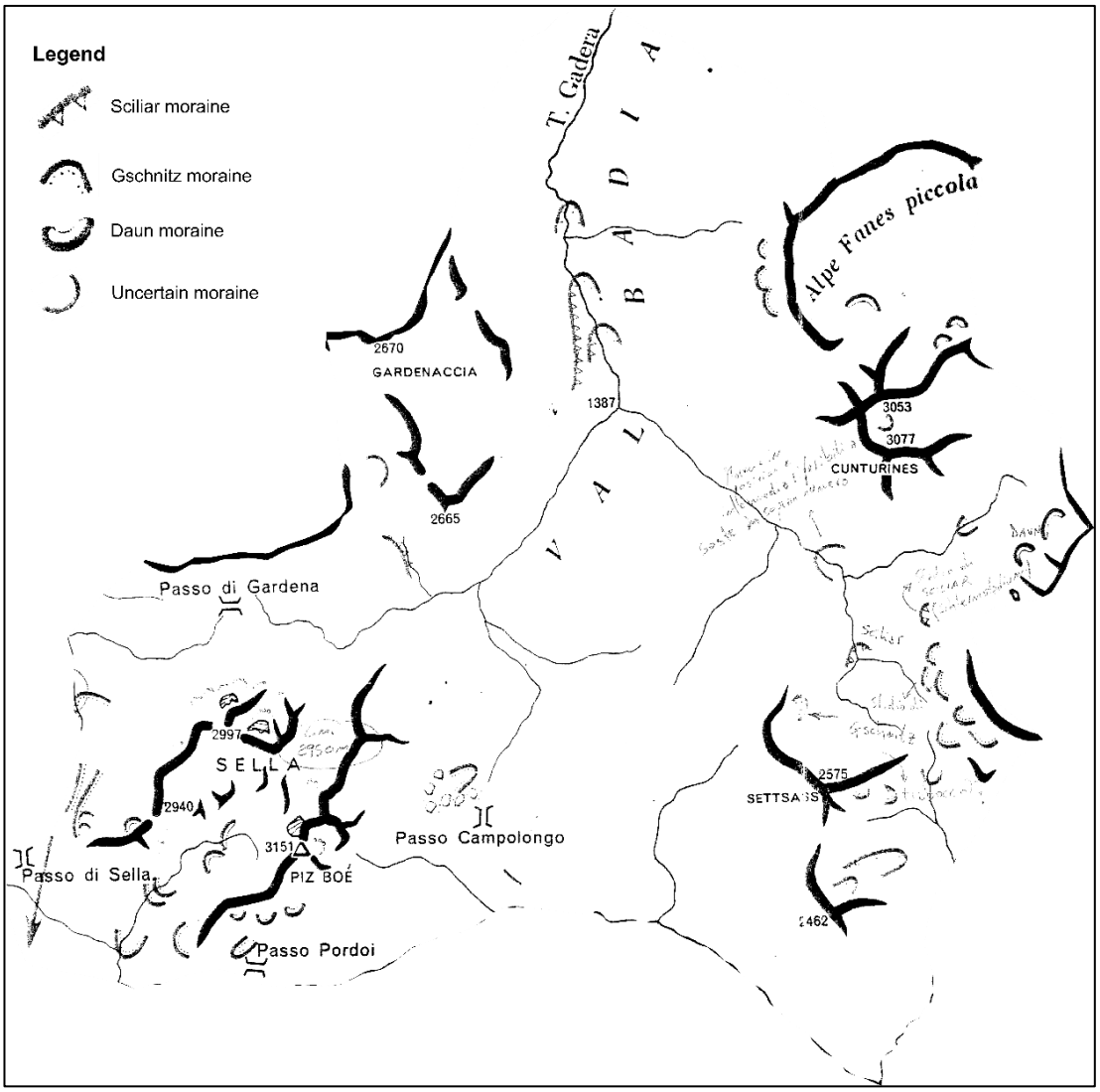

Fig. 2.18 Frontal moraines and their stadial attribution in the Alta Badia valley. Modified from G.B. Castiglioni (1964).

More recently, within the Geological Sheet n°28 "La Marmolada" at 1:50,000 scale (Servizio Geologico d'Italia, 1977), glacial deposits attributed to the Lateglacial period were mapped in correspondence of the village of La Villa as well as several systems of moraine ridges at Armentarola and Valparola localities (south-eastern part of the study area) and at Gardena and Sella mountain passes (western sector of the study area).

Later on, in correspondence with the Bamby Hut (around 1800 m a.s.l.), west of the locality of Piz de Sorega, rounded pebbles of Rosso Ammonitico were found within a massive silty diamicton (Montorsi, 1998). These allochthonous pebbles are likely to

have been transported by LGM glaciers from the Gardenaccia summit – at some 5 km from the finding site and at 2500 m in altitude – were Rosso Ammonitico crops out.
It should be noticed that evidence was found that the upper part of the Pralongià plateau was already ice free during the Lateglacial, as witnessed by the dating of a charcoal sample taken from an excavation made close to Piz de Sorega, at an elevation of 1937 m. This sample was dated back to around 16,000 cal years BP showing that at least the central sector of Alta Badia valley was already ice free at that time (Panizza et al., 2011).
A recent research by Ghinoi and Soldati (2017) was devoted to the reconstruction of glaciers' fluctuations in the south-eastern sector of the Alta Badia valley, in Valparola, by reconstructing glacier ELAs. To this aim the authors used an automated ArcGIS tool provided by Pellitero et al. (2016) and reconstructed the relative glacial chronology on the basis of ELA fluctuations. From here, started the necessity to compare their results with the ones obtained from a manual method (e.g. Porter, 2001; Osmaston, 2005) and to validated the obtained relative chronology with quantitative dating techniques. A reiterative sketch of the outputs provided by Ghinoi and Soldati (2017) is reported in Fig. 2.19.

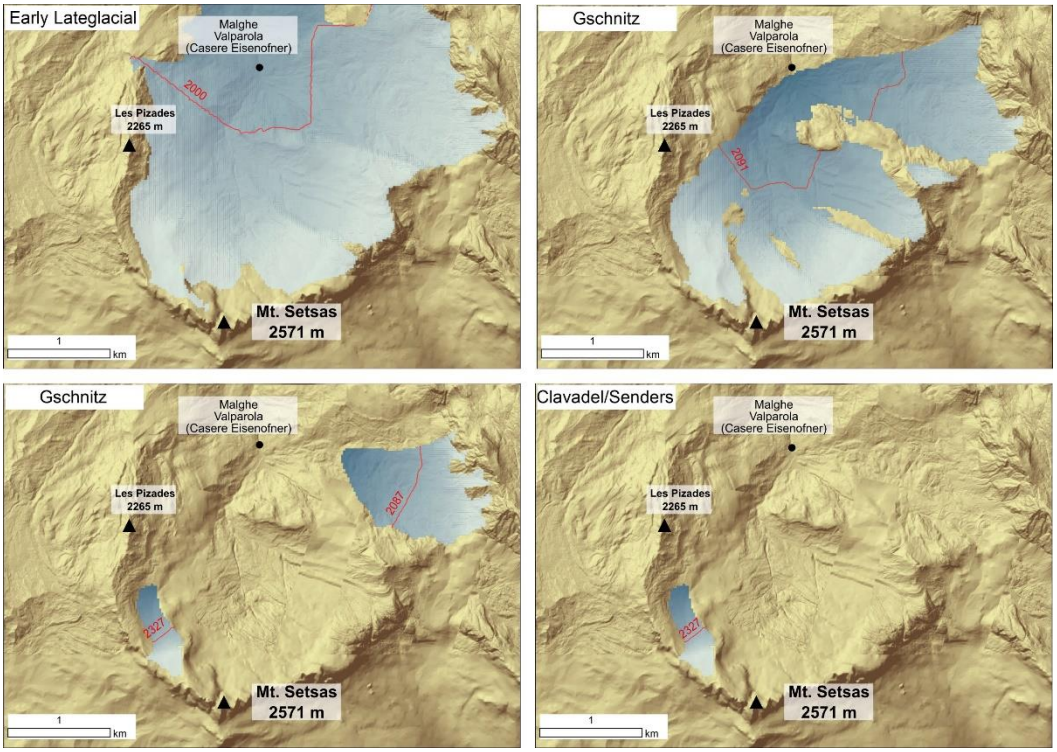

Fig. 2.19 Reconstructed glaciers evolution of Valparola (Alta Badia) according to Ghinoi and Soldati (2017). The ELAs reconstructed were calculated by means of the Pellitero ArcGIS tool "GLARE" by applying the AABR (Area Altitude Balance Ratio) method using a balance ratio of 1.6.

3. Materials and methods

The reconstruction of Late Pleistocene glacial history of the Alta Badia valley was developed on several research steps (Fig. 3.1).

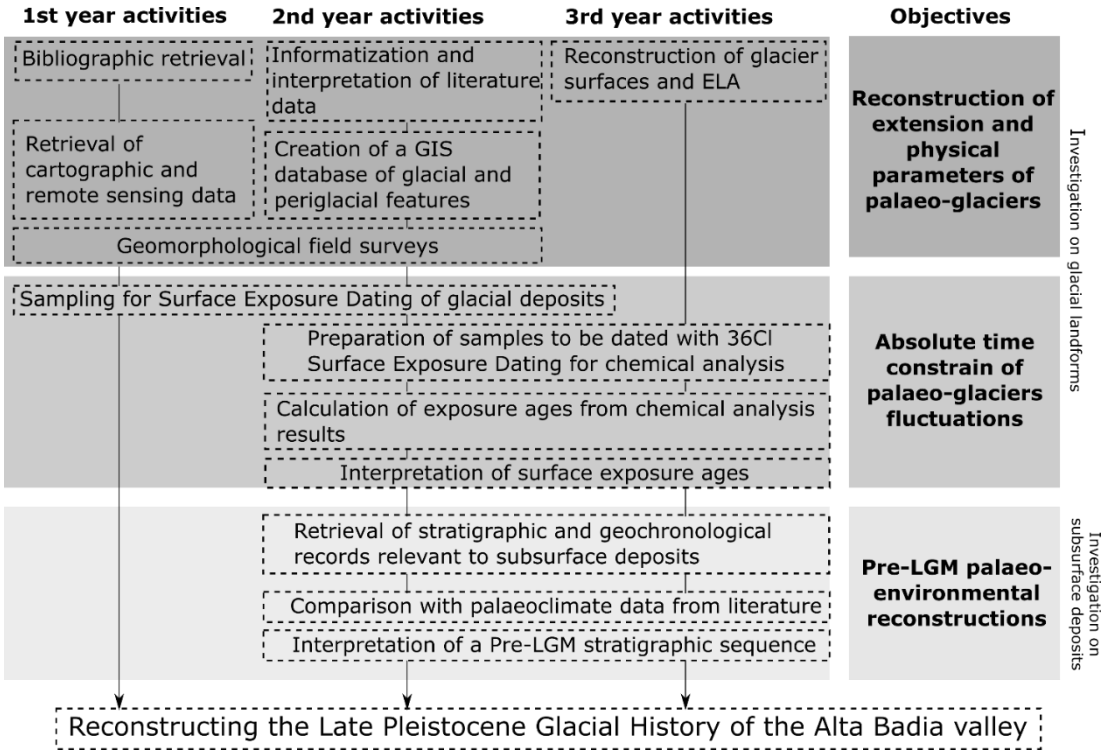

Fig. 3.1 Scheme representing the principal research phases carried out from the first to the third year of PhD research activity with reference to its aims and objectives.

In a preliminary phase the retrieval of literature data was carried out, aimed at collecting and analysing papers related to the geology and geomorphology of the study area and, more in general, of the Alpine chain, as well as studies concerning dating techniques, ELA calculation and paleoclimatic and paleoenvironmental reconstructions.

Together with literature data also the retrieval of cartographic material was carried out. The technical maps, at 1:5,000 and 1:10,000 scale, retrieved from the on-line geoportal of the Autonomous Province of Bolzano, as well as the Tabacco topographic maps at 1:25,000 (cf. Tab. 3.1) were used as a topographic base for geomorphological investigations, mapping and data representation.

Geomorphological and geological maps, listed in Table 3.1, were scanned and imported in GIS. In particular, the maps by Mutschlechner (1932, 1933), Castiglioni (1964), Panizza et al. (2011), Ghinoi and Soldati (2017) have been collected in raster format and georeferenced (spatial reference: WGS84 / UTM zone 32) in ArcGIS 10.1. Glacial and periglacial features reported in these maps were digitalized in vector

format (shapefile) as punctual, linear or polygon features. The genesis and the spatial extensions of glacial and periglacial landforms and deposits, inferred by previous authors, were re-examined and if necessary reinterpreted and/or reallocated on the basis of geomorphological evidence from field surveys and remote sensing data analysis. In particular, remote sensed data included: i) multitemporal orthophotos (1992/97, 2000, 2008, 2014) available on the on-line geoportal implemented by the Autonomous Province of Bolzano (at http://geocatalogo.retecivica.bz.it/geokatalog/#!), ii) LiDAR Digital Elevation Model (DEM) 2.5x2.5 metres of resolution courtesy of the Autonomous Province of Bolzano, iii) DEM 5x5 metres of resolution including the Belluno Province retrieved from the geoportal of the Veneto Region (at https://www.regione.veneto.it/web/ambiente-e-territorio/geoportale) and iv) Google Earth images. The geological map at 1:25,000 scale by the Autonomous Province of Bolzano (Brandner, 2007) as well as the inventory of rock glaciers (Mair et al., 2011), available from the above-mentioned geoportal, were also considered. The LiDAR DEM and the technical cartography (Tab. 3.1) were also used as base maps to represent the data.

The compilation and harmonization of all available information on former glacial and periglacial landscape features was supposed to be fundamental for the reconstruction of the paleogeography of the study area.

Tab. 3.1 Cartographic data covering the Alta Badia valley and used for the study.

Type of map	Source/Reference	Scale	Format
Technical map	http://geocatalogo.retecivica.bz.it/geokatalog/#!	1:10,000	GeoTIFF
Technical map	http://geocatalogo.retecivica.bz.it/geokatalog/#!	1:5,000	GeoTIFF
Topographic map	Tabacco 07 Alta Badia Arabba – Marmolada (2017)	1:25,000	Paper
Geological map	Brandner et al. (2007)	1:25,000	Paper and vector
Geological map	Servizio geologico d'Italia (1977)	1:50,000	Paper
Geological map	Mutschlechner (1932)	1:25,000	Raster
Geological map	Mutschlechner (1933)	1:25,000	Raster
Geomorphological map	Castiglioni (1964)	1:125,000	Raster
Geomorphological map	Panizza et al. (2011)	1:20,000	Raster
Geomorphological map	Ghinoi and Soldati (2017)	ca. 1:30,000	Raster

Tab. 3.2 Features of the aerophotographic and orthophotographic documents used for the study.

Flight	Document	Nominal scale	Cromatism
Volo Provincia Autonoma di Bolzano 1992/1997	Aerial photographs	1:10,000	b/n
Volo Provincia Autonoma di Bolzano 2000	Orthophotographs	–	Colours
Volo Agea (Agenzia per le Erogazioni in Agricoltura) 2008	Orthophotographs	–	Colours
Volo MATTM (Ministero dell'ambiente e della tutela del territorio e del mare) 2014	Orthophotographs	–	Colours

3.1 Investigation on subsurface deposits

The investigation of subsurface deposits took advantage of the analysis of stratigraphic data from cores collected by means of eight continuous-coring boreholes, ranging in depth from 15 to 25 m, carried out during drilling surveys for the construction of a water-retention basin. These boreholes were located west of the Ciampai Hut, on the Pralongià plateau, at an altitude of ca. 1910 m to 1930 m (Fig. 3.2). The stratigraphic analysis of cores was supported by observations made in correspondence of excavation fronts exposed during the basin construction. Within the eight cores (Figs. 3.2 and 3.3), different types of deposits were recognised, and their genetic interpretation was provided, as shown in Table 3.3. They correspond to silty/sandy diamicton, cohesive deposits (including silt and clay) and dolostone monolithic deposits. On the latter petrographic analysis were also carried out to identify the geological formations to which the dolostone belong and eventually infer its provenance. A total of six samples of bulk organic sediment, essentially dark coloured silt, were collected and radiocarbon dated: five samples from three of the eight cores (BS6, BS7-P, BS8-P) and one sample from an excavation wall (Fig. 3.4), the latter located close to BS8-P core. Samples were prepared and analysed at Beta Analytic Inc. laboratories (Florida) using Accelerator Mass Spectrometry (AMS). Ages were calibrated by Beta Analytic using IntCal13 database (Reimer et al., 2013) according to Talma and Vogel (1993). Calibrated ages are reported with two sigma (95% of confidence).

Tab. 3.3 Types of deposits and their morphogenetic interpretation from stratigraphic records retrieved at the Pralongià plateau.

Sediment types	Description	Morphogenetic interpretation
Diamicton	Silty matrix with faceted and striated polygenic elements	Lodgement till
	Sandy matrix with clastic angular/sub-angular polygenic elements, sterile	Gravity-induced (debris flow-like) deposit
Cohesive deposit	Silt and clay with abundant polygenic elements	Eluvial-colluvial deposit
	Silt and clay with elements of the bedrock	Eluvial deposit
	Mainly silt and clay, organic-bearing	Stagnant water deposit
Dolostone monolithic deposit	Dolomite sandy matrix with clastic dolomitic elements, sterile	Gravity-induced (debris flow-like) deposit

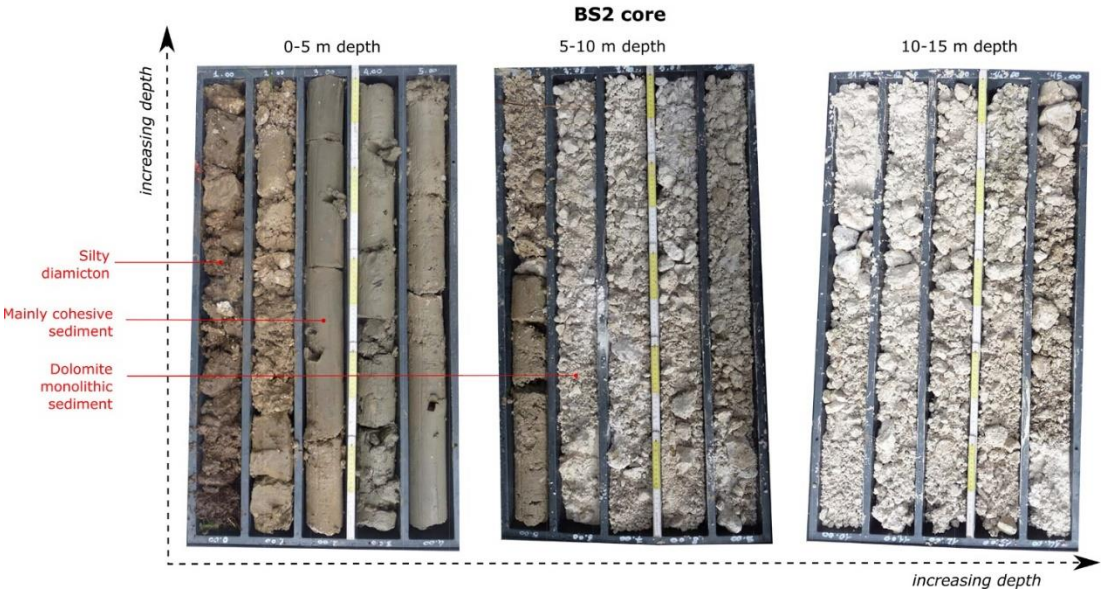

Fig. 3.3 Example of one of the eight cores from the Pralongià plateau: BS2 core (15-m deep).

3.2 Investigation on glacial landforms

Investigation of glacial landforms was fundamental for the reconstruction of the Late Pleistocene glacial history of the Alta Badia valley. The investigation was carried out by means of remote sensed data analysis and interpretation as well as detailed geomorphological field surveys. Additionally, in situ cosmogenic ^{36}Cl surface exposure dating was used to infer the depositional ages of moraines within the valley.

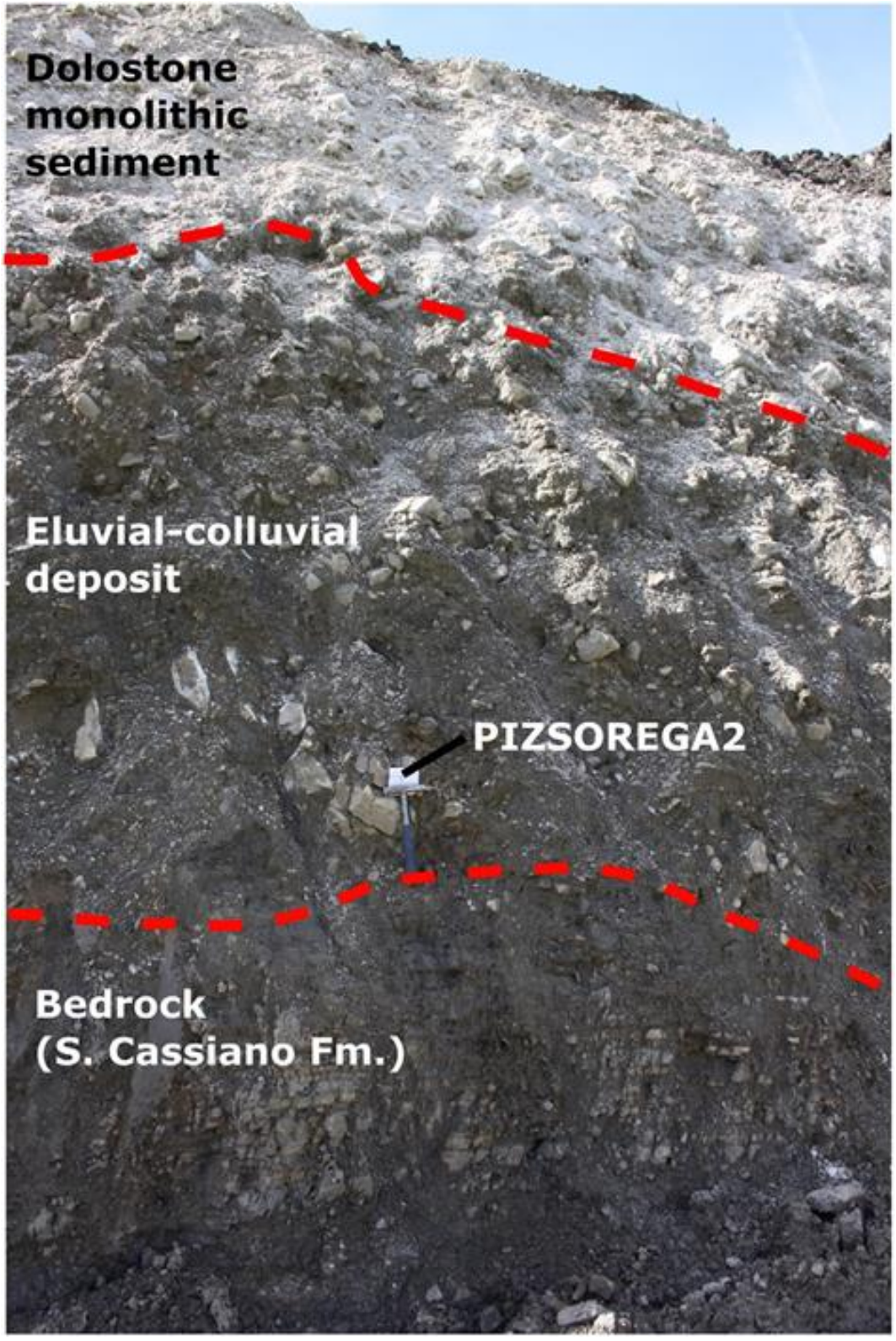

Fig. 3.4 Excavation wall, close to BS8-P borehole site, where PIZSOREGA2 sample was collected for radiocarbon dating. Dashed lines indicate the lithological boundary between different sediment types.

3.2.1 Reconstruction of glacial surfaces

The extension of the icefield which was supposed to cover the Alta Badia valley during the LGM (cf. section 2.4) was reconstructed by identifying and mapping the altitude of the trimlines (Fig. 3.5). The latter are understood as lines separating sectors of unglacierised terrain of notably different appearance; the appearance of one of the sectors is interpretable as the result of a more recent deglaciation (Cogley et al., 2011). In particular, trimlines can be used to identify portion of the relief, within former glaciated terrains, that escaped glacial erosion. This is the case of unglaciated nunataks, emerging from the ice surface, thus the trimline of the area represents the maximum surface elevation of the ice (McCarroll, 2014). The trimlines within the Alta Badia valley were identified both in the field and by the analysis of remote sensed data, then mapped and stored in a GIS database.

The Lateglacial extension of the former glaciers of the Alta Badia valley was reconstructed by considering the spatial distribution and shape of the moraine deposits. Glacier surface topography was reconstructed in GIS environment by using contour lines with 50 m equidistance, according to Porter (1975) and Porter and Orombelli (1982). The Equilibrium Line Altitudes (ELAs) for the single glaciers were calculated using the Accumulation Area ratio (AAR), which is the most widely applied and consolidated method (Kerschner et al., 2000; Porter, 2001; Benn and Ballantyne, 2005; Lukas, 2007; Stansell et al., 2007; Pellitero et al., 2015), using an AAR index of 0.67 ± 0.05 (cf. Baroni et al., 2018). The calculated ELAs were also compared to the ones calculated with another popular method, the Area Altitude Balance Ratio (AABR) which was applied by following the procedure developed by Osmaston (2005) and considering a Balance Ratio of 1.59 ± 0.5 (Rea, 2009).

A parametric analysis was also performed, looking at the change of the reconstructed paleo-ELA varying the AAR and BR value within the confidence interval of the mean 0.67 ± 0.05 and 1.6 ± 0.5 respectively. The resulting ELA value was the one obtained from the mean of the ELAs calculated with both AAR and AABR methods. In order to compare the paleo-ELAs obtained for the Alta Badia valley with other paleo-ELAs calculated in other Alpine valleys, the ELA depression with respect to a reference value was calculated. Following the most common approach, the LIA ELA was chosen as a reference value (Gross et al., 1977; Maisch, 1982). The local LIA ELA in the Alta Badia valley was estimated by Ghinoi and Soldati (2017) from the assumption that the LIA ELA is some 100 m lower (cf. Kerschner et al. 2000) than the present-day one, as

found by several authors such as: Kerschner et al. (1999) for the Gschnitz valley; Pelfini (1994) for Ortles-Cevedale glaciers; Masini (1998) for Altopiani di Fanes, Sennes e Fosses. In the work by Ghinoi and Soldati, the local LIA ELA was estimated at 2800 m in agreement with literature data (e.g. Masini, 1998) and being validated considering the present-day ELA of the near Marmolada glacier at some 2900 m, as calculated by the authors.

3.2.2 Geomorphological surveys and sampling campaigns

Geomorphological field surveys were carried out during the months of June 2017, 2018 and 2019 and in October 2017. Sampling campaigns were carried out during the months of August 2017 and 2018.

In particular, geomorphological field surveys were aimed at: i) investigating the origin of the deposits supposed as glacial by previous authors; ii) identifying glacial deposits suitable to be dated with Cosmic Ray Exposure dating (CRE); ii) outlining the geomorphological framework of the sampling sites.

The detailed geomorphological analysis, carried out on the numerous moraine ridges and glacial deposits of the valley, has limited the number of boulders reliable for successfully applying ^{36}Cl CRE.

A total of 16 samples were collected for cosmogenic ^{36}Cl dating (Figs. 3.6 and 3.7) from the top surfaces of moraine boulders which were selected on the basis of: i) their prominent position on the moraine crest; ii) the presence of evidence of non-remobilized context and no post – depositional overturning, iii) their size, possibly >1.5 m in height (Tab. 3.4, Ivy-Ochs and Kober, 2008).

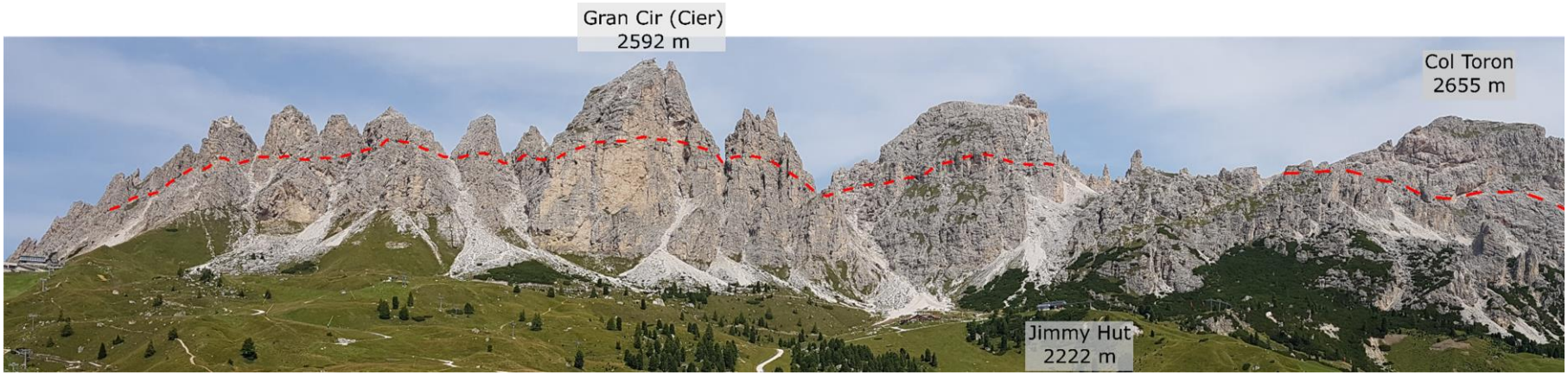

Fig. 3.5 Trimline ranging from ca. 2350 to ca. 2450 m a.s.l. (red dashed line) in correspondence of the Cir Group (north of the Gardena Pass). Angular and jagged peaks witness that they were exposed to intense and prolonged weathering processes. Their appearance contrast with the lower part of the massif which is characterized by less eroded and locally levigated surfaces.

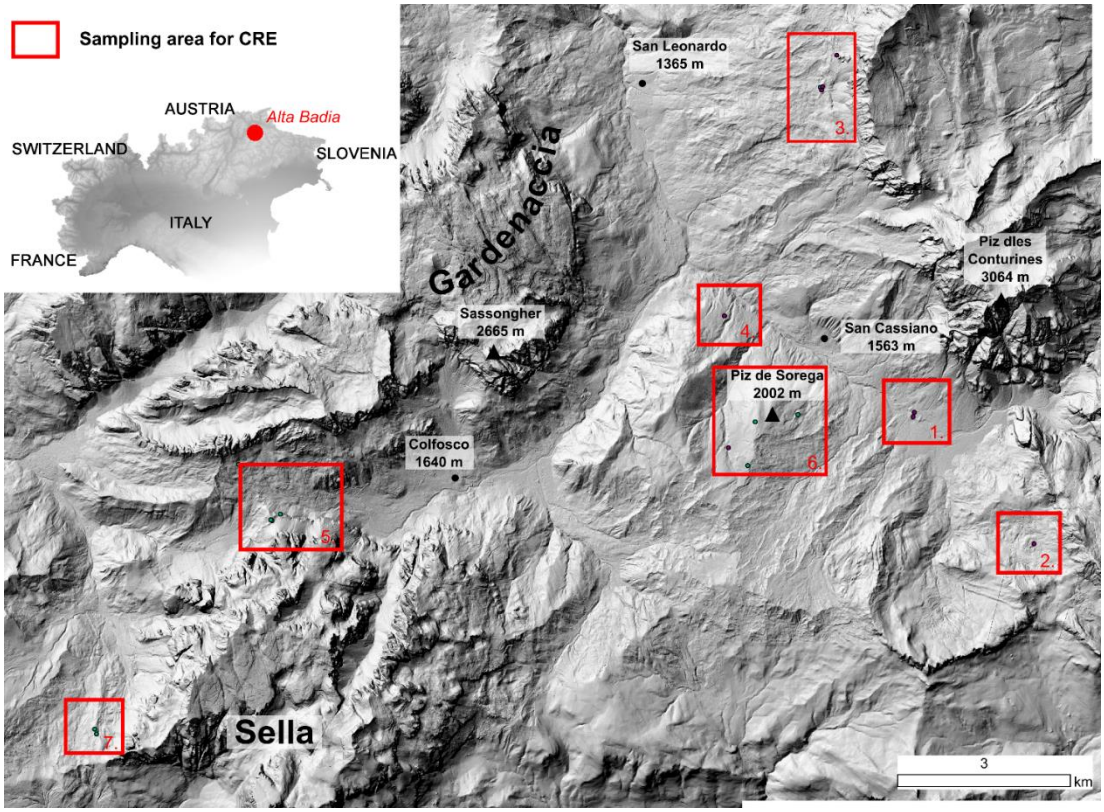

Fig. 3.6 Sampling sites for Cosmic Ray Exposure dating (CRE) of boulders found within glacial deposits: 1. Armentarola; 2. Valparola Pass; 3. Sas Crusc; 4. Alting; 5. Gardena Pass; 6. Piz de Sorega and Pralongià plateau; 7. Sella Pass.

In particular, the topmost 1 to 3 cm of the surface of large and wide-based moraine boulders ranging from 60-cm to 18-m height were sampled. Longitude and latitude of sampling sites were measured by means of a hand-held GPS. Elevation was derived from topographic maps. In case of non-horizontal boulder tops also dip and inclination of the sampled surfaces were measured through a magnetic compass. The topographic shielding factor was obtained by means of the "Point-based Shielding Model" GIS-tool devised by Li (2018). Moreover, thin sections were provided by cutting orthogonally the sampled surface to verify the presence of weathering traces (weathering rinds) (Fig. 3.8).

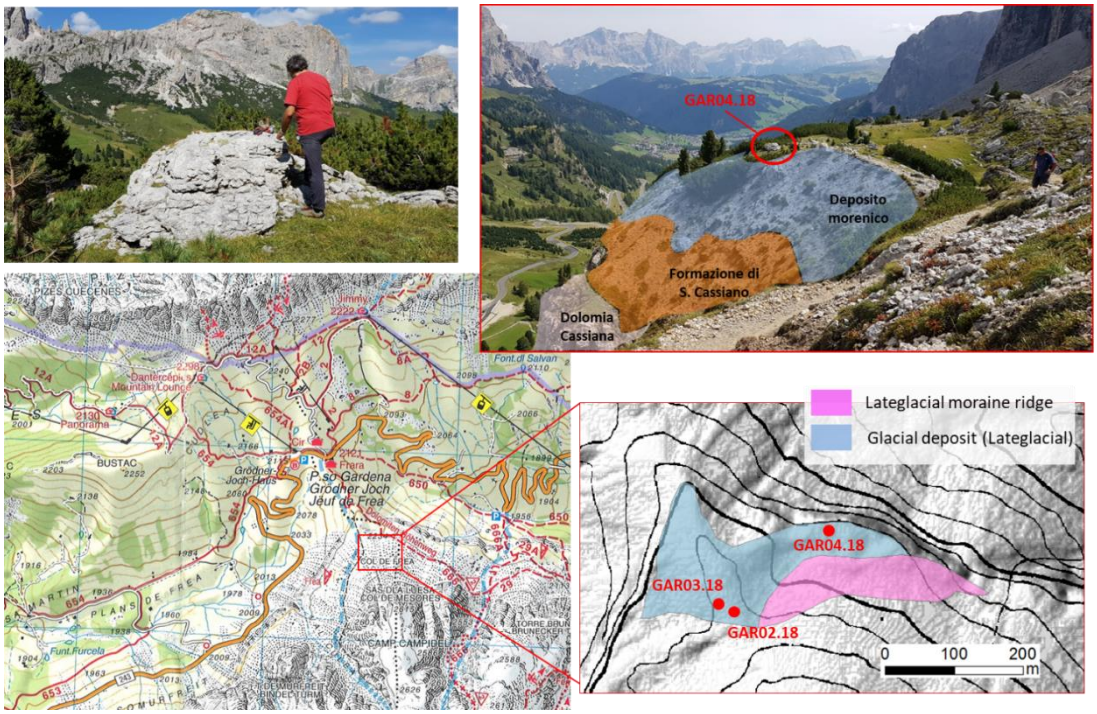

Fig. 3.7 Example of sampling sites for Cosmic Ray Exposure dating (CRE) of boulders at the Gardena Pass (western sector of the Alta Badia valley).

3.2.3 Deriving exposure ages from in situ cosmogenic ^{36}Cl

Physical and chemical sample preparation

The time of surface exposure can be calculated from measured concentration of cosmogenically produced isotopes such as ^{36}Cl, ^{10}Be and ^{26}Al, in rocks or sediment. The time of exposure can be approximately considered as the time when the glacier started to retreat, that is, the minimum age of stabilization of the moraine deposit (cf. Ivy-Ochs and Briner, 2014).

In this study, ^{36}Cl was used because in the Alta Badia valley mainly dolostone boulders can be found on moraines, and ^{36}Cl is abundantly produced in dolostone due to the high concentrations of the target element Ca in this lithology (Tab. 3.5). In fact, ^{36}Cl is produced through: i) spallation of Ca, K, Ti and Fe (target elements), ii) slow-negative muon capture by K and Ca and iii) low-energy (thermal and epithermal) neutron capture by ^{35}Cl. Thus, the ^{36}Cl production in a rock strongly depends on its chemical composition and in particular on the concentrations of the target elements and the elements that modify the low-energy neutron flux (e.g. Li, B, Sm, Gd; cf. Schimmelpfennig et al., 2009).

Tab. 3.4 Sample locations, attributes, and local corrections to production rates.

Sample and landform ID	Latitude WGS84	Longitude WGS 84	Landform Elevation (m asl)	Boulder height (cm)	Sample thickness	Shielding Factor	Boulder location
170829.02	46,55813	11,95757	1651	340	2,5	0,979	Moraine ridge (Lateglacial)
170829.03	46,5588	11,95785	1652	210	2,5	0,983	Moraine ridge (Lateglacial)
170830.01	46,53759	11,98381	2012	135	3,8	0,966	Glacial deposit (Lateglacial)
170830.02	46,60965	11,93955	2066	420	2,5	0,95	Moraine ridge (LGM)
170830.03	46,61017	11,93981	2049	390	3,5	0,939	Moraine ridge (LGM)
170831.01	46,57496	11,91566	1626	140	3	0,989	Moraine ridge (Lateglacial)
GAR01.18	46,55453	11,80436	2265	120	3	0,935	Glacial deposit (LGM)
GAR02.18	46,54558	11,81147	2235	120	2,5	0,931	Glacial deposit (Lateglacial)
GAR03.18	46,54568	11,81121	2232	140	3	0,935	Glacial deposit (Lateglacial)
GAR04.18	46,54653	11,81339	2196	140	3,5	0,927	Glacial deposit (Lateglacial)
CRU01.18	46,61012	11,93934	2050	140	3,5	0,953	Moraine ridge (LGM)
SOR01.18	46,55823	11,92171	1973	90	2,5	0,990	Glacial deposit (LGM)
VEG01.18	46,55149	11,91971	1998	60	3	0,997	Glacial deposit (LGM)
PIC01.18	46,55915	11,9315	1852	1800	2,5	0,996	Glacial deposit (LGM)
SEL01.18	46,51324	11,77005	2192	300	2,5	0,959	Moraine ridge (LGM)
SEL02.18	46,51397	11,76967	2176	250	3	0,962	Moraine ridge (LGM)

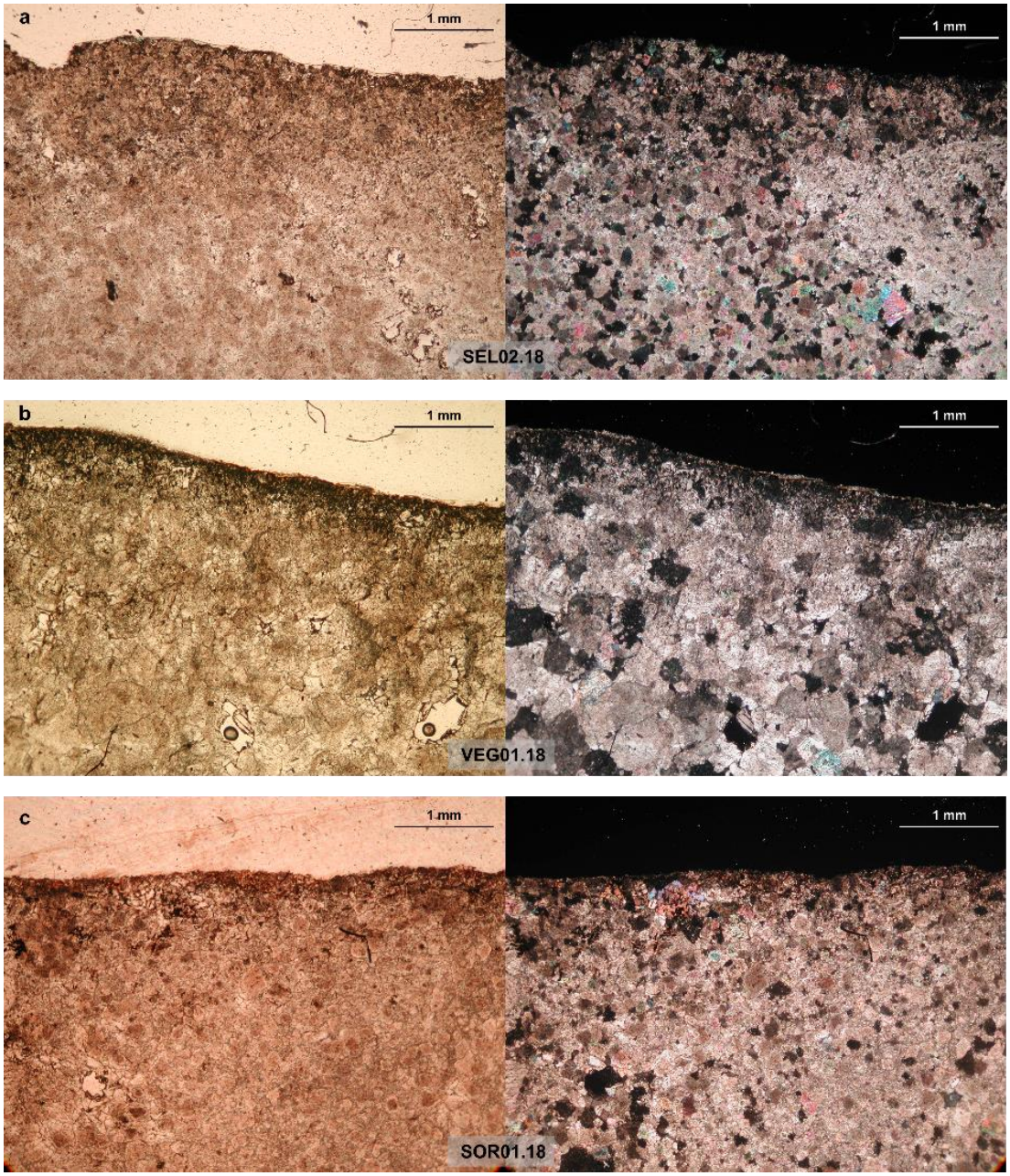

Fig. 3.8 Detail of dolostone samples in thin section. Well-defined weathering rind bands in SEL02.18 (a), VEG01.18 (b), SOR01.18 (c).

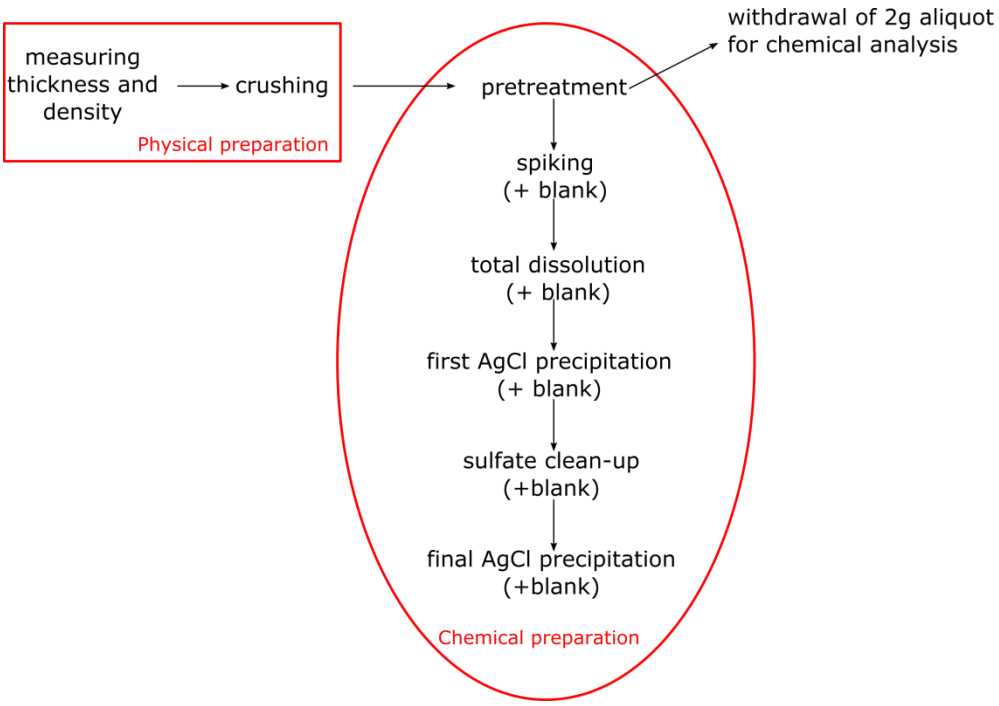

Fig. 3.9 Step of sample preparation for AMS measurements to determine the surface exposure age; after Schimmelpfenning (2009).

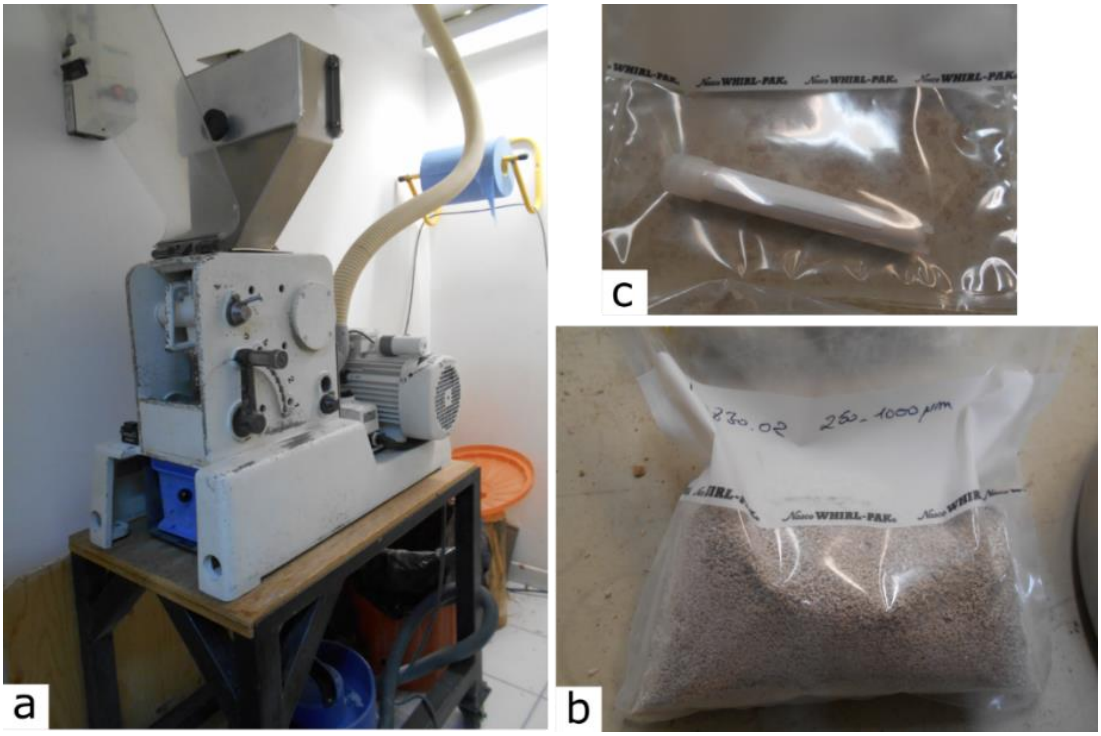

Fig. 3.10 Example of materials for sample physical preparation: a) Jaw crusher at CEREGE; b) sample size fraction < 250 µm, intended for chemical analysis of the bulk rock composition; c) sample size fraction < 250 µm, intended for chloride content measurement.

Tab. 3.5 AMS measurements results

Sample ID	Sample weight (g)	Mass of Cl in spike (g)	35Cl/37Cl	36Cl/35Cl (10^{-13})	Cl concentration (ppm)	36Cl concentration (10^5 atoms g^{-1})	CaO concentrations (%)
170829.02	91,03	0,2938	5,39±0,09	6,50±0,27	54,19±2,34	7,90±0,40	30,00±0,59
170829.03	92,93	0,2965	4,19±0,07	4,81±0,22	125,62±8,72	10,00±0,70	29,40±0,58
170830.01	91,15	0,2978	3,70±0,06	5,34±0,26	227,19±26,07	18,00±2,00	29,50±0,58
170830.02	93,03	0,2961	7,17±0,13	3,17±0,15	50,63±1,73	4,80±0,20	30,10±0,59
170830.03	90,45	0,2984	5,47±0,10	5,71±0,25	53,44±2,34	6,90±0,30	30,00±0,60
170831.01	94,84	0,2938	8,13±0,14	14,35±0,60	21,76±0,67	11,00±0,50	53,20±1,05
GAR01.18	93,78	0,2950	3,54±0,12	4,17±0,21	284,85±82,22	17,30±4,49	29,58±0,14
GAR02.18	96,10	0,2970	4,36±0,15	9,95±0,50	90,46±10,91	16,18±1,62	33,90±0,16
GAR03.18	97,20	0,2946	5,48±0,19	12,67±0,62	46,02±3,72	13,17±0,89	43,38±0,26
GAR04.18	94,43	0,2945	4,47±0,15	9,44±0,49	87,79±9,96	15,26±1,45	36,39±0,14
CRU01.18	93,29	0,2943	5,57±0,19	6,17±0,31	49,36±3,92	6,98±0,47	29,67±0,17
SOR01.18	93,37	0,2954	4,12±0,14	6,43±0,32	123,93±17,66	13,51±1,61	29,58±0,11
VEG01.18	94,99	0,2967	4,18±0,14	5,93±0,29	124,03±17,12	12,64±1,45	29,38±0,11
PIC01.18	95,34	0,2912	4,32±0,15	7,85±0,40	97,73±12,16	13,63±1,41	29,48±0,10
SEL01.18	96,61	0,3025	3,85±0,13	6,72±0,34	183,19±33,20	19,51±3,04	29,53±0,14
SEL02.18	94,87	0,2943	4,08±0,14	7,38±0,38	128,01±18,92	15,87±1,98	29,67±0,11

The samples were physically and chemically prepared at CEREGE (Centre Européen de Recherche et d'Enseignement des Géosciences de l'Environnement, Aix en Provence, France), following standard procedures (Fig. 3.9) modified from Stone et al. (1996) (Schlagenhauf et al., 2010). In particular, the physical preparation consisted in crushing and sieving the samples to retain the grain size fraction 250 μm-1000 μm for the extraction of the cosmogenic ^{36}Cl, while the grain size fractions <250 μm was used for chemical analysis of the bulk rock composition (Tab. 3.6) to calculate the low-energy neutron distribution in the dolostone samples (Fig. 3.10). Before crushing, pictures of sample fragments selected to undergo to physical and chemical preparation were taken and the thickness of each fragment was measured (Tab. 3.4). Dry rock densities were determined in laboratory on the basis of the Archimedes principle on rock pieces (one representative for each sample) and they were found to vary between 2.7-2.8 g/cm^3. The chemical preparation (cf. Appendix 1) was applied to 90-95 g of sample grain and to a blank solution used to track any contamination of Cl during the chemical preparation. The first step of chemical preparation consisted in the pre-treatment of the samples aiming at eliminating atmospheric Cl, firstly with a washing with MQ water and secondly with HNO_3 (2M), which dissolved about 10% of the sample material (Fig. 3.11a). Then, after drying and weighing the remaining sample material (target fraction; Tab. 3.5), an inhouse spike solution (carrier) of known $^{35}Cl/^{37}Cl$ ratio of 918 and containing ~2 mg of chlorine (Tab. 3.5) was added to the samples, allowing to determine the concentrations of both ^{36}Cl and total Cl in the sample simultaneously from one AMS measurement by the principle of isotope dilution (Ivy-Ochs et al., 2004; Desilets et al., 2006). After spiking, the samples were totally dissolved in HNO_3 (2M). The solutions were filtered to remove any solid residues (Fig. 3.11b). Then, 1 ml aliquots of the sample solutions were collected to measure target element concentrations (Ca and K) in the target fraction, by inductive coupled plasma atomic emission spectrometry (ICP-AES) at CEREGE.

After addition of AgCl, Cl precipitated from the sample and blank solutions in form of AgCl. This precipitate was re-dissolved in NH_3(aq), then Cl was separated from S (including ^{36}S, an interfering isobar of ^{36}Cl) by the addition of $Ba(NO_3)_2$ causing the precipitation of $BaSO_4$, which was removed from the solutions by filtering (Figs. 3.11c and 3.11d). Finally, AgCl was re-precipitated by acidifying the solution with HNO_3, (Fig. 3.11e) then recovered and dried for measurements of the $^{36}Cl/^{35}Cl$ and $^{35}Cl/^{37}Cl$

ratios (Table 3.5) at the French AMS national facility ASTER at CEREGE (Arnold et al., 2013).

The chemical analysis of the bulk rock (Tab. 3.6) composition of ten of the 16 samples was performed at the DSCG - UNIMORE laboratories. X-ray fluorescence spectroscopy and optical emission spectroscopy (ICP-OES) were used for the determination of major elements concentrations while, the ICP-MS was applied for minor element concentrations.

Calculation of exposure ages

Calculation of exposure ages was performed using the Excel spreadsheet implemented by Schimmelpfennig et al. (2009) (cf. Appendix 3). A ^{36}Cl production rate for spallation of Ca, referenced to Sea Level and High Latitude (SLHL), of 42 ± 2 atoms ^{36}Cl (g Ca)$^{-1}$ yr^{-1} was used with the scaling method by Stone (2000) to convert production rates from SLHL to the sampled location. The chosen SLHL ^{36}Cl production rate for spallation of Ca was the one inferred by Braucher et al. (2011) by fitting modelled ^{36}Cl concentrations to ^{36}Cl measurements from a calcium carbonate core depth profile in south-eastern France, which is the nearest to the Alta Badia valley of the existing ^{36}Cl calibration sites. This value is also in agreement with the ^{36}Cl production rate for spallation of Ca calibrated by Schimmelpfennig et al. (2011) in Ca-rich feldspars from lava surface samples collected at Mount Etna volcano (southern Italy).

A production rate of epithermal neutrons from fast neutrons in atmosphere at land/atmosphere interface of 696 ±185 n cm^{-2} a^{-1} was adopted (Marrero et al., 2016) and a high-energy neutron attenuation length of 160 g cm^{-2} was used. Spallation of Ca was revealed to be the main responsible for the production of ^{36}Cl in most of the samples (between 80% and 30%). Due to the relatively high natural chloride content measured in some of the samples (from less than 20 ppm to more than 200 ppm), the complex low-energy neutron production pathway contributed significantly to the total ^{36}Cl production (between 6% and 64%) causing an increase in the age estimation uncertainty (more than 10%). A minor contribution in the total ^{36}Cl production was from negative muon capture reactions (between 4% and 13%).

In the lack of quantitative estimates for denudation of the dolostone formations in the study area and considering that samples boulders showed slight traces of erosion, the ages are discussed without any correction for denudation.

Table 3.6 Geochemical analytical data of the bulk rock

Sample ID	Major Elements										Trace Elements					
	SiO2 (%)	Al2O3 (%)	Fe2O3 (%)	MnO (%)	MgO (%)	CaO (%)	Na2O (%)	K2O (%)	TiO2 (%)	P2O5 (%)	Li [ppm]	B [ppm]	Sm [ppm]	Gd [ppm]	Th [ppm]	U [ppm]
170829.02	0,32	0,20	0,09	0,00	21,12	30,83	0,03	0,05	0,01	< L.D.	1,46	4,80	0,08	0,08	0,14	6,61
170829.03	0,26	0,13	0,07	0,01	21,36	29,80	0,03	0,02	0,01	0,02	0,78	2,60	0,14	0,14	0,13	1,23
170830.01	< L.D.	0,03	0,04	0,01	21,65	30,35	0,03	0,01	0,00	< L.D.	0,70	<2	0,07	0,08	0,04	0,48
170830.02	6,22	1,84	0,36	0,03	19,23	27,81	0,09	1,29	0,07	< L.D.	2,54	8,60	0,88	0,77	1,59	1,55
170830.03	0,32	0,20	0,08	0,00	21,14	30,83	0,03	0,04	0,01	< L.D.	1,24	4,20	0,10	0,09	0,12	4,16
170831.01	0,62	0,39	0,16	0,00	0,78	53,91	0,01	0,07	0,02	< L.D.	2,25	4,70	0,13	0,12	0,24	0,38
GAR01.18	1,46	0,89	0,27	0,01	21,26	28,98	0,05	0,07	0,03	< L.D.	0,82	2,96	0,23	0,26	0,04	1,44
GAR02.18	1,33	0,65	0,25	0,03	14,73	36,60	< L.D.	0,12	0,03	< L.D.	0,16	1,48	0,30	0,35	0,03	0,16
GAR03.18	1,43	0,67	0,24	0,02	9,25	42,78	0,04	0,15	0,03	< L.D.	0,23	1,06	0,25	0,30	0,03	0,24
GAR04.18	1,42	0,66	0,21	0,03	13,93	37,56	0,05	0,13	0,02	< L.D.	0,16	0,79	0,20	0,24	0,05	0,19
CRU01.18	0,39	0,24	0,08	0,01	21,70	30,71	0,02	0,02	0,01	< L.D.	1,58	3,25	0,07	0,08	0,05	4,04
SOR01.18	0,11	0,12	0,06	0,02	22,62	30,51	0,02	< L.D.	0,01	< L.D.	0,72	2,13	0,09	0,11	0,02	1,18
VEG01.18	0,16	0,14	0,07	0,01	22,65	30,45	0,03	< L.D.	< L.D.	< L.D.	0,55	2,45	0,09	0,12	0,01	0,88
PIC01.18	0,46	0,40	0,06	0,01	22,36	30,16	0,04	0,02	0,01	< L.D.	0,84	2,17	0,09	0,12	0,03	1,45
SEL01.18	0,90	0,54	0,26	0,03	21,53	29,23	0,03	0,07	0,02	< L.D.	0,78	2,09	0,14	0,16	0,06	1,30
SEL02.18	0,38	0,29	0,12	0,02	22,16	30,00	0,02	0,02	0,01	< L.D.	0,75	2,26	0,08	0,10	0,04	1,04

Therefore, they correspond to minimum exposure ages. Snow shielding was not applied for boulder because they were supposed to stick out to the snow.

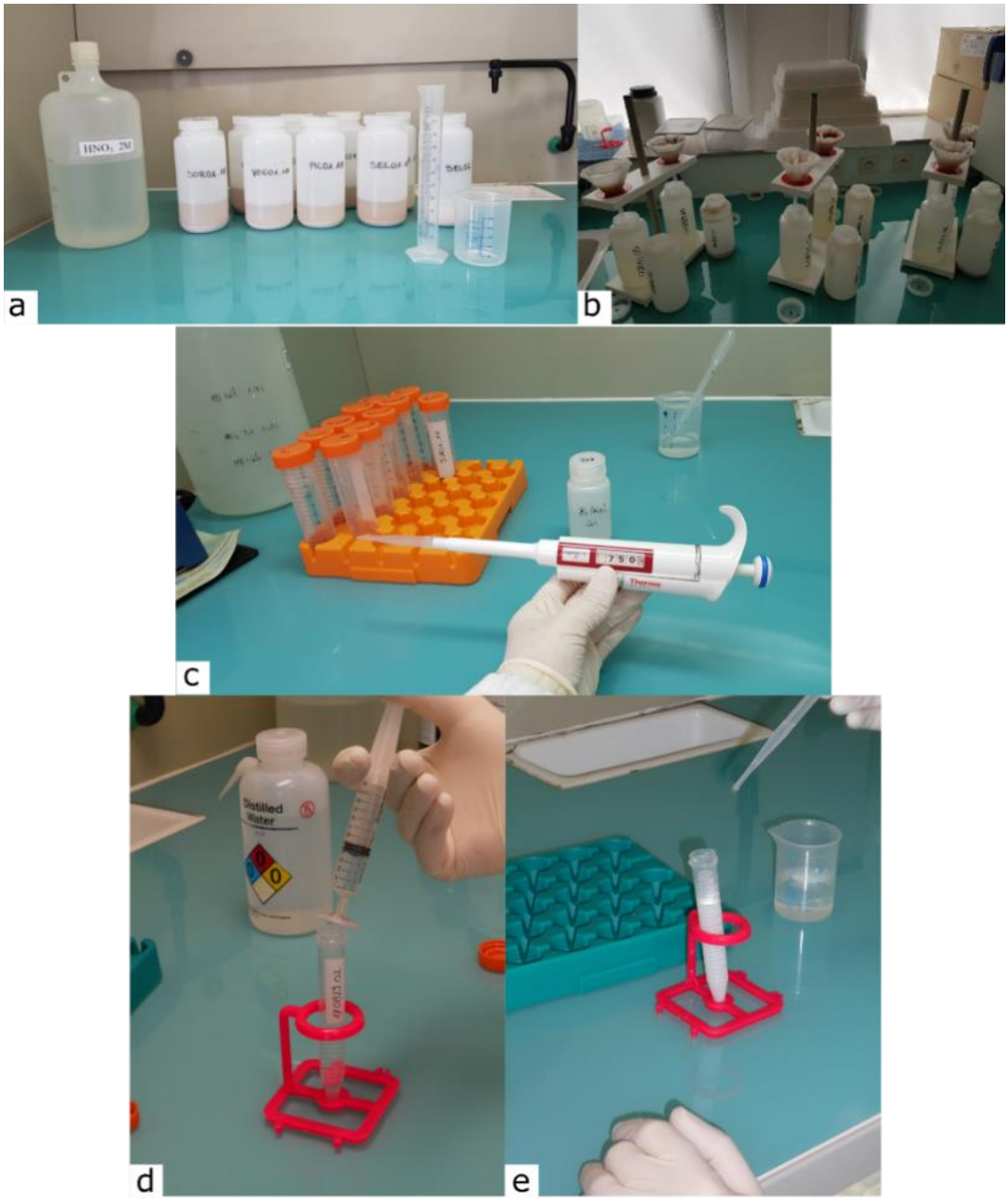

Fig. 3.11 Phases of sample chemical preparation: a) 10% sample dissolution in HNO_3 (2M); b) filtering of the sample solution after total dissolution in new bottles by means of a plated filter insert into a funnel; c) addition of $Ba(NO_3)_2$ for sulfate clean-up.

4. Results

4.1 Results on the investigation of subsurface deposits

4.1.1 Sedimentary and radiocarbon dating evidence on Pre-LGM deposits

The results on the investigation and analysis of subsurface deposits retrieved from eight cores and an excavation wall (cf. section 3.1) performed on the Pralongià plateau are shown in the text below. In detail, the investigations revealed that each of the eight cores showed an individual litho-stratigraphy, with variations from core to core. However, it was possible to identify different types of deposits above the Triassic bedrock – the latter constituted by marls, marly limestones and calcarenites of S. Cassiano and Wengen formations – as shown in Figure 4.1. The bedrock was reached in five out of eight drillings (BS3-P, BS5(I), BS6, BS7-P, BS8-P) at depths of 9.3 to 19 m.

The lowermost part of the cores was prevalently characterized by cohesive deposits with some clasts from the weathering/alteration of the underlying bedrock.

The central part of the cores is generally constituted by sandy diamicton, a light brown sandy matrix with silt, which envelops angular to sub-angular polygenic elements, among which dolomite clasts are found. A monolithic deposit, similar in texture to sandy diamicton, was also encountered (cf. Fig. 4.1); it is made up of dolostone of varied particle-sizes. The monolithic nature of this deposit, the rather good sorting degree and the massive structure together with stratigraphic and geomorphological evidence which will be discussed further on (cf. this section and section 5), make unlikely a subglacial/englacial transport of the clasts. The sandy diamicton and monolithic deposits are devoid of organic matter. This probably indicates that they were deposited in unfavourable conditions for organic matter production (e.g. periglacial environment).

In most of the cores, silty diamicton was encountered from the top of the cores as far as 1.5/2 m in depth. The silty diamicton is composed of a dark silty matrix, which envelops polygenic elements of dolostone, marls and sandstones of variable shape and size. These elements appear as faceted and striated. These features enable to infer a glacial origin of the deposit.

The analysis of the stratigraphic records provided by the cores, with the fundamental support of radiocarbon dating results, finally led to the overall genetic interpretation of the deposits.

The sample taken from the excavation wall (Fig. 3.4) at the interface between bedrock and sediment showed the oldest age of the deposit, corresponding to 44,915 ± 785 cal years BP (Tab. 4.1).

Eluvial and/or colluvial deposits

In most of the cores (Fig. 3.2) cohesive deposits, including some clasts of the underlying bedrock, were interpreted as eluvial in origin, from bedrock weathering in subaerial conditions. It is likely that organic matter found within the eluvial deposits was leached from topsoil. Radiocarbon dating on a sediment sample from BS7 core (9.90-10 m deep), within the eluvial deposits, provided a calibrated (cal) age of 41,918 ± 443 years BP (Fig. 4.1). The sample taken within the eluvial deposit from BS8-P core (Fig. 4.1), between 14.50 and 14.60, was dated at 39,058 ± 528 cal years BP. Radiocarbon dating on the sample taken within the eluvial deposit from BS8 core and between 16.40 and 16.50 m in depth, provided an age of 41,665 ± 490 cal years BP. Sandy diamicton and dolostone monolithic deposits are interrupted or overlain by massive cohesive deposits, mainly made up of dark-coloured and organic-bearing silt with some polygenic elements, among which sub-angular granules and pebbles of dolostone are found. These deposits were interpreted as colluvial/eluvial deposits.

The sample collected from BS6 core (Fig. 4.1) (2.8 m deep), within the colluvial-eluvial deposit, was dated at 38,715 ± 380 cal years BP (Tab. 4.1). However, considering its stratigraphic position, it is likely that the deposit is more recent than the age obtained owing to possible inclusion of organic-matter, older than the time of the emplacement of the deposit within the colluvial-eluvial sediments.

Stagnant water deposits

Within all the eight cores recovered at various depths (e.g. Fig. 4.1), cohesive and organic bearing sediments, ranging in thickness from some decimetres to 3 m, constituted by dark-coloured silt, were found including rare polygenic pebbles. A low-energy depositional environment was inferred for these silt deposits, although the topography of the area did not permit the storage of a large amount of water. Possibly, the area might have hosted stagnant water pools allowing fine suspended sediments to settle.

The sample taken from BS8-P core (Fig. 4.1), between 9.5 and 9.8 m in depth within the stagnant water deposit, was dated at 41,043 ± 563 cal years BP. Since this age is older than that of the sample taken from the underlying eluvial deposit (between 14.50

and 14.60 m depth), it probably pre-dates the true age of the stagnant water deposit. It is likely that organic-matter older than the deposit was included in it.

Gravity-induced deposits

The central part of the cores BS1-P, BS3-P, BS5(I), BS6, BS7-P, BS8-P is generally made up of massive sandy diamicton (Fig. 4.1), which is dominated by a light brownish sandy matrix with a massive structure, which envelopes polygenic granules, pebbles and cobbles angular to subangular. These polygenic elements are prevalently made up of dolostone although marls and sandstones are not rare. No evidence of glacial erosion (striated and faceted granules) was found. Sandy diamicton reaches its highest thickness, more than 10 m, within BS1-P and BS3-P cores, and constitutes almost the entire BS5-I core. On the other hand, in BS6 core the sandy diamicton is limited to a thinner layer of only 1 m, overlain by a thick massive layer of cohesive sediment. Monolithic sediment, similar in texture to sandy diamicton, was also recovered; this is made up of whitish dolostone of varied particle-sizes, from fine sand to pebbles and some cobbles. No evidence of organic matter was found within the sandy diamicton and the dolostone monolithic sediment, letting us suppose that these deposits might have settled under glacial/paraglacial conditions. The sandy diamicton and the monolithic dolostone sediment seem to have been transported and accumulated by debris flows originating from the dolomite cliffs or by reworking/washout of possible rock avalanche deposits. The conditions and patterns for material transport to the plateau are described in section 5.

LGM lodgement till

In most of the cores examined (BS1-P, BS2, BS3-P, BS4-P, BS6-P) consolidated silty diamicton was encountered from the top of the cores up to 1.5/2 m in depth (Figs. 3.2, 3.3, 4.1). Silty diamicton is characterised by a dark silty matrix, which envelops abundant polygenic elements of dolostone, marls and arenites with variable shapes and sizes. These elements appear as faceted and striated and enable to infer a glacial origin for the deposit. Silty diamicton constitutes a sediment blanket partially covering the Pralongià plateau. For its textural features and its uppermost stratigraphic position, silty diamicton was interpreted as LGM lodgement till.

Tab. 4.1 Results of radiocarbon dating on bulk organic sediment from samples collected on the Pralongià plateau.

Sample name	Sample lab code	Depth (m)	Elevation (m a.s.l.)	Material	13 12 C/ C ratio	Measured radiocarbon age (years BP)	Cal years BP (2 sigma)	Interpreted genesis of the deposit
BS6	Beta - 395393	2.8	1911	Bulk organic soil	-24.5	34,180 ± 230	39,095-38,335	Colluvial-eluvial deposit
BS7-P	Beta - 395394	9.90-10	1924	Bulk organic soil	-24.0	37,510 ± 340	42,360-41,475	Eluvial deposit
BS8-Pa	Beta - 395395	9.5-9.8	1919	Bulk organic soil	-23.3	36,420 ± 290	41,605-40,480	Stagnant water deposit
BS8-Pb	Beta - 395396	14.5-14.6	1914	Bulk organic soil	-23.6	34,500 ± 250	39,585-38,530	Eluvial deposit
BS8-Pc	Beta - 395397	16.40	1913	Bulk organic soil	-24.0	37,160 ± 350	42,155-41,175	Eluvial deposit
PIZSOREGA2	Beta - 371854	2.5	1921	Bulk organic sediment	-23.5	41,280 ± 620	45,700-44,130	Eluvial deposit

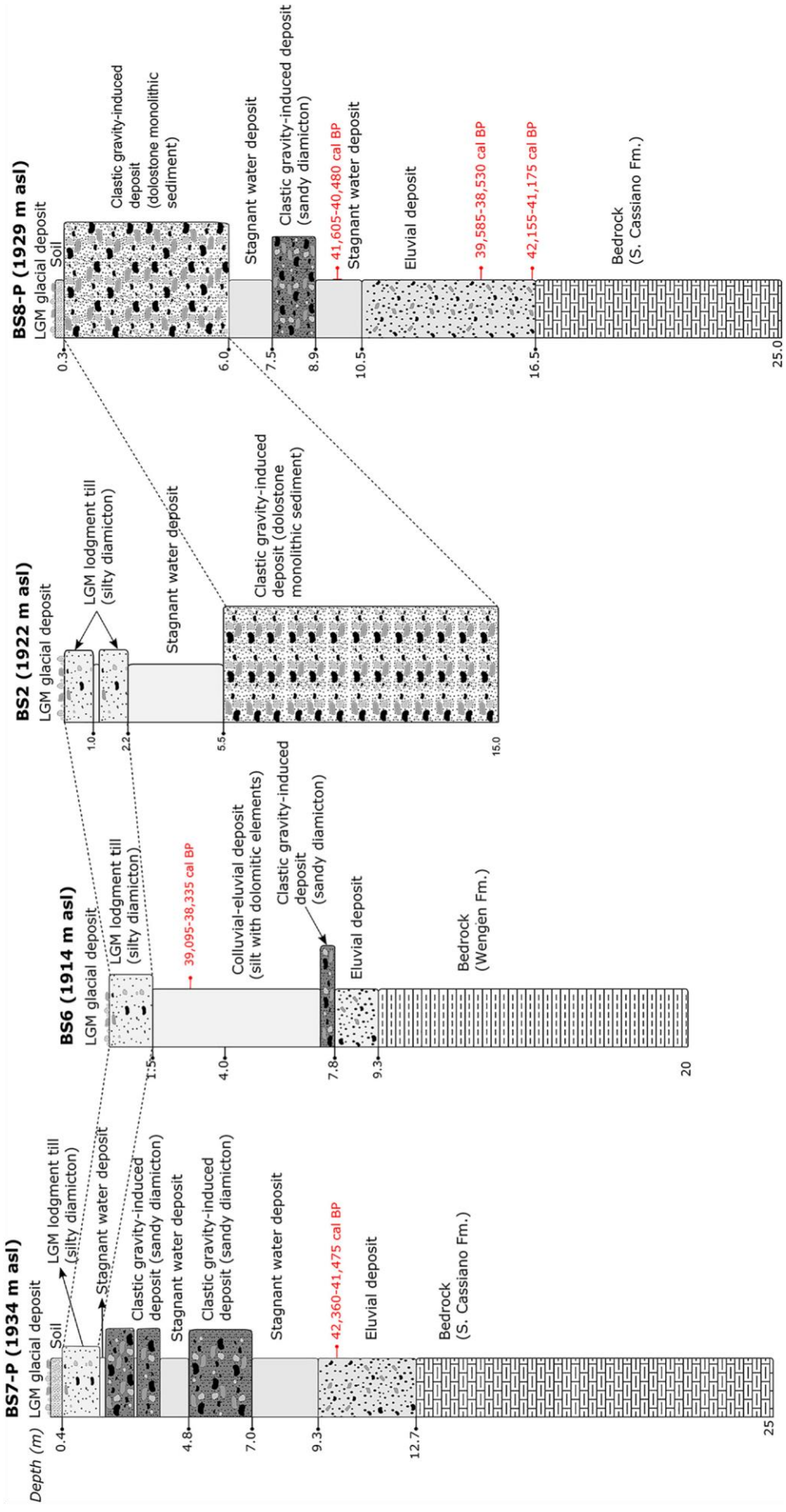

Fig. 4.1 Stratigraphy of BS7-P, BS6, BS2 and BS8-P cores (cf. Appendix 2) and radiocarbon ages.

4.2 Results on the investigation of glacial landforms

4.2.1 Cosmic Ray Exposure dating results

In this paragraph the results of ^{36}Cl Cosmic Ray Exposure dating are presented. In particular, in Figures 4.2 and 4.3, for the sake of internal comparison between all ^{36}Cl ages, the latter are presented with the analytical errors only, thus excluding from the estimate the error contribution due to the production rates. In Table 4.2 the ^{36}Cl ages are reported with their total uncertainty which considers both the analytical error and the production rate error. This uncertainty has to be considered when comparing ages at regional scale.

The ages range within a wide period of time, from 18 ± 2.2 to 6 ka BP ± 0.5 ka BP (see also appendixes 3 and 4), that is from the end of the Late Pleistocene to the early Holocene. The results showed that the exposure ages of 12 moraine boulders out of 16 are from the Late Pleistocene period, whilst only four samples revealed a Holocene exposure time. Some outliers among ^{36}Cl ages were identified (Tab. 4.2), they correspond to samples taken from re-exhumated boulders, as it will be discussed further on in this section.

Tab. 4.2 ^{36}Cl exposure ages of the collected samples. Ages are reported with their uncertainty which takes into account both analytical and production rate errors. Between parenthesis the analytical (inner) uncertainty is reported. In bold the Holocene ages and in italics the outliers resulting from the re-exhumation of sampled boulders are shown.

Sample name	Age (ka BP)	Sampling site
170829.02	13.3±1.4 (1.0)	Armentarola
170829.03	14.3±2.1 (1.3)	Armentarola
170830.01	14.4±2.8 (1.8)	Valparola
170830.02	**6.3±0.6 (0.5)**	**Sas Crusc**
170830.03	**9.5±1.0(0.7)**	**Sas Crusc**
170831.01	14.4±1.3(1.0)	Alting
GAR01.18	**9.9±3.2(2.8)**	**Gardena Pass**
GAR02.18	17.1±2.5(2.0)	Gardena Pass
GAR03.18	13.4±1.4(1.2)	Gardena Pass
GAR04.18	15.9±2.2(1.8)	Gardena Pass
CRU01.18	9.8±1.1(0.9)	Sas Crusc
SOR01.18	*14.8±2.6(2.0)*	*Pralongià*
VEG01.18	*13.6±2.4(1.8)*	*Pralongià*
PIC01.18	18.0±2.8(2.2)	Pralongià
SEL01.18	15.8±3.4(2.7)	Sella Pass
SEL02.18	15.4±2.8(2.1)	Sella Pass

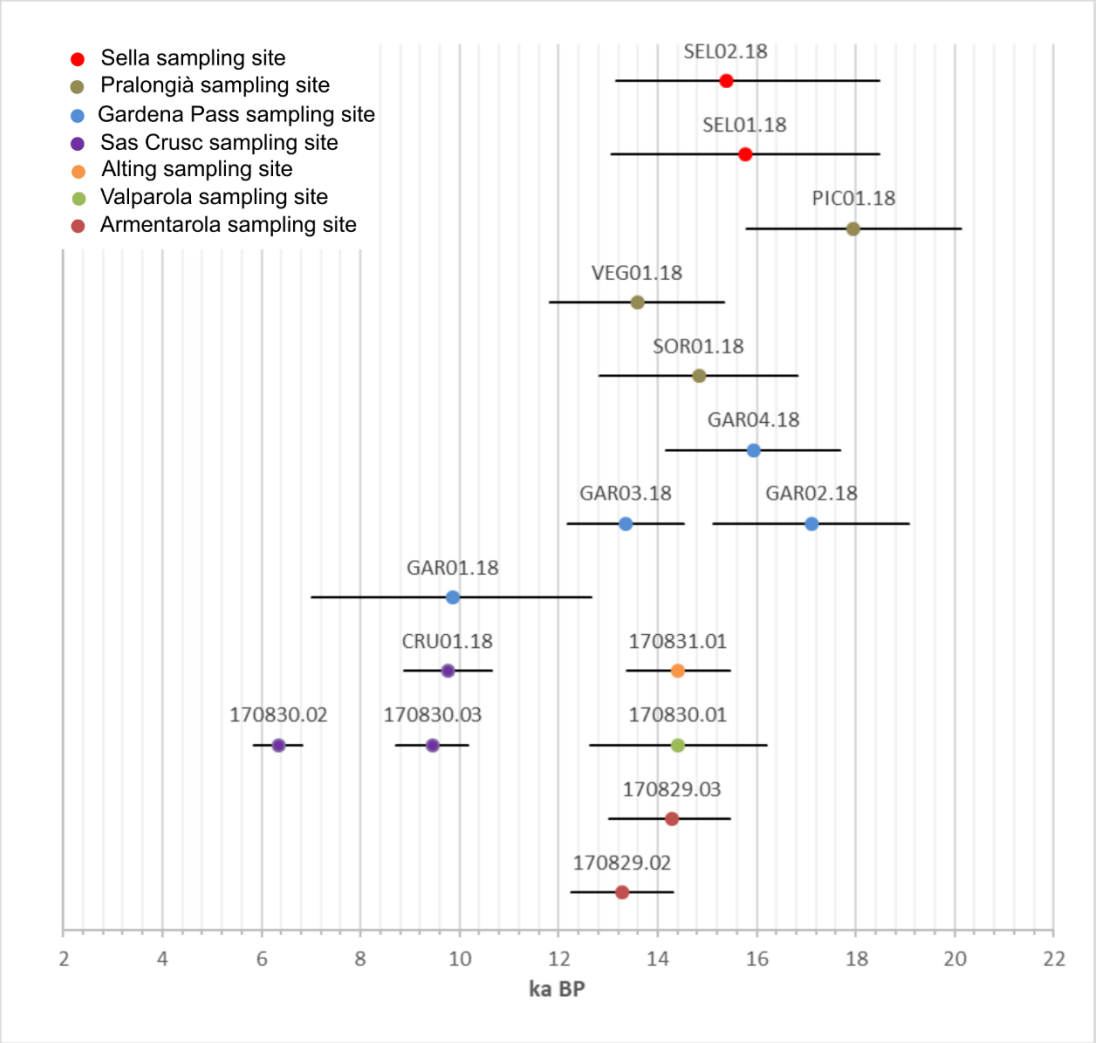

Fig. 4.2 Mean ^{36}Cl ages (dots) presented with their analytical (inner) uncertainty (black lines). Labels indicate sample names, whilst different colours refer to different sampling locations.

The Late Pleistocene ages were fundamental for the reconstruction and the characterization of glacial fluctuations within the valley, while the Holocene ages were indicative of different processes rather than the glacial ones. In fact, it is well-known from literature data that during the Holocene the Alta Badia valley was almost completely ice-free, as witnessed by marked slope instability phases occurred since at least the Greenlandian in response to the withdrawal of Lateglacial glaciers (cf. Soldati et al., 2006; Borgatti and Soldati, 2010).

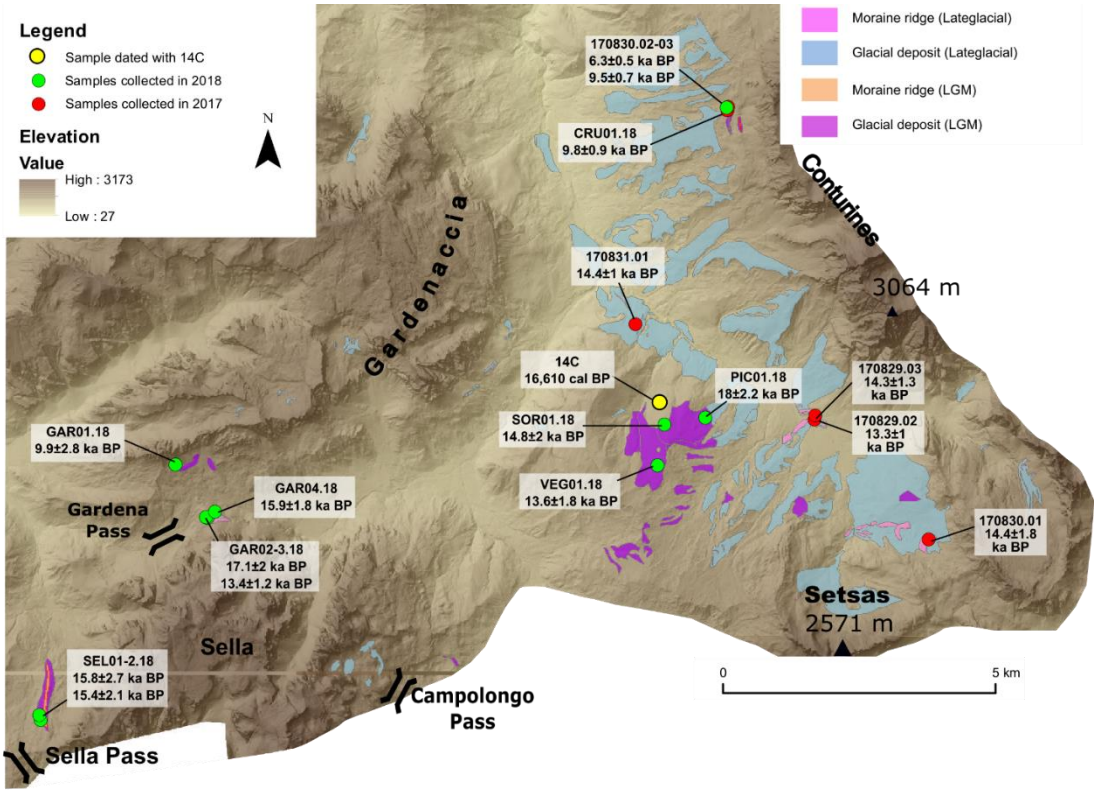

Fig. 4.3 ^{36}Cl exposure dating results for the collected samples with their location. Yellow dot represents the location of the ^{14}C dating performed on a charcoal sample and published in Panizza et al. (2011). In the picture, glacial deposits of the LGM and of the Lateglacial periods are also shown. LiDAR DEM courtesy of servizio cartografia provinciale e coordinamento geodati, Autonomous Province of Bolzano.

Armentarola sampling site

The Armentarola sampling site is located in the south-eastern part of the study area within the valley bottom at some 1600 m where several moraine ridges as well as widespread glacial deposits were recognized and mapped. Two samples (170829.02; 170829.03) were taken for ^{36}Cl dating, from dolostone moraine boulders located in a topmost position on a moraine ridge. Dating results revealed exposure ages of 13.3 ± 1 and 14.3 ± 1.3 ka BP respectively which agree with each other. The found exposure ages can be thus attributed to the Lateglacial period confirming the relative chronology proposed in literature (e.g. Panizza et al., 2011). On the basis of geomorphological evidence and dating results, these moraine deposits were interpreted as witnesses of a minor phase of glacial readvance occurred after the disappearance of the LGM icefield, at least at some 14-13 ka BP.

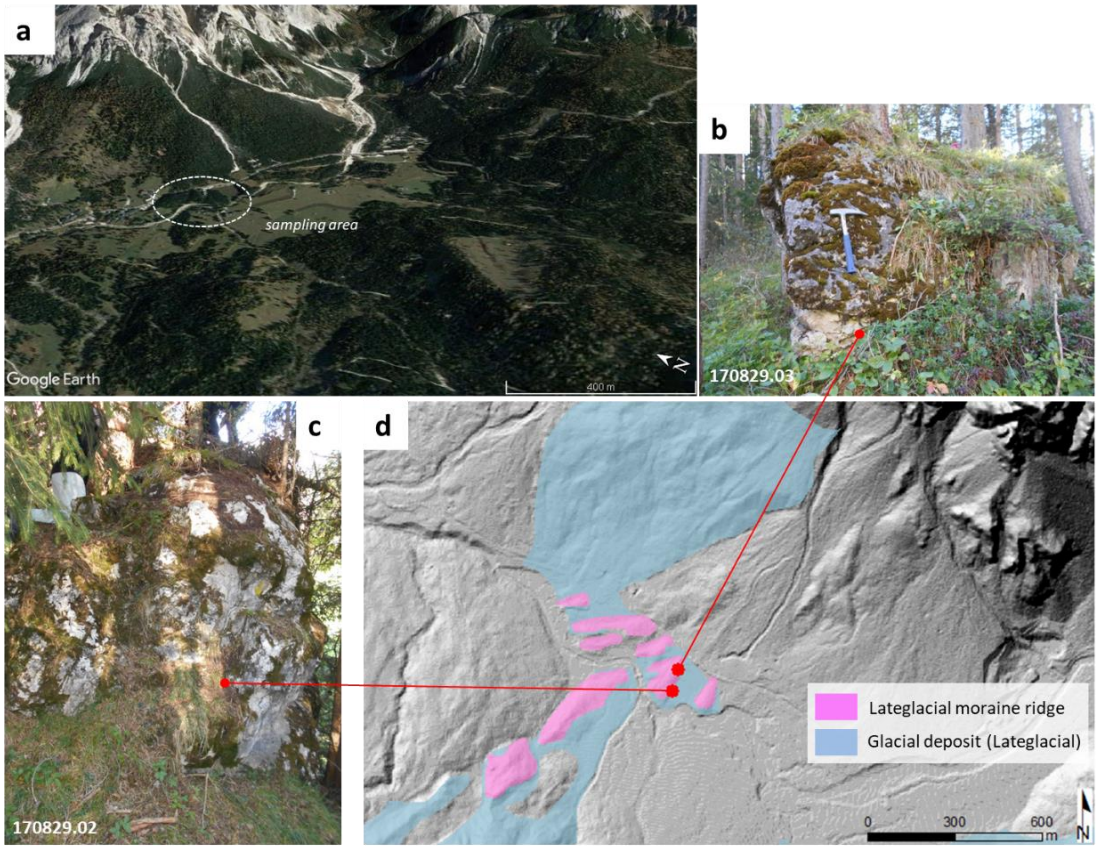

Fig. 4.4 Armentarola sampling area: a) Google Earth image of the Armentarola sampling site; b) and c) dolostone boulders (lab name: 170829.02-03) sampled for ^{36}Cl Cosmic Ray Exposure dating; d) location of the sampled boulders with respected to moraine features relatively attributed to the Lateglacial by Castiglioni (1964), Brandner et al. (2007), Panizza et al. (2011).

Valparola sampling site

The Valparola sampling site is located at some 2000 m in the south-eastern sector of the study area. Several frontal moraine ridges arranged in sequence were identified and mapped, they are witnesses of different phases of glacial advances; the higher the elevation of moraine ridge location the younger the glacier advance evidence. A boulder suitable to be dated with ^{36}Cl dating was found behind the uppermost moraine ridge, supposed to be the youngest on the basis of its relative topographic position. Dating results revealed an exposure age of 14.4 ± 1.8 ka BP. The found exposure ages can be thus attributed to the Lateglacial period confirming the relative chronology proposed by literature (e.g. Panizza et al., 2011). On the basis of geomorphological evidence and dating results these moraine deposits were interpreted as witnesses of minor phases of glacial advance occurred after the disappearance of the LGM icefield, at least at ca. 14 ka BP and synchronous to the glacial advance recorded at the Armentarola sampling site.

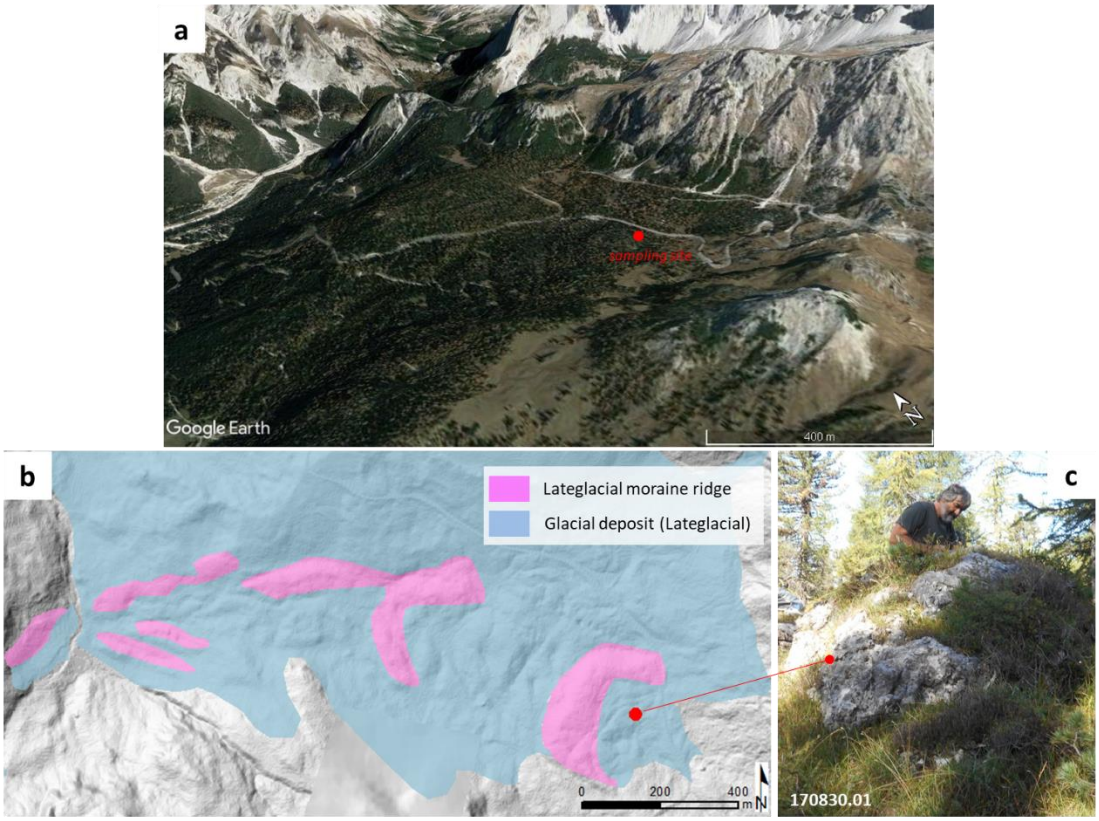

Fig. 4.5 Valparola sampling site: a) Google Earth image of the Valparola sampling site; b) location of the sampled boulders with respected to moraine features relatively attributed to the Lateglacial by Castiglioni (1964) and Panizza et al. (2011); c) dolostone boulder (lab name: 170830.01) sampled for ^{36}Cl Cosmic Ray Exposure dating.

Sas Crusc sampling site

The Sas Crusc sampling site is located in the northern part of the study area along the western slope of the Conturines Group. In the area, a ridge, backed by a smaller one, reaching up to ca. 2050 m in elevation was identified from aerial photos and LiDAR DEM analysis as well as confirmed also by field surveys. The origin of this ridge is controversial; in fact, on the basis of geomorphological evidence it was interpreted by von Klebelsberg (1927) and Panizza et al. (2011) as of glacial origin. The same authors inferred, on the basis of its relative position, an LGM age for the deposit (Fig. 4.6). On the contrary, in the geological map by Brandner et al. (2007) the ridge was included within an extensive landslide deposit constituted by huge blocks.

Three samples from three different dolostone boulders located on the top of the ridge were sampled for cosmogenic dating. The results revealed surface exposure ages dating to the Holocene. It is well-know from extensive climate records, provided for the valley by investigating landslide processes and their relation to climate changes,

that during the Holocene the Alta Badia valley was almost completely ice-free. In fact, marked slope instability phases were recognized since at least 10,700 years BP following the withdrawal of Lateglacial glaciers (cf. Soldati et al., 2006; Borgatti and Soldati, 2010).

Additionally, the former presence of a local glacier at Sas Crusc locality can be excluded for the lack of an area suitable to accommodate snow/ice accumulation along the subvertical Conturines slopes. Moreover, the westerly aspect of the slopes does not constitute favourable conditions for ice persistence at the ground, in fact the west-facing Conturines slopes receive sun's rays from the west at the hottest time of day in the afternoon, and they are warmer than the sheltered east-facing slope of the Gardenaccia Group.

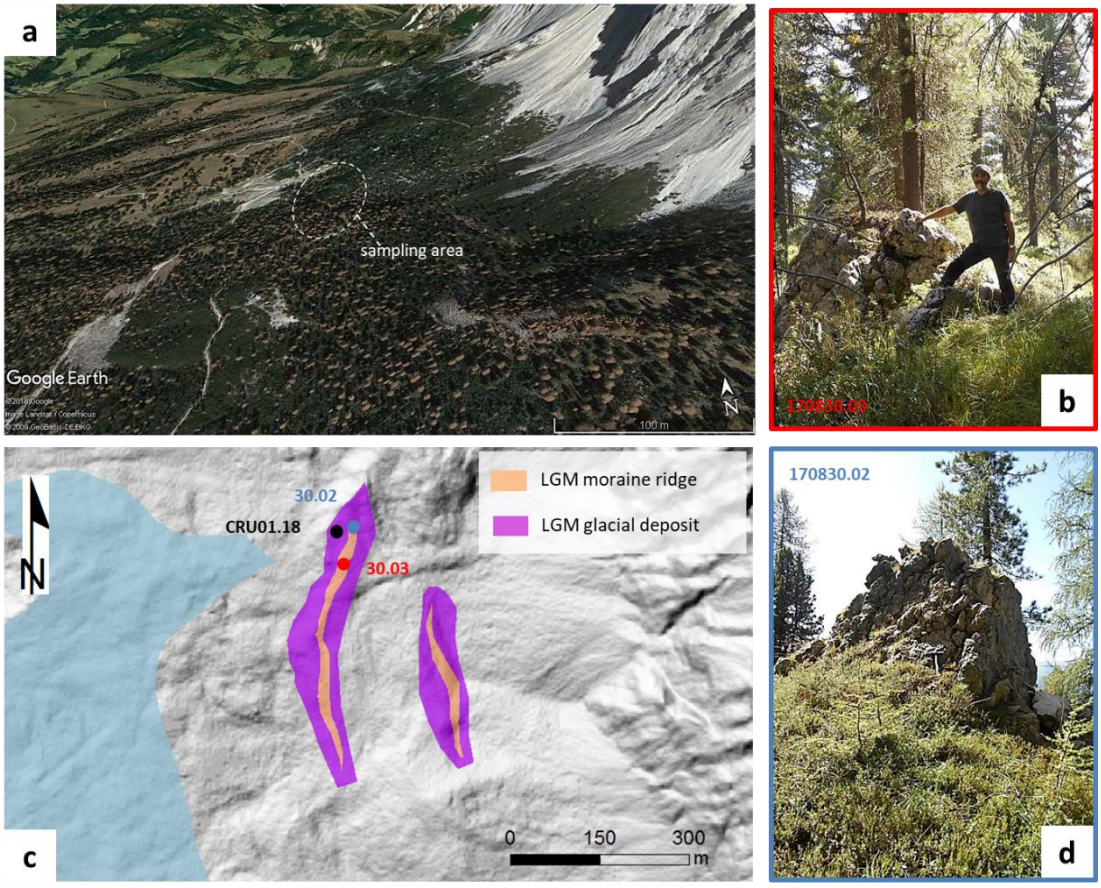

Fig. 4.6 Sas Crusc sampling site: a) Google Earth image of the Sas Crusc sampling site; b), d) boulders sampled for ^{36}Cl Cosmic Ray Exposure dating (lab name:170830.02-03); c) location of the sampled boulders with respected to the moraine features relatively attributed to the LGM by Panizza et al. (2011).

Alting sampling site

The Alting sampling site is located in the central sector of the study area at some 1600 m. One discontinuous moraine system elongated in a north to north-western direction has been identified and mapped. Considering its peculiar and elongated shape it has been interpreted as a system of lateral moraines. However, it is likely that running water action has reshaped the morphology of the moraine system that could have been dissected. A boulder suitable to be dated with ^{36}Cl dating was found in an uppermost position on one of the moraine ridges. Dating results revealed exposure ages of 14.4 ± 1.3 ka BP confirming the Lateglacial age of the deposits, this is indicative of a glacial advance phase occurred at least at ca. 14 ka BP synchronous to the ones recorded at Valparola and Armentarola sampling sites.

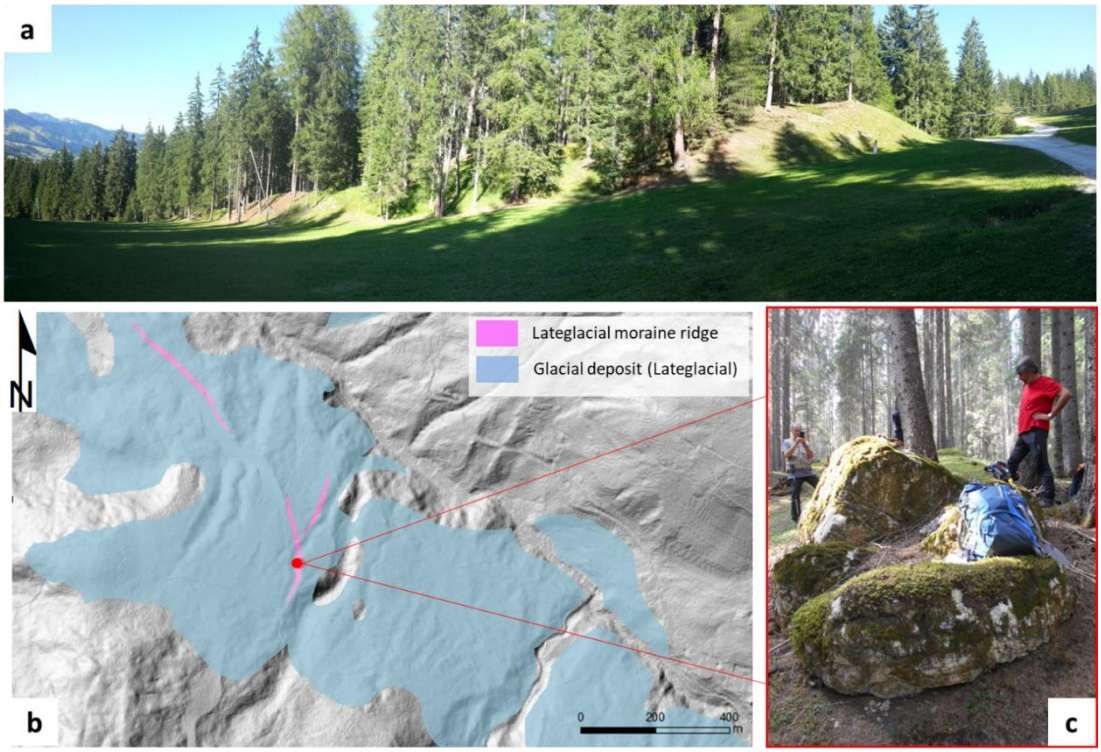

Fig. 4.7 a) Alting sampling site; b) location of the sampled boulder with respect to moraine features relatively attributed to the Lateglacial by Brandner et al. (2007) and Panizza et al. (2011); c) boulder sampled for ^{36}Cl Cosmic Ray Exposure dating (lab name:170831.01);

Gardena Pass sampling site

The Gardena Pass sampling site is located in the western sector of the study area at elevations ranging between ca. 2190 and 2265 m. Four samples were taken from the top surfaces of dolostone moraine boulders. In particular, one sample was collected from the northern part of the Gardena Pass (GAR01.18) at 2265 m, in correspondence of a glacial deposit supposed of LGM age on the basis of its relatively high position. Dating results for GAR01.18 sample revealed an exposure age of 9.9 ± 2.8 ka BP which is younger than the inferred relative age. As witnessed by numerous dating records from literature for the valley, the Alta Badia was ice-free during the Holocene. Admittedly, the slope adjacent to the sampled boulder is characterized by debris flow deposits and extensive screes of gravitational origin. It is likely that the sampled boulder was transported by gravity-driven slope processes and possibly set down on the LGM glacial deposit. The given exposure age reflects the depositional age of the boulder.

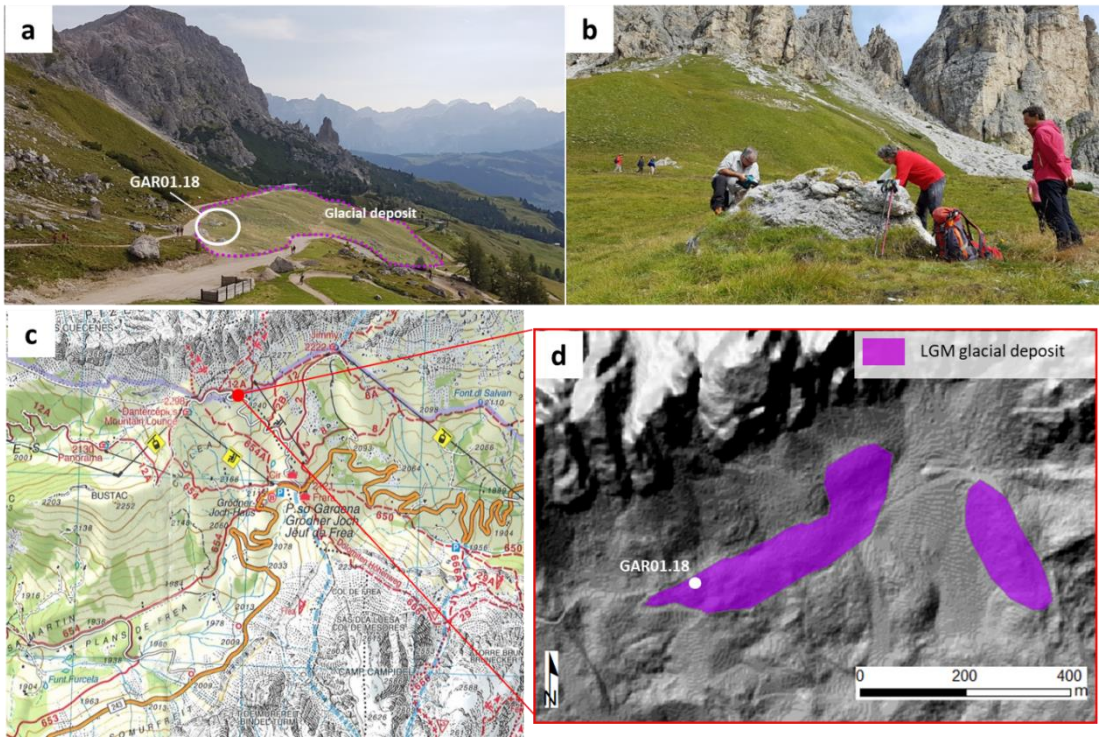

Fig. 4.8 Gardena Pass sampling site: a) and b) boulder sampled for ^{36}Cl Cosmic Ray Exposure dating (lab name: GAR01.18); c) location of the sampling site on the topographic map (Tabacco 07 Alta Badia Arabba – Marmolada; d) location of the sampled boulder with respect to moraine features relatively attributed to the LGM by Panizza et al. (2011).

Three more samples (GAR02.18; GAR03.18; GAR04.18) were collected respectively at 2235, 2232 and 2196 m, from three moraine boulders, located on a widespread moraine deposit supposed by Panizza et al. (2011) to be originated due to Lateglacial local glaciers developing along the north-facing slopes of Gardena Pass. New field surveys revealed the lack of an accumulation zone for the development of local glaciers. Moreover, the glacial sediment resulted to be mainly constituted by dolostone cobbles and boulders, widespread all along the lower slope and constituting a ca. 5 m thick blanket above the bedrock. Due to the morphology, the topographic conditions and the extensiveness of the deposit, which unlikely was emplaced by a local process, the glacial deposit was interpreted as released by the downwasting LGM icefield which was likely stagnant at the Gardena Pass. This interpretation was confirmed also by the dating results for GAR02.18 sample, located at the highest elevation (2235 m), which revealed one of the oldest ages for the valley, of 17.1 ± 2 ka BP, close to the end of the LGM.

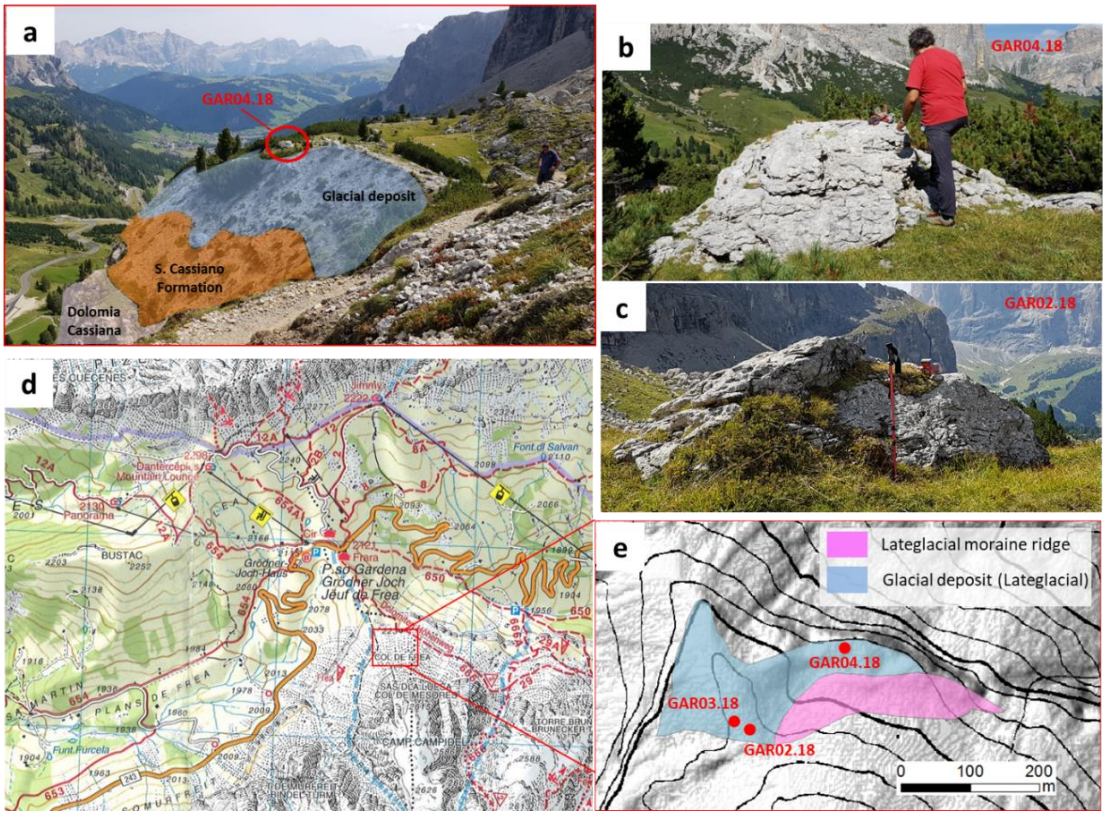

Fig. 4.9 Gardena Pass sampling site: a) and b) location of the boulder sampled for ^{36}Cl Cosmic Ray Exposure dating (lab name: GAR04.18); c) boulder from which the sample GAR02.18 was collected; d) location of the sampling site on the topographic map (Tabacco 07 Alta Badia Arabba – Marmolada); e) location of the sampled boulders with respect to moraine features relatively attributed to the LGM by Panizza et al. (2011).

Pralongià sampling site

The Pralongià sampling site corresponds to an isolated plateau within the central sector of the study area. Three samples (SOR01.18; VEG01.18; PIC01.18) were collected at altitudes ranging between 1852 and 1998 m on the plateau in correspondence of a glacial deposit attributed by previous authors to the LGM period based on its topographic conditions. Worthy of note was the sample PIC01.18 which was collected from the top surface of an erratic mass 18-m high close to the boundary (Fig. 4.10) with the glacial deposits supposed Lateglacial in age on the basis of their position. The huge erratic mass was likely transported by the LGM ice mass and exposed due to the following ice lowering; certainly, it was not affected by Lateglacial advances as it can be inferred from its relatively dominant position with respect to the valley bottom.

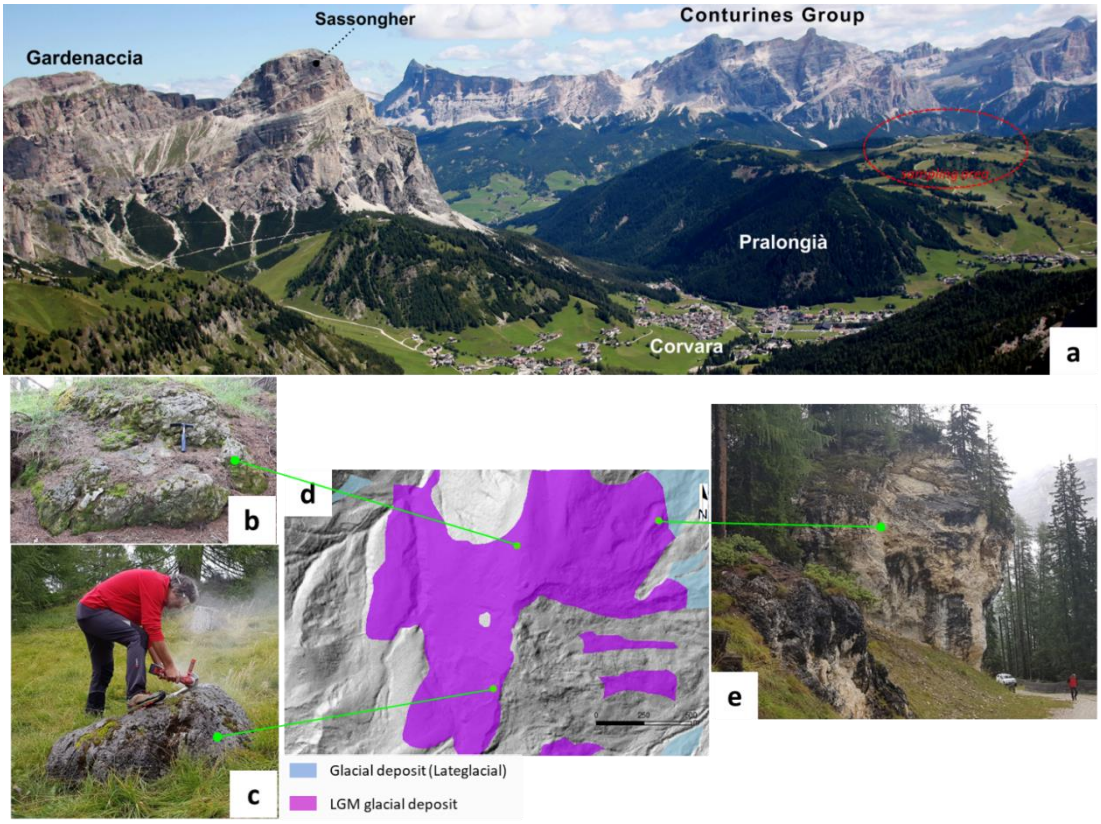

Fig. 4.10 Pralongià sampling site: a) the Pralongià plateau (photo by F. Planinschek, courtesy of Tourist Board Alta Badia); b), c) and e) boulders sampled for ^{36}Cl exposure dating (lab name: SOR01.18, VEG01.18 and PIC01.18 respectively); d) location of the sampled boulders with respect to moraine features identified by Brandner et al. (2007) and relatively attributed to the LGM by Panizza et al. (2011).

Dating results revealed an exposure age for the mass of 18 ± 2.2 ka BP witnessing the occurrence of LGM ice lowering at least since ca. 18 ka BP.

The samples SOR01.18 and VEG01.18 were collected from dolostone boulders less than 1-m high and embedded in the soil. Considering the younger (with respect to the inferred ages) exposure ages resulted for these boulders, it is reasonable that they were buried within the glacial sediment and then exposed only at some 15-13 ka BP.

Sella Pass sampling site

The Sella Pass sampling site is located at the western margin of the study area at altitudes ranging from 2176 and 2192 m. Two samples (SEL01.18 and SEL02.18) were collected from the top surfaces of two boulders located in a prominent position on a sinuous moraine ridge stretching towards the north for approximately 800 m. Dating results revealed exposure ages of 15.8 ± 2.7 and 15.4 ± 2.1 ka BP, this is indicative of a glacial advance phase occurred at least at ca. 15 ka BP preceding the glacier advance recorder at 13-14 ca. BP at Alting and Armentarola localities and at Valparola Pass.

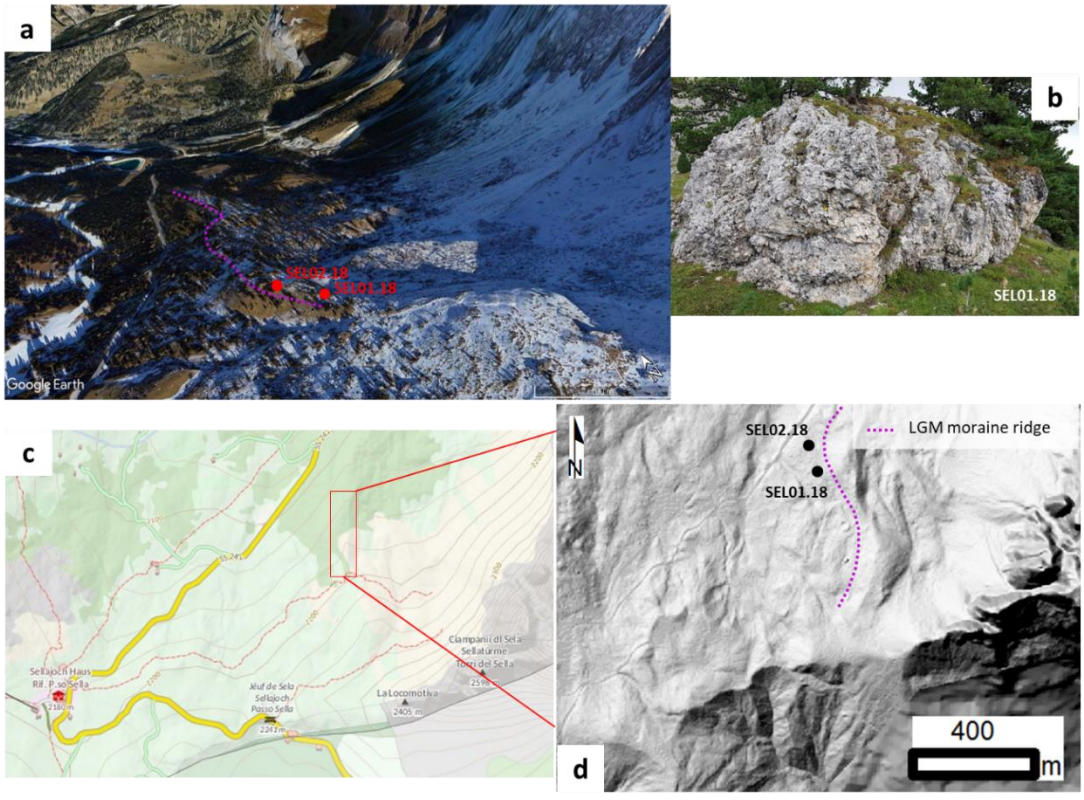

Fig. 4.11 Sella Pass sampling site: a) Google Earth image of the Sella sampling site; b) boulder sampled for ^{36}Cl Cosmic Ray Exposure dating (lab name: SEL01.18); c) location of the Sella sampling site on the topographic map by OpenStreetMap; d) moraine ridge and location of the sampled boulders.

4.2.2 Reconstruction of glacier surfaces

LGM ice surface

The LGM trimlines – representative of the maximum elevation reached by the LGM icefield – were reconstructed on the basis of the evidence from remote sensing data analysis and interpretation supported by field surveys. The trimlines were mapped in ArcGIS environment and were used to delimit the extent and reconstruct the LGM ice surface (Fig. 4.12). From the reconstruction emerged that the icefield covered the Alta Badia and reached a maximum altitude of ca. 2400 m a.s.l. within the valley, e.g. in correspondence of the Gardena Pass and along the eastern slope of the Conturines Group. Local glaciers departing from the Gardenaccia and Sella groups as well as from the Setsas and Lagazuoi mounts joined and flowed into the icefield.

From the reconstructed ice surface, the volume of the LGM ice mass was provided thanks to automated tolls integrated in ArcGIS (e.g. Raster Calculator tool). The LGM icefield covering the Alta Badia valley extended for some 160 km^2 with an approximate volume of 30 km^3 and a maximum thickness with respect to the valley bottom of 800 m.

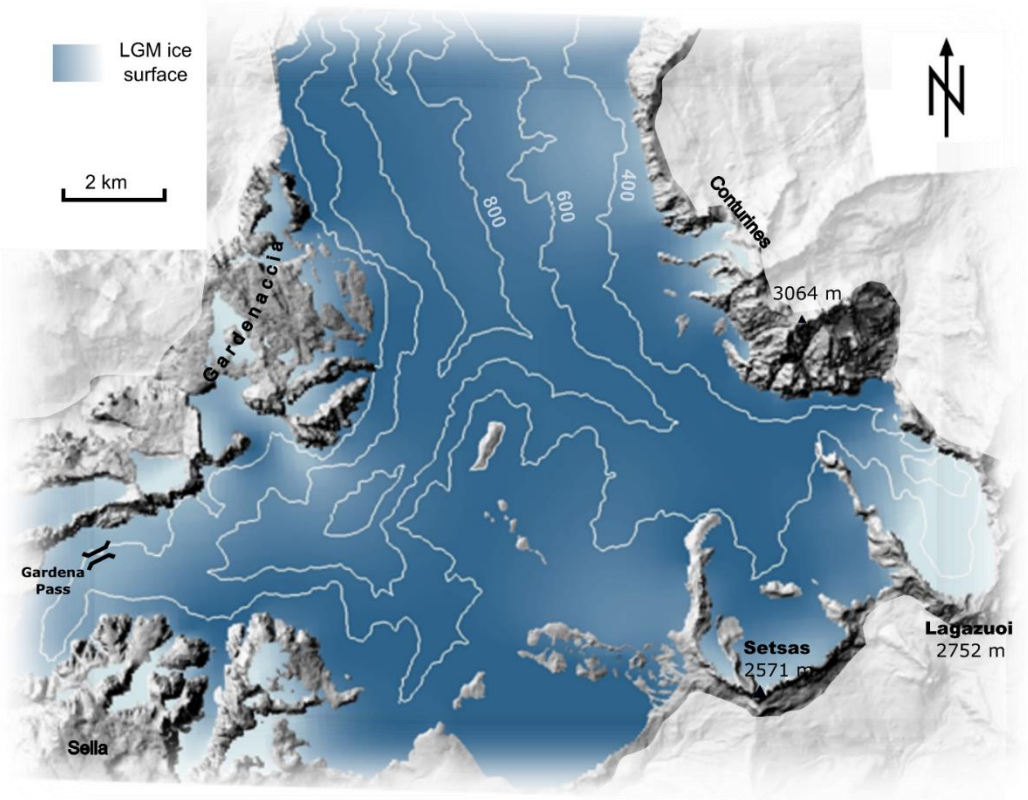

Fig. 4.12 Maximum extension of the reconstructed LGM icefield within the Alta Badia valley. Contour lines refer to ice thickness with respect to the valley bottom.

Armentarola paleoglacier

The geometry of the paleoglacier settled at the Armentarola locality at around 14 ka BP was provided and its ELA was calculated. The Armentarola paleoglacier (Fig. 4.13) was located in the central sector of the study area, flowing from the Pralongià plateau toward a north-northeast direction to the valley bottom reaching ca. 1577 m (Tab. 4.3). The glacier developed along a gentle path (Fig. 4.14) on the western flank of the Les Pizades mount (or Le Pizzade, in Italian). A set of dissected moraine ridges delimits the maximum extent reached by the glacier within the valley bottom. The north-facing slope, along which the paleoglacier developed, is subject to low solar radiation (Fig. 4.14) which may have favoured the persistence of snow and the formation of ice. The paleoglacier occupied a total surface of ca. 2.27 km^2 for a total volume of 0.01 km^3.

Tab. 4.3 Main geometrical parameters of Armentarola reconstructed glacier surface and ELAs. The mean ELA is the average value between ELA calculated with AAR method (eighth row) and ELA calculated with AABR method (ninth row). The ELA depression (tenth row) is calculated by subtracting the mean ELA to the local LIA ELA (2800 m, cf. section 3.2.1).

NAME	Armentarola glacier
Aspect	N-NE
Min Altitude	1577 m
Max Altitude	2116 m
Mean Altitude	1935 m
Volume	0.01 km^3
Area	2.27 km^2
ELA aar	1852 m ± 45
ELA aabr	1905 m ± 25
ELA mean	1878 m ± 35
ΔELA	922 m

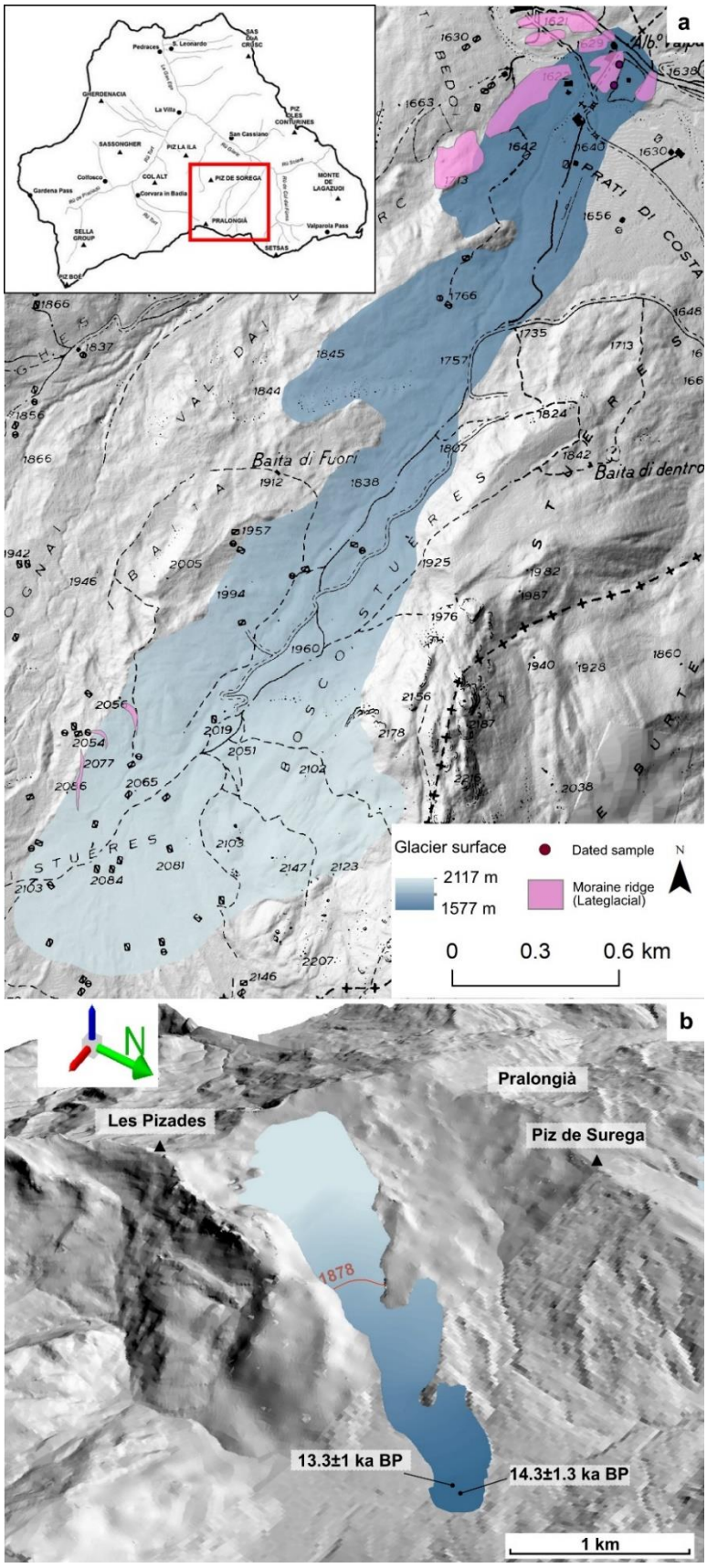

Fig. 4.13 The reconstructed surface of the Armentarola paleoglacier: a) 2D representation and location of the glacier within the Alta Badia valley; b) 3D representation of the glacier (in shaded blue) and mean paleo-ELA (red line).

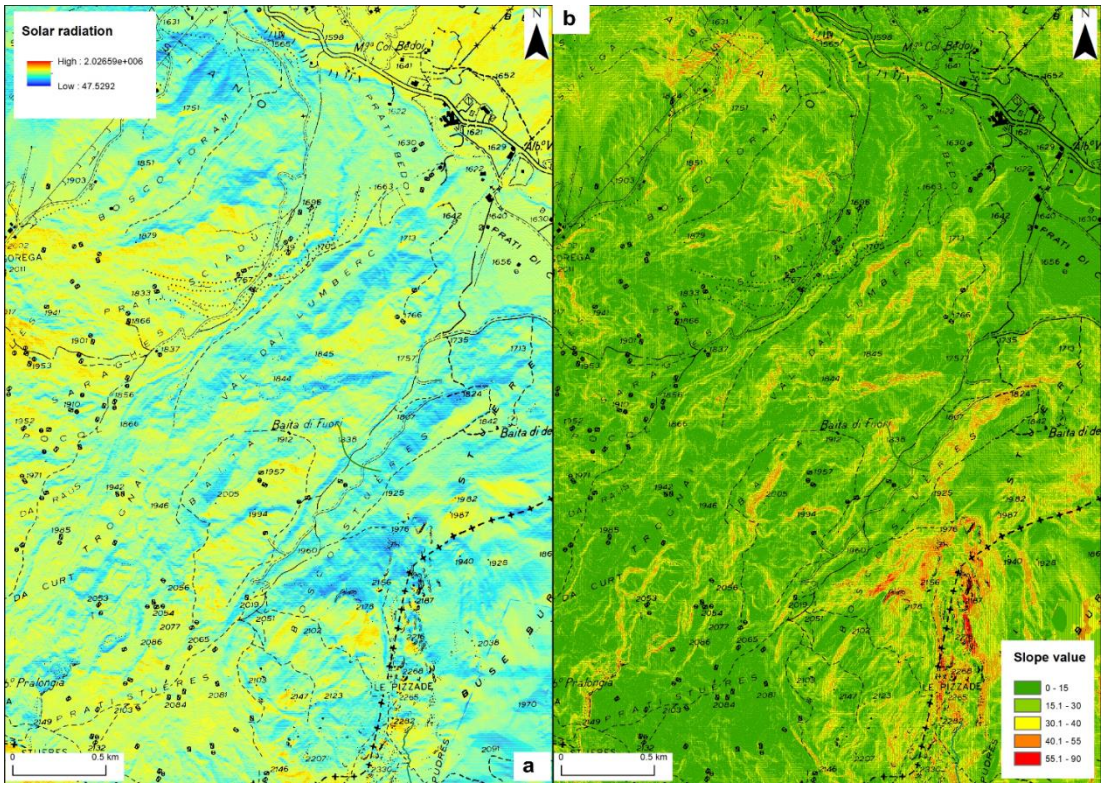

Fig 4.14 a) Distribution of yearly global solar radiation (expressed in Wh/m^2, watt hours per meter square) for the area which was formerly occupied by the Armentarola paleoglacier; b) distribution of slope angles expressed in decimal degrees and relevant to the same area.

Valparola paleoglaciers

The geometry of the paleoglaciers extending at the Valparola Pass at least at/before of ca. 14 ka BP was provided and their ELA was calculated (Tab. 4.4). Three main glaciers were identified: Prà de Dlira, Malghe Valparola and Pudres paleoglaciers, plus some minor glaciarets. The names assigned to the glaciers reflect those assigned in the paper by Ghinoi and Soldati (2017) on the basis of local toponyms. The Valparola paleoglaciers were located in the southeastern sector of the study area, departing toward the north from the Mount Setsas and extending on a total surface of ca. 3.2 km^2 for a total volume of 0.04 km^3. As it can be inferred from the slope map (Fig. 4.15), the Mount Setsas has a wide gently inclined slope which can accommodate only moderate snow accumulation, but the low solar radiation to which it is subject may have favoured the persistence of snow and the formation of ice.

The upper limit of Pudres and Malghe Valparola paleoglaciers is outlined by glacial cirques partially remodelled by slope processes, whilst the lower limit of the Prà de Dlira glacier lies in correspondence of the most prominent frontal moraine ridge (Fig. 4.16a).

The mean ELAs calculated for the three glaciers range between 2223 m for the Pudres glacier, to 2051 m for the Prà de Dlira glacier. These values are in good agreement with the ones calculated by Ghinoi and Soldati (2017) that range from 2300 m for the Pudres glacier and 2087 for the Prà de Dlira glacier.

Tab. 4.4 Main geometrical parameters of Valparola reconstructed glacier surfaces and their ELAs. The mean ELA is the average value between ELA calculated with AAR method (eighth column) and ELA calculated with AABR method (ninth column). The ELA depression (tenth column) is calculated by subtracting the mean ELA to the local LIA ELA (2800 m, cf. section 3.2.1).

Name	Aspect	Min Altitude	Max Altitude	Mean Altitude	Volume	Area	ELA aar	ELA aabr	ELA mean	ΔELA
Pudres	N-NE	2032 m	2500 m	2259 m	0.01 km^3	0.53 km^2	2206 ± 19	2239 ± 12	2223 +/-16	577 m
Malghe Valparola	N	1861 m	2540 m	2159 m	0.02 km^3	1.87 km^2	2093 ± 23	2140 ± 15	2117 ± 19	683 m
Prà de Dlira	NW	1897 m	2469 m	2096 m	0.01 km^3	0.78 km^2	2026 ±13	2076 ±13	2051 ±13	749 m

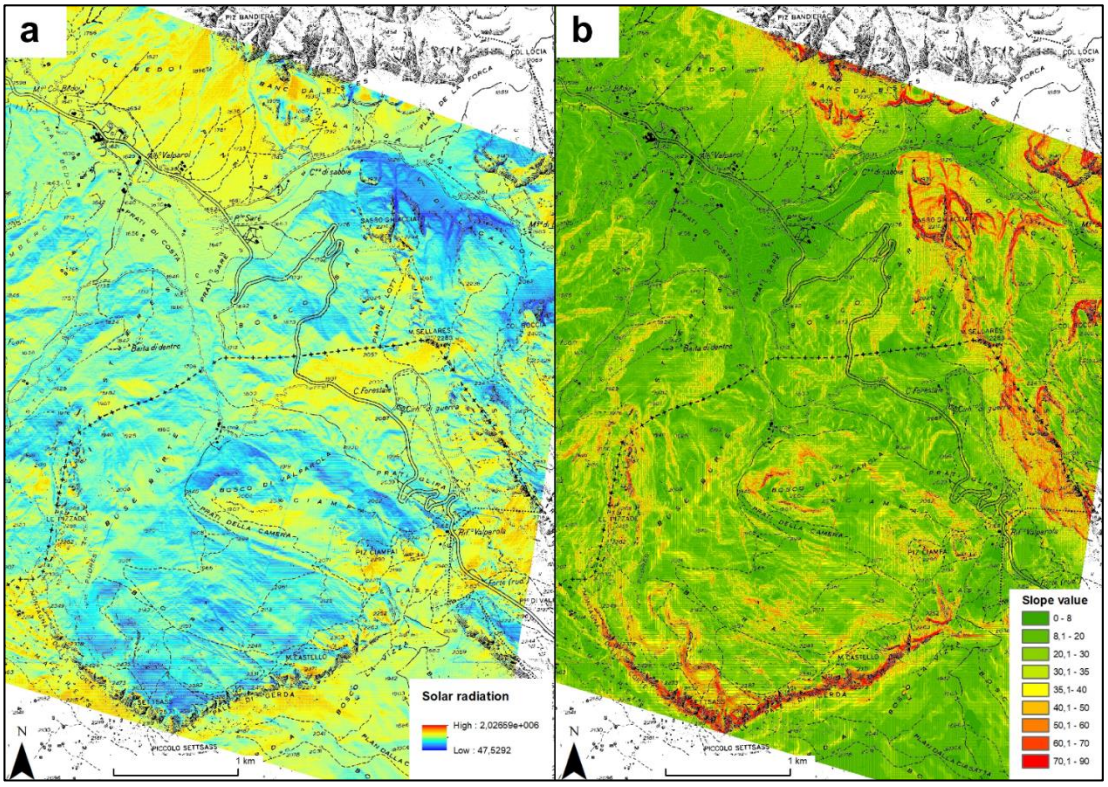

Fig. 4.15 a) Distribution of yearly global solar radiation (expressed in Wh/m^2, watt hours per meter square) for the area which was formerly occupied by the Valparola paleoglaciers; b) distribution of slope angles expressed in decimal degrees and relevant to the same area.

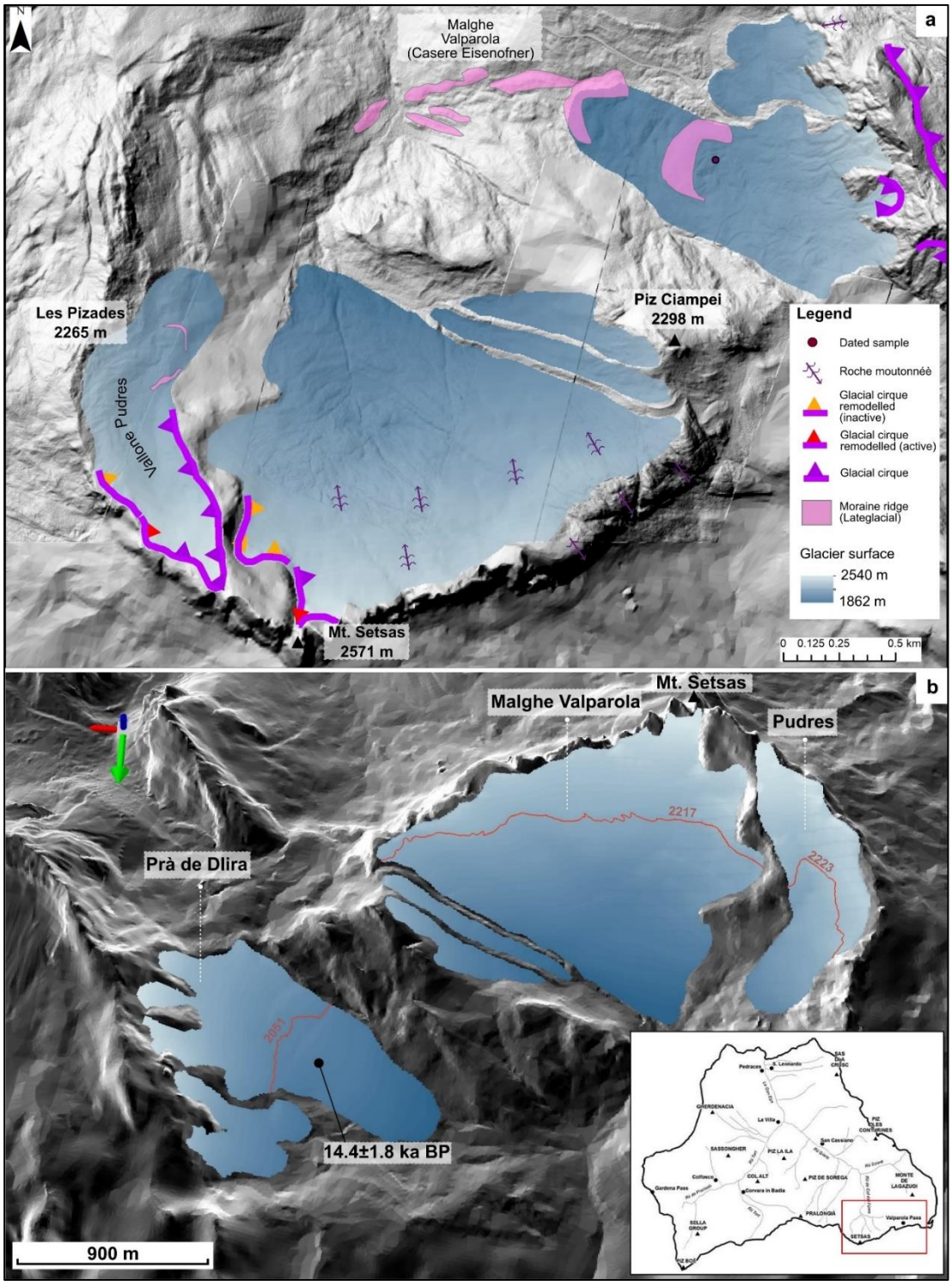

Fig. 4.16 The reconstructed surface of the Valparola paleoglaciers that are, from west to east: Pudres, Malghe Valparola and Prà de Dlira paleoglaciers. a) 2D representation of the paleoglaciers (in shaded blue) and glacial features of the area; b) 3D representation of the paleoglaciers (in shaded blue) and their location within the Alta Badia valley. Red lines represent the mean paleo-ELAs. The green arrow indicates the north direction.

Alting paleoglacier

The geometry of the paleoglacier departing from the Pralongià plateau and settled at least at around 14.4± 1.3 ka BP was provided, and the ELA was calculated. The Alting paleoglacier (Fig. 4.17) was located in the central sector of the study area, the accumulation zone was confined within Piz de Surega and Piz la Ila ridges while the ablation zone developed along the north-east facing slope toward the valley bottom. The lower limit of the paleoglacier stretched out toward a north-northwest direction along an elongated system of lateral moraines.

Along this stretch of the valley, yearly global solar radiation is relatively low partly due to the shade effect of the surrounding reliefs (Fig. 4.18). These local conditions may have favoured the accumulation of snow and the formation of ground ice.

The Alting paleoglacier covered an area of 1.71 km^2 for a total volume of 0.04 km^3 (Tab. 4.5). The ELA calculated with AAR and AABR methods are respectively of 1749 and 1767 m, and the mean value is 1758 m.

Tab. 4.5 Main geometrical parameters of the reconstructed surface of the Alting glacier and their ELAs. The mean ELA is the average value between ELA calculated with AAR method (eighth row) and ELA calculated with AABR method (ninth row). The ELA depression (tenth row) is calculated by subtracting the mean ELA to the local LIA ELA (2800 m, cf. section 3.2.1).

NAME	Alting glacier
Aspect	N-NE
Min Altitude	1491 m
Max Altitude	1972 m
Mean Altitude	1785 m
Volume	0.04 km3
Area	1.71 km2
ELA aar	1749 m ± 14
ELA aabr	1767 m ± 14
ELA mean	1758 m ± 14
ΔELA	1042 m

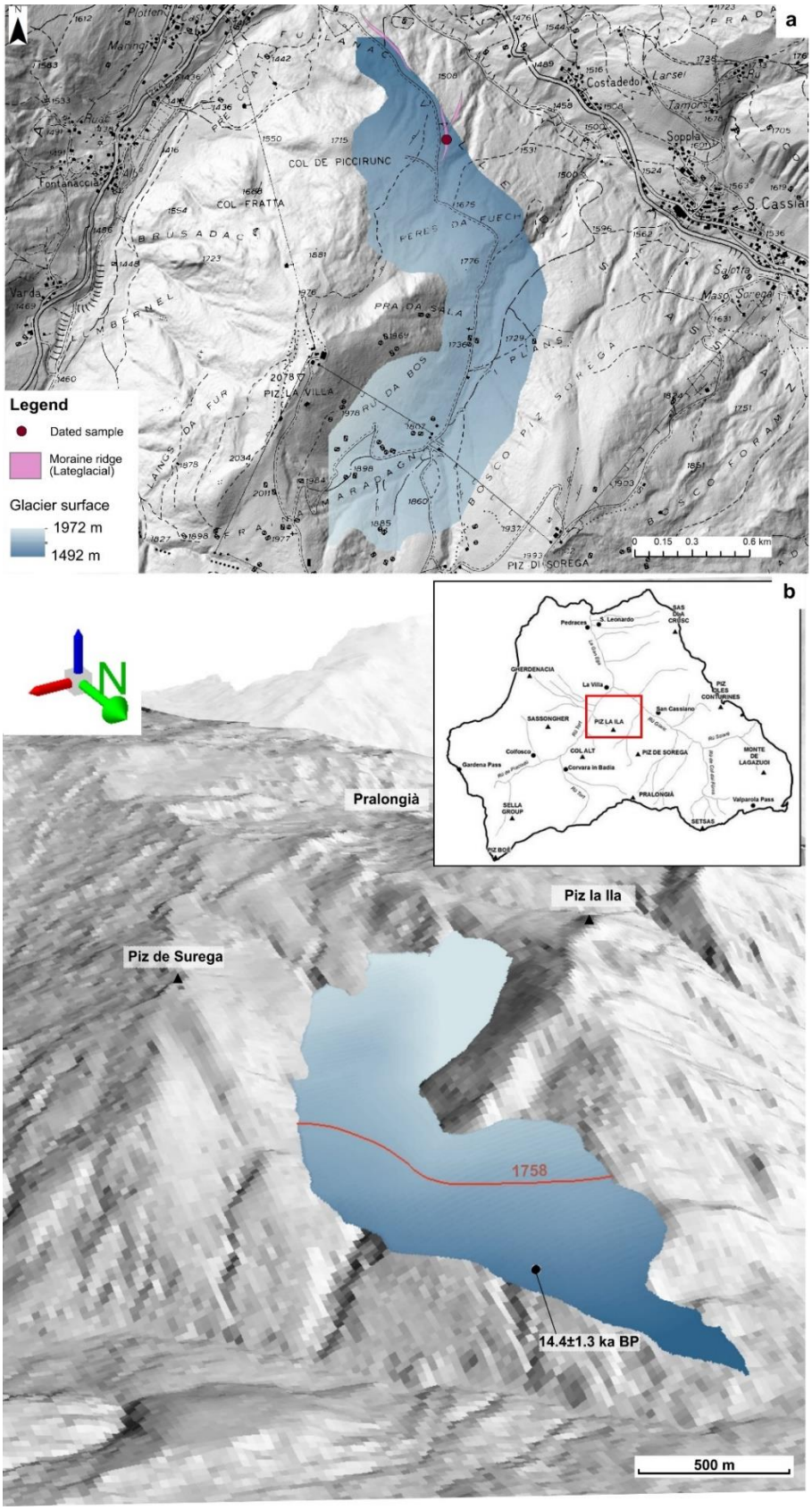

Fig. 4.17 The reconstructed surface of the Alting paleoglacier: a) 2D representation and glacial features of the area; b) 3D representation of the glaciers (in shaded blue) and their location within the Alta Badia valley. Red lines represent the mean paleo-ELAs. The green arrow indicates the north direction.

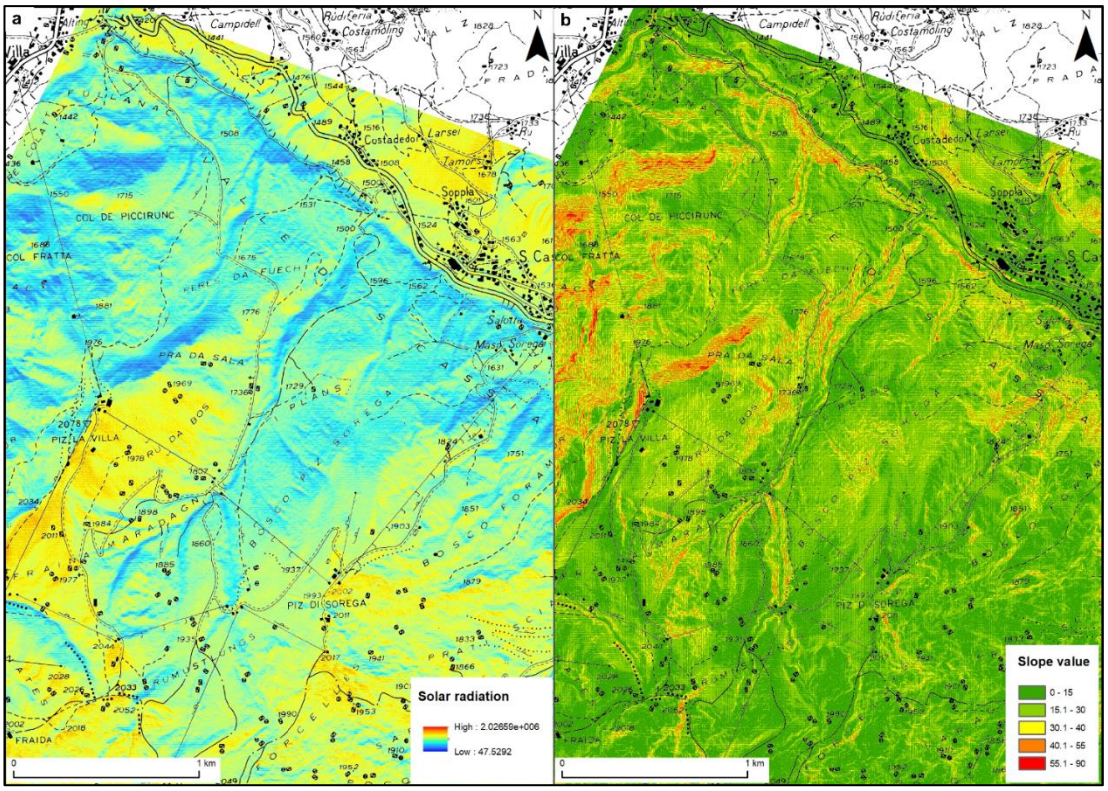

Fig. 4.18 a) Distribution of yearly global solar radiation (expressed in Wh/m^2, watt hours per meter square) for the area which was formerly occupied by the Alting paleoglacier; b) distribution of slope angles expressed in decimal degrees and relevant to the same area.

Sella paleoglacier

The geometry of the former glaciers extending at the Sella Pass at least at ca. 15 ka BP was provided and the ELA was calculated (Tab. 4.6).

The area on which the paleoglacier extended is subject to low yearly solar radiation (Fig. 4.19) which, together with the low slope gradient, may have favoured the persistence of snow and the formation of ice at the ground.

Sella paleoglacier (Fig. 4.20) was located on the north-western side of the Sella Group and it was delimited by a well-developed moraine ridge 1.3 km long. The reconstructed glacier surface varies in altitudes between 1939 and 2775 m, covering an area of 1.04 km^2.

Next to the Sella glacier a glaciaret departing from Piz Ciavazes was also mapped.

The ELAs calculated with AAR and AABR methods are respectively of 2064 and 2178 m, and the mean value is 2121 m.

Tab. 4.6 Main geometrical parameters of the reconstructed surface of the Sella glacier and its ELA. The mean ELA is the average value between ELA calculated with AAR method (eighth row) and ELA calculated with AABR method (ninth row). The ELA depression (tenth row) is calculated by subtracting the mean ELA to the local LIA ELA (2800 m, cf. section 3.2.1).

NAME	Sella glacier
Aspect	N
Min Altitude	1939 m
Max Altitude	2775 m
Mean Altitude	2114 m
Volume	0.02 km^3
Area	1.04 km^2
ELA aar	2064 m ± 10
ELA aabr	2178 m ± 11
ELA mean	2121 m ± 10,5
ΔELA	679 m

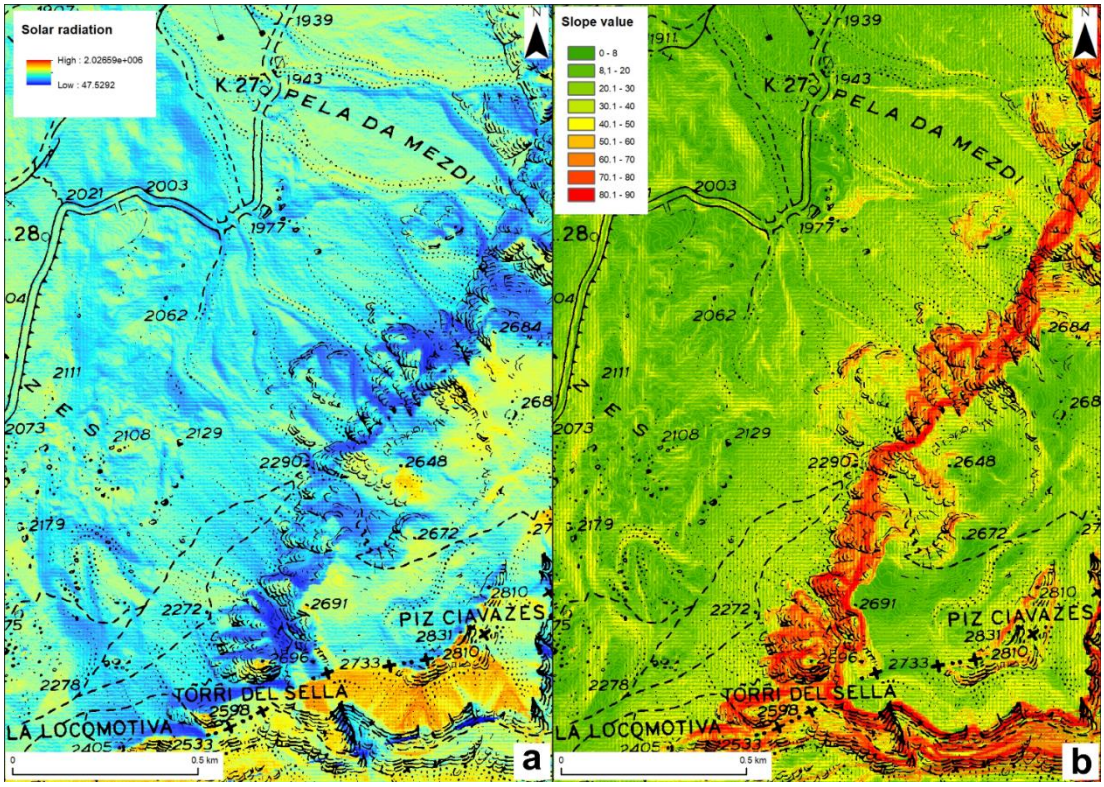

Fig. 4.19 a) Distribution of yearly global solar radiation (expressed in Wh/m^2, watt hours per meter square) for the area which was formerly occupied by the Sella paleoglacier; b) distribution of slope angles expressed in decimal degrees and relevant to the same area.

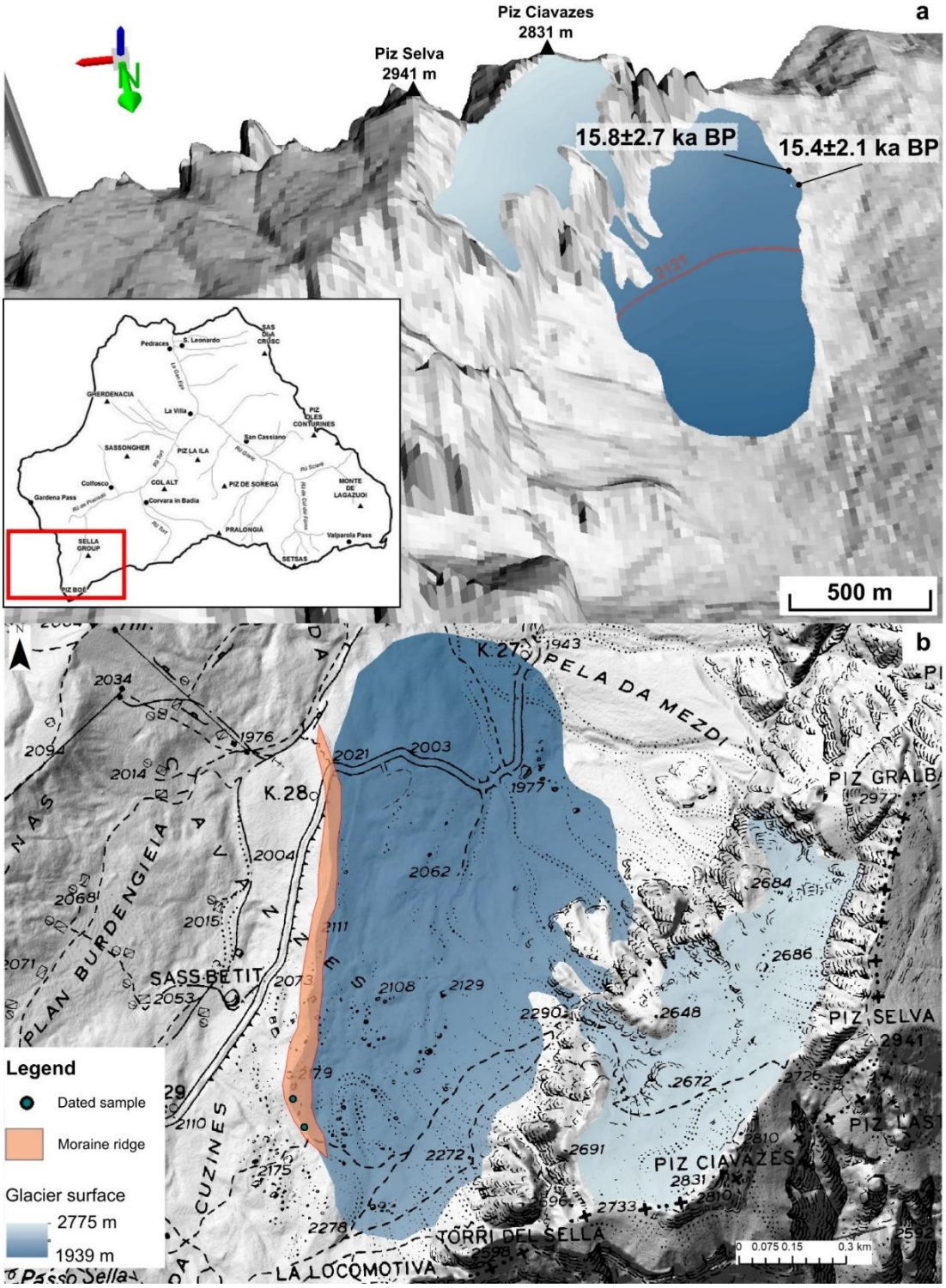

Fig. 4.20 The reconstructed surface of the Sella paleoglacier: a) 3D representation of the glacier (in shaded blue) and its location within the Alta Badia valley; b) 2D representation and glacial features of the area. Red lines represent the mean paleo-ELAs. The green arrow indicates the north direction.

5. Discussion

5.1 Pre-LGM period and emplacement of supraglacial gravity-induced deposits on the Pralongià plateau

Radiocarbon data from the investigated subsurface deposits (cf. section 4.1), retrieved on the Pralongià plateau through eight boreholes and an excavation wall, revealed that in some cases, the found ages pre-date the deposits; this might be due to colluvial processes that could be responsible for the inclusion of pre-aged organic remains within these deposits. However, the radiocarbon ages obtained are still significant because they indicate that between some 45 and 38 ka BP the Pralongià plateau was likely to have been ice-free and conditions enabling organic matter production occurred. As previously mentioned, sandy diamicton, monolithic sediment and colluvial-eluvial deposits are dolostone bearing, even if there are no dolomite outcrops within the Pralongià plateau. This let us suppose that dolostone might has been transported from sources outside the Pralongià plateau. Endoglacial or subglacial transport is excluded owing to the lack of evidence within the deposits and the dominance of dolostone monolithic angular material. Thus, significant gravity-induced input should be taken into account. It is likely that slope instability processes – vast enough to reach the Pralongià plateau from the surrounding dolomite cliffs – took place. This hypothesis is supported by the fact that large-scale landslides are common during and after the LGM in the Italian Alps (e.g. Genevois et al., 2006; Soldati et al., 2006; Borgatti and Soldati, 2010; Carton, 2017; Rossato et al., 2018). The Masiere di Vedana rock avalanches (Mt. Peron, Belluno Province) are worthy of note in the Eastern Alps, with a total rock mass of 100 million m^3 and an extension of 5.5 km. These mass movements occurred within the Cordevole valley when the valley floor was still occupied by the Cordevole glacier, some 16-15 ka BP (Pellegrini et al., 2006). However, it should be pinpointed that the isolation of the Pralongià plateau from the surrounding dolomite peaks – due to the presence of deep valleys bounding it – would have precluded mass movements from reaching the plateau. Nevertheless, this could have occurred in the presence of ice masses filling the valleys and hence, linking the dolomite cliffs to the plateau. In such a situation, supraglacial transport would have occurred (Fig. 5.1). At present, there are many examples of rock avalanches or debris flows occurring on glaciers in Alpine environments that travel for kilometres from their source areas (McSaveney, 1978; Kirkbride and Sugden, 1992; Fort, 2000, 2003; Jibson et al., 2006; Hewitt, 2009; Stoffel and Huggel, 2012). In

glacial conditions, these types of mass movements can have an enhanced mobility and a remarkable runout, mainly due to the incorporation of ice and snow, which reduce the friction within the debris mass (e.g. Deline, 2009).

Considering the sedimentary features of the gravity-induced deposits analysed – particularly their scant sorting and the angular/sub-angular shape of the clasts and their monolithic nature – their origin can be related to the occurrence of a series of debris flows from dolomite cliffs or the wash out/reworking of rock avalanche deposits, which accumulated over the ice mass. According to our reconstructions (Fig. 5.1), between 38 ka BP and the LGM, large-scale slope movements detaching from the main ridges surrounding the Pralongià plateau might have occurred. This would have required a large source area of dolostone, which can be identified in the Conturines (to the north) and/or in the Sassongher massifs (to the west) (Fig. 5.2). If we suppose an ice bridge attaining 1900 m a.s.l. (Scenario 1 in Fig. 5.1), the only possible source area can be identified in the southern side of the Conturines, located some 5 km from the sampling site and characterised by a travel slope of 70%, from the cliff to the ice surface. This would be related to the surfacing of a physical barrier represented by a mountain ridge higher than 1990 m between the Sassongher and the Pralongià, which would have prevented sediment to reach the plateau (Fig. 5.2a). If the ice surface is raised to 2010 m (Scenario 2 in Fig. 5.1; Fig. 5.2b), two source areas can be identified: i) one along the slopes of the Sassongher massif (to the west), 4 km away from the sampling site, ii) the other in correspondence with the southern Conturines cliff; both source areas show a subvertical travel slope which could have enabled the detached material to reach the ice surface.

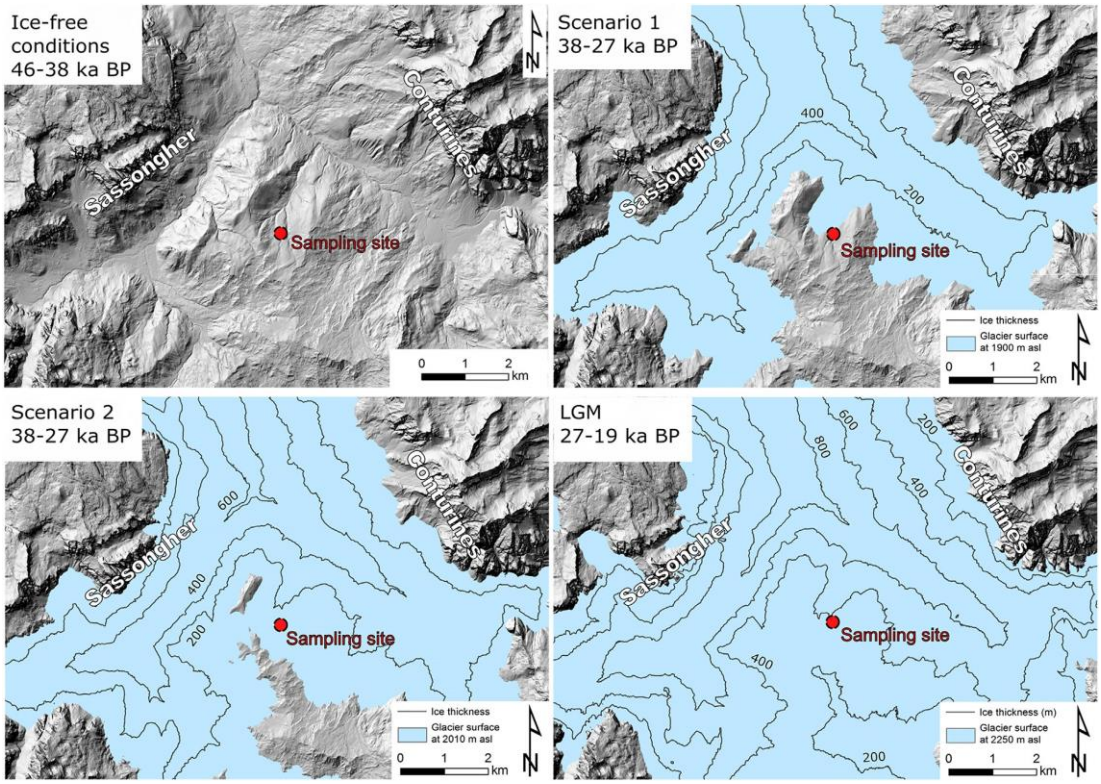

Fig. 5.1 Ice cover reconstructions within the Alta Badia valley. Between 38 and 27 ka BP an ice bridge is supposed to have connected the main dolomite massifs (Sassongher and Conturines) to the Pralongià plateau, before the onset of full glacial conditions (LiDAR data courtesy of Servizio cartografia provinciale coordinamento geodati, Autonomous Province of Bolzano). For scenarios 1 and 2 see Fig. 5.2a and b respectively.

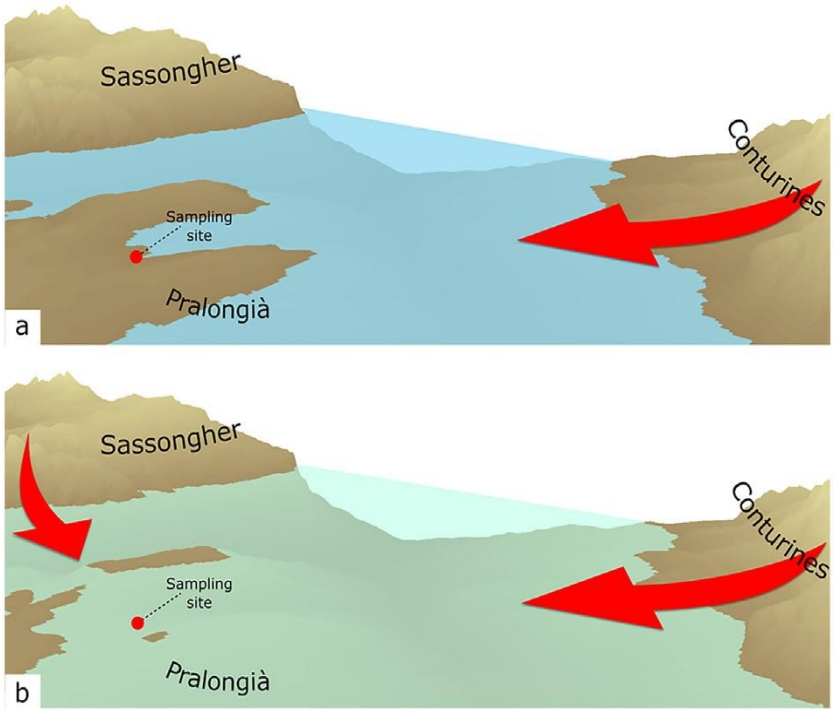

Fig. 5.2 Possible sediment sources within the dolomite ridges surrounding the Pralongià plateau. 3D reconstruction of the ice surface a) at 1900 m a.s.l.; b) at 2010 m a.s.l.

5.1.1 Correlation of Pre-LGM ^{14}C ages with local and global paleoenvironmental and paleoclimatic data

Radiocarbon dating showed that the bulk organic sediments found at the Pralongià plateau could be attributed to the MIS3 period. The radiocarbon ages indicated that the Pralongià plateau was likely to have been ice-free between at least 45 and 38 ka BP. No other MIS3 records are currently known from the Italian Dolomites except for radiocarbon dating on cave bear remains found at about 2800m a.s.l., within a cave on the southern side of the Conturines Group. Originally, bear remains were dated at 44 ka BP (cf. Döppes et al., 2011 and references therein) but ages were recently revised by Spötl et al. (2018) and attributed to a period older than MIS3, possibly the Last Interglacial. Thus, it is necessary to take a look at the larger paleoenvironmental database obtained from other Alpine regions and surroundings. Evidence that the eastern part of the Southern Alpine foreland was ice free during MIS3 is provided by several authors (Fontes and Bortolami, 1973; Canali et al., 2007; Fontana et al., 2012; Rossato and Mozzi, 2016; Hajdas et al., 2017).

We generally know from literature that during MIS3 the European ice caps receded from their outer positions achieved in MIS4, and extensive portions of the landscape were abandoned by the ice; sea level stood between -55 and -90 m below the present level. MIS3 was characterised by intense and abrupt climate changes, indicated by significant $\delta^{18}O$ variations (Rabassa and Ponce, 2016 and references therein). The climate pattern revealed by the $\delta^{18}O$ curve from Greenland ice cores resemble the one from northern Alpine speleothems (Moseley et al., 2014). In this context, the $\delta^{18}O$ curve from Greenland ice cores (e.g. Svensson et al., 2008) can be considered a reliable climate proxy for central Europe. The time frame in which our samples stand (46-38 ka BP) is characterised by five rapid warming events in Greenland, known as Greenland Interstadials (GI) 12-8, separated by four stadials (GS) 12-9 (Fig. 5.3). The ^{14}C ages of BS6, BS7-Pa and BS8-Pa, b, c fall partly or totally within stadial periods (Fig. 5.3), witnessing that even during the latter event the area was in ice-free conditions. On the other hand, PIZSOREGA2 sample can be attributed to GI-12, during which period a significant interstadial phase was recorded in speleothems (between 50 and 45 ka BP) in the northern Alpine foreland, when air temperature was some 4°C lower than today (Tütken et al., 2007). However, the level of precision of

the radiocarbon ages available does not permit their unequivocal relation to a single peak/down in the δ18O curve.

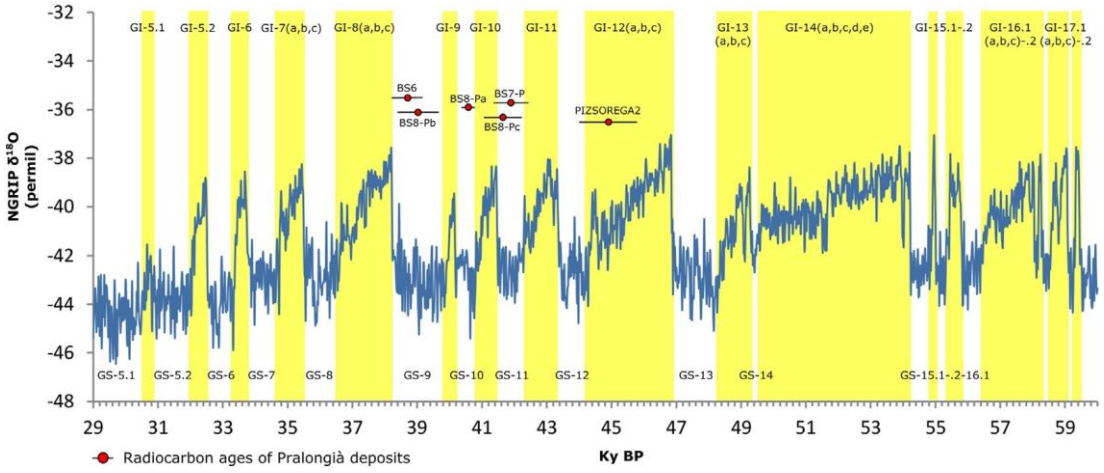

Fig. 5.3 Greenland $\delta^{18}O$ ice core chronology relevant to the MIS3 (data from Svensson et al., 2008). Glacial Stadials (GS) and Glacial Interstadial (GI) were numbered according to Rasmussen et al. (2014).

The interpretation of continuous pollen profiles covering MIS3 offers a possibility to learn more about vegetation and climate conditions in the Alps and surrounding areas. Boreal and continental conditions mainly prevailed during all MIS3 at the northern Alpine foreland, which was dominated during stadials by arctic tundra, with open landscapes and was characterised by loess accumulation (de Beaulieu and Reille, 1992; Reille et al., 1998; Spötl et al., 2018 and references therein). This is in contrast with palyno-stratigraphic data from the southern Alpine foreland, according to which afforestation persisted for all MIS3 and an estimated surface air temperature around 7 °C, with 600 mm/year of rainfall, characterised the stadial intervals (Pini et al., 2010). Paleoenvironmental data from mountain regions of Central Europe demonstrated that during most of MIS3 the main valleys were ice-free (Ivy-Ochs et al., 2008 and references therein; Engel et al., 2010). Climate deterioration in the Northern and Southern Alps is witnessed by the disappearance of the cave bear between some 35-31 ka BP (Spötl et al., 2014), as well as by remains of cold climate fauna dating back to 30 ka BP in the Carnic Prealps (South-Eastern Alps) (Carrera et al., 2018). Full glacial conditions occurred only since the transition between MIS3 and MIS2. Between 46 and 38 ka BP, the global atmospheric surface air temperature – ranging between -11 to -13.6°C with respect to the present (Bintanja et al., 2005) – was comparable to the period following the LGM, around 18-16 ka BP (Fig. 5.4). Additionally, the estimated Eurasian ice volume, between 46 and 38 kyr BP (from -

34.8 to -32 m sea level equivalent relative to the present; Bintanja et al., 2005), was similar to the one occurring between 16 and 15 ka BP. Between 17 and 15 ka BP, a stadial period was recognised in the Alps, the Gschnitz stadial (cf. Ivy-Ochs et al., 2008 and references therein). Thus, it is likely that between 46 and 38 ka BP, the glacier surface was more extensive than today and probably comparable to the Lateglacial, approximatively between 17 and 15 ka BP. During this period, 80%-90% of LGM glacier volume was already lost and glacier termini were situated well inside the Alpine valleys (Ivy-Ochs et al., 2008). Literature data and radiocarbon ages here presented seem to confirm that the Pralongià plateau was in ice-free conditions for most of MIS3.

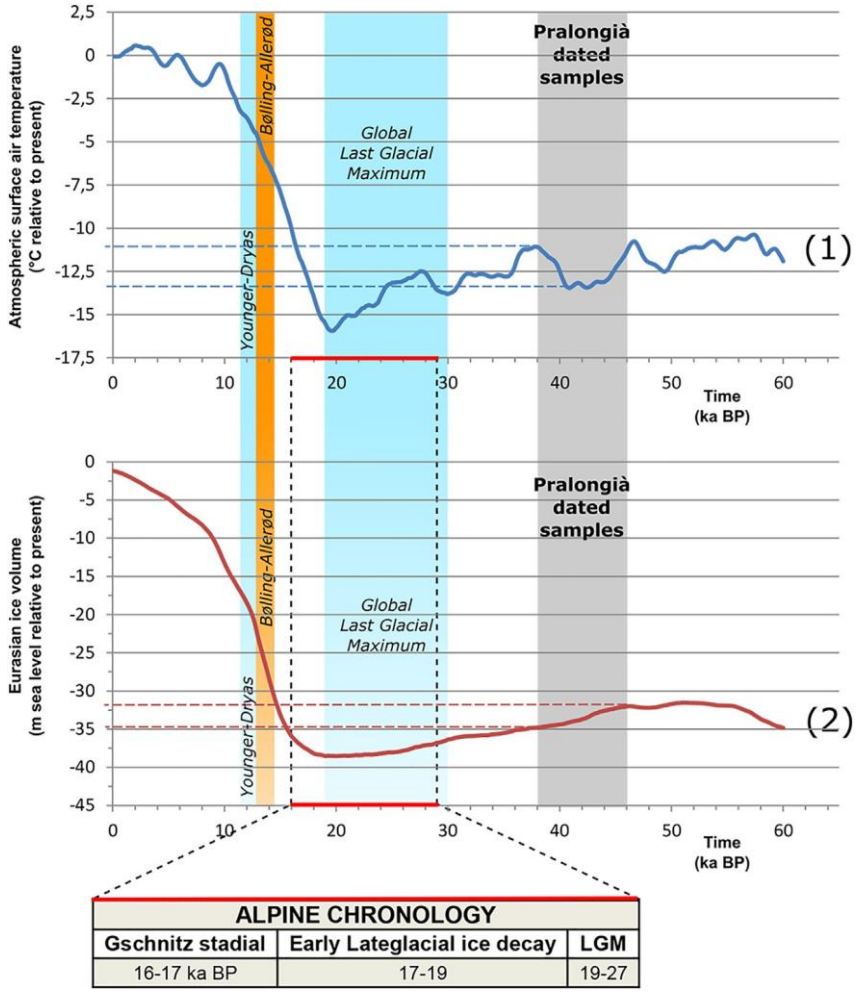

Fig. 5.4 Correlation between radiocarbon ages obtained from subsurface deposits on the Pralongià plateau and global/regional paleoclimate data: (1) global variation of atmospheric surface air temperature with respect to the present (°C) and (2) variation of Eurasian ice volume with respect to the present in sea level equivalent (m) (data from Bintanja et al., 2005); timing of Younger-Dryas and Bølling Allerød climate events according to Rasmussen et al. (2014); timing of Global Last Glacial Maximum event according to Lambeck et al. (2002); Alpine chronology according to Ivy-Ochs, 2015 and references therein.

5.2 The glacial history of the Alta Badia valley during the LGM and the Lateglacial

During the LGM the Piave basin, including the Eastern Dolomites, was affected by widespread glacial coverage (Brückner, 1909; B. Castiglioni, 1940; G.B. Castiglioni, 1964). A reconstruction of the extent of ice at the LGM is provided by B. Castiglioni (1940) and in the LGM map of Italy by Vai and Cantelli (2004), whilst in Penck and Brückner (1909) the reconstructed surface of the Piave glacier is presented. The retreat of the Piave glacier occurred at least in three phases (Pellegrini, 2005; Carton et al., 2009). The first occurred at ^{14}C 16,210±50 ka BP (17,537-17,261 BC) while the complete disappearance of the glacier from the foreland occurred likely before ^{14}C 15 ka BP, this is supported also by pollen data (Pellegrini, 2000). The onset and decay of the LGM in the Upper Piave basin has not been yet described in detail.

According to the findings presented in this thesis (cf. section 4), The Alta Badia valley (Fig. 5.5), as part of the Piave catchment, was covered by an extensive icefield which extended for ca. 160 km^2 and local glaciers departing from the main Dolomites groups of the valley flowed into it. The LGM trimlines ranged from 2300 and 2400 m in agreement with the observations made by Penck and Brückner (1909) for a maximum ice thickness, with respect to the valley bottom, of 800 m. Moreover, at the Gardena Pass (at 2235 m), the dating of a glacial deposit interpreted as emplaced by the downwasting LGM icefield revealed an exposure age of 17±2.5 (2.0) ka BP. This age has been interpreted as the minimum age for LGM ice lowering and it is supported also by the exposure age of 18 ± 2.8(2.2) ka BP obtained from the erratic boulder located along the north-eastern slope of the Pralongià plateau (at 1852 m). If the elevation difference of the two individual sample spots to the reconstructed ice surface is calculated this would indicate an ice lowering, since the end of the Global LGM at 19 ka BP (Monegato et al., 2007), of ca. 100 m at the Gardena Pass in ca. 2 ka and of ca. 200 m on the Pralongià plateau in ca. 1 ka. Similar lowering rate was found in the Aosta valley (Wirsig et al., 2016). The ice is likely to have persisted more at the Gardena Pass possibly due to the higher altitude (colder climate conditions) and the shading effect provided by the adjacent mountain peaks of the Sella Group (lower solar radiation). Thus, the Alta Badia ice surface lowered roughly synchronously to the downwasting of the glacier tongues in the Southern Alpine foreland that could have occurred around 22-18 ka BP according to the general framework proposed by several

authors (e.g. Gianotti et al., 2015; Ravazzi et al., 2012; Ravazzi et al., 2014; Fontana et al., 2014; Wirsig et al., 2016). This is also synchronous with the first signs of recession of other LGM glaciers at the northern side of the Eastern Alps (van Husen 1997, Reuther et al., 2011; Starnberger et al., 2011).

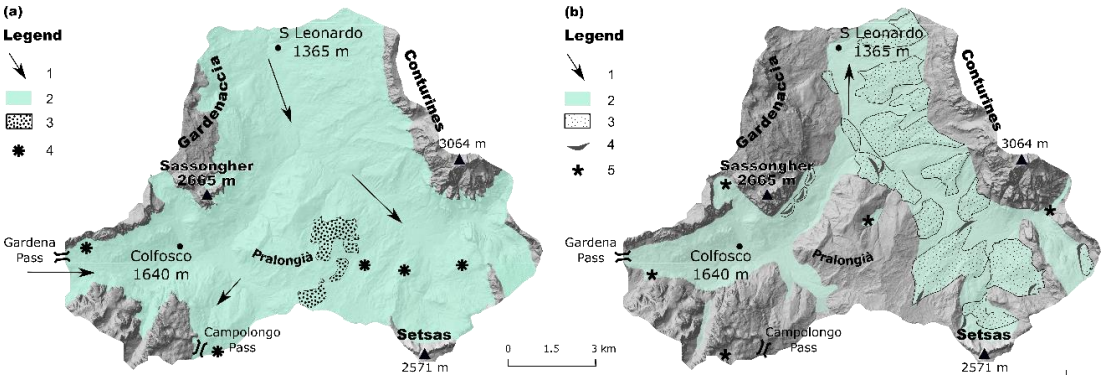

Fig. 5.5 Glacial features in the Alta Badia valley (modified after Marchetti et al., 2017). (a) Extent of glaciers during the LGM, inferred by assuming a glacial surface at 2300 m a.s.l.: 1) flow direction of the LGM ice masses; 2) LGM ice cover extent; 3) LGM glacial deposit; 4) unmappable glacial deposit (LGM). (b) Extent of early Lateglacial ice mass inferred from maximum elevation of Lateglacial deposits: 1) flow direction of the early Lateglacial ice mass 2) early Lateglacial ice mass; 3) glacial deposit (Lateglacial); 4) Lateglacial moraine ridge; 5) unmappable glacial deposit (Lateglacial). LiDAR data courtesy of Servizio cartografia provinciale e coordinamento geodati, Autonomous Province of Bolzano.

From the results of ^{36}Cl exposure ages and the reconstructed ELAs, Lateglacial advances were identified between ca. 15 ka BP and 13 ka BP. The reconstructed paleoglaciers at Valparola Pass and at Armentarola and Alting localities, in the south-eastern sector of the study area as well as at the Sella Pass, in the western sector of the study area, recorded these glacial advances.

The manually reconstructed glacier surfaces as well as the ELA of Malghe Valparola, Pudres and Prà de Dlira glaciers, at the Valparola Pass are comparable with those reconstructed for the area by Ghinoi and Soldati (2017) using the automated ArcGIS tool by Pellitero et al. (2016). On the basis of ELA depression with respect to LIA ELA Ghinoi and Soldati (2017) attributed the maximum Lateglacial advance after the retreat of the LGM icefield to the Gschnitz stadial (17-16 ka BP). In this study, evidence from cosmogenic dating of moraine boulders at Valparola pass revealed an exposure age of 14.4 ± 2(1.8) ka BP, that represents the minimum age for the stabilisation of the Lateglacial moraine in the area. The high uncertainty attributed to the exposure age does not allow to unequivocally attribute the reconstructed

paleoglaciers to one stadial rather than other. The age is included within the time period between the Oldest Dryas and Bolling Allerod climatic event and a Gschnitz attribution, as inferred by Ghinoi and Soldati (2017), cannot be excluded (Fig. 5.6). If we consider a reference ELA of 2800 m (local LIA ELA) as suggested by Ghinoi and Soldati (2017), the ΔELA ranges approximately between 700-600 ± 50 m which corresponds to the value proposed for the Gschnitz stadial by Ivy-Ochs et al. (2006 and reference therein) for the central and eastern Alps (cf. van Husen, 2004). The findings at Valparola Pass appear to be consistent with the ages of other Gschnitz moraines and the relative ELAs found in the Maritime Alps (Federici et al., 2017).

The exposure ages found for the Alting and Armentarola paleoglaciers are synchronous with the one obtained at the Valparola pass; they witness the presence of ice in this sector of the valley before ca. 13-14 ka BP. However, the reconstructed Alting and Armentarola paleoglaciers are located at lower altitudes with respect to the Valparola paleoglaciers. The north aspect as well as the gentle inclination of the slopes at Armentarola and Alting localities may have favoured the formation of ice at the ground in response to the Oldest Dryas climate deterioration also at relatively lower altitudes within the Alta Badia valley. However, from the inconsistently lower ELAs of Alting and Armentarola paleoglaciers with respect to the ones calculated in Valparola (of ca. 150-250 m), they have to be reconsidered as downwasting glaciers or glacierets for which, since they lay almost completely within the ablation zone, it is not suitable calculating equilibrium line altitudes.

At Sella Pass the found exposure ages are of 15.8 ± 3.4(2.7) ka BP and 15.4 ± 2.8(2.1). Those ages seem slightly older with respect to the ones obtained from the eastern sector of the study area. The great uncertainty associated to those ^{36}Cl ages does not allow to attribute the Sella paleoglacier to an Oldest Dryas stadial phase rather than another. The reconstructed ELA value is comparable to one obtained at the Valparola Pass, we can suppose that they can be attributed to the same stadial phase, the Gschnitz one; probably the response of the glaciers in Valparola bear a delay with respect to the paleoglacier at the Sella Pass due to the different local topographic conditions.

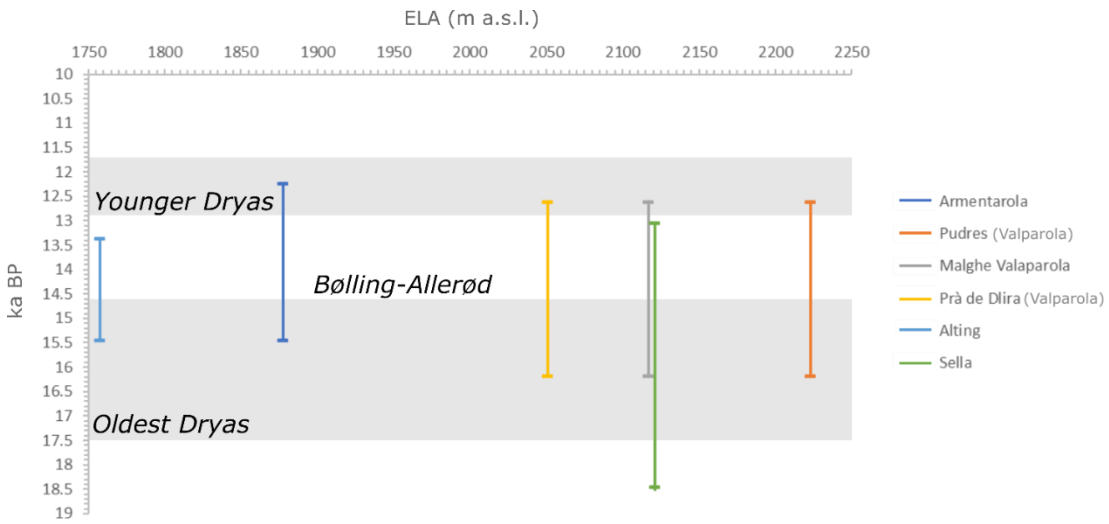

Fig. 5.6 Lateglacial exposure ages obtained for the paleoglaciers in the south-eastern sector of the study area (Armentarola, Pudres, Malghe Valparola, Prà de Dlira and Alting paleoglaciers) and at the Sella Pass. The exposure ages are plotted vs. the mean ELAs calculated for each of the reconstructed paleoglaciers.

In agreement with the youngest ^{36}Cl exposure age found for the glacial deposits of 13.3 ± 1.4(1.0) ka BP, the glaciers disappeared from the Alta Badia valley, at least at the investigated altitudes (≤ 2360 m a.s.l.), before of/at 13 ka BP. This agrees with the ice-free conditions recorded at 13 ka BP, through peat bog analysis, by Poto et al. (2013) in the neighbouring Danta di Cadore locality (1400 m a.s.l.) and ^{14}C and pollen data analysis retrieved from the lower part of the Piave catchment (cf. Pellegrini, 2005 and Carton et al., 2009).

It is well-know from extensive climate records, provided for the valley by investigating landslide processes and their relation to climate changes, that during the early Holocene the Alta Badia valley was ice-free – excluding possible ice remnants and glacierets in shaded areas at the highest elevations (>2600 m) possibly located where today there are active/inactive rock glaciers (cf. section 2.3.3). Marked slope instability phases were recognized since at least 10,700 years BP following the withdrawal of Lateglacial glaciers (cf. Soldati et al., 2006; Borgatti and Soldati, 2010). Ice-free conditions during the early Holocene are also confirmed in Soldati et al. (1997) at the near Alpe Federa (altitudes > 2000 m a.s.l.) which is located some kilometres south of Cortina d'Ampezzo (Belluno Province).

In particular, based on ^{14}C dating, Borgatti and Soldati (2010) identified four periods of enhanced landsliding activity occurred during the Holocene: i) from 10,700 to 8400 cal BP, between Younger Dryas and the Preboreal; ii) from 8200 to 6900 cal BP,

during the older Atlantic; iii) from 5800 to 4500 cal BP, between Atlantic and Subboreal; and iv) from 4000 to 2100 cal BP, between Subboreal and Subatlantic.

Thus, the ^{36}Cl exposure ages found in this work and dated to the Holocene should be related to slope instability processes rather than glacial ones. In particular, at the northern part of the Gardena Pass a sample from a boulder revealed an exposure age of 9.9 ± 3.2(2.8) ka BP which was considered as indicative about the time of boulder emplacement due to gravity-induced slope processes active at that time. These latter can be related to the first phase of enhanced landsliding activity found by Borgatti and Soldati (2010), that is between Younger Dryas and the Preboreal. The age found at the Gardena Pass is more or less synchronous to the ones found at Sas Crusc locality which range from 9.8 ± 1.1(0.9) and 9.5 ± 1.0(0.7) to 6.3 ± 0.6(0.5) ka BP. The latter is the youngest ^{36}Cl exposure age obtained for the Alta Badia valley and can be possibly related to the second slope instability phase identified in the area by Borgatti and Soldati (2010).

6. Conclusions

The PhD research aimed at extending the dataset on the glacial geochronology of the Alps and at providing further insights and to contribute in the characterization, from a high-Alpine perspective, of paleoenvironmental and paleclimate conditions occurred during Late Pleistocene in the Alta Badia valley, as part of the Eastern Dolomites, the southernmost distal segment of the Alpine chain. The research was based on: i) retrieving paleoenvironmental record through the study of subsurface deposits possibly attributable to the Pre-LGM period, and ii) constraining in space and time the Late Pleistocene glacial history of the Alta Badia valley by investigating glacial landforms possibly attributable to the LGM and to the Lateglacial.

The investigation on subsurface deposits took advantage of the analysis of stratigraphic data from an excavation wall and from eight continuous-coring boreholes ranging in depth from 15 to 25 m, carried out on the formerly glaciated Pralongià plateau in the central sector of the Alta Badia Valley. As mentioned above, the research was also based on the investigation on glacial landforms and deposits, widespread in the latter valley, attributable to the LGM (ca. 27-19 ka) and Lateglacial (ca. 16-14 ka) periods by geomorphological evidence. The contribution of cosmogenic nuclide geochronology (^{36}Cl Cosmic Ray Exposure dating) resulted as fundamental for the reconstruction of glacier extension and time constrain.

Geomorphological field surveys supported by remote sensing data analyses, ^{14}C dating results and the interpretation of stratigraphic data from subsurface deposits on the Pralongià plateau, enabled us to conclude that:

- Between 45 and 38 ka BP the Pralongià plateau (ca. 2000 m) was ice-free.
- Between 38 ka BP and the onset of full-glacial conditions (LGM ~ 27 ka BP) clastic gravity-induced sediments were deposited within the study site.
    - Debris flows or also possibly the wash out/reworking of rock avalanche deposits were considered the main processes providing sediment supply. It should be noted that large-scale landslides, including rock avalanches, might have occurred in the area also due to earthquakes that could have been related to neotectonic activity for which geomorphological evidence was recognised in the Alta Badia valley (Corsini and Panizza, 2003).

    - The main source area could be identified in the Conturines Group (NE of the Pralongià plateau) or, alternatively, in correspondence with the Sassonger massif (W of the plateau).
    - Supraglacial transport is supposed to have played a role in the emplacement of the gravity-induced deposits over the plateau.
- Full glacial conditions occurred afterwards, in accordance with literature data (cf. Monegato et al., 2017), probably since about 27 ka BP.

^{36}Cl cosmogenic dating results and the interpretation of morphostratigraphic data from moraine deposits of the Alta Badia valley, supported by geomorphological field surveys and remote sensing data analyses, enabled us to conclude that:

- During the LGM the whole Alta Badia valley was covered by an extensive icefield flowing from the north and reaching a maximum of 800 m of thickness and an elevation of 2400 m a.s.l.. Only the highest peaks emerged from the ice mass and local glaciers departing from the main Dolomite groups flowed into the main ice body occupying the valley.
- The LGM ice lowering started at least at 18-17 ka BP as found e.g. at the Gardena Pass. According to literature data the downwasting of the glacier tongues in the Southern Alpine foreland occurred around 22-18 ka BP (e.g. Gianotti et al., 2015; Ravazzi et al., 2012; Ravazzi et al., 2014; Fontana et al., 2014; Wirsig et al., 2016). From the found ^{36}Cl ages it can be inferred that ice surface lowering in the Alta Badia valley, as part of the accumulation area of the Piave glacier, started at least at 18-17 ka BP after the beginning of/synchronous to the retreat of significant distances of the Piave glacier tongue.
- From the results of ^{36}Cl exposure ages and the reconstructed ELAs and by comparing them with literature data, Lateglacial advances were identified and attributed to the Gschnitz stadial. Apparently, these advances were locally asynchronous within the valley, bearing the glaciers of the eastern sectors 1 ka of delay with respect to the one in the western sector. ELA depressions of ca. 700-600 ± 50 m with respect to the local LIA ELA (2800 m a.s.l.) were calculated. The calculated ELAs are consistent with the values found for other Gschnitz moraines in other Alpine areas (e.g. van Husen, 2004; Ivy-Ochs et al., 2006; Federici et al., 2017). The relative chronological difference observed in the Alta Badia valley for the reconstructed paleoglaciers, attributed to the

Gschnitz stadial, should be related to the local topographic conditions characterizing the valley. In fact, it is well-known that glacier dynamics in the Eastern Alps was strongly controlled, rather than other Alpine sectors, by the topography (Mayr and Heuberger, 1968; van Husen, 1987). The present study confirmed the Gschnitz stadial as the most important one within the Alta Badia valley (cf. Ghinoi and Soldati, 2017).

- Evidence from ^{36}Cl glacial chronology, in agreement with the available literature data relevant to Piave catchment, revealed that the glaciers disappeared from the Alta Badia valley, at least at the investigated altitudes ≤2360 m a.s.l., before ca.13 ka BP.
- Ice free conditions persisted in the Alta Badia valley during the Holocene as witnessed by the occurrence of enhanced slope instability phases in response to climate changes (e.g. deglaciation) (cf. Borgatti and Soldati, 2010).

Tab. 6.1 Main events constituting the Late Pleistocene glacial history of the Alta Badia.

Age	Interpretation
45-38 ka BP	Ice free conditions on the Pralongià plateau
38 ka BP-LGM (ca. 27 ka)	Emplacement of dolostone gravity-induced deposits on the Pralongià plateau through supraglacial transport
LGM (ca. 27-19 ka)	Icefield covering the Alta Badia valley and connecting local glaciers
18/17 ka BP	Minimum age for icefield lowering
17-13 ka BP	Glacial advances
13 ka BP-present	The Alta Badia valley was ice free

The study carried out on the Pralongià plateau resulted in the first Pre-LGM record of sedimentation and paleoenvironmental conditions inside the Eastern Dolomites in the period between 46 and 38 ka BP. Moreover, this study intends to provide the ground basis for further insights on the environmental conditions relevant to the Pre-LGM period at high elevations in the Alps.

The Late Pleistocene chronology based on ^{36}Cl ages, provided by this study for the first time in the Alta Badia valley, significantly extends the Alpine geochronological dataset, adding new information on the onset of the LGM and the subsequent response to the Lateglacial stadials, contributing to the current debate driven by the INTIMATE (INTegration of Ice-core, MArine and TErrestrial records) project group on the synchronization of records for the Last Glacial–Interglacial Transition (cf. Rasmussen et al., 2014).

References

Agassiz, L., 1837. Discours prononcé à l'ouverture des séances de la Société Helvétique des Sciences Naturelles. Actes de la Société Helvétique des Sciences Naturelles, Neuchâtel.

Agassiz, L. 1840. Études sur les Glaciers. Jent & Gassman: Neuchâtel, Switzerland, 346 pp.

Antonioli, F., Vai, G.B. (Eds.), 2004. Climex Maps Italy – explanatory notes. Museo Geologico Giovanni Capellini, Bologna, 80 pp.

Arnold, M., Aumaître, G., Bourlès, D. L., Keddadouche, K., Braucher, R., Finkel, R. C., Nottoli, E., Benedetti, L., Merchel, S., 2013. The French accelerator mass spectrometry facility ASTER after 4 years: status and recent developments on ^{36}Cl and ^{129}I. Nuclear Instruments and Methods in Physics Research Section B: Beam Interactions with Materials and Atoms, 294, 24-28.

Assereto, R., Desio, A., Di Cobertaldo, D., Passeri, L.D., 1968. Note illustrative della carta Geologica d'Italia alla scala 1: 100.000; foglio 14A, Tarvisio. Servizio Geologico d'Italia, Poligrafiea Ercolano, Naples, 1-70.

Baroni, C., Bruschi, G., Veronese, L., Zanchetta, G., 2001. Younger Dryas to Early Holocene palaeoenvironmental evolution of the Lake Terlago (Southern Alps, Italy). Geografia Fisica e Dinamica Quaternaria 24(1), 13-24.

Baroni, C., Zanchetta, G., Fallick, A.E., Longinelli, A., 2006. Mollusca stable isopote record of a core from Lake Frassino, northern Italy: hydrological and climatic changes during the last 14 ka. Holocene 16 (6), 827-837.

Baroni, C., Guidobaldi, G., Salvatore, M. C., Christl, M., Ivy-Ochs, S., 2018. Last glacial maximum glaciers in the Northern Apennines reflect primarily the influence of southerly storm-tracks in the western Mediterranean. Quaternary Science Reviews 197, 352-367.

Beaulieu de, J.L., Reille, M., 1992. The last climatic cycle at La Grande Pile (Vosges, France). A new pollen profile. Quaternary Science Reviews 11, 431-438.

Bertoglio, G., De Simoni, G., 1979. Partizione delle Alpi in 220 gruppi. Bollettino A.I.C. XVI 46, pp. 7-17.

Benn, D.I., Ballantyne, C.K., 2005. Palaeoclimatic reconstruction from Loch Lomond Readvance glaciers in the West Drumochter Hills Scotland. Journal of Quaternary Science 20, 577-592.

Bintanja, R., van de Wal, R.S., Oerlemans, J., 2005. Modelled atmospheric temperatures and global sea levels over the past million years. Nature 437 (7055), 125.

Bondesan, A., 1999. Una nuova data ^{14}C nell'anfiteatro morenico di Vittorio Veneto e la costruzione del suo sandur (Pianura del F. Meschio). 8th Italian Glaciological Meeting 'Alpine glaciers and climate change,' Abstract volume, pp. 87-89.

Borgatti, L., Soldati, M., 2010. Landslides as a geomorphological proxy for climate change: a record from the Dolomites (northern Italy). Geomorphology 120 (1-2), 56-64.

Borgatti, L., Ravazzi, C., Donegana, M., Corsini, A., Marchetti, M., Soldati, M., 2006. A lacustrine record of early Holocene watershed events and vegetation history, Corvara in Badia, Dolomites, Italy. Journal of Quaternary Science 22, 173-189.

Bosellini, A., 1984. Progradation geometries of carbonate platforms: examples from the Triassic of the Dolomites, northern Italy. Sedimentology 31(1), 1-24.

Bosellini, A., 1996. Geologia delle Dolomiti. Athesia, Bolzano, 192 pp.

Bosellini, A., Gianolla, P., Stefani, M., 2003. Geology of the Dolomites. Episodes 26(3), 181-185.

Brandner, R., Keim, L., Gruber, A., Gruber, J., 2007. Geologische Karte der Westlichen Dolomiten - Carta Geologica delle Dolomiti Occidentali 1:25.000. Autonome Provinz Bozen - Südtirol - Provincia Autonoma di Bolzano - Alto Adige. Amt für Geologie & Baustoffprüfung - Ufficio Geologia e Prove Materiali, Kardaun/Cardano (BZ).

Braucher, R., Merchel, S., Borgomano, J., Bourlès, D. L., 2011. Production of cosmogenic radionuclides at great depth: A multi element approach. Earth and Planetary Science Letters 309(1-2), 1-9.

Brückner, E., 1909. Die venezianischen Gletscher. In: Penck, A., Buckner (Eds.), Die Alpen im Eiszeitalter, pp. 954-1042.

Bruschi, V.M., Coratza, P., Corsini, A., Marchetti, M., Panizza, M., Piacentini, D., Soldati, M., 2009. Alta Badia field-trip guide. The Role of Geomorphology in Land Management, Modena - Alta Val Badia 13-18 September 2009, III National AIGeo Conference, 1-61.

Budd, W.F., Jenssen, D., 1975. Numerical modelling of glacier systems. International Association of Hydrological Sciences Publications 104, 257-291.

Canali, G., Capraro, L., Donnici, S., Rizzetto, F., Serandrei-Barbero, R., Tosi, L. (2007). Vegetational and environmental changes in the eastern Venetian coastal plain (Northern Italy) over the past 80,000 years. Palaeogeography, paleoclimatology, Palaeoecology, 253(3-4), 300-316.

Carrera, L., Pavia, M., Romandini, M., Peresani, M., 2018. Avian fossil assemblages at the onset of the LGM in the eastern Alps: a palaecological contribution from the Rio Secco Cave (Italy). Comptes Rendus Palevol 17 (3), 166-177.

Carton, A., Soldati, M., 1993. Geomorphological features of the Dolomites (Italy). In: Panizza, M., Soldati, M., Barani, D. (Eds.), First European Intensive Course on Applied Geomorphology - Proceedings, ERASMUS ICP-91/93-I-1226/07 publ. n. 4. Istituto di Geologia - Università degli Studi di Modena, pp. 13-29.

Carton, A., 2017. Large ancient landslides in Trentino, Northeastern Alps, as evidence of postglacial dynamics. In: Soldati, M., Marchetti, M. (Eds.), Landscapes and Landforms of Italy. Springer, Cham, pp. 113-122.

Carton, A., Castaldini, D., Mantovani, F., Panizza, M., Spina, R., 1978. Dati preliminari sulla neotettonica dei folgio 11 (M. Marmolada) e 97 (S. Marcello Pistoiese). In: Contributi preliminari alla realizzazione della Carta Neotettonica d'Italia, C.N.R. Progetto Finalizzato alla Geodinamica, Pubb. 155, Napoli, pp. 277-246.

Carton, A., Castaldini, D., Panizza, M., 1980. Schema neotettonico riassuntivo dell'area fra Trento e Cortina d'Ampezzo (Fogli P.P. Bolzano (10), M. Marmolada (11), Cortina d'Ampezzo (12), Trento (21) e Feltre (22)). In: Contributi alla realizzazione della Carta Neotettonica d'Italia, C.N.R. Progetto Finalizzato alla Geodinamica, Pubbl. 356, pp. 621-641.

Carton, A., Bondesan, A., Fontana, A., Meneghel, M., Miola, A., Mozzi, P., Primon, S., Surian, N., 2009. Geomorphological evolution and sediment transfer in the Piave River watershed (north-eastern Italy) since the LGM. Géomorphologié: Relief, Processus, Environment 3, 37-58.

Castiglioni, B., 1940. L'Italia nell'Età Quaternaria. In: Touring Club Italiano (Ed.), Atlante Fisico d'Italia. Milano, Map 1:1.200.000.

Castiglioni, G.B., 1964. Sul morenico stadiale delle Dolomiti. Memorie degli Istituti di Geologia e Mineralogia dell'Università di Padova, 24, pp. 1-16.

Cavallin, A., Baroni, C., Bini, A., Carton, A., Marchetti, M., Orombelli, G., Pelfini, M., Zanchi, A., 1997. Geomorphology of the Central and Southern Alps. Fourth International Conference on Geomorphology, Guide for the Excursion. Supplementi di Geografia Fisica e Dinamica Quaternaria III(T2), pp. 13-47.

Chaline, J., Jerz, H., 1984. Arbeitsergebnisse der Sbkommission fur Europaische Quartarstratgraphie. Stratotypen des Würm-Glazials. Eiszeitalter und Gegenwart 35, 185-206.

Charpentier de, J., 1841. Essai sur les glaciers et sur le terrain erratique di Bassin du Rhône. Karte und 8 Abbildungen, Lausanne, Switzerland, 363 pp.

Clark, P.U., Dyke, A.S., Shakun, J.D., Carlson, A.E., Clark, J., Wohlfarth, B., Mitrovica, J.X., Hostetler, S.W., McCabe, A.M., 2009. The last glacial maximum. Science 325, 710-713.

Cogley, J.G., Hock, R., Rasmussen, L.A., Arendt, A.A., Bauder, A., Braithwaite, R.J., Jansson, P., Kaser, G., Möller, M., Nicholson, L., Zemp, M., 2011. Glossary of glacier mass balance and related terms. Technical Report. IHP-VII technical documents in hydrology No. 86, IACS Contribution No. 2. UNESCO-IHP, Paris.

Colucci, R. R., Monegato, G., Žebre, M., 2014. Glacial and proglacial deposits of the Resia Valley (NE Italy): new insights on the onset and decay of the last Alpine Glacial Maximum in the Julian Alps. Alpine and Mediterranean Quaternary 27(2), 85-104.

Corsini, A., Panizza, M., 2003. Conseguenze geomorfologiche di una faglia neotettonica nell'Alta Val Badia (Dolomiti). In: Biancotti, A., Motta, M. (Eds.), Risposta dei processi geomorfologici alle variazioni ambientali. Glauco Brigati Editore, Genova, pp. 163-176.

Corsini, A., Panizza, M., Pasuto, A., Silvano, S., Siorpaes, C., Soldati, M., 1998. Indagini preliminari per la definizione della pericolosità da frana nella conca di Corvara in Badia (Dolomiti). Memorie della Società Geologica Italiana 53, 207-224.

Corsini, A., Pasuto, A., Soldati, M., 1999. Geomorphological investigation and management of the Corvara landslide (Dolomites, Italy). Japanese Geomorphological Union Transactions 20 (3), 169-186.

Corsini, A., Marchetti, M., Soldati, M., 2001. Holocene slope dynamics in the area of Corvara in Badia (Dolomites, Italy). Geografia Fisica e Dinamica Quaternaria 24 (2), 127-139.

Corsini, A., Pasuto, A., Soldati, M., Zannoni, A., 2005. Field monitoring of the Corvara landslide (Dolomites, Italy) and its relevance for hazard assessment. Geomorphology 66, 149-165.

Cremaschi, M., 1987. Paleosol and Vetusols in the Central Po Plain (Northern Italy) a study in Quaternary geology and soil development. Edizioni Unicopli, Milano.

Dansgaard, W., Johnsen, S.J., Clausen, H.B., Dahl-Jensen, D., Gundestrup, N.S., Hammer, C.U., Hvidberg, C.S., Steffensen, J.P., Sveinbjörnsdottir, A.E., Jouzel, J., Bond, G., 1993. Evidence for general instability of past climate from a 250-kyr ice-core record. Nature 364, 218-220.

De Zanche, V., Gianolla, P., Mietto, P., Siorpaes, C., Vail, P.R., 1993. Triassic sequence stratigraphy in the Dolomites (Italy). Memorie della Società Geologica 45, 1-27.

Deline, P., 2009. Interactions between rock avalanches and glaciers in the Mont Blanc massif during the late Holocene. Quaternary Science Reviews 28 (11-12), 1070-1083.

Desilets, D., Zreda, M., Almasi, P.F., Elmore, D., 2006. Determination of cosmogenic ^{36}Cl in rocks by isotope dilution: innovations, validation and error propagation. Chemical Geology, 233(3-4), 185-195.

Doglioni, C., 1987. Tectonics of the Dolomites (Southern Alps-Northern Italy). Journal of Structural Geology 9, 181-193.

Doglioni, C., Carminati, E., 2008. Structural styles and Dolomites field trip. Memorie Descrittive della Carta Geologica d'Italia 82, 1-299.

Döppes, D., Rabeder, G., Stiller, M., 2011. Was the Middle Würmian in the High Alps warmer than today? Quaternary International 245 (2), 193-200.

Engel, Z., Nývlt, D., Křížek, M., Treml, V., Jankovská, V., Lisá, L., 2010. Sedimentary evidence of landscape and climate history since the end of MIS 3 in the Krkonoše Mountains, Czech Republic. Quaternary Science Reviews 29 (7-8), 913-927.

Englemark, R., Buckland, P.I., 2005. The early Holocene environment of North Fennoscandia and its implications for Colonisation. In: Knutsson, H. (Ed.), Pioneer Settlements and Colonization Processes in the Barents Region, Vuollerim. Vuollerim Papers in Hunter-Gatherer Archaeology, vol. 1, pp. 97-108.

Erdtman, G., 1921. Pollenanalysiche Untersuchungen von Torfmooren und Marinen Sedimenten in Sudwest-Schweden. Arkiv før Botanik 17, 1-273.

Federici, P.R., Granger, D.E., Pappalardo, M., Ribolini, A., Spagnolo, M., Cyr, A.J., 2008. Exposure age dating and equilibrium line altitude reconstruction of an Egesen moraine in the Maritime Alps, Italy. Boreas 37 (2), 245-253.

Federici, P.R., Granger, D.E., Ribolini, A., Spagnolo, M., Pappalardo, M., Cyr, A.J., 2012. Last glacial maximum and the Gschnitz stadial in the Maritime Alps according to ^{10}Be cosmogenic dating. Boreas 41 (2), 277-291.

Federici, P.R., Ribolini, A., Spagnolo, M., 2017. Glacial history of the Maritime Alps from the last glacial maximum to the little ice age. Geological Society, London, Special Publications 433(1), 137-159.

Fischer, H., Wahlen, M., Smith, J., Mastroianni, D., Deck, B., 1999. Ice core records of atmospheric CO_2 around the last three glacial terminations. Science 283(5408), 1712-1714.

Fontana, A., Bondesan, A., Meneghel, M., Toffoletto, Vitturi, A., Bassan, V. (Eds.), 2012. Carta Geologica d'Italia alla scala 1:50.000 — Foglio 107 'Portogruaro'. Regione Veneto, Infocartografica, Piacenza, 2 maps 196, 168 pp.

Fontana, A., Mozzi, P., Marchetti, M., 2014. Alluvial fans and megafans along the southern side of the Alps. Sedimentary Geology 301, 150-171.

Fontes, J.C., Bortolami, G., 1973. Subsidence of the Venice area during the past 40,000 yr. Nature 244(5415), 339.

Fort, M., 2000. Glaciers and mass wasting processes: their influence on the shaping of the Kali Gandaki valley (higher Himalaya of Nepal). Quaternary International 65, 101-119.

Fort, M., 2003. Are high altitude, lava stream-like, debris mixtures all rock glaciers? A perspective from the Western Himalaya. Zeitschrift für Geomorphologie 47, 11-29.

Fuganti, A., Bazzoli, G., Morteani, G., 1998. The Quaternary evolution of the Adige Valley near the city of Trento (Northern Italy) as deduced from wells and radiocarbon dating. Studi Trentini di Scienze Naturali, Acta Geologica 73, 93-97.

Genevois, R., Armento, C., Tecca, P.R., 2006. Failure mechanisms and runout behaviour of three rock avalanches in the North-Eastern Italian Alps. In: Evans, S.G., Scarascia Mugnozza, G., Strom, A., Hermanns, R.L. (Eds.), Landslides from Massive Rock Slope Failure. NATO Science Series vol. 49. Springer, Dordrecht, pp. 407-427.

Ghinoi, A., Soldati, M., 2017. Reappraisal of Lateglacial stadials in the Eastern Alps: the case study of Valparola (eastern Dolomites, Italy). Alpine and Mediterranean Quaternary 30 (1), 51-67.

Ghinoi, A., Freddi, R., Pasuto, A., Soldati, M., 2014. Geomorphological analysis of the historic landslide of Sottrù (Badia Valley, Italy) reactivated on December 12, 2012. In: Proceedings of the international conference on the Analysis and management of changing risks for natural hazards, Padua, Italy, AP19 1-8, 18-19 November 2014.

Gianolla, P., Andreetta, R., Furin, S., Furlanis, S., Riva, A., 2008. Geology of the Dolomites. In Nomination of the Dolomites for Inscription on the World Natural Heritage List Unesco. Artimedia, Trento, Italy, pp. 3-77.

Gianotti, F., Forno, M.G., Ivy-Ochs, S., Kubik, P., 2008. New chronological and stratigraphical data on the Ivrea amphitheater (Piedmont, NW Italy). Quaternary International 190 (1), 123-135.

Gianotti, F., Forno, M.G., Ivy-Ochs, S., Monegato, G., Pini, R., Ravazzi, C., 2015. Stratigraphy of the Ivrea morainic amphitheatre (NW Italy): an updated synthesis. Alpine Mediterranean Quaternary 28, 29-58.

Giardino, M., Mortara, G., Chiarle, M., 2017. The glaciers of the Valle d'Aosta and Piemonte regions: records of present and past environmental and climate changes. In: Soldati, M., Marchetti, M. (Eds.), Landscapes and landforms of Italy. Springer, Cham, pp 77-88.

Gross, G., Kerschner, H., Patzelt, G., 1977. Methodische Untersuchungen über die Schneegrenze in alpinen Gletschergebieten. Zeitschrift für Gletscherkunde und Glazialgeologie 12, 223-251.

Hajdas, I., Hendriks, L., Fontana, A., Monegato, G., 2017. Evaluation of preparation methods in radiocarbon dating of old wood. Radiocarbon 59(3), 727-737.

Heiri, O., Koinig, K.A., Spötl, C., Barrett, S., Brauer, A., Drescher-Schneider, R., Gaar, D., Ivy-Ochs, S., Kerschner, H., Luetscher, M., Moran, A., 2014. Palaeoclimate records 60–8 ka in the Austrian and Swiss Alps and their forelands. Quaternary Science Reviews 106, 186-205.

Hewitt, K., 2009. Rock avalanches that travel onto glaciers and related developments, Karakoram Himalaya, Inner Asia. Geomorphology 103 (1), 66-79.

Hormes, A., Ivy-Ochs, S., Kubik, P. W., Ferreli, L., Michetti, A. M., 2008. ^{10}Be exposure ages of a rock avalanche and a late glacial moraine in Alta Valtellina, Italian Alps. Quaternary International 190(1), 136-145.

Hughes, P.D., Gibbard, P.L., Ehlers, J., 2013. Timing of glaciation during the last glacial cycle: evaluating the concept of a global 'Last Glacial Maximum'(LGM). Earth-Science Reviews 125, 171-198.

Husen van, D., 1987. Die Ostalpen in den Eiszeiten. Verlag der geologischen Bundesanstalt.

Husen van, D., 1997. LGM and late-glacial fluctuations in the Eastern Alps. Quaternary International 38, 109-118.

Husen van, D., 2000. Geological processes during the Quaternary. Mitteilungen der Österreichischen Geologischen Gesellschaft 92, 135-156.

Husen van, D., 2004. Quaternary glaciations in Austria. In: Ehlers, J., Gibbard, P.L. (Eds.), Quaternary glaciations – Extent and chronology, Part I: Europe. Elsevier, London, pp. 1-13.

Imbrie, J., Imbrie, K. P., 1986. Ice ages: solving the mystery. Harvard University Press, 224 pp.

Ivy-Ochs, S., 2015. Glacier variations in the European Alps at the end of the last glaciation. Cuadernos de investigación geográfica/Geographical Research Letters 41, 295-315.

Ivy-Ochs, S., Kober, F., 2008. Surface exposure dating with cosmogenic nuclides. Quaternary Science Journal 57(1-2), 179-209.

Ivy-Ochs, S., Briner, J.P., 2014. Dating disappearing ice with cosmogenic nuclides. Elements 10(5), 351-356.

Ivy-Ochs, S., Schlüchter, C., Kubik, P.W., Synal, H.A., Beer, J., Kerschner, H., 1996. The exposure age of an Egesen moraine at Julier Pass, Switzerland, measured with the cosmogenic radionuclides ^{10}Be, ^{26}Al and ^{36}Cl. Eclogae geologicae Helvetiae 89, 1049-1063.

Ivy-Ochs, S., Synal, H.A., Roth, C., Schaller, M., 2004. Initial results from isotope dilution for Cl and ^{36}Cl measurements at the PSI/ETH Zurich AMS facility. Nuclear Instruments and Methods in Physics Research Section B: Beam Interactions with Materials and Atoms 223, 623-627.

Ivy-Ochs, S., Kerschner, H., Kubik, P.W., Schlüchter, C., 2006a. Glacier response in the European Alps to Heinrich event 1 cooling: the Gschnitz stadial. Journal of Quaternary Science 21, 115-130.

Ivy-Ochs, S., Kerschner, H., Reuther, A., Maisch, M., Sailer, R., Schaefer, J., Kubik, P.W., Synal, H.A., Schlüchter, C., 2006b. The timing of glacier advances in the northern European Alps based on surface exposure dating with cosmogenic ^{10}Be, ^{26}Al, ^{36}Cl, and ^{21}Ne. In: Siame, L.L., Bourlès, D.L., Brown, E.T. (Eds.), In Situ-Produced Cosmogenic Nuclides and Quantification of Geological Processes. Geological Society of America Special Paper 415, pp. 43-60.

Ivy-Ochs, S., Kerschner, H., Reuther, A., Preusser, F., Heine, K., Maisch, M., Kubik, P.W., Schlüchter, C., 2008. Chronology of the last glacial cycle in the European Alps. Journal of Quaternary Science 23, 559-573.

Ivy-Ochs, S., Kerschner, H., Maisch, M., Christl, M., Kubik, P.W., Schlüchter, C., 2009. Latest Pleistocene and Holocene glacier variations in the European Alps. Quaternary Science Reviews 28, 2137-2149.

Jibson, R.W., Harp, E.L., Schulz, W., Keefer, D.K., 2006. Large rock avalanches triggered by the M 7.9 Denali Fault, Alaska, earthquake of 3 November 2002. Engineering Geology 83 (1-3), 144-160.

Kelly, M.A., Kubik, P.W., Blanckenburg von, F., Schlüchter, C., 2004. Surface exposure dating of the Great Aletsch Glacier Egesen moraine system, western Swiss Alps, using the cosmogenic nuclide ^{10}Be. Journal of Quaternary Science 19, 431-441.

Kerschner, H., Ivy-Ochs, S., Schlüchter, C., 1999. Paleoclimatic interpretation of the early late-glacial glacier in the Gschnitz valley, Central Alps, Austria. Annals of Glaciology 28, 135-140.

Kerschner, H, Kaser, G, Sailer, R., 2000. Alpine Younger Dryas glaciers as paleo-precipitation gauges. Annals of Glaciology 31, 80-84.

Kirkbride, M.P., Sugden, D., 1992. New Zealand loses its top. Geographical magazine 64 (7), 30-34.

Klasen, N., Fiebig, M., Preusser, F., Reitner, J.M., Radtke, U., 2007. Luminescence dating of proglacial sediments from the Eastern Alps. Quaternary International 164-165, 21-32.

Klebelsberg von, R.V., 1927. Beitrage zur Geologie der Sudtiroler Dolomiten. I. Ruckzugstande der Eiszeitgletscher in den Dolomitentalern. Zeitschrift der Deutschen Geologischen Gesellschaft 79(3), pp. 280-337.

Klebelsberg von, R., 1948. Handbuch der Gletscherkunde und Glaziologie, Bd.1. Springer, Wien, 1028 pp.

Klebelsberg von, R., 1950. Südtiroler geomorphologische Studien. Das mittlere Eisacktal (II. Die höheren Tallagen und die einfassende Berge). Museum Ferdin, Innsbruck, vol. XXX.

Köppen, W., 1931. Grundriss der Klimakunde. Walter De Gruyter, Berlin, pp. 388.

Lambeck, K., Esat, T.M., Potter, E.K., 2002. Links between climate and sea levels for the past three million years. Nature 419 (6903), 199.

Lambeck, K., Rouby, H., Purcell, A., Sun, Y., Sambridge, M., 2014. Sea level and global ice volumes from the Last Glacial Maximum to the Holocene. Proceedings of the National Academy of Sciences 111(43), 15296-15303.

Lauterbach, S., Chapron, E., Brauer, A., Hüls, M., Gilli, A., Arnaud, F., Piccin, A., Nomade, J., Desmet, M., von Grafenstein, U., DecLakes Participants, 2012. A sedimentary record of Holocene surface runoff events and earthquake activity from Lake Iseo (Southern Alps, Italy). The Holocene 22 (7), 749-760.

Li, Y.K., 2018. Determining topographic shielding from digital elevation models for cosmogenic nuclide analysis: a GIS model for discrete sample sites. Journal of Mountain Science, 15(5), 939-947.

Libby, W.F., 1951. Radiocarbon dates II. Science 114, 291-296.

Lowe, J.J., Rasmussen, S.O., Bjorck, S., Hoek, W.Z., Steffensen, J.P., Walker, M.J.C., Yu, Z.C., Grp, I., 2008. Synchronisation of palaeoenvironmental events in the North Atlantic region during the Last Termination: a revised protocol recommended by the INTIMATE group. Quaternary Science Reviews 27, 6-17.

Lukas, S., 2007. Early-Holocene glacier fluctuations in Krundalen, southcentral Norway: palaeo-glacier dynamics and palaeoclimate. Holocene 17, 585-598.

Lukeneder, A., 2010. Lithostratigraphic definition and stratotype for the Puez Formation: formalisation of the Lower Cretaceous in the Dolomites (S. Tyrol, Italy). Austrian Journal of Earth Sciences 103(1), 138-158.

Magny, M., Joannin, S., Galop, D., Vannière, B., Haas, J.N., Bassetti, M. Bellintani, P., Scandolari, R., Desmet, M., 2012. Holocene palaeohydrological changes in the northern Mediterranean borderlands as reflected by the lake-level record of Lake Ledro, northeastern Italy. Quaternary Research 77, 382-396.

Mayr, F., Heuberger, H., 1968. Type areas of Late Glacial and Post Glacial deposits in Tyrol, Eastern Alps. In: Richmond, G.M. (Ed.), Glaciation of the Alps, (University of Colorado Studies, Series in Earth Sciences 7), pp. 143-165.

Mair, V., Zischg, A., Lang, K., Tonidandel, D., Krainer, K., Kellerer-Pirklbauer, A., Deline, P., Schoeneich, P., Cremonese, E., Pogliotti, P., Gruber, S., Böckli, L., 2012. PermaNET – Rete di monitoraggio a lungo termine del permafrost. Relazione di sintesi. INTERPRAEVENT Serie della rivista 1, Rapporto 3. Klagenfurt.

Mair, V., Lang, K., Tonindandel, D., Thaler, B., Alber, R., Lösch, B., Tait, D., Nickus, U., Krainer, K., Thies, H., Hirnsperger, M., Sapelza, A., Tolotti, M., 2015. Progetto Permaqua – Permafrost e il suo effetto sul bilancio idrico e sull'eologia delle acque di alta montagna. Provincia Autonoma di Bolzano, Bolzano, Italy: Ufficio geologia e prove dei materiali, 31 pp.

Maisch, M., 1987. Zur Gletschergeschichte des alpinen Spätglazials: Analyse und Interpretation von Schneegrenzdaten. Geographica Helvetica 42, 63-71.

Marazzi, S., 2005. Atlante orografico delle Alpi: SOIUSA: suddivisione orografica internazionale unificata del sistema alpino. Priuli & Verlucca, Scarmagno, Torino, 416 pp.

Marchetti, M., Ghinoi, A., Soldati, M., 2017. The dolomite landscape of the Alta Badia (Northeastern Alps): a remarkable record of geological and geomorphological history. In:

Soldati, M., Marchetti, M. (Eds.), Landscapes and Landforms of Italy. Springer, Cham, pp. 123-134.

Marrero, S.M., Phillips, F.M., Caffee, M.W., Gosse, J.C., 2016. CRONUS-Earth cosmogenic ^{36}Cl calibration. Quaternary Geochronology 31, 199-219.

Martinson, D.G., Pisias, N. H., Hays, H. D., Imbrie, J., Moore, T. C., Shackleton, N.J., 1987. Age, dating, and the orbital theory of the ice ages: development of a high-resolution 0 to 300,000-year chronostratigraphy. Quaternary Research 27, 1-29.

Masini, M., 1998. Limite delle nevi perenni, oscillazioni frontali tardiglaciali e postglaciali e relazioni con il clima degli Altopiani di Fanes, sennes e Fosses (Dolomiti - Alpi meridionali). Studi Trentini di Scienze Naturali - Acta Geologica 73, 107-117.

McCarroll, 2014. Trimline. In: H. Hargitai, Á. Kereszturi (Eds.), Encyclopedia of Planetary Landforms, Springer, New York, pp. 1-3.

McSaveney, M.J., 1978. Sherman glacier rock avalanche, Alaska, USA. In: Voigt, B. (Ed.), Rockslides and Rock Avalanches 1, Natural Phenomena. Elsevier, New York, pp. 197-258.

Monegato, G., 2012. Local glaciers in the Julian Prealps (NE Italy) during the Last Glacial Maximum. Alpine and Mediterranean Quaternary 25(1), 5-14.

Monegato, G., Ravazzi, C., Donegana, M., Pini, R., Calderoni, G., Wick, L., 2007. Evidence of a two-fold glacial advance during the last glacial maximum in the Tagliamento end moraine system (eastern Alps). Quaternary Research 68(2), 284-302.

Monegato, G., Scardia, G., Hajdas, I., Rizzini, F., Piccin, A., 2017. The Alpine LGM in the boreal ice-sheets game. Scientific reports 7(1), 2078.

Montorsi, E., 1998. Aspetti geomorfologici del versante sinistro del Rio S. Cassiano, Dolomiti. Bachelor dissertation, University of Modena and Reggio Emilia, 63 pp.

Moseley, G.E., Spötl, C., Svensson, A., Cheng, H., Brandstätter, S., Edwards, R.L., 2014. Multispeleothem record reveals tightly coupled climate between central Europe and Greenland during Marine Isotope Stage 3. Geology 42 (12), 1043-1046.

Murray-Wallace, C.V., 2018. Quaternary History of the Coorong Coastal Plain, Southern Australia: An Archive of Environmental and Global Sea-Level Changes. Springer, Cham, 229 pp.

Mutschlechner, G., 1932. Geologie der St. Vigiler Dolomiten: mit 1 geologischen Karte von G. Mutschlechner und P.Maibaur. Jahrbuch der Geologischen Bundesanstalt 82, 163-273.

Mutschlechner, G., 1933. Geologie des Gebietes zwischen St. Cassian und Buchenstein. (Südtiroler Dolomiten). Jahrbuch der Geologischen Bundesanstalt 83, 199-232.

Osmaston, H., 2005. Estimates of glacier equilibrium line altitudes by the Area× Altitude, the Area× Altitude Balance Ratio and the Area× Altitude Balance Index methods and their validation. Quaternary International 138, 22-31.

Panizza, M., 1973. Glacio pressure implications in the production of landslides in the dolomitic area. Geologia Applicata e Idrogeologia 3(1), 289-297.

Panizza, M., Corsini, A., Ghinoi, A., Marchetti, M., Pasuto, A., Soldati, M., 2011. Explanatory notes of the geomorphological map of the Alta Badia valley (Dolomites, Italy). Geografia Fisica Dinamica Quaternaria 34(1), 105-126.

Pelfini, M., 1994. Equilibrium Line Altitude (ELA) variations recorded by Ortles-Cevedale glaciers (Lombardy, Italy) from Little Ice Age to present. Geografia Fisica e Dinamica Quaternaria 17, 197-206.

Pellegrini, G.B. (Ed.), 2000. Note della Carta Geomorfologica d'Italia alla scala 1:50.000 Foglio "063" Belluno, Servizio Geologico Nazionale.

Pellegrini, G.B., Albanese, D., Bertoldi, R., Surian, N., 2005. La deglaciazione alpina nel vallone bellunese, Alpi meridionali orientali. Geografia Fisica e Dinamica Quaternaria Suppl. 7, 271-280.

Pellegrini, G.B., Surian, N., Albanese, D., 2006. Landslide activity in response to alpine deglaciation: the case of the Belluno Prealps (Italy). Geografia Fisica Dinamica Quaternaria 29(2), 185-196.

Penck, A., 1909. Der Etschgletscher. In: Penck, A., Buckner (Eds.), Die Alpen im Eiszeitalter, pp. 846-867.

Penck, A., Brückner, E., 1909. Die Eiszeiten in den nördlichen Ostalpen, Bd.1. In: Die Alpen Im Eiszeitalter. Chr. Herm. Tauchnitz, Leipzig, 393 pp.

Pellitero, R., Rea, B.R., Spagnolo, M., Bakke, J., Hughes, P., Ivy-Ochs, S., Lukas, S., Ribolini, A., 2015. A GIS tool for automatic calculation of glacier equilibrium-line altitudes. Computers & Geosciences 82, 55-62.

Pellitero, R., Rea, B.R., Spagnolo, M., Bakke, J., Ivy-Ochs, S., Frew, C.R., Hughes, P., Ribolini, A., Lukas, S., Renssen, H., 2016. Glare, a GIS tool to reconstruct the 3D surface of palaeoglaciers. Computers & Geosciences 94, 77-85.

Pini, R., Ravazzi, C., Reimer, P.J., 2010. The vegetation and climate history of the last glacial cycle in a new pollen record from Lake Fimon (southern Alpine foreland, N-Italy). Quaternary Science Reviews 29(23), 3115-3137.

Pisa, G., Marinelli, M., Viel, G., 1980. Infraraibl Group: a proposal (Southern Calcareous Alps, Italy): Rivista Italiana di Paleontologia e Stratigrafia 85, 983-1002.

Porter, S.C., 1975. Equilibrium-line altitudes of late Quaternary glaciers in the Southern Alps, New Zealand. Quaternary Research 5(1), 27-47.

Porter, S.C., 2001. Snowline depression in the tropics during the last Glaciation. Quaternary Science Review 20, 1067-1091.

Porter, S.C., Orombelli, G., 1982. Late-glacial ice advances in the western Italian Alps. Boreas 11(2), 125-140.

Preto, N., Hinnov, L.A., 2003. Unraveling the Origin of Carbonate Platform Cyclothems in the Upper Triassic Durrestein Formation (Dolomites, Italy). Journal of Sedimentary Research 73 (5), 774-789.

Phillips, F.M., Leavy, B.D., Jannik, N.O., Elmore, D., Kubik, P.W., 1986. The accumulation of cosmogenic chlorine-36 in rocks: a method for surface exposure dating. Science 231, 41-43.

Pini, R., Ravazzi, C., Reimer, P.J., 2010. The vegetation and climate history of the last glacial cycle in a new pollen record from Lake Fimon (southern Alpine foreland, N-Italy). Quaternary Science Reviews 29(23), 3115-3137.

Poto, L., Gabrieli, J., Crowhurst, S.J., Appleby, P.G., Ferretti, P., Surian, N., Cozzi, G., Zaccone, C., Turetta, C., Pini, R., Kehrwald, N., Barbante, C., 2013. The first continuous Late Glacial–Holocene peat bog multi-proxy record from the Dolomites (NE Italian Alps). Quaternary International 306, 71-79.

Preusser, F., Schlüchter, C., 2004. Dates from an important early Late Pleistocene ice advance in the Aare Valley, Switzerland. Eclogae geologicae Helvetiae 97, 245-253.

Preusser, F., Geyh, M.A., Schlüchter, C., 2003. Timing of Late Pleistocene climate change in lowland Switzerland. Quaternary Science Reviews 22, 1435-1445.

Preusser, F., Blei, A., Graf, H.R., Schlüchter, C., 2007. Luminescence dating of Würmian (Weichselian) proglacial sediments from Switzerland: methodological aspects and stratigraphical conclusions. Boreas 36, 130-142.

Rabassa, J., Ponce, J.F., 2016. The Heinrich and Dansgaard–Oeschger climatic events during Marine Isotopic Stage 3. In: Gasparini, G., Rabassa, J., Deschamps, C., Tonni, E. (Eds.), Marine Isotope Stage 3 in Southern South America, 60 ka BP–30 ka BP. Springer, Cham, pp. 7-21.

Rasmussen, S.O., Bigler, M., Blockley, S.P., Blunier, T., Buchardt, S.L., Clausen, H.B., Cvijanovic, I., Jensen, D.D., Johnsen, S.J., Fischer, H., Gkinis, V., Guillevic, M., Hoek, W.Z., Lowe, J.J., Pedro, J.B., Popp, T., Seierstad, I.K., Steffensen, J.P., Svensson, A.M., Vallelonga, P., Bo, M., Vinther, B.M., Walker, M.J.C., Wheatley, J.J., Winstrup, M., 2014. A stratigraphic framework for abrupt climatic changes during the Last Glacial period based on three synchronized Greenland ice-core records: refining and extending the INTIMATE event stratigraphy. Quaternary Science Reviews 106, 14-28.

Ravazzi, C., Badino, F., Marsetti, D., Patera, G., Reimer, P.J., 2012. Glacial to paraglacial history and forest recovery in the Oglio glacier system (Italian Alps) between 26 and 15 kyr cal BP. Quaternary Science Reviews 58, 146-161.

Ravazzi, C., Pini, R., Badino, F., De Amicis, M., Londeix, L., Reimer, P.J., 2014. The latest LGM culmination of the Garda Glacier (Italian Alps) and the onset of glacial termination. Age of glacial collapse and vegetation chronosequence. Quaternary Science Reviews 105, 26-47.

Rea, B.R., 2009. Defining modern day Area-Altitude Balance Ratios (AABRs) and their use in glacierclimate reconstructions. Quaternary Science Reviews 28, 237-248.

Reille, M., Andrieu, V., de Beaulieu, J.L., Guenet, P., Goeury, C., 1998. A long pollen record from Lac du Bouchet, Massif Central, France: for the period ca. 325 to 100 ka BP (OIS 9c to OIS 5e). Quaternary Science Reviews 17 (12), 1107-1123.

Reimer, P.J., Bard, E., Bayliss, A., Beck, J.W., Blackwell, P.G., Ramsey, C.B., Buck, C.E., Cheng, H., Edwards, L.R., Friedrich, M., Grootes, P.M., Guilderson, T.P., Haflidason, H.,

Hajdas, I., Hatté, C., Heaton, T.J., Hoffmann, D.L., Hogg, A.G., Hughen, K.A., Kaiser, K.F., Kromer, B., Manning, S.W., Niu, M., Reimer, R.W., Richards, D.A., Scott, E.M., Southon, J.R., Staff, R.A, Turney, C.S.M., van der Plicht, J., 2013. IntCal13 and Marine13 radiocarbon age calibration curves 0–50,000 years cal BP. Radiocarbon 55 (4), 1869-1887.

Reitner, J., 2005. Quartärgeologie und Landschaftsentwicklung im Raum Kitzbühel - St. Johann i.T.-Hopfgarten (Nordtirol) vom Riss bis in das Würm-Spätglazial (MIS 6-2). PhD dissertation, Universität Wien.

Reitner, J., 2007. Glacial dynamics at the beginning of Termination 1 in the Eastern Alps and their stratigraphic implications. Quaternary International 164/165, 64-84.

Reuther, A., Fiebig, M., Ivy-Ochs, S., Kubik, P., Reitner, J., Jerz, H., Heine, K., 2011. Deglaciation of a large piedmont lobe glacier in comparison with a small mountain glacier e new insight from surface exposure dating. Two studies from SE Germany. Journal of Quaternary Science 60, 248-269.

Rossato, S., Mozzi, P., 2016. Inferring LGM sedimentary and climatic changes in the southern Eastern Alps foreland through the analysis of a ^{14}C ages database (Brenta megafan, Italy). Quaternary Science Reviews 148, 115-127.

Rossato, S., Martin, S., Ivy-Ochs, S., Viganò, A., Vockenhuber, C., Rigo, M., Surian, N., Mozzi, P., 2018. Post-LGM catastrophic landslides in the Dolomites: when, where and why. Alpine and Mediterranean Quaternary 31(1), 239-242.

Sanchez Goñi, M.F., Harrison, S.P., 2010. Millennial-scale climate variability and vegetation changes during the Last Glacial: Concepts and terminology. Quaternary Science Reviews 29(21-22), 2823-2827.

Scapozza, C., Castelletti, C., Soma, L., Dall'Agnolo, S., Ambrosi, C., 2014. Timing of LGM and deglaciation in the Southern Swiss Alps. Géomorphologie: relief, processus, environnement 20(4), 307-322.

Schimmelpfennig, I., 2009. Cosmogenic ^{36}Cl in Ca and K rich minerals: analytical developments, production rate calibrations and cross calibration with ^{3}He and ^{21}Ne. Doctoral dissertation, University of Paul Cezanne, Aix-Marseille 3, 317 pp.

Schimmelpfennig, I., Benedetti, L., Finkel, R., Pik, R., Biard, P.H., Bourles, D., Burnard, P., Williams, A., 2009. Sources of in-situ ^{36}Cl in basaltic rocks. Implications for calibration of production rates. Quaternary Geochronoly 6, 441-461.

Schimmelpfennig, I., Benedetti, L., Garreta, V., Pik, R., Blard, P.H., Burnard, P., Bourlès, D., Robert Finkel, R., Katja Ammon, K., Dunai, T., 2011. Calibration of cosmogenic ^{36}Cl production rates from Ca and K spallation in lava flows from Mt. Etna (38 N, Italy) and Payun Matru (36 S, Argentina). Geochimica et Cosmochimica Acta 75(10), 2611-2632.

Schlagenhauf, A., Gaudemer, Y., Benedetti, L., Manighetti, I., Palumbo, L., Schimmelpfennig, I., Finkel, R., Pou, K., 2010. Using in situ Chlorine-36 cosmonuclide to recover past earthquake histories on limestone normal fault scarps: a reappraisal of methodology and interpretations. Geophysical Journal International 182(1), 36-72.

Servizio Geologico d'Italia, 1977. Foglio 028 "La Marmolada". Carta Geologica d'Italia alla scala 1:50.000.

Shakun, J.D., Carlson, A.E., 2010. A global perspective on Last Glacial Maximum to Holocene climate change. Quaternary Science Reviews 29(15-16), 1801-1816.

Soldati, M., 2010. Dolomites: The spectacular landscape of the “Pale Mountains”. In: Migon, P. (Ed.), Geomorphological Landscapes of the World. Springer Science+Business Media B.V., 191-199.

Soldati, M., Dibona, D., Paganelli, A., Panizza, V., 1997. Evoluzione ambientale dell'area dell'Alpe Fedéra (Croda da Lago, Dolomiti). Studi Trentini di Scienze Naturali. ActaGeologica 71 (1994), 21-56.

Soldati, M., Corsini, A., Pasuto, A., 2004. Landslides and climate change in the Italian Dolomites since the Lateglacial. Catena 55 (2), 141-161.

Soldati, M., Borgatti, L., Cavallin, A., De Amicis, M., Frigerio, S., Giardino, M., Mortasa, G., Pellegrini, G.B., Ravazzi, C., Surian, N., Tellini, C., in collaboration with Alberto, W., Albanese, D., Chelli, A., Corsini, A., Marchetti, M., Palomba, M., Panizza, M., 2006. Geomorphological evolution of slopes and climate changes in Northern Italy during the Late Quaternary: spatial and temporal distribution of landslides and landscape sensitivity implications. Geografia Fisica e Dinamica Quaternaria 29 (2), 165-183.

Spötl, C., Mangini., A., 2006. U/Th age constraints on the absence of ice in the central Inn Valley (eastern Alps, Austria) during Marine Isotope Stages 5c to5a. Quaternary Research 66, 167-175.

Spötl, C., Reimer, P.J., Rabeder, G., Scholz, D., 2014. Presence of cave bears in western Austria before the onset of the Last Glacial Maximum: new radiocarbon dates and palaeoclimatic considerations. Journal of Quaternary Science 29 (8), 760-766.

Spötl, C., Reimer, P.J., Rabeder, G., Ramsey, C.B., 2018. Radiocarbon constraints on the age of the world's highest-elevation cave-bear population, Conturines Cave (Dolomites, Northern Italy). Radiocarbon 60 (1), 299-307.

Stansell, N.D., Polissar, P.J., Abbott, M.B., 2007. Last glacial maximum equilibrium-line altitude and paleo-temperature reconstructions for the Cordillera de Mérida, Venezuelan Andes. Quaternary Research 67, 115-127.

Starnberger, R., Rodnight, H., Spötl, C., 2011. Chronology of the last glacial maximum in the Salzach Palaeoglacier area (Eastern Alps). Journal of Quaternary Science 26(5), 502-510.

Starnberger, R., Drescher-Schneider, R., Reitner, J.M., Rodnight, H., Reimer, P.J., Spötl, C., 2013. Late Pleistocene climate change and landscape dynamics in the Eastern Alps: the inner-alpine Unterangerberg record (Austria). Quaternary science reviews 68, 17-42.

Stoffel, M., Huggel, C., 2012. Effects of climate change on mass movements in mountain environments. Progress in Physical Geography 36 (3), 421-439.

Stone, J.O., Allan, G.L., Fifield, L.K., Cresswell, R.G., 1996. Cosmogenic chlorine-36 from calcium spallation. Geochimica et Cosmochimica Acta 60 (4), 679-692.

Stone, J.O., 2000. Air pressure and cosmogenic isotope production. Journal of Geophysical Research: Solid Earth 105(B10), 23753-23759.

Svensson, A., Nielsen, S.W., Kipfstuhl, S., Johnsen, S.J., Steffensen, J.P., Bigler, M., Ruth, U., Röthlisberger, R., 2005. Visual stratigraphy of the North Greenland Ice Core Project (NorthGRIP) ice core during the last glacial period. Journal of Geophysical Research: Atmospheres 110, 1-11.

Svensson, A., Andersen, K.K., Bigler, M., Clausen, H.B., Dahl-Jensen, D., Davies, S.M., Johnsen, S.J., Muscheler, R., Parrenin, F., Rasmussen, S.O., Röthlisberger, R., Seierstad, I., Steffensen, J.P., Vinther, B.M., 2008. A 60 000 year Greenland stratigraphic ice core chronology. Climate of the Past 4 (1), 47-57.

Talma, A.S., Vogel, J.C., 1993. A simplified approach to calibrating ^{14}C dates. Radiocarbon 35 (2), 317-322.

Tütken, T., Furrer, H., Vennemann, T.W., 2007. Stable isotope compositions of mammoth teeth from Niederweningen, Switzerland: implications for the Late Pleistocene climate, environment, and diet. Quaternary International 164, 139-150.

Vai, G.B., Cantelli, L. (Eds), 2004. Litho-palaeoenvironmental maps of Italy during the last two climatic extremes. Litografia Artistica Cartografica, Firenze

Vandelli, V., Ghinoi, A., Marchetti, M., Soldati, M., 2019. Discovery and dating of Pre-LGM deposits in a high catchment of the Dolomites (Italy): New insights on climate-related geomorphological processes during the Late Pleistocene. Geomorphology 332, 22-32.

Venetz, I., 1833. Mémoire sur les variation de la temperature dans les Alps de la Suisse. – Denkschriften der allgemeinen Schweizerischen Gesellschaft für die gesamte Natur, 1.

Viel, G., 1979, Litostratigrafia ladinica: una revisione. Ricostruzione paleogeografica e paleostrutturale dell'area Dolomitico-Cadorina (Alpi Meridionali): Rivista Italiana di Paleontologia e Stratigrafia 85(2), 297-352.

Wirsig, C., Zasadni, J., Christl, M., Akçar, N., Ivy-Ochs, S., 2016. Dating the onset of LGM ice surface lowering in the High Alps. Quaternary Science Reviews 143, 37-50.

Consulted websites

Meteo Browser of the Autonomous Province of Bolzano:
http://meteobrowser.eurac.edu/app_direct/meteobrowser/ (last access 30 August 2019)

Geoportal of the Autonomous Province of Bolzano:
http://geocatalogo.retecivica.bz.it/geokatalog/#! (last access 25 September 2019)

Geoportal of the Veneto Region:
https://www.regione.veneto.it/web/ambiente-e-territorio/geoportale
(last access 25 September 2019)

Acknowledgments

First of all, I would like to thank my supervisor Prof. Mauro Soldati for his guidance during the PhD, at many stages in the course of these three years. His careful editing contributed significantly to the production of this thesis.

A big thank also to my co-supervisor Prof. Mauro Marchetti; I benefited from his advice, particularly when exploring new ideas. I am also grateful to Dr. Alessandro Ghinoi for helping me in the literature review and for providing me with helpful suggestions.

I am grateful to Prof. Carlo Baroni and Prof. Maria Cristina Salvatore for their guidance during sampling compaigns, as well as for the fruitful discussions and thoroughful suggestions.

I am very grateful to Dr. Lucilla Benedetti and Dr. Irene Schimmelpfennig for welcoming me at CEREGE for performing ^{36}Cl Cosmic Ray Exposure dating and for their guidance in the calculation of the exposure ages. I am once more grateful to Irene for her supervision and suggestions in writing the methodology section. A big thank also to Valéry Guillou for guide me through the preparation of the samples in the Laboratoire National des Nucléides Cosmogéniques (CEREGE, Aix-en-Provence, France).

Many thanks also to Dr. Simona Bigi and Dr. Monica Malavasi of the Department of Chemical and Geological Sciences (UNIMORE) for having introduced me to the X-ray fluorescence (XRF) technique and to the Inductively Coupled Plasma - Optical Emission Spectrometry (ICP-OES) respectively. I am also thankful to Dr. Daniela Manzini of the Centro Interdipartimentale Grandi Strumenti (C.I.G.S.) for performing Inductively Coupled Plasma Mass Spectrometry (ICP-MS) on bulk rock samples. The latter analyses would have not been possible without the fundamental help in sample preparation provided by Dr. Lisa Lancellotti, I would like to thank her as well.

Moreover, I would like to thank the Autonomous Province of Bolzano for providing LiDAR data and to Ski Carosello for providing access to borehole cores. I am also thankful to Dr. Hermann Nicolussi's Geological Company for technical information on boreholes. Furthermore, I would like to thank Prof. Piero Gianolla and Dr. Chiara Siorpaes for their advice in the recognition of dolomite facies. Many thanks also to Mr. Markus Valentini for constant updating on the excavation works.

Finally, I would like to thank Prof. Monique Fort and Prof. Leonidas Stamatopoulos for careful reading the manuscript and for their thoughtful suggestions.

Appendix 1

Chemical sample preparation

This method was used to extract and purify Cl from carbonate rock samples and produce AgCl for AMS analysis.

After dissolution, Cl was separated from the rock matrix by AgCl precipitation. This precipitate was re-dissolved in NH_3 and Cl separated from S (including ^{36}S, an interfering isobar of ^{36}Cl) by $BaSO_4$ precipitation. AgCl was recovered by acidifying the $[Ag(NH_3)_2]Cl$ solution, then recovered and dried for AMS analysis.

For the extraction procedure we used Nalgene bottles of 1-litre size. The bottle size depends on the sample amount that will be processed. The right bottle size has to be chosen before starting the procedure by estimating how much acid will be needed to totally dissolve the sample material.

1) A 1-litre Nalgene bottle per sample have been labelled and weighted and 90-95 g of 250-1000 µm grain size fraction have been put inside. The weight of the bottles plus the sample have been noted down.

2)The sample was so ready for the first phase of leaching to remove atmospheric ^{36}Cl or resulting from handling in the field. The samples in the bottles have been rinsed with MQ (ultra-pure) water until the leaking water became clear. Then, the bottles have been filled with 4/5 of MQ water and stirred for 2 hours. The supernatant has been discarded and samples have been rinsed again several times. Bottles have been so put in the oven (80°) to dry overnight. Once at room temperature, bottles plus samples have been weight another time.

3) The third step was aimed to partly dissolve the samples (around 10%), in order to remove secondary carbonates Then samples in the bottles have been cover with 1-2 cm of MQ water. The proper volume of 2M HNO_3 has been poured in the bottles considering that 10 ml of 2M nitric acid dissolve 1 g of carbonate., while stirring gently to homogenize. Samples have been let rest for at least 1 hour with the cap not closed. Then, the supernatant has been discarded and the samples rinsed several times with MQ water. The samples have been then put in the oven (80°) to be dried. Once dried, samples have been taken off the oven and weighted once reached room temperature.

4)The samples were so ready to undergo total dissolution. The total amount of spike per all the samples has been collected in a centrifuge tube (2 mg of Cl per sample and 2 mg for the blank). The spike has been transferred from the centrifuge tube to a vial (one per each sample) by means of a specific pipette (one per sample) and has been then weighted into the vial by means of a precision weight scale. The spike has been then transferred from the vial to the

sample. The vial has been rinsed 3 times with 1 ml of MQ water in order to guarantee that all the spike has been transferred to the sample. Then around 80 ml of MQ water have been added to the sample, and after, a certain volume of 2M HNO_3 – necessary for the total dissolution – has been added slowly, without stirring. The samples rested overnight with the cap not closed completely till the complete dissolution.

5) A new bottle for each sample and for the blank solution (carrier) has been labelled, weighted and rinsed with MQ water. A pleated filter has been placed on a funnel (one per each sample). Then, the solution has been filtered and residues, that remained on the filter, have been re-transferred to the "old" bottles. The bottles with the residues have been dried in the oven (80°C) and weighted after reaching room temperature. The filtrate has been homogenized by shaking the bottles and degassed by opening the caps. The weight of the bottles containing the sample solution has been then taken. 1 ml of the sample solution as aliquots has been taken from the sample solution (changing the micropipette for each sample) using it to measure Ca concentration, the aliquots have been stored in the fridge.

6) This was the final step of the chemical preparation of samples and it was aimed at the precipitation of AgCl. 1.5 ml of $AgNO_3$ (10% solution) has been added with a Pasteur pipette and stirred. Bottles have been taken far from the light for at least one day. Once the AgCl has precipitated, the supernatant has been pumped out by means of a membrane pump. The precipitate has been then transferred to a 50-ml centrifuge tube, previously rinsed, and centrifuged for 5 minutes. Then, the supernatant has been discarded. In order to transfer all the precipitate into the centrifuge tubes, the bottles have been rinsed with 1 ml of NH_3 (1: 1) and 2 ml of MQ water. 2 ml of NH_3 (1: 1) were added to the centrifuge tubes and vortex until the precipitate dissolved. In order to precipitate sulphates (^{36}S is an isobar of ^{36}Cl), 0.5 ml of saturated solution of barium nitrate ($Ba(NO_3)_2$) has been added. The so prepared 50 ml centrifuge tubes have been left one night with unscrewed caps with the hood off. The supernatant within each of the 50-ml centrifuge tubes has been filtered by means of a syringe and an acrodisc filter into a 15-ml centrifuge tube (labelled and washed accurately). Then, nitric acid (1: 1) in large excess has been added by a Pasteur pipette to precipitate AgCl until the solution have reached 12 ml. The solution has been then vortexed and put in the refrigerator for 20 minutes. Then the solution has been put in the centrifuge for 5 minutes and after the supernatant has been discarded. Then 5 ml of MQ water have been added and the solution vortexed and centrifuged again. After the supernatant has been discarded, 5 ml of MQ water have been added again and the solution has been vortex and centrifuged again except for the carrier in order to avoid losses of chlorine. The precipitate has been dried in an oven (80°) for at least 24 hours. Then centrifuge tubes have been stored far from the light until they have been analysed at the AMS.

Appendix 2

Core: BS2 Depth: 0-5 m

Core: BS2 Depth: 5-10 m

Core: BS2 Depth: 10-15 m

Core: BS6 Depth: 0-5 m

Core: BS6 Depth: 5-10 m

Core: BS6 Depth: 10-15 m

Core: BS6 Depth: 15-20 m

Core: BS7-P Depth: 0-5 m

Core: BS7-P Depth: 5-10 m

Core: BS7-P Depth: 10-15 m

Core: BS7-P Depth: 15-20 m

Core: BS7-P Depth: 20-25 m

Core: BS8-P Depth: 0-5 m

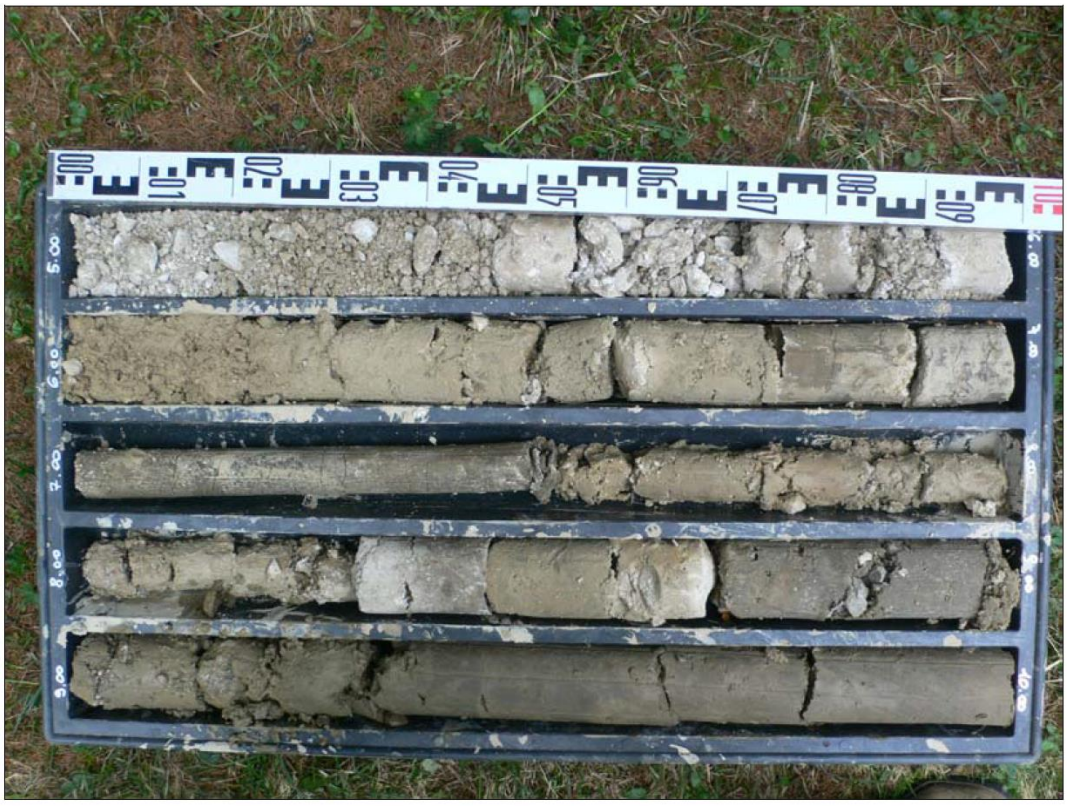

Core: BS8-P Depth: 5-10 m

Core: BS8-P Depth: 10-15 m

Core: BS8-P Depth: 15-20 m

Core: BS8-P Depth: 20-25 m

Appendix 3: Spreadsheet for in-situ ^{36}Cl production calculations

Sources of in-situ ^{36}Cl in basaltic rocks: Implications for calibration of production rate

I. Schimmelpfennig, L. Benedetti, R. Finkel, R. Pik, P.H. Blard, D. Bourlès, P. Burnard, A. Williams
(correspondance: e-mail 1: schimmel@cerege.fr, e-mail 2: irene.lois@yahoo.de)

Quaternary Geochronology

Legend

input cells

output cells

10000 input and output cells

calculations and values of parameters taken from Gosse & Phillips 2001

calculations and values of parameters taken from Fabryka-Martin 1988

values of parameters taken from CHLOE (Phillips & Plummer, 1996)

according to Heisinger et al. 2002

according to Farber et al. 2008

according to Schlagenhauf et al. (in prep.)

uncertainties uncertainties

References:

Evans, J.M., Stone, J.O., Fifield, L.K., Cresswell, R.G., 1997. Cosmogenic chlorine-36 production in K-feldspar. Nuclear Instruments and Methods in Physics Research Section B, 123, 334-340.
Fabryka-Martin, J.T., 1988. Production of radionuclides in the earth and their hydrogeologic significance, with emphasis on chlorine-36 and iodine-129. PhD Thesis, Univ. of Arizona, Tucson, USA.
Farber, D.L., Mériaux, A.S., Finkel, R.C., 2008. Attenuation length for fast nucleon production of 10Be derived from near-surface production profiles. Earth and Planetary Science Letters, 274, 295-300.
Fink, D., Vogt, S., Hotchkis, M., 2000. Cross-sections for 36Cl from Ti at Ep = 35-150 MeV: Applications to in-situ exposure dating. Nuclear Instruments and Methods in Physics Research Section B, 172, 861-866.
Gosse, J.C., Phillips, F.M., 2001. Terrestrial in situ cosmogenic nuclides: theory and application. Quaternary Science Reviews, 20, 1475-1560.
Heisinger, B., Lal, D., Jull, A.J.T., Kubik, P., Ivy-Ochs, S., Knie, K., Nolte, E., 2002. Production of selected cosmogenic radionuclides by muons: 2. Capture of negative muons. Earth and Planetary Science Letters, 200, 357-369.
Masarik, J., 2002. Numerical simulation of in-situ production of cosmogenic nuclides. Geochimica Cosmochimica Acta, 66, A491.
Phillips, F.M., Plummer, M.A., 1996. CHLOE: A program for interpreting in-situ cosmogenic nuclide data for surface exposure dating and erosion studies. Abstracts of the 7th international conference on Accelerator mass spectrometry. Tucson, Arizona, USA, pp. 98-99.
Phillips, F.M., Stone, W.D., Fabryka-Martin, J.T., 2001. An improved approach to calculating low-energy cosmic-ray neutron fluxes near the land/atmosphere interface. Chemical Geology, 175, 689-701.
Schlagenhauf, A., Gaudemer, Y., Benedetti, L., Manighetti, I., Palumbo, L., Schimmelpfennig, I., Finkel, R., Pou, K., Using in-situ chlorine-36 cosmonuclide to recover past earthquake histories on limestone normal fault scarps: A reappraisal of methodology and interpretations. Submitted to Geophysical Journal International.
Stone, J.O., Allan, G.L., Fifield, L.K. Cresswell, R.G., 1996. Cosmogenic chlorine-36 from calcium spallation. Geochimica et Cosmochimica Acta, 60, 679-692.
Stone, J.O., 2000. Air pressure and cosmogenic isotope production. Journal of Geophysical Research, 105, 23753-23759.
Vermeesch, P., 2007. CosmoCalc: An Excel add-in for cosmogenic nuclide calculations. Geochemistry Geophysics Geosystems, 8, 1525-2027.

The default values in Box 1 correspond to a plagioclase sample from a basaltic rock at Mt. Etna (PLG SI43 - D4 in the paper).

How to use this excel spreadsheet

You have to use one calculation worksheet per sample! More than one sample on one sheet is not possible! (except on worksheet "depth profile")

This spreadsheet works for any type of rock and any composition. It allows:
(1) calculation of the ^{36}Cl exposure age of an uneroded surface sample (Box 2- Output A).
(2) calculation of the ^{36}Cl exposure age or erosion rate of a sample from an eroding surface (Box 3- Output B).
(3) calculation of ^{36}Cl contributions from all production mechanism (Box 4- Output C).
(4) fitting calculated to measured ^{36}Cl concentrations in a depth profile (worksheet "depth profile").

The calculations are possible for a buried surface sample which has not been reexposed. In this case the formation age of the rock is older than the exposure age.

Calculations are adjusted to the case that ^{36}Cl is extracted from a part of the rock (target fraction) and not from the bulk rock. Therefore, the chemical composition of bulk rock and target fraction are distinguished.

Detailed formulas can be found in Appendix A1 of this paper.

Box 1: Input
In this box all sample relevant information has to be input in the **black-framed yellow cells**.
Element concentrations of the bulk rock should be input for all elements at least up to and including the element U (column Z) for correct calculation of the low-energy neutron flux.
Major element concentrations are in wt-% (as oxides), trace element concentrations in wt-ppm. You have to input the composition of both bulk rock and target fraction.

These sample calculations can be done for surface samples (depth reference z=0 cm in cell D8) or for individual samples in a depth profile (depth reference z>0 cm in cell D8).

The elevation-latitude scaling factors $S_{el,s}$ and $S_{el,\mu}$ have to be input from an external source (e.g. in CosmoCalc, Vermeesch 2007). Also, the shielding factor S_T has to be calculated elsewhere.

An exposure duration t_{expo} has to be input in the case of inheritance, for the calculations of erosion rates (see Box 3) and for the theoretical ^{36}Cl inventory $N_{calc,total}$ and the ^{36}Cl contributions (see Box 4).
In the case of erosion and if the erosion rate is estimated t_{expo} can also be output, but it has to be found iteratively by the user (see Box 3).
The formation age t_{form} has to be input in any case (even if it is equal to t_{expo}!). It is necessary to allow correcting for the radiogenic component. You can give an estimate for t_{form} if it is unknown.

There are other **black-framed yellow cells** in Box 6: Here you can change the SLHL spallation production rates by replacing the default values.

Box 2: Output A
The **black-framed blue cell** gives the exposure age of the sample, but only for uneroded surfaces.

Box 3: Output B
Gives the theoretical ^{36}Cl inventory of an eroding surface sample for a known or estimated erosion rate and a known or estimated exposure duration (input in Box 1).
In case the erosion rate is fixed, the exposure duration will be found by adjusting t_{expo} iteratively in Box 1 until the difference between measured and calculated ^{36}Cl concentration is minimized (black-framed cell D39). In case, the exposure duration is fixed, the erosion rate can be found be adjusting ε in the same way.

Box 4: Output C
Shows the theoretical ^{36}Cl inventory of the sample in case the exposure duration is known or estimated (input in Box 1). Erosion is not taken into account.
In the **black-framed blue cells**, the ^{36}Cl contribution from each production mechanism is given.

Boxes 6-10:
Sample-specific production rates for all production mechanisms. The values of single constants can be changed, e.g. Λ_f in cell D126 or $P_f(0)$ in cell D123.

Box 11:
Thickness integration factors.

Worksheet "depth profile"
Automatically presents two graphs showing the vertical distributions of the theoretical ^{36}Cl inventory $N_{calc,total}$ and the sample-specific production rates from all production mechanisms using the sample relevant input on the worksheet "sample calculations".
The individual points of the depth profiles are not integrated over the sample thickness, but are given at a specific depth.

In the **Input-Box** the measured ^{36}Cl concentrations N_{meas} of samples from a depth profile and their corresponding depths are required. They will be automatically plotted in the first graph.
$N_{calc,total}$ can be fitted to N_{meas} by adjusting individual unknown parameters on the worksheet "sample calculations", e.g. the erosion rate ε, the exposure duration t_{expo}
and/or the ^{36}Cl concentration from inheritance $N_{inher}(0)$.

Chlorine-36 exposure age and erosion rate determination: Please follow the instructions on the first worksheet

modifications regarding muonic 36Cl production

Sample name 170829.02

1- Input

(and output for eroding surfaces)

	symbol	units	calculations	Uncertainties
element concentration in bulk rock: maior element as oxides [wt-%] and trace elements [wt-ppm]				
element concentration in target fraction: major element as oxides [wt-%] and Cl in [wt-ppm]				
uncertainty target element concentration in target fraction (oxides in [wt-%] and Cl in [wt-ppm])				
depth reference: top of sample		cm	0	
sample thickness		cm	2.5	
bulk rock density	rho	g cm^{-3}	2.8	
mass depth reference: center of sample	z	g cm^{-2}	3.5	
mass thickness	z_s	g cm^{-2}	7	
scaling factor for nucleonic production as a function of elevation, latitude (and temporal v	$S_{sp,ne}$, $S_{st,ne}$	-	3.966	0.198
scaling factor for muonic production as a function of elevation, latitude (and temporal var	$S_{sp,\mu}$	-	2.083	0.104
correction factor for shielding of a sample of arbitrary orientation by surrounding topogra	S_T	-	0.979	0.00979
correction factor for geometry effects on spallogenic production	S_{shape}	-	1	0.03
correction factor for snow shielding for spallogenic production	S_{snow}	-	1	0.01
effective fast neutron attenuation coefficient	$\Lambda_{f,e}$	g cm^{-2}	160	
estimated ^{36}Cl concentration from inheritance at t_{expo}=0	$N_{inher}(0)$	atoms ^{36}Cl g^{-1}		
measured ^{36}Cl concentration in sample	N_{meas}	atoms ^{36}Cl g^{-1}	7.87E+05	3.86E+04
exposure duration (independently determined or estimated)	t_{expo}	a	13274	1422.91018
formation age of rock (independently determined or estimated) for radiogenic correction	t_{form}	a	200000000	1000
erosion rate	ε	mm ka^{-1}	0	0

	CaO [wt-%]	K2O [wt-%]	TiO2 [wt-%]	Fe2O3 [wt-%]	Cl [ppm]
bulk rock:					
30.830	0.05	0.01	0.09	49	
target fraction:					
29.97	0.05	0.01	0.09	54.19	
0.59	0.01	0.01	0.01	2.34	

	SiO2 [wt-%]	Na2O [wt-%]	MgO [wt-%]	Al2O3 [wt-%	MnO [wt-%]	P2O5 [wt-%]	CO2 [wt-%]	H2O [wt-%]
	0.32	0.03	21.12	0.20	0.00	0.00		0.43
	0.32	0.03	21.12	0.20	0.00	0.00		0.43

	Li [ppm]	B [ppm]	Sm [ppm]	Gd [ppm]	Th [ppm]	U [ppm]
	1.46	4.8	0.08	0.08	0.14	6.61
	1.46	4.8	0.0806	0.0797	0.1383	6.6086

	Cr [ppm]	Be [ppm]	N [ppm]	F [ppm]	S [ppm]	Sc [ppm]	Co [ppm]	Ni [ppm]	Se [ppm]	Br [ppm]	Rb [ppm]	Sr [ppm]	Zr [ppm]	Mo [ppm]	Ru [ppm]	Te [ppm]	I [ppm]	Cs [ppm]	Ba [ppm]
	4.33	0.00				0.16	0.16	0.00			2.01	78.09	2.10	2.63				0.09	0.00
	4.3315	0				0.16	0.1584	0	0	0	2.0099	78.0913	2.0983	2.6322	0	0	0	0.0905	0
	4.3315	0	0	0	0	0.16	0.1584	0	0	0	2.0099	78.0913	2.0983	0	0	0	0	0.0905	0

2- Output A: exposure age of sample (only for uneroded surface)

decay constant for ^{36}Cl	λ_{36}	a^{-1}	2.30E-06	1.51998E-08
scaled total sample specific ^{36}Cl production rate without radiogenic	P_{total}	atoms ^{36}Cl q^{-1} a	53.9	4.9
time factor radiogenic	t_i		434216	2865.8
calculated concentration of radiogenically produced ^{36}Cl atoms for estimated age	N_i	atoms ^{36}Cl q^{-1}	82337.0	4152.6
estimated ^{36}Cl concentration from inheritance at time of sampling	$N_{inher}(t)$	atoms ^{36}Cl q^{-1}	0.0	
measured ^{36}Cl concentration in sample corrected from radiogenic component and inheritance	$N_{meas-inher}$	atoms ^{36}Cl g^{-1}	7.05E+05	38775.8
exposure age of sample	**t**	**a**	13274	764.3

3- Output B: eroding surface

calculated ^{36}Cl concentration for an eroding sample	$N_{calc,total}$	atoms ^{36}Cl q^{-1}	7.87E+05	
difference measured/calculated ^{36}Cl concentration in eroding sample	$\Delta N_{meas-calc}$		0.00%	
erosion rate	ε	cm a^{-1}	0	0
time factor with erosion for spallation reaction	$t_{cosm,s}$		13073	1380
time factor with erosion for capture of epithermal neutrons	$t_{cosm,eth}$		13073	1380
time factor with erosion for capture of thermal neutrons	$t_{cosm,th}$		13073	1380
time factor with erosion for capture of slow negative muons	$t_{cosm,\mu}$		13073	1380
depth reference factor for spallogenic reaction	d_s		0.978	
depth reference factor for capture of epithermal neutrons	d_{eth}		0.897	
depth reference factor for capture of thermal neutrons	d_{th}		0.943	
depth reference factor for capture of slow negative muons	d_μ		0.998	
production rate coefficient corrected for sample thickness for spallogenic reaction	$J_{Cl,s}$		24.96	
production rate coefficient corrected for sample thickness for capture of epithermal neutrons	$J_{Cl,eth}$		1.89	
production rate coefficient corrected for sample thickness for capture of thermal neutrons	$J_{Cl,th}$		-15.18	
production rate coefficient corrected for sample thickness for capture of slow negative muons	$J_{Cl,\mu}$		2.08	
production rate coefficient for spallogenic reaction	J_s		24.98	
production rate coefficient for capture of epithermal neutrons	J_{eth}		1.89	
production rate coefficient for capture of thermal neutrons	J_{th}		-15.19	
production rate coefficient for capture of slow negative muons	J_μ		2.08	

4- Output C: calculated ^{36}Cl contributions from all production mechanism

time factor cosmogenic without erosion	t_{cosm}		13073	1380
calculated ^{36}Cl concentration for given time + radiogenic	$N_{calc,total}$	atoms ^{36}Cl q^{-1}	7.87E+05	97885
difference measured/calculated ^{36}Cl concentration	$\Delta N_{meas-calc}$		0.00%	
contribution from each production mechanism:				
number of atoms ^{36}Cl per q by spallation of Ca	$N_{s,Ca}$	atoms ^{36}Cl q^{-1}	447089	56.81%
number of atoms ^{36}Cl per q by spallation of K	$N_{s,K}$	atoms ^{36}Cl q^{-1}	2748	0.35%
number of atoms ^{36}Cl per q by spallation of Ti	$N_{s,Ti}$	atoms ^{36}Cl q^{-1}	35	0.00%
number of atoms ^{36}Cl per g by spallation of Fe	$N_{s,Fe}$	atoms ^{36}Cl g^{-1}	59	0.01%
number of atoms ^{36}Cl per g by spallation of target elements	N_s	atoms ^{36}Cl g^{-1}	449930	57.17%
number of atoms ^{36}Cl per q by capture of thermal neutrons	N_{th}	atoms ^{36}Cl q^{-1}	134510	17.09%
number of atoms ^{36}Cl per q by capture of epithermal neutrons	N_{eth}	atoms ^{36}Cl q^{-1}	41918	5.33%
number of atoms ^{36}Cl per g by capture of thermal and epithermal neutrons	N_n	atoms ^{36}Cl g^{-1}	176426	22.42%
number of atoms ^{36}Cl per g by capture of slow negative muons	N_μ	atoms ^{36}Cl g^{-1}	78326	9.95%
number of atoms ^{36}Cl per g by radiogenic production	N_r	atoms ^{36}Cl q^{-1}	82337	10.46%
				100.00%

5- elemental parameters

			Ca	K	Ti	Fe	Cl	O, rock	Si	Na	Mg	Al	Mn	P	C	H	O, water	Li	B	Sm	Gd	Th	U	Cr
element concentration [wt-ppm] **bulk rock**		ppm	220435	374	54	622	49	174801	1494	223	127323	1053	29	0	0	481	3844	1.46	4.8	0.1	0.1	0.1383	6.6086	4.3315
element concentration dissolved samole [wt-ppm] in **taroet fraction**		ppm	214311	374	54	622	54	172360	1494	223	127323	1053	29	0	0	481	3844	1.46	4.8	0.0806	0.0797	0.1383	6.6086	4.3315
atomic mass of element k (Reference: http://www.ciaaw.org/atomic-weights.htm)	A_k	g mol^{-1}	40.078	39.0983	47.867	55.845	35.453	15.999	28.085	22.98977	24.305	26.981538	54.938043	30.973761	12.01	1.008	15.999	6.941	10.811	150.36	157.25	232.0377	238.02891	51.9961
avoqadro			6.02E+23																					
atomic concentration of element k in **bulk rock**	N_k	atoms q^{-1}	3.31E+21	5.75E+18	6.79E+17	6.71E+18	8.32E+17	6.58E+21	3.20E+19	5.83E+18	3.15E+21	2.35E+19	3.14E+17	0.00E+00	0.00E+00	1.03E+20	1.45E+20	1.27E+17	2.67E+17	3.23E+14	3.05E+14	3.59E+14	1.67E+16	5.02E+16
atomic concentration of element k in **target fraction**	N_{Cl}	atoms g^{-1}					########																	
dilute resonance integral for absorption of epithermal neutrons by element k	$I_{0,k}$	E^{-24} cm^2	0.233	1	3.1	1.36	13.83	0.0002693	0.082	0.311	0.038	0.17	13.4	0.079	0.0018	0	0.0002693	0	343	1400	390	83.3	277	1.6
average log decrement of energy loss per collision for element k	x_k	-	0.049	0.05	0.041	0.035	0.055	0.12	0.07	0.084	0.08	0.072	0.036	0.06321	0.157760474	1	0.12	0.264	0.174	0.013	0.013	0.008594	0.008379	0.038
neutron scattering cross section of element k	$\sigma_{s,k}$	E^{-24} cm^2	2.93	2.04	4.09	11.35	15.8	3.76	2.04	3.028	3.414	1.41	2.06	3.134	4.74	20.5	3.76	0.95	4.27	38	172	13.55	9.08	3.38
thermal neutron absorption cross section of element k	$\sigma_{a,k}$	E^{-24} cm^2	0.43	2.1	6.41	2.56	33.14	0.0002	0.171	0.517	0.0666	0.231	13.36	0.165	0.0035	0.33		70.5	767	9640	41560	7.34	2.68	3.1
proportion of muons stopped in element i that are captured by the nucleus	f_{cik}		0.864	0.83		0.906		0.223	0.671	0.432	0.538	0.582			0.09									
average neutron yield per captured muon	Y_k		0.75	1.25		1.125		0.8	0.86	1	0.6	1.26			0.76									

			Be	N	F	S	Sc	Co	Ni	Se	Br	Rb	Sr	Zr	Mo	Ru	Te	I	Cs	Ba
							0.16	0.1584	0	0	0	2.0099	78.0913	2.0983	2.6322	0	0	0	0	0.0905
			0	0	0	0	0.16	0.1584	0	0	0	2.0099	78.0913	2.0983	0	0	0	0	0	0.0905
			0.00E+00	0.00E+00	0.00E+00	0.00E+00	0.00E+00	2.14E+15	1.62E+15	0.00E+00	0.00E+00	0.00E+00	1.42E+16	5.37E+17	1.39E+16	1.65E+16	0.00E+00	0.00E+00	0.00E+00	4.10E+14	0.00E+00
			0.233	1	3.1	1.36	13.83	0.0002693	0.082	0.311	0.038	0.17	13.4	0.079	0.0018	0	0.0002693	0	343	1400	390	83.3	277	1.6
			0.049	0.05	0.041	0.035	0.055	0.12	0.07	0.084	0.08	0.072	0.036	0.06321	0.157760474	1	0.12	0.264	0.174	0.013	0.013	0.008594	0.008379	0.038
			2.93	2.04	4.09	11.35	15.8	3.76	2.04	3.028	3.414	1.41	2.06	3.134	4.74	20.5	3.76	0.95	4.27	38	172	13.55	9.08	3.38
			0.43	2.1	6.41	2.56	33.14	0.0002	0.171	0.517	0.0666	0.231	13.36	0.165	0.0035	0.33		70.5	767	9640	41560	7.34	2.68	3.1
			0.864	0.83		0.906		0.223	0.671	0.432	0.538	0.582			0.09									
			0.75	1.25		1.125		0.8	0.86	1	0.6	1.26			0.76									

6- unscaled sample specific ^{36}Cl production rate by spallation of target elements

spallation production rate for Ca, SLHL	PR_{Ca}	atoms ^{36}Cl (g C	42	2	Braucher et al. 2011
mass concentration of Ca in **target fraction**	C_{Ca}	q Ca (q rock)$^{-1}$	0.214	0.004	
result unscaled ^{36}Cl production by spallation of ^{40}Ca	$\mathbf{P_{s,Ca}}$	atoms ^{36}Cl (q C	8.806	0.454	
spallation production rate for K, SLHL	PR_K	atoms ^{36}Cl (g K	148.1	7.8	Schimmelpfennig et al., 2014, St scaling
mass concentration of K in **target fraction**	C_K	q K (q rock)$^{-1}$	0.000	0.000	
result unscaled ^{36}Cl production by spallation of ^{39}K	$\mathbf{P_{s,K}}$	atoms ^{36}Cl (q K	0.054	0.012	
spallation production rate for Ti, SLHL	PR_{Ti}	atoms ^{36}Cl (g T	13	3	Fink et al., 2002
mass concentration of Ti in **target fraction**	C_{Ti}	q Ti (q rock)$^{-1}$	0.000	0.000	
result unscaled ^{36}Cl production by spallation of Ti	$\mathbf{P_{s,Ti}}$	atoms ^{36}Cl (q Ti	0.001	0.001	
spallation production rate for Fe, SLHL	PR_{Fe}	atoms ^{36}Cl (g F	1.9	0.399	Stone et al., 2005
mass concentration of Fe in **target fraction**	C_{Fe}	q Fe (q rock)$^{-1}$	0.001	0.000	
result unscaled ^{36}Cl production by spallation of Fe	$\mathbf{P_{s,Fe}}$	atoms ^{36}Cl (q Fe	0.001	0.000	
result unscaled sample specific ^{36}Cl production rate by spallation of target elements	$\mathbf{P_s}$	atoms ^{36}Cl (g)	8.862	0.454	

7- unscaled sample specific ^{36}Cl production rate by capture of epithermal neutrons

| | | | | | | | | | | | | | | | | | | |

epithermal neutron diffusion length in atmosphere	$L_{eth,a}$	g cm^{-2}	4.015	
epithermal neutron flux at land/atmosphere interface that would be observed in atm if interface wa	$\phi^*_{eth,a}$	n cm^{-2} a^{-1}	12709	
difference between hypothetical equilibrium epithermal neutron fluxes in atmosphere and subsurf	$\Delta\phi^*_{eth}$	n cm^{-2} a^{-1}	-127511	
adjusted difference between hypothetical equilibrium epithermal neutron fluxes in atmosphere an	$\Delta\phi^{**}_{eth,a}$	n cm^{-2} a^{-1}	138571	
epithermal neutron diffusion length in subsurface	L_{eth}	g cm^{-2}	32.343	
difference between phi_star_eth and actual epithermal neutron flux at land surface	$(F.\Delta\phi)^*_{eth}$	-	-78875	
slow muon attenuation length	Λ_μ	g cm^{-2}	1510	
epithermal neutron flux (concentration)	$\phi_{eth,total}$	n cm^{-2} a^{-1}	68804	
result unscaled sample specific ^{36}Cl production rate by capture of epithermal neutrons	**P_{eth}**	**atoms ^{36}Cl g^{-1} a^{-1}**	**0.827**	0.24821

| | | | |

Chlorine-36 exposure age and erosion rate determination: Please follow the instructions on the first worksheet

modifications regarding muonic 36Cl production

Sample name 170829.03

1- Input

(and output for eroding surfaces)

	symbol	units	calculations	Uncertainties
element concentration in bulk rock: maior element as oxides [wt-%] and trace elements [wt-ppm]				
element concentration in target fraction: major element as oxides [wt-%] and Cl in [wt-ppm]				
uncertainty target element concentration in target fraction (oxides in [wt-%] and Cl in [wt-ppm])				
depth reference: top of sample		cm	0	
sample thickness		cm	2.5	
bulk rock density	rho	g cm^{-3}	2.7	
mass depth reference: center of sample	z	g cm^{-2}	3.375	
mass thickness	z_s	g cm^{-2}	6.75	
scaling factor for nucleonic production as a function of elevation, latitude (and temporal v	S_{eLin} , S_{eLim}	-	3.969	0.198
scaling factor for muonic production as a function of elevation, latitude (and temporal var	$S_{\mu(z)}$	-	2.084	0.104
correction factor for shielding of a sample of arbitrary orientation by surrounding topogra	S_T	-	0.983	0.00983
correction factor for geometry effects on spallogenic production	S_{shape}	-	1	0.03
correction factor for snow shielding for spallogenic production	S_{snow}	-	1	0.01
effective fast neutron attenuation coefficient	$\Lambda_{f,e}$	g cm^{-2}	160	
estimated ^{36}Cl concentration from inheritance at t_{exp}=0	$N_{inher}(0)$	atoms ^{36}Cl g^{-1}		
measured ^{36}Cl concentration in sample	N_{meas}	atoms ^{36}Cl g^{-1}	1.05E+06	7.16E+04
exposure duration (independently determined or estimated)	t_{expo}	a	14285	2113.946736
formation age of rock (independently determined or estimated) for radiogenic correction	t_{form}	a	200000000	1000
erosion rate	ε	mm ka^{-1}	0	0

bulk rock:	CaO [wt-%]	K2O [wt-%]	TiO2 [wt-%]	Fe2O3 [wt-%	Cl [ppm]	SiO2 [wt-%]	Na2O [wt-%]	MgO [wt-%]	Al2O3 [wt-%]	MnO [wt-%]	P2O5 [wt-%]	CO2 [wt-%]	H2O [wt-%]
	28.795												
target fraction:													
	29.42	0.02	0.01	0.07	125.62	0.26	0.03	21.36	0.13	0.01	0.02		1.05
	0.58	0.01	0.01	0.01	8.72	0.26	0.03	21.36	0.13	0.01	0.02		1.05

	Li [ppm]	B [ppm]	Sm [ppm]	Gd [ppm]	Th [ppm]	U [ppm]
	0.78	2.6	0.14	0.14	0.13	1.23
	0.78	2.6	0.1357	0.1442	0.1254	1.2297

	Cr [ppm]	Be [ppm]	N [ppm]	F [ppm]	S [ppm]	Sc [ppm]	Co [ppm]	Ni [ppm]	Se [ppm]	Br [ppm]	Rb [ppm]	Sr [ppm]	Zr [ppm]	Mo [ppm]	Ru [ppm]	Te [ppm]	I [ppm]	Cs [ppm]	Ba [ppm]
	2.13	0.00				0.13	0.19	0.00			1.56	76.63	1.76	0.00				0.11	0.00
	2.134	0				0.13	0.19	0.00			1.56	76.63	1.76	0.00				0.11	0.00

2- Output A: exposure age of sample (only for uneroded surface)

decay constant for ^{36}Cl	λ_{36}	a^{-1}	2.30E-06	1.51998E-08
scaled total sample specific ^{36}Cl production rate without radiogenic	P_{total}	atoms ^{36}Cl g^{-1} a	71.6	9.1
time factor radiogenic	t_i		434216	2865.8
calculated concentration of radiogenically produced ^{36}Cl atoms for estimated age	N_i	atoms ^{36}Cl g^{-1}	38352.0	1934.2
estimated ^{36}Cl concentration from inheritance at time of sampling	$N_{inher}(t)$	atoms ^{36}Cl g^{-1}	0.0	
measured ^{36}Cl concentration in sample corrected from radiogenic component and inheritance	$N_{meas-r-inher}$	atoms ^{36}Cl g^{-1}	1.01E+06	71599.5
exposure age of sample	**t**	**a**	14285	1013

3- Output B: eroding surface

calculated ^{36}Cl concentration for an eroding sample	$N_{calc,total}$	atoms ^{36}Cl g^{-1}	1.05E+06
difference measured/calculated ^{36}Cl concentration in eroding sample	$\Delta N_{meas-calc}$		0.00%
erosion rate	ε	cm a^{-1}	0
time factor with erosion for spallation reaction	$t_{cosm,s}$		14053
time factor with erosion for capture of epithermal neutrons	$t_{cosm,eth}$		14053
time factor with erosion for capture of thermal neutrons	$t_{cosm,th}$		14053
time factor with erosion for capture of slow negative muons	$t_{cosm,\mu}$		14053
depth reference factor for spallogenic reaction	d_s		0.979
depth reference factor for capture of epithermal neutrons	d_{eth}		0.876
depth reference factor for capture of thermal neutrons	d_{th}		0.944
depth reference factor for capture of slow negative muons	d_μ		0.998
production rate coefficient corrected for sample thickness for spallogenic reaction	J_{Cs}		45.99
production rate coefficient corrected for sample thickness for capture of epithermal neutrons	J_{Ceth}		2.13
production rate coefficient corrected for sample thickness for capture of thermal neutrons	J_{Cth}		-33.05
production rate coefficient corrected for sample thickness for capture of slow negative muons	$J_{C\mu}$		2.67
production rate coefficient for spallogenic reaction	J_s		46.02
production rate coefficient for capture of epithermal neutrons	J_{eth}		2.13
production rate coefficient for capture of thermal neutrons	J_{th}		-33.07
production rate coefficient for capture of slow negative muons	J_μ		2.67

4- Output C: calculated ^{36}Cl contributions from all production mechanism

time factor cosmogenic without erosion	t_{cosm}		14053	2046
calculated ^{36}Cl concentration for given time + radiogenic	$N_{calc,total}$	atoms ^{36}Cl g^{-1}	1.05E+06	194483
difference measured/calculated ^{36}Cl concentration	$\Delta N_{meas-calc}$		0.00%	
contribution from each production mechanism:				
number of atoms ^{36}Cl per g by spallation of Ca	$N_{s,Ca}$	atoms ^{36}Cl g^{-1}	474336	45.39%
number of atoms ^{36}Cl per g by spallation of K	$N_{s,K}$	atoms ^{36}Cl g^{-1}	1254	0.12%
number of atoms ^{36}Cl per g by spallation of Ti	$N_{s,Ti}$	atoms ^{36}Cl g^{-1}	21	0.00%
number of atoms ^{36}Cl per g by spallation of Fe	$N_{s,Fe}$	atoms ^{36}Cl g^{-1}	46	0.00%
number of atoms ^{36}Cl per g by spallation of target elements	N_s	atoms ^{36}Cl g^{-1}	475657	45.52%
number of atoms ^{36}Cl per g by capture of thermal neutrons	N_{th}	atoms ^{36}Cl g^{-1}	366820	35.10%
number of atoms ^{36}Cl per g by capture of epithermal neutrons	N_{eth}	atoms ^{36}Cl g^{-1}	81609	7.81%
number of atoms ^{36}Cl per g by capture of thermal and epithermal neutrons	N_n	atoms ^{36}Cl g^{-1}	448429	42.91%
number of atoms ^{36}Cl per g by capture of slow negative muons	N_μ	atoms ^{36}Cl g^{-1}	82608	7.90%
number of atoms ^{36}Cl per g by radiogenic production	N_i	atoms ^{36}Cl g^{-1}	38352	3.67%
				100.00%

5- elemental parameters

			Ca	K	Ti	Fe	Cl	O, rock	Si	Na	Mg	Al	Mn	P	C	H	O, water	Li	B	Sm	Gd	Th	U	Cr	Be	N	F	S	Sc	Co	Ni	Se	Br	Rb	Sr	Zr	Mo	Ru	Te	I	Cs	Ba
element concentration [wt-ppm] **bulk rock**		ppm	213034	158	30	454	110	172122	1214	186	128771	661	94	87	0	1175	9387	0.78	2.6	0.1	0.1	0.1254	1.2297	2.134	0	0	0	0	0.13	0.1875	0	0	0	1.5626	76.6323	1.7613	0	0	0	0	0.1073	0
element concentration dissolved sample (wt-ppm) in **target fraction**		ppm	210342	158	30	454	126	171049	1214	186	128771	661	94	87	0	1175	9387	0.78	2.6	0.1357	0.1442	0.1254	1.2297	2.134	0	0	0	0	0.13	0.1875	0	0	0	1.5626	76.6323	1.7613	0	0	0	0	0.1073	0
atomic mass of element k (Reference: http://www.ciaaw.org/atomic-weights.htm)	A_k	g mol^{-1}	40.078	39.0983	47.867	55.845	35.453	15.999	28.085	22.98977	24.305	26.981538	54.938043	30.973761	12.01	1.008	15.999	6.941	10.811	150.36	157.25	232.0377	238.02891	51.9961	9.012182	14.0067	18.998403	32.065	44.95591	58.9332	58.6934	78.96	79.904	85.4678	87.62	91.224	95.94	101.07	127.6	126.90447	132.90545	137.327
avoqadro			6.02E+23																																							
atomic concentration of element k in **bulk rock**	N_k	atoms g^{-1}	1.35E+22	3.20E+21	2.43E+18	3.77E+17	4.90E+18	1.87E+18	6.48E+21	2.60E+19	4.86E+18	3.19E+21	1.48E+19	1.03E+18	1.70E+18	0.00E+00	2.60E+20	3.53E+20	6.77E+16	1.45E+17	5.43E+14	5.52E+14	3.25E+14	3.11E+15	2.47E+16	0.00E+00	0.00E+00	0.00E+00	0.00E+00	1.74E+15	1.92E+15	0.00E+00	0.00E+00	0.00E+00	1.10E+16	5.27E+17	1.16E+16	0.00E+00	0.00E+00	0.00E+00	0.00E+00	4.86E+14	0.00E+00
atomic concentration of element k in **target fraction**	N_{Cl}	atoms g^{-1}						#########																																			
dilute resonance integral for absorption of epithermal neutrons by element k	$I_{0,k}$	E^{-24} cm^2		0.233	1	3.1	1.36	13.83	0.0002693	0.082	0.311	0.038	0.17	13.4	0.079	0.0018	0	0.0002693	0	343	1400	390	83.3	277	1.6																	
average log decrement of energy loss per collision for element k	x_k	-		0.049	0.05	0.041	0.035	0.055	0.12	0.07	0.084	0.08	0.072	0.036	0.06321	0.15776047	1	0.12	0.264	0.174	0.013	0.013	0.008594	0.008379	0.038																	
neutron scattering cross section of element k	$\sigma_{s,k}$	E^{-24} cm^2		2.93	2.04	4.09	11.35	15.8	3.76	2.04	3.036	3.414	1.41	2.66	3.134	4.74	20.5	3.76	0.95	4.27	38	172	13.55	9.08	3.38																	
thermal neutron absorption cross section of element k	$\sigma_{a,k}$	E^{-24} cm^2		0.43	2.1	6.41	2.56	33.14	0.0002	0.171	0.517	0.0666	0.231	13.36	0.165	0.0035	0.33		70.5	767	9640	41560	7.34	2.68	3.1																	
proportion of muons stopped in element i that are captured by the nucleus	f_{cik}			0.864	0.83		0.906		0.223	0.671	0.432	0.538	0.582			0.09																											
average neutron yield per captured muon	Y_k			0.75	1.25		1.125		0.8	0.86	1	0.6	1.26			0.76																											

6- unscaled sample specific ^{36}Cl production rate by spallation of target elements

spallation production rate for Ca, SLHL	PR_{Ca}	atoms ^{36}Cl (g C	42		Braucher et al. 2011
mass concentration of Ca in **target fraction**	C_{Ca}	g Ca (g rock)$^{-1}$	0.210	0.004	
result unscaled ^{36}Cl production by spallation of ^{40}Ca	$\mathbf{P_{s,Ca}}$	atoms ^{36}Cl (g C	8.650	0.445	
spallation production rate for K, SLHL	PR_K	atoms ^{36}Cl (g K	148.1	7.8	Schimmelpfennig et al., 2014, St scaling
mass concentration of K in **target fraction**	C_K	g K (g rock)$^{-1}$	0.000	0.000	
result unscaled ^{36}Cl production by spallation of ^{39}K	$\mathbf{P_{s,K}}$	atoms ^{36}Cl (g K	0.023	0.012	
spallation production rate for Ti, SLHL	PR_{Ti}	atoms ^{36}Cl (g T	13		Fink et al., 2002
mass concentration of Ti in **target fraction**	C_{Ti}	g Ti (g rock)$^{-1}$	0.000	0.000	
result unscaled ^{36}Cl production by spallation of Ti	$\mathbf{P_{s,Ti}}$	atoms ^{36}Cl (g Ti	0.000	0.001	
spallation production rate for Fe, SLHL	PR_{Fe}	atoms ^{36}Cl (g F	1.9	0.288	Stone et al., 2005
mass concentration of Fe in **target fraction**	C_{Fe}	g Fe (g rock)$^{-1}$	0.000	0.000	
result unscaled ^{36}Cl production by spallation of Fe	$\mathbf{P_{s,Fe}}$	atoms ^{36}Cl (g Fe	0.001	0.000	
result unscaled sample specific ^{36}Cl production rate by spallation of target elements	$\mathbf{P_s}$	atoms ^{36}Cl (g)$^{-1}$	8.674	0.445	

7- unscaled sample specific ^{36}Cl production rate by capture of epithermal neutrons

effective macroscopic resonance integral for absorption of epithermal neutrons	I_{eff}	cm^2 g^{-1}	0.0010		
fraction of epithermal neutrons absorbed by ^{35}Cl (**target fraction**)	f_{eth}	-	0.0302		
neutron macroscopic scattering cross section in subsurface	Σ_{scl}	cm^2 g^{-1}	0.0515		
scattering rate parameter	B		9.75E-03		
mean macroscopic log decrement of energy loss per collision in subsurface	X_{sk}		0.189		
macroscopic absorption and moderation cross section for epithermal neutrons	Σ_{ath}	cm^2 g^{-1}	0.010		
attenuation length for absorption and moderation of epithermal neutron flux	Λ_{ath}	g cm^{-2}	100.616		
	$A_a * N_k$	atoms mol^{-1}	3.12E+23	1.28E+23	9.50E+19	1.81E+19	2.74E+20	6.62E+19	1.04E+23	7.31E+20	1.12E+20	7.75E+22	3.98E+20	5.64E+19		0.00E+00	2.62E+20		4.70E+17	1.57E+18	8.17E+16	8.68E+16		1.29E+18																	
average atomic weight in subsurface	A_{ss}	g mol^{-1}	23.002																																						
production rate of epithermal neutrons from fast neutrons in atmosphere at land/atm interface	$P_n(0)$	n cm^{-2} a^{-1}	696	185	Marrero et al. 2016, St scaling																																					
Ratio of epithermal neutron production in subsurface to that in atmosphere	R_{eth}	-	1.26																																					
epithermal neutron diffusion coefficient in subsurface	D_{eth}	g cm^{-2}	6.67																																					
apparent fast neutron attenuation coefficient	Λ_f	g cm^{-2}	160																																					
epithermal neutron flux at land/atmosphere interface that would be observed in ss if interface was	$\phi*_{eth}$	n cm^{-2} a^{-1}	90576																																					
average neutron yield per stopped negative muon	Y_μ		0.401	0.262	0.000		0.001		0.058	0.001	0.000	0.078	0.001			0.000																									
slow negative muon stopping rate at land surface SLHL	$\Psi_\mu(0)$	μ g^{-1} a^{-1}	190																																					
fast muon flux at land surface SLHL	$\phi_{\mu 0}$	μ cm^{-2} a^{-1}	7.90E+05																																					
total muon induced neutron production at land surface	$P_{n\mu 0}$	μ cm^{-2} a^{-1}	80.840																																					
ratio of muon production rate to epithermal neutron production rate	R_μ	-	0.048																																					
macroscopic neutron scattering cross section of atmosphere	$\Sigma_{scl,a}$	cm^2 g^{-1}	0.3773																																					
thermal neutron diffusion coefficient in atmosphere	D_a	g cm^{-2}	0.926																																					
macroscopic absorption and moderation cross section for epithermal neutrons in atmosphere	$\Sigma_{ath,a}$	cm^2 g^{-1}	0.0548																																					

epithermal neutron diffusion length in atmosphere	$L_{eth,a}$	g cm^{-2}	4.015	
epithermal neutron flux at land/atmosphere interface that would be observed in atm if interface we	$\phi^*_{eth,a}$	n cm^{-2} a^{-1}	12709	
difference between hypothetical equilibrium epithermal neutron fluxes in atmosphere and subsurf	$\Delta\phi^*_{eth}$	n cm^{-2} a^{-1}	-77867	
adjusted difference between hypothetical equilibrium epithermal neutron fluxes in atmosphere an	$\Delta\phi^{**}_{eth,a}$	n cm^{-2} a^{-1}	88811	
epithermal neutron diffusion length in subsurface	L_{eth}	g cm^{-2}	25.525	
difference between phi_star_eth and actual epithermal neutron flux at land surface	$(\Gamma.\Delta\phi)^*_{eth}$	-	-44035	
slow muon attenuation length	Λ_μ	g cm^{-2}	1510	
epithermal neutron flux (concentration)	$\phi_{eth,total}$	n cm^{-2} a^{-1}	52128	
result unscaled sample specific ^{36}Cl production rate by capture of epithermal neutrons	$\mathbf{P_{eth}}$	**atoms ^{36}Cl g^{-1}**	**1.492**	0.44747

| **8- unscaled sample specific ^{36}Cl production rate by capture of thermal neutrons** | | | |

Chlorine-36 exposure age and erosion rate determination: Please follow the instructions on the first worksheet

modifications regarding muonic 36Cl production

Sample name 170830.01

1- Input

(and output for eroding surfaces)

	symbol	units	calculations	Uncertainties
element concentration in bulk rock: maior element as oxides [wt-%] and trace elements [wt-ppm]				
element concentration in target fraction: major element as oxides [wt-%] and Cl in [wt-ppm]				
uncertainty target element concentration in target fraction (oxides in [wt-%] and Cl in [wt-ppm])				
depth reference: top of sample		cm	0	
sample thickness		cm	3.8	
bulk rock density	rho	g cm^{-3}	2.7	
mass depth reference: center of sample	z	g cm^{-2}	5.13	
mass thickness	z_s	g cm^{-2}	10.26	
scaling factor for nucleonic production as a function of elevation, latitude (and temporal v	S_{eLin} , S_{eLsc}	-	5.167	0.258
scaling factor for muonic production as a function of elevation, latitude (and temporal var	$S_{\mu(z)}$	-	2.420	0.121
correction factor for shielding of a sample of arbitrary orientation by surrounding topogra	S_T	-	0.966	0.00966
correction factor for geometry effects on spallogenic production	S_{shape}	-	1	0.03
correction factor for snow shielding for spallogenic production	S_{snow}	-	1	0.01
effective fast neutron attenuation coefficient	$\Lambda_{f,e}$	g cm^{-2}	160	
estimated ^{36}Cl concentration from inheritance at t_{exp}=0	$N_{inher}(0)$	atoms ^{36}Cl g^{-1}		
measured ^{36}Cl concentration in sample	N_{meas}	atoms ^{36}Cl g^{-1}	1.85E+06	2.01E+05
exposure duration (independently determined or estimated)	t_{expo}	a	14411	2839.3861
formation age of rock (independently determined or estimated) for radiogenic correction	t_{form}	a	200000000	1000
erosion rate	ε	mm ka^{-1}	0	0

bulk rock:	CaO [wt-%]	K2O [wt-%]	TiO2 [wt-%]	Fe2O3 [wt-%]	Cl [ppm]	SiO2 [wt-%]	Na2O [wt-%]	MgO [wt-%]	Al2O3 [wt-%]	MnO [wt-%]	P2O5 [wt-%]	CO2 [wt-%]	H2O [wt-%]	Li [ppm]	B [ppm]	Sm [ppm]	Gd [ppm]	Th [ppm]	U [ppm]	Cr [ppm]	Be [ppm]	N [ppm]	F [ppm]	S [ppm]	Sc [ppm]	Co [ppm]	Ni [ppm]	Se [ppm]	Br [ppm]	Rb [ppm]	Sr [ppm]	Zr [ppm]	Mo [ppm]	Ru [ppm]	Te [ppm]	I [ppm]	Cs [ppm]	Ba [ppm]
30.345	0.01	0.00	0.04	215		0.00	0.03	21.65	0.03	0.01	0.00		0.42	0.7	0	0.07	0.08	0.04	0.48	1.77	0.00				0.09	0.09	0.00			0.16	79.91	0.00	0.00				0.00	0.00
target fraction:																																						
28.49	0.01	0.00	0.04	227.19		0.00	0.03	21.65	0.03	0.01	0.00		0.42	0.7	0	0.0707	0.0774	0.0409	0.4828	1.7663	0	0	0	0	0.09	0.0945	0	0	0	0.1633	79.9122	0	0	0	0	0.00	0.00
0.68	0.01	0.01	0.01	26.07																																		

2- Output A: exposure age of sample (only for uneroded surface)

decay constant for ^{36}Cl	λ_{36}	a^{-1}	2.30E-06	1.51998E-08
scaled total sample specific ^{36}Cl production rate without radiogenic	P_{total}	atoms ^{36}Cl g^{-1} a	128.3	20.3
time factor radiogenic	t_i		434216	2865.8
calculated concentration of radiogenically produced ^{36}Cl atoms for estimated age	N_i	atoms ^{36}Cl g^{-1}	28573.7	1441.1
estimated ^{36}Cl concentration from inheritance at time of sampling	$N_{inher}(t)$	atoms ^{36}Cl g^{-1}	0.0	
measured ^{36}Cl concentration in sample corrected from radiogenic component and inheritance	$N_{meas-r-inher}$	atoms ^{36}Cl g^{-1}	1.82E+06	200833.9
exposure age of sample	**t**	**a**	14411	2839

3- Output B: eroding surface

calculated ^{36}Cl concentration for an eroding sample	$N_{calc,total}$	atoms ^{36}Cl g^{-1}	1.85E+06
difference measured/calculated ^{36}Cl concentration in eroding sample	$\Delta N_{meas-calc}$		0.00%
erosion rate	ε	cm a^{-1}	0
time factor with erosion for spallation reaction	$t_{cosm,s}$		14174
time factor with erosion for capture of epithermal neutrons	$t_{cosm,eth}$		14174
time factor with erosion for capture of thermal neutrons	$t_{cosm,th}$		14174
time factor with erosion for capture of slow negative muons	$t_{cosm,\mu}$		14174
depth reference factor for spallogenic reaction	d_s		0.968
depth reference factor for capture of epithermal neutrons	d_{eth}		0.854
depth reference factor for capture of thermal neutrons	d_{th}		0.921
depth reference factor for capture of slow negative muons	d_μ		0.997
production rate coefficient corrected for sample thickness for spallogenic reaction	$J_{Cl,s}$		82.36
production rate coefficient corrected for sample thickness for capture of epithermal neutrons	$J_{Cl,eth}$		7.66
production rate coefficient corrected for sample thickness for capture of thermal neutrons	$J_{Cl,th}$		-69.54
production rate coefficient corrected for sample thickness for capture of slow negative muons	$J_{Cl,\mu}$		3.54
production rate coefficient for spallogenic reaction	J_s		82.49
production rate coefficient for capture of epithermal neutrons	J_{eth}		7.66
production rate coefficient for capture of thermal neutrons	J_{th}		-69.64
production rate coefficient for capture of slow negative muons	J_μ		3.54

4- Output C: calculated ^{36}Cl contributions from all production mechanism

time factor cosmogenic without erosion	t_{cosm}		14174	2737
calculated ^{36}Cl concentration for given time + radiogenic	$N_{calc,total}$	atoms ^{36}Cl g^{-1}	1.85E+06	454130
difference measured/calculated ^{36}Cl concentration	$\Delta N_{meas-calc}$		0.00%	
contribution from each production mechanism:				
number of atoms ^{36}Cl per g by spallation of Ca	$N_{s,Ca}$	atoms ^{36}Cl g^{-1}	605625	33.79%
number of atoms ^{36}Cl per g by spallation of K	$N_{s,K}$	atoms ^{36}Cl g^{-1}	589	0.03%
number of atoms ^{36}Cl per g by spallation of Ti	$N_{s,Ti}$	atoms ^{36}Cl g^{-1}	11	0.00%
number of atoms ^{36}Cl per g by spallation of Fe	$N_{s,Fe}$	atoms ^{36}Cl g^{-1}	39	0.00%
number of atoms ^{36}Cl per g by spallation of target elements	N_s	atoms ^{36}Cl g^{-1}	606263	32.83%
number of atoms ^{36}Cl per g by capture of thermal neutrons	N_{th}	atoms ^{36}Cl g^{-1}	863441	46.75%
number of atoms ^{36}Cl per g by capture of epithermal neutrons	N_{eth}	atoms ^{36}Cl g^{-1}	252164	13.65%
number of atoms ^{36}Cl per g by capture of thermal and epithermal neutrons	N_n	atoms ^{36}Cl g^{-1}	1115605	60.40%
number of atoms ^{36}Cl per g by capture of slow negative muons	N_μ	atoms ^{36}Cl g^{-1}	96497	5.22%
number of atoms ^{36}Cl per g by radiogenic production	N_i	atoms ^{36}Cl g^{-1}	28574	1.55%
				100.00%

5- elemental parameters

			Ca	K	Ti	Fe	Cl	O, rock	Si	Na	Mg	Al	Mn	P	C	H	O, water	Li	B	Sm	Gd	Th	U	Cr	Be	N	F	S	Sc	Co	Ni	Se	Br	Rb	Sr	Zr	Mo	Ru	Te	I	Cs	Ba
element concentration [wt-ppm] **bulk rock**		ppm	216967	58	12	301	215	172829	0	230	130550	159	86	0	0	470	3755	0.7	0.0	0.1	0.1	0.0409	0.4828	1.7663	0	0	0	0	0.09	0.0945	0	0	0	0.1633	79.9122	0	0	0	0	0	0
element concentration dissolved sample [wt-ppm] in **target fraction**		ppm	210833	58	12	301	227	170384	0	230	130550	159	86	0	0	470	3755	0.7	0	0.0707	0.0774	0.0409	0.4828	1.7663	0	0	0	0	0.09	0.0945	0	0	0	0.1633	79.9122	0	0	0	0	0	0
atomic mass of element k (Reference: http://www.ciaaw.org/atomic-weights.htm)	A_k	g mol^{-1}	40.078	39.0983	47.867	55.845	35.453	15.999	28.085	22.98977	24.305	26.981538	54.938043	30.973761	12.01	1.008	15.999	6.941	10.811	150.36	157.25	232.0377	238.02891	51.9961	9.012182	14.0067	18.998403	32.065	44.95591	58.9332	58.6934	78.96	79.904	85.4678	87.62	91.224	95.94	101.07	127.6	126.90447	132.90545	137.327
avoqadro			6.02E+23																																						
atomic concentration of element k in **bulk rock**	N_k	atoms g^{-1}	1.33E+22	3.26E+21	8.95E+17	1.51E+17	3.24E+18	3.65E+18	6.51E+21	0.00E+00	6.03E+18	3.23E+21	3.54E+18	9.42E+17	0.00E+00	0.00E+00	1.04E+20	1.41E+20	6.07E+16	0.00E+00	2.83E+14	2.96E+14	1.06E+14	1.22E+15	2.05E+16	0.00E+00	0.00E+00	0.00E+00	0.00E+00	1.21E+15	9.66E+14	0.00E+00	0.00E+00	0.00E+00	1.15E+15	5.49E+17	0.00E+00	0.00E+00	0.00E+00	0.00E+00	0.00E+00	0.00E+00
atomic concentration of element k in **target fraction**	N_{Cl}	atoms g^{-1}					########																																			
dilute resonance integral for absorption of epithermal neutrons by element k	$I_{0,k}$	E^{-04} cm^2		0.233	1	3.1	1.36	13.83	0.0002693	0.082	0.311	0.038	0.17	13.4	0.079	0.0018	0	0.0002693	0	343	1400	390	83.3	277	1.6																
average log decrement of energy loss per collision for element k	x_k	-		0.049	0.05	0.041	0.035	0.055	0.12	0.07	0.084	0.08	0.072	0.036	0.06321	0.1577605	1	0.12	0.264	0.174	0.013	0.013	0.008594	0.008379	0.038																
neutron scattering cross section of element k	$\sigma_{scat,k}$	E^{-24} cm^2		2.93	2.04	4.09	11.35	15.8	3.76	2.04	3.038	1.414	1.41	2.06	3.134	4.74	20.5	3.76	0.95	4.27	38	172	13.55	9.08	3.38																
thermal neutron absorption cross section of element k	$\sigma_{a,k}$	E^{-24} cm^2		0.43	2.1	6.41	2.56	33.14	0.0002	0.171	0.517	0.0666	0.231	13.36	0.165	0.0035	0.33		70.5	767	9640	41560	7.34	2.68	3.1																
proportion of muons stopped in element i that are captured by the nucleus	f_{cik}			0.864	0.83		0.906		0.223	0.671	0.432	0.538	0.582			0.09																										
average neutron yield per captured muon	Y_k			0.75	1.25		1.125		0.8	0.86	1	0.6	1.26			0.76																										

6- unscaled sample specific ^{36}Cl production rate by spallation of target elements

spallation production rate for Ca, SLHL	PR_{Ca}	atoms ^{36}Cl (g C	42		Braucher et al. 2011
mass concentration of Ca in **target fraction**	C_{Ca}	g Ca (g rock)$^{-1}$	0.211	0.004	
result unscaled ^{36}Cl production by spallation of ^{40}Ca	$\mathbf{P_{s,Ca}}$	atoms ^{36}Cl (g C	8.576	0.441	
spallation production rate for K, SLHL	PR_K	atoms ^{36}Cl (g K	148.1	7.5	Schimmelpfennig et al., 2014, St scaling
mass concentration of K in **target fraction**	C_K	g K (g rock)$^{-1}$	0.000	0.000	
result unscaled ^{36}Cl production by spallation of ^{39}K	$\mathbf{P_{s,K}}$	atoms ^{36}Cl (g K	0.008	0.012	
spallation production rate for Ti, SLHL	PR_{Ti}	atoms ^{36}Cl (g T	13		Fink et al., 2002
mass concentration of Ti in **target fraction**	C_{Ti}	g Ti (g rock)$^{-1}$	0.000	0.000	
result unscaled ^{36}Cl production by spallation of Ti	$\mathbf{P_{s,Ti}}$	atoms ^{36}Cl (g Ti	0.000	0.001	
spallation production rate for Fe, SLHL	PR_{Fe}	atoms ^{36}Cl (g F	1.9	0.285	Stone et al., 2005
mass concentration of Fe in **target fraction**	C_{Fe}	g Fe (g rock)$^{-1}$	0.000	0.000	
result unscaled ^{36}Cl production by spallation of Fe	$\mathbf{P_{s,Fe}}$	atoms ^{36}Cl (g Fe	0.001	0.000	
result unscaled sample specific ^{36}Cl production rate by spallation of target elements	$\mathbf{P_s}$	atoms ^{36}Cl (g)$^{-1}$	8.585	0.442	

7- unscaled sample specific ^{36}Cl production rate by capture of epithermal neutrons

						Ca	K	Ti	Fe	Cl	O, rock	Si	Na	Mg	Al	Mn	P	C	H	O, water	Li	B	Sm	Gd	Th	U	Cr	Be	N	F	S	Sc	Co	Ni	Se	Br	Rb	Sr	Zr	Mo	Ru	Te	I	Cs	Ba
effective macroscopic resonance integral for absorption of epithermal neutrons	I_{eff}	cm^2 g^{-1}	0.0010		7.60E-04	8.95E-07	4.68E-07	4.41E-06	5.05E-05	1.75E-06	0.00E+00	1.87E-06	1.23E-04	6.02E-07	1.26E-05		0.00E+00	0.00E+00		0.00E+00	0.00E+00	3.96E-07	1.16E-07		3.27E-08																			
fraction of epithermal neutrons absorbed by ^{35}Cl (**target fraction**)	f_{eth}	-	0.0558																																								
neutron macroscopic scattering cross section in subsurface	Σ_{scl}	cm^2 g^{-1}	0.0478		9.55E-03	1.83E-06	6.17E-07	3.68E-05	5.77E-05	2.45E-02	0.00E+00	1.83E-05	1.10E-02	4.99E-06	1.94E-06	0.00E+00	0.00E+00	2.13E-03	5.31E-04	5.77E-08	0.00E+00	1.08E-08	5.10E-08	1.44E-09	1.11E-08	6.91E-08	0.00E+00	0.00E+00	0.00E+00	0.00E+00	0.00E+00	0.00E+00	0.00E+00	0.00E+00	0.00E+00	0.00E+00	0.00E+00	0.00E+00	0.00E+00	0.00E+00	0.00E+00	0.00E+00	0.00E+00	0.00E+00
scattering rate parameter	B		6.49E-03		4.68E-04	9.13E-08	2.53E-08	1.29E-06	3.17E-06	2.94E-03	0.00E+00	1.54E-06	8.83E-04	3.60E-07	6.98E-08	0.00E+00	0.00E+00	2.13E-03	6.38E-05	1.52E-08	0.00E+00	1.40E-10	6.63E-10	1.24E-11	9.29E-11	2.63E-09	0.00E+00	0.00E+00	0.00E+00	0.00E+00	0.00E+00	0.00E+00	0.00E+00	0.00E+00	0.00E+00	0.00E+00	0.00E+00	0.00E+00	0.00E+00	0.00E+00	0.00E+00	0.00E+00	0.00E+00	0.00E+00
mean macroscopic log decrement of energy loss per collision in subsurface	X_{ss}		0.136																																							
macroscopic absorption and moderation cross section for epithermal neutrons	Σ_{ath}	cm^2 g^{-1}	0.007																																							
attenuation length for absorption and moderation of epithermal neutron flux	λ_{ath}	g cm^{-2}	151.092																																							
	$A_a * N_k$	atoms mol^{-1}	3.14E+23		1.31E+23	3.50E+19	7.23E+18	1.81E+20	1.29E+20	1.04E+23	0.00E+00	1.39E+20	7.86E+22	9.56E+19	5.17E+19		0.00E+00	1.05E+20		4.22E+17	0.00E+00	4.26E+16	4.66E+16		1.06E+18																			
average atomic weight in subsurface	A_{ss}	g mol^{-1}	23.680																																							
production rate of epithermal neutrons from fast neutrons in atmosphere at land/atm interface	$P_n(0)$	n cm^{-2} a^{-1}	696	185	Marrero et al. 2016, St scaling																																						
Ratio of epithermal neutron production in subsurface to that in atmosphere	R_{eth}	-	1.28																																							
epithermal neutron diffusion coefficient in subsurface	D_{eth}	g cm^{-2}	7.17																																							
apparent fast neutron attenuation coefficient	λ_f	g cm^{-2}	160																																							
epithermal neutron flux at land/atmosphere interface that would be observed in ss if interface was	$\phi_{*,eth}$	n cm^{-2} a^{-1}	140324																																							
average neutron yield per stopped negative muon	Y_μ		0.407		0.268	0.000		0.001		0.059	0.000	0.000	0.079	0.000		0.000																												
slow negative muon stopping rate at land surface SLHL	$\Psi_\mu(0)$	μ g^{-1} a^{-1}	190																																							
fast muon flux at land surface SLHL	$\phi_{\mu 0}$	μ cm^{-2} a^{-1}	7.90E+05																																							
total muon induced neutron production at land surface	$P_{n\mu 0}$	μ cm^{-2} a^{-1}	81.920																																							
ratio of muon production rate to epithermal neutron production rate	R_μ	-	0.043																																							
macroscopic neutron scattering cross section of atmosphere	$\Sigma_{scl,a}$	cm^2 g^{-1}	0.3773																																							
thermal neutron diffusion coefficient in atmosphere	D_a	g cm^{-2}	0.926																																							
macroscopic absorption and moderation cross section for epithermal neutrons in atmosphere	$\Sigma_{ath,a}$	cm^2 g^{-1}	0.0548																																							

epithermal neutron diffusion length in atmosphere	$L_{eth,a}$	g cm^{-2}	4.015	
epithermal neutron flux at land/atmosphere interface that would be observed in atm if interface wa	$\phi^*_{eth,a}$	n cm^{-2} a^{-1}	12709	
difference between hypothetical equilibrium epithermal neutron fluxes in atmosphere and subsurf	$\Delta\phi^*_{eth}$	n cm^{-2} a^{-1}	-127615	
adjusted difference between hypothetical equilibrium epithermal neutron fluxes in atmosphere an	$\Delta\phi^{**}_{eth,a}$	n cm^{-2} a^{-1}	138682	
epithermal neutron diffusion length in subsurface	L_{eth}	g cm^{-2}	32.446	
difference between phi_star_eth and actual epithermal neutron flux at land surface	$(F.\Delta\phi)^*_{eth}$	-	-78934	
slow muon attenuation length	Λ_μ	g cm^{-2}	1510	
epithermal neutron flux (concentration)	$\phi_{eth,total}$	n cm^{-2} a^{-1}	70827	
result unscaled sample specific ^{36}Cl production rate by capture of epithermal neutrons	$\mathbf{P_{eth}}$	**atoms ^{36}Cl g^{-1} a^{-1}**	**3.585**	1.07551

| **8- unscaled sample specific ^{36}Cl production rate by capture of thermal neutrons** | | | |

Chlorine-36 exposure age and erosion rate determination: Please follow the instructions on the first worksheet

modifications regarding muonic 36Cl production

Sample: nam 170830.02

1- Input

(and output for eroding surfaces)

	symbol	units	calculation	Uncertainties
element concentration in bulk rock: major element as oxides [wt-%] and trace elements [wt-ppm]				
element concentration in target fraction: major element as oxides [wt-%] and Cl in [wt-pom]				
uncertainty target element concentration in target fraction (oxides in [wt-%] and Cl in [wt-ppm])				
depth reference: top of sample		cm	0	
sample thickness		cm	2.5	
bulk rock density	rho	g cm^{-3}	2.7	
mass depth reference: center of sample	z	g cm^{-2}	3.375	
mass thickness	z_s	g cm^{-2}	6.75	
scaling factor for nucleonic production as a function of elevation, latitude (and temporal v	$S_{el,a}$, $S_{el,n}$	-	5.364	0.268
scaling factor for muonic production as a function of elevation, latitude (and temporal var	$S_{el,\mu}$	-	2.475	0.124
correction factor for shielding of a sample of arbitrary orientation by surrounding topogra	S_T	-	0.95	0.0095
correction factor for geometry effects on spallogenic production	S_{shape}	-	1	0.03
correction factor for snow shielding for spallogenic production	S_{snow}	-	1	0.01
effective fast neutron attenuation coefficient	$\Lambda_{f,e}$	g cm^{-2}	160	
estimated ^{36}Cl concentration from inheritance at t_{expo}=0	$N_{inher}(0)$	atoms ^{36}Cl g^{-1}		
measured ^{36}Cl concentration in sample	N_{meas}	atoms ^{36}Cl g^{-1}	4.78E+05	2.43E+04
exposure duration (independently determined or estimated)	t_{expo}	a	6342	614.963238
formation age of rock (independently determined or estimated) for radiogenic correction	t_{form}	a	200000000	1000
erosion rate	ε	mm ka^{-1}	0	0

bulk rock:

CaO [wt-%]	K2O [wt-%]	TiO2 [wt-%]	Fe2O3 [wt-%]	Cl [ppm]	SiO2 [wt-%]	Na2O [wt-%]	MgO [wt-%]	Al2O3 [wt-%]	MnO [wt-%]	P2O5 [wt-%]	CO2 [wt-%]	H2O [wt-%]
27.865	1.29	0.07	0.36	33	6.22	0.09	19.23	1.84	0.03	0.00		0.51

target fraction:

30.08	1.29	0.07	0.36	50.63	6.22	0.09	19.23	1.84	0.03	0.00		0.51
0.30	0.01	0.01	0.01	1.73								

Li [ppm]	B [ppm]	Sm [ppm]	Gd [ppm]	Th [ppm]	U [ppm]
2.54	8.6	0.88	0.77	1.59	1.55
2.54	8.6	0.8782	0.7674	1.5924	1.5519

Cr [ppm]	Be [ppm]	N [ppm]	F [ppm]	S [ppm]	Sc [ppm]	Co [ppm]	Ni [ppm]	Se [ppm]	Br [ppm]	Rb [ppm]	Sr [ppm]	Zr [ppm]	Mo [ppm]	Ru [ppm]	Te [ppm]	I [ppm]	Cs [ppm]	Ba [ppm]
5.09	0.13				1.13	1.17	0.00			17.85	76.29	19.89	0.00				0.61	40.43
5.0879	0.1261				1.13	1.17	0.00			17.85	76.29	19.89	0.00				0.61	40.43

2- Output A: exposure age of sample (only for uneroded surface)

decay constant for ^{36}Cl	λ_{36}	a^{-1}	2.30E-06	1.52E-08
scaled total sample specific ^{36}Cl production rate without radiogenic	P_{total}	atoms ^{36}Cl g^{-1} a	73.3	5.9
time factor radiogenic	t_r		434216	2865.8
calculated concentration of radiogenically produced ^{36}Cl atoms for estimated age	N_r	atoms ^{36}Cl g^{-1}	16784.1	846.5
estimated ^{36}Cl concentration from inheritance at time of sampling	$N_{inher}(t)$	atoms ^{36}Cl g^{-1}	0.0	
measured ^{36}Cl concentration in sample corrected from radiogenic component and inheritance	$N_{meas-r-inher}$	atoms ^{36}Cl g^{-1}	4.62E+05	24359.2
exposure age of sample	**t**	**a**	6342	614.9

3- Output B: eroding surface

calculated ^{36}Cl concentration for an eroding sample	$N_{calc,total}$	atoms ^{36}Cl g^{-1}	**4.78E+05**
difference measured/calculated ^{36}Cl concentration in eroding sample	$\Delta N_{meas-calc}$		0.00%
erosion rate	ε	cm a^{-1}	0
time factor with erosion for spallation reaction	$t_{corr,s}$		6296
time factor with erosion for capture of epithermal neutrons	$t_{corr,eth}$		6296
time factor with erosion for capture of thermal neutrons	$t_{corr,th}$		6296
time factor with erosion for capture of slow negative muons	$t_{corr,\mu}$		6296
depth reference factor for spallogenic reaction	d_s		0.979
depth reference factor for capture of epithermal neutrons	d_{eth}		0.889
depth reference factor for capture of thermal neutrons	d_{th}		0.933
depth reference factor for capture of slow negative muons	d_μ		0.998
production rate coefficient corrected for sample thickness for spallogenic reaction	$J_{Q,s}$		20.73
production rate coefficient corrected for sample thickness for capture of epithermal neutrons	$J_{Q,eth}$		1.59
production rate coefficient corrected for sample thickness for capture of thermal neutrons	$J_{Q,th}$		-9.50
production rate coefficient corrected for sample thickness for capture of slow negative muons	$J_{Q,\mu}$		1.55
production rate coefficient for spallogenic reaction	J_s		20.74
production rate coefficient for capture of epithermal neutrons	J_{eth}		1.59
production rate coefficient for capture of thermal neutrons	J_{th}		-9.51
production rate coefficient for capture of slow negative muons	J_μ		1.55

4- Output C: calculated ^{36}Cl contributions from all production mechanism

time factor cosmogenic without erosion	t_{corr}		6296	606
calculated ^{36}Cl concentration for given time + radiogenic	$N_{calc,total}$	atoms ^{36}Cl g^{-1}	**4.78E+05**	57940
difference measured/calculated ^{36}Cl concentration	$\Delta N_{meas-calc}$		0.00%	
contribution from each production mechanism:				
number of atoms ^{36}Cl per g by spallation of Ca	$N_{s,Ca}$	atoms ^{36}Cl g^{-1}	283804	59.32%
number of atoms ^{36}Cl per g by spallation of K	$N_{s,K}$	atoms ^{36}Cl g^{-1}	49929	10.44%
number of atoms ^{36}Cl per g by spallation of Ti	$N_{s,Ti}$	atoms ^{36}Cl g^{-1}	172	0.04%
number of atoms ^{36}Cl per g by spallation of Fe	$N_{s,Fe}$	atoms ^{36}Cl g^{-1}	149	0.03%
number of atoms ^{36}Cl per g by spallation of target elements	N_s	atoms ^{36}Cl g^{-1}	334055	69.82%
number of atoms ^{36}Cl per g by capture of thermal neutrons	N_{th}	atoms ^{36}Cl g^{-1}	66080	13.81%
number of atoms ^{36}Cl per g by capture of epithermal neutrons	N_{eth}	atoms ^{36}Cl g^{-1}	22059	4.61%
number of atoms ^{36}Cl per g by capture of thermal and epithermal neutrons	N_n	atoms ^{36}Cl g^{-1}	88139	18.42%
number of atoms ^{36}Cl per g by capture of slow negative muons	N_μ	atoms ^{36}Cl g^{-1}	39466	8.25%
number of atoms ^{36}Cl per g by radiogenic production	N_r	atoms ^{36}Cl g^{-1}	16784	3.51%
				100.00%

5- elemental parameters

				Ca	K	Ti	Fe	Cl	O, rock	Si	Na	Mg	Al	Mn	P	C	H	O, water	Li	B	Sm	Gd	Th	U	Cr	Be	N	F	S	Sc	Co	Ni	Se	Br	Rb	Sr	Zr	Mo	Ru	Te	I	Cs	Ba
element concentration [wt-ppm] **bulk rock**		ppm		198806	10732	420	2502	33	201239	29047	653	115927	9734	240	0	0	571	4559	2.54	8.6	0.9	0.8	1.5924	1.5519	5.0879	0.1261				1.13	1.1658	0	0	0	17.8497	76.2879	19.8875	0	0	0	0	0.6123	40.4345
element concentration dissolved sample [wt-ppm] in **target fraction**		ppm		215102	10732	420	2502	51	207735	29047	653	115927	9734	240	0	0	571	4559	2.54	8.6	0.8782	0.7674	1.5924	1.5519	5.0879	0.1261	0	0	0	1.13	1.1658	0	0	0	17.8497	76.2879	19.8875	0	0	0	0	0.6123	40.4345
atomic mass of element k (Reference: http://www.ciaaw.org/atomic-weights.htm)	A_k	g mol^{-1}		40.078	39.0983	47.867	55.845	35.453	15.999	28.085	22.98977	24.305	26.981538	54.938043	30.973761	12.01	1.008	15.999	6.941	10.811	150.36	157.25	232.0377	238.02891	51.9961	9.012182	14.0067	18.998403	32.065	44.95591	58.9332	58.6934	78.96	79.904	85.4678	87.62	91.224	95.94	101.07	127.6	126.90447	132.90545	137.327
avogadro			6.02E+23																																								
atomic concentration of element k in **bulk rock**	N_k	atoms g^{-1}	1.48E+22	2.99E+21	1.65E+20	5.28E+18	2.70E+19	5.61E+17	7.57E+21	6.23E+20	1.71E+19	2.87E+21	2.17E+20	2.63E+18	0.00E+00	0.00E+00	1.26E+20	1.72E+20	2.20E+17	4.79E+17	3.52E+15	2.94E+15	4.13E+15	3.93E+15	5.89E+16	8.43E+15	0.00E+00	0.00E+00	0.00E+00	1.51E+16	1.19E+16	0.00E+00	0.00E+00	0.00E+00	1.26E+17	5.24E+17	1.31E+17	0.00E+00	0.00E+00	0.00E+00	0.00E+00	2.77E+15	1.77E+17
atomic concentration of element k in **target fraction**	N_{Cl}	atoms g^{-1}						#########																																				
dilute resonance integral for absorption of epithermal neutrons by element k	$I_{0,k}$	E^{-24} cm^2		0.233	1	3.1		1.36	13.83	0.0002693	0.062	0.311	0.038	0.17	13.4	0.079	0.0018	0	0.0002693	0	343	1400	390	83.3	277	1.6																	
average log decrement of energy loss per collision for element k	x_k	-		0.049	0.05	0.041	0.035	0.055	0.12	0.07	0.084	0.08	0.072	0.036	0.06321	0.15776047	1	0.12	0.264	0.174	0.013	0.013	0.008594	0.008379	0.038																		
neutron scattering cross section of element k	$\sigma_{sc,k}$	E^{-24} cm^2		2.93	2.04	4.09	11.35	15.8	3.76	2.04	3.038	3.414	1.41	2.06	3.134	4.74	20.5	3.76	0.95	4.27	38	172	13.55	9.08	3.38																		
thermal neutron absorption cross section of element k	$\sigma_{a,k}$	E^{-24} cm^2		0.43	2.1	6.41	2.56	33.14	0.0002	0.171	0.517	0.0666	0.231	13.36	0.165	0.0035	0.33		70.5	767	9640	41560	7.34	2.68	3.1																		
proportion of muons stopped in element i that are captured by the nucleus	f_{cik}			0.864	0.83		0.906		0.223	0.671	0.432	0.538	0.582			0.09																												
average neutron yield per captured muon	Y_n			0.75	1.25		1.125		0.8	0.86	1	0.6	1.26			0.76																												

6- unscaled sample specific ^{36}Cl production rate by spallation of target elements

spallation production rate for Ca, SLHL	PR_{Ca}	atoms ^{36}Cl (g C	42		Braucher et al. 2011
mass concentration of Ca in **target fraction**	C_{Ca}	g Ca (g rock)$^{-1}$	0.215	0.004	
result unscaled ^{36}Cl production by spallation of ^{40}Ca	$\mathbf{P_{s,Ca}}$	atoms ^{36}Cl (g C	**8.846**	0.456	
spallation production rate for K, SLHL	PR_K	atoms ^{36}Cl (g K	148.1	7.7	Schimmelpfennig et al., 2014, St scaling
mass concentration of K in **target fraction**	C_K	g K (g rock)$^{-1}$	0.011	0.000	
result unscaled ^{36}Cl production by spallation of ^{39}K	$\mathbf{P_{s,K}}$	atoms ^{36}Cl (g K	**1.556**	0.080	
spallation production rate for Ti, SLHL	PR_{Ti}	atoms ^{36}Cl (g T	13	1.3	Fink et al., 2002
mass concentration of Ti in **target fraction**	C_{Ti}	g Ti (g rock)$^{-1}$	0.000	0.000	
result unscaled ^{36}Cl production by spallation of Ti	$\mathbf{P_{s,Ti}}$	atoms ^{36}Cl (g T	**0.005**	0.001	
spallation production rate for Fe, SLHL	PR_{Fe}	atoms ^{36}Cl (g F	1.9	0.285	Stone et al., 2005
mass concentration of Fe in **target fraction**	C_{Fe}	g Fe (g rock)$^{-1}$	0.003	0.000	
result unscaled ^{36}Cl production by spallation of Fe	$\mathbf{P_{s,Fe}}$	atoms ^{36}Cl (g F	**0.005**	0.001	
result unscaled sample specific ^{36}Cl production rate by spallation of target elements	$\mathbf{P_s}$	atoms ^{36}Cl (g)$^{-1}$	**10.412**	0.463	

7- unscaled sample specific ^{36}Cl production rate by capture of epithermal neutrons

| | | | | | | | | | | | | | | | | | | |

total muon induced neutron production at land surface	$P_{n\mu 0}$	$\mu\ cm^{-2}\ a^{-1}$	83.749	
ratio of muon production rate to epithermal neutron production rate	R_μ	-	0.044	
macroscopic neutron scattering cross section of atmosphere	$\Sigma_{sct,a}$	$cm^2\ g^{-1}$	0.3773	
thermal neutron diffusion coefficient in atmosphere	D_a	q cm^2	0.926	
macroscopic absorption and moderation cross section for epithermal neutrons in atmosphere	$\Sigma_{eth,a}$	$cm^2\ g^{-1}$	0.0548	
epithermal neutron diffusion length in atmosphere	$L_{eth,a}$	g cm^2	4.015	
epithermal neutron flux at land/atmosphere interface that would be observed in atm if interface w	$\phi^*_{eth,a}$	$n\ cm^{-2}\ a^{-1}$	12709	
difference between hypothetical equilibrium epithermal neutron fluxes in atmosphere and subsur	$\Delta\phi^*_{eth}$	$n\ cm^{-2}\ a^{-1}$	-106623	
adjusted difference between hypothetical equilibrium epithermal neutron fluxes in atmosphere ar	$\Delta\phi^{**}_{eth,a}$	$n\ cm^{-2}\ a^{-1}$	117529	
epithermal neutron diffusion length in subsurface	L_{eth}	g cm^{-2}	28.823	
difference between phi_star_eth and actual epithermal neutron flux at land surface	$(F,\Delta\phi)^*_{eth}$	-	-64289	
slow muon attenuation length	Λ_μ	q cm^{-2}	1510	
epithermal neutron flux (concentration)	$\phi_{eth,total}$	$n\ cm^{-2}\ a^{-1}$	61708	
result unscaled sample specific ^{36}Cl production rate by capture of epithermal neutrons	**P_{eth}**	**atoms ^{36}Cl g^{-1}**	**0.689**	0.20671

| **8- unscaled sample specific ^{36}Cl production rate by capture of thermal neutrons** | | | |

Chlorine-36 exposure age and erosion rate determination: Please follow the instructions on the first worksheet

modifications regarding muonic 36Cl production

Sample name 170830.03

1- Input

(and output for eroding surfaces)

	symbol	units	calculation	Uncertainties
element concentration in bulk rock: major element as oxides [wt-%] and trace elements [wt-ppm]				
element concentration in target fraction: major element as oxides [wt-%] and Cl in [wt-pm]				
uncertainty target element concentration in target fraction (oxides in [wt-%] and Cl in [wt-ppm])				
depth reference: top of sample		cm	0	
sample thickness		cm	3.5	
bulk rock density	rho	g cm^{-3}	2.6	
mass depth reference: center of sample	z	g cm^{-2}	4.9	
mass thickness	z_s	g cm^{-2}	9.8	
scaling factor for nucleonic production as a function of elevation, latitude (and temporal v	$S_{el,e}$, $S_{el,n}$	-	5.300	0.265
scaling factor for muonic production as a function of elevation, latitude (and temporal var	$S_{el,\mu}$	-	2.458	0.123
correction factor for shielding of a sample of arbitrary orientation by surrounding topogra	S_T	-	0.939	0.00939
correction factor for geometry effects on spallogenic production	S_{shape}	-	1	0.03
correction factor for snow shielding for spallogenic production	S_{snow}	-	1	0.01
effective fast neutron attenuation coefficient	$\Lambda_{f,e}$	g cm^{-2}	160	
estimated ^{36}Cl concentration from inheritance at t_{expo}=0	$N_{inher}(0)$	atoms ^{36}Cl g^{-1}		
measured ^{36}Cl concentration in sample	N_{meas}	atoms ^{36}Cl g^{-1}	6.91E+05	3.46E+04
exposure duration (independently determined or estimated)	t_{expo}	a	9455	1611.87253
formation age of rock (independently determined or estimated) for radiogenic correction	t_{form}	a	200000000	1000
erosion rate	ε	mm ka^{-1}	0	0

bulk rock: 30.825

CaO [wt-%]	K2O [wt-%]	TiO2 [wt-%]	Fe2O3 [wt-%]	Cl [ppm]	SiO2 [wt-%]	Na2O [wt-%]	MgO [wt-%]	Al2O3 [wt-%]	MnO [wt-%]	P2O5 [wt-%]	CO2 [wt-%]	H2O [wt-%]
0.04	0.01	0.08	49		0.32	0.03	21.14	0.20	0.00	0.00		0.31

target fraction:

30.01	0.04	0.01	0.08	53.44	0.32	0.03	21.14	0.20	0.00	0.00		0.31
0.30	0.01	0.01	0.01	2.34								

Li [ppm]	B [ppm]	Sm [ppm]	Gd [ppm]	Th [ppm]	U [ppm]
1.24	4.2	0.10	0.09	0.12	4.16
1.24	4.2	0.1028	0.0895	0.1211	4.1573

Cr [ppm]	Be [ppm]	N [ppm]	F [ppm]	S [ppm]	Sc [ppm]	Co [ppm]	Ni [ppm]	Se [ppm]	Br [ppm]	Rb [ppm]	Sr [ppm]	Zr [ppm]	Mo [ppm]	Ru [ppm]	Te [ppm]	I [ppm]	Cs [ppm]	Ba [ppm]
3.38	0.00				0.13	0.25	0.00			1.46	82.67	2.15	1.35				0.08	0.00
3.3788	0				0.13	0.25	0.00			1.46	82.67	2.15	1.35				0.08	0.00

2- Output A: exposure age of sample (only for uneroded surface)

decay constant for ^{36}Cl	λ_{36}	a^{-1}	2.30E-06	1.52E-08
scaled total sample specific ^{36}Cl production rate without radiogenic	P_{total}	atoms ^{36}Cl g^{-1} a	68.3	6.2
time factor radiogenic	t_r		434216	2865.8
calculated concentration of radiogenically produced ^{36}Cl atoms for estimated age	N_r	atoms ^{36}Cl g^{-1}	52093.8	2627.3
estimated ^{36}Cl concentration from inheritance at time of sampling	$N_{inher}(t)$	atoms ^{36}Cl g^{-1}	0.0	
measured ^{36}Cl concentration in sample corrected from radiogenic component and inheritance	$N_{meas-r-inher}$	atoms ^{36}Cl g^{-1}	6.39E+05	34656.0
exposure age of sample	**t**	**a**	9455	529.5

3- Output B: eroding surface

calculated ^{36}Cl concentration for an eroding sample	$N_{calc,total}$	atoms ^{36}Cl g^{-1}	**6.91E+05**	
difference measured/calculated ^{36}Cl concentration in eroding sample	$\Delta N_{meas-calc}$		0.00%	
erosion rate	ε	cm a^{-1}	0	0
time factor with erosion for spallation reaction	$t_{corr,s}$		9353	990
time factor with erosion for capture of epithermal neutrons	$t_{corr,eth}$		9353	990
time factor with erosion for capture of thermal neutrons	$t_{corr,th}$		9353	990
time factor with erosion for capture of slow negative muons	$t_{corr,\mu}$		9353	990
depth reference factor for spallogenic reaction	d_s		0.970	
depth reference factor for capture of epithermal neutrons	d_{eth}		0.867	
depth reference factor for capture of thermal neutrons	d_{th}		0.923	
depth reference factor for capture of slow negative muons	d_μ		0.997	
production rate coefficient corrected for sample thickness for spallogenic reaction	$J_{Q,s}$		25.16	
production rate coefficient corrected for sample thickness for capture of epithermal neutrons	$J_{Q,eth}$		2.21	
production rate coefficient corrected for sample thickness for capture of thermal neutrons	$J_{Q,th}$		-15.64	
production rate coefficient corrected for sample thickness for capture of slow negative muons	$J_{Q,\mu}$		1.86	
production rate coefficient for spallogenic reaction	J_s		25.18	
production rate coefficient for capture of epithermal neutrons	J_{eth}		2.21	
production rate coefficient for capture of thermal neutrons	J_{th}		-15.66	
production rate coefficient for capture of slow negative muons	J_μ		1.86	

4- Output C: calculated ^{36}Cl contributions from all production mechanism

time factor cosmogenic without erosion	t_{coscn}		9353	990
calculated ^{36}Cl concentration for given time + radiogenic	$N_{calc,total}$	atoms ^{36}Cl g^{-1}	**6.91E+05**	89183
difference measured/calculated ^{36}Cl concentration	$\Delta N_{meas-calc}$		0.00%	
contribution from each production mechanism:				
number of atoms ^{36}Cl per g by spallation of Ca	$N_{s,Ca}$	atoms ^{36}Cl g^{-1}	406908	**58.87%**
number of atoms ^{36}Cl per g by spallation of K	$N_{s,K}$	atoms ^{36}Cl g^{-1}	2275	**0.33%**
number of atoms ^{36}Cl per g by spallation of Ti	$N_{s,Ti}$	atoms ^{36}Cl g^{-1}	35	**0.01%**
number of atoms ^{36}Cl per g by spallation of Fe	$N_{s,Fe}$	atoms ^{36}Cl g^{-1}	46	**0.01%**
number of atoms ^{36}Cl per g by spallation of target elements	N_s	atoms ^{36}Cl g^{-1}	409265	**59.21%**
number of atoms ^{36}Cl per g by capture of thermal neutrons	N_{th}	atoms ^{36}Cl g^{-1}	125229	**18.12%**
number of atoms ^{36}Cl per g by capture of epithermal neutrons	N_{eth}	atoms ^{36}Cl g^{-1}	41041	**5.94%**
number of atoms ^{36}Cl per g by capture of thermal and epithermal neutrons	N_n	atoms ^{36}Cl g^{-1}	166270	**24.06%**
number of atoms ^{36}Cl per g by capture of slow negative muons	N_μ	atoms ^{36}Cl g^{-1}	63527	**9.19%**
number of atoms ^{36}Cl per g by radiogenic production	N_r	atoms ^{36}Cl g^{-1}	52094	**7.54%**
				100.00%

5- elemental parameters

			Ca	K	Ti	Fe	Cl	O, rock	Si	Na	Mg	Al	Mn	P	C	H	O, water	Li	B	Sm	Gd	Th	U	Cr	Be	N	F	S	Sc	Co	Ni	Se	Br	Rb	Sr	Zr	Mo	Ru	Te	I	Cs	Ba
element concentration [wt-ppm] **bulk rock**		ppm	220399	340	60	538	49	174822	1494	200	127444	1053	37	0	0	347	2771	1.24	4.2	0.1	0.1	0.1211	4.1573	3.3788	0	0	0	0	0.13	0.2541	0	0	0	1.4564	82.6712	2.1501	1.3508	0	0	0	0.0758	0
element concentration dissolved sample [wt-ppm] in **target fraction**		ppm	214587	340	60	538	53	172506	1494	200	127444	1053	37	0	0	347	2771	1.24	4.2	0.1028	0.0895	0.1211	4.1573	3.3788	0	0	0	0	0.13	0.2541	0	0	0	1.4564	82.6712	2.1501	1.3508	0	0	0	0.0758	0
atomic mass of element k (Reference: http://www.ciaaw.org/atomic-weights.htm)	A_k	g mol^{-1}	40.078	39.0983	47.867	55.845	35.453	15.999	28.085	22.98977	24.305	26.981538	54.938043	30.973761	12.01	1.008	15.999	6.941	10.811	150.36	157.25	232.0377	238.02891	51.9961	9.012182	14.0067	18.998403	32.065	44.95591	58.9332	58.6934	78.96	79.904	85.4678	87.62	91.224	95.94	101.07	127.6	126.90447	132.90545	137.327
avogadro			6.02E+23																																							
atomic concentration of element k in **bulk rock**	N_k	atoms g^{-1}	1.33E+22	3.31E+21	5.24E+18	7.55E+17	5.80E+18	8.32E+17	6.58E+21	3.20E+19	5.25E+18	3.16E+21	2.35E+19	4.07E+17	0.00E+00	0.00E+00	7.40E+19	1.04E+20	1.08E+17	2.34E+17	4.12E+14	3.43E+14	3.14E+14	1.05E+16	3.91E+16	0.00E+00	0.00E+00	0.00E+00	0.00E+00	1.74E+15	2.60E+15	0.00E+00	0.00E+00	0.00E+00	1.03E+16	5.68E+17	1.42E+16	8.48E+15	0.00E+00	0.00E+00	0.00E+00	3.43E+14	0.00E+00
atomic concentration of element k in **target fraction**	N_{Cl}	atoms g^{-1}					#########																																			
dilute resonance integral for absorption of epithermal neutrons by element k	$I_{0,k}$	E^{-24} cm^2		0.233	1	3.1	1.36	13.83	0.0002693	0.082	0.311	0.038	0.17	13.4	0.079	0.0018	0	0.0002693	0	0.264	0.174	0.013	0.013	0.008594	0.008379	0.038																	
average log decrement of energy loss per collision for element k	x_k	-		0.049	0.05	0.041	0.035	0.055	0.12	0.07	0.084	0.08	0.072	0.036	0.06321	0.157760474	1	0.12	1.24	0.174	0.013	0.013	0.008594	0.008379	0.038																	
neutron scattering cross section of element k	$\sigma_{sc,k}$	E^{-24} cm^2		2.93	2.04	4.09	11.35	15.8	3.76	2.04	3.038	3.414	1.41	2.06	3.134	4.74	20.5	3.76	0.95	4.27	38	172	13.55	9.08	3.38																	
thermal neutron absorption cross section of element k	$\sigma_{a,k}$	E^{-24} cm^2		0.43	2.1	6.41	2.56	33.14	0.0002	0.171	0.517	0.0666	0.231	13.36	0.165	0.0035	0.33		70.5	767	9640	41560	7.34	2.68	3.1																	
proportion of muons stopped in element i that are captured by the nucleus	f_{cli}			0.864	0.83		0.906		0.223	0.671	0.432	0.538	0.582			0.09																											
average neutron yield per captured muon	Y_n			0.75	1.25		1.125		0.8	0.86	1	0.6	1.26			0.76																											

6- unscaled sample specific ^{36}Cl production rate by spallation of target elements

spallation production rate for Ca, SLHL	PR_{Ca}	atoms ^{36}Cl (g C	42		Braucher et al. 2011
mass concentration of Ca in **target fraction**	C_{Ca}	g Ca (g rock)$^{-1}$	0.215	0.004	
result unscaled ^{36}Cl production by spallation of ^{40}Ca	$\mathbf{P_{s,Ca}}$	atoms ^{36}Cl (g C	**8.741**	0.452	
spallation production rate for K, SLHL	PR_K	atoms ^{36}Cl (g K	148.1	7.7	Schimmelpfennig et al., 2014, St scaling
mass concentration of K in **target fraction**	C_K	g K (g rock)$^{-1}$	0.000	0.000	
result unscaled ^{36}Cl production by spallation of ^{39}K	$\mathbf{P_{s,K}}$	atoms ^{36}Cl (g K	**0.049**	0.012	
spallation production rate for Ti, SLHL	PR_{Ti}	atoms ^{36}Cl (g T	13	1.2	Fink et al., 2002
mass concentration of Ti in **target fraction**	C_{Ti}	g Ti (g rock)$^{-1}$	0.000	0.000	
result unscaled ^{36}Cl production by spallation of Ti	$\mathbf{P_{s,Ti}}$	atoms ^{36}Cl (g T	**0.001**	0.001	
spallation production rate for Fe, SLHL	PR_{Fe}	atoms ^{36}Cl (g F	1.9	0.285	Stone et al., 2005
mass concentration of Fe in **target fraction**	C_{Fe}	g Fe (g rock)$^{-1}$	0.001	0.000	
result unscaled ^{36}Cl production by spallation of Fe	$\mathbf{P_{s,Fe}}$	atoms ^{36}Cl (g F	**0.001**	0.000	
result unscaled sample specific ^{36}Cl production rate by spallation of target elements	$\mathbf{P_s}$	atoms ^{36}Cl (g)$^{-1}$	**8.791**	0.452	

7- unscaled sample specific ^{36}Cl production rate by capture of epithermal neutrons

						Ca	K	Ti	Fe	Cl	O, rock	Si	Na	Mg	Al	Mn	P	C	H	O, water	Li	B	Sm	Gd	Th	U	Cr	Be	N	F	S	Sc	Co	Ni	Se	Br	Rb	Sr	Zr	Mo	Ru	Te	I	Cs	Ba
effective macroscopic resonance integral for absorption of epithermal neutrons	I_{eff}	cm^2 g^{-1}	0.0010		7.72E-04	5.24E-06	2.34E-06	7.89E-06	1.15E-05	1.77E-06	2.63E-06	1.63E-06	1.20E-04	3.99E-06	5.46E-06		0.00E+00	0.00E+00		0.00E+00	8.02E-05	5.76E-07	1.34E-07		6.26E-08																			
fraction of epithermal neutrons absorbed by ^{35}Cl **(target fraction)**	f_{eth}	-	0.0124																																								
neutron macroscopic scattering cross section in subsurface	Σ_{scl}	cm^2 g^{-1}	0.0473		9.70E-03	1.07E-05	3.09E-06	6.59E-05	1.32E-05	2.47E-02	6.54E-05	1.59E-05	1.08E-02	3.31E-05	8.39E-07	0.00E+00	0.00E+00	1.52E-03	3.92E-04	1.02E-07	9.99E-07	1.56E-08	5.90E-08	4.26E-09	9.55E-08	1.32E-07	0.00E+00	0.00E+00	0.00E+00	0.00E+00	0.00E+00	0.00E+00	0.00E+00	0.00E+00	0.00E+00	0.00E+00	0.00E+00	0.00E+00	0.00E+00	0.00E+00	0.00E+00	0.00E+00	0.00E+00	0.00E+00
scattering rate parameter	B		5.88E-03		4.75E-04	5.35E-07	1.27E-07	2.31E-06	7.23E-07	2.97E-03	4.58E-06	1.34E-06	8.62E-04	2.39E-06	3.02E-08	0.00E+00	0.00E+00	1.52E-03	4.71E-05	2.70E-08	1.74E-07	2.03E-10	7.66E-10	3.66E-11	8.00E-10	5.03E-09	0.00E+00	0.00E+00	0.00E+00	0.00E+00	0.00E+00	0.00E+00	0.00E+00	0.00E+00	0.00E+00	0.00E+00	0.00E+00	0.00E+00	0.00E+00	0.00E+00	0.00E+00	0.00E+00	0.00E+00	0.00E+00
mean macroscopic log decrement of energy loss per collision in subsurface	X_{ss}		0.124																																							
macroscopic absorption and moderation cross section for epithermal neutrons	Σ_{eth}	cm^2 g^{-1}	0.006																																							
attenuation length for absorption and moderation of epithermal neutron flux	Λ_{eth}	g cm^{-2}	166.400																																							
	A_k* N_K	atoms mol^{-1}	3.17E+23		1.33E+23	2.05E+20	3.61E+19	3.24E+20	2.95E+19	1.05E+23	9.00E+20	1.21E+20	7.67E+22	6.34E+20	2.24E+19		0.00E+00	7.46E+19		7.47E+17	2.53E+18	6.19E+16	5.39E+16		2.03E+18																			
average atomic weight in subsurface	A_{ss}	g mol^{-1}	23.837																																							
production rate of epithermal neutrons from fast neutrons in atmosphere at land/atm interface	$P_n(0)$	n cm^{-2} a^{-1}	696	185	Marrero et al. 2016, St scaling																																							
Ratio of epithermal neutron production in subsurface to that in atmosphere	R_{eth}	-	1.28																																							
epithermal neutron diffusion coefficient in subsurface	D_{eth}	g cm^{-2}	7.24																																							
apparent fast neutron attenuation coefficient	Λ_f	g cm^{-2}	160																																							
epithermal neutron flux at land/atmosphere interface that would be observed in ss if interface wa	ϕ^*_{eth}	n cm^{-2} a^{-1}	155830																																							
average neutron yield per stopped negative muon	Y_n		0.411		0.270	0.001		0.001		0.059	0.002	0.000	0.077	0.001			0.000																											
slow negative muon stopping rate at land surface SLHL	$\Psi_\mu(0)$	μ g^{-1} a^{-1}	190																																							
fast muon flux at land surface SLHL	$\phi_{\mu f0}$	μ cm^{-2} a^{-1}	7.90E+05																																							

total muon induced neutron production at land surface	$P_{n,0}$	μ cm^{-2} a^{-1}	82.651	
ratio of muon production rate to epithermal neutron production rate	R_μ	-	0.043	
macroscopic neutron scattering cross section of atmosphere	$\sum_{sc,a}$	cm^2 g^{-1}	0.3773	
thermal neutron diffusion coefficient in atmosphere	D_a	g cm^{-2}	0.926	
macroscopic absorption and moderation cross section for epithermal neutrons in atmosphere	$\sum_{eth,a}$	cm^2 g^{-1}	0.0548	
epithermal neutron diffusion length in atmosphere	$L_{eth,a}$	g cm^{-2}	4.015	
epithermal neutron flux at land/atmosphere interface that would be observed in atm if interface w	$\phi^+_{eth,c}$	n cm^{-2} a^{-1}	12709	
difference between hypothetical equilibrium epithermal neutron fluxes in atmosphere and subsur	$\Delta\phi^+_{eth}$	n cm^{-2} a^{-1}	-143121	
adjusted difference between hypothetical equilibrium epithermal neutron fluxes in atmosphere ar	$\Delta\phi^{++}_{eth,a}$	n cm^{-2} a^{-1}	154205	
epithermal neutron diffusion length in subsurface	L_{eth}	g cm^{-2}	34.228	
difference between phi_star_eth and actual epithermal neutron flux at land surface	$(F,\Delta\phi)^+_{eth}$	-	-90423	
slow muon attenuation length	Λ_μ	g cm^{-2}	1510	
epithermal neutron flux (concentration)	$\phi_{eth,total}$	n cm^{-2} a^{-1}	75124	
result unscaled sample specific ^{36}Cl production rate by capture of epithermal neutrons	**P_{eth}**	**atoms ^{36}Cl g^{-1} a^{-1}**	**0.885**	0.26544

8- unscaled sample specific ^{36}Cl production rate by capture of thermal neutrons

| | | | |

Chlorine-36 exposure age and erosion rate determination: Please follow the instructions on the first worksheet

modifications regarding muonic 36Cl production

Sample name 170831.01

1- Input
(and output for eroding surfaces)

	symbol	units	calculations	Uncertainties
element concentration in bulk rock: maior element as oxides [wt-%] and trace elements [wt-ppm]				
element concentration in target fraction: major element as oxides [wt-%] and Cl in [wt-ppm]				
uncertainty target element concentration in target fraction (oxides in [wt-%] and Cl in [wt-ppm])				
depth reference: top of sample		cm	0	
sample thickness		cm	3	
bulk rock density	rho	g cm^{-3}	2.7	
mass depth reference: center of sample	z	g cm^{-2}	4.05	
mass thickness	z_s	g cm^{-2}	8.1	
scaling factor for nucleonic production as a function of elevation, latitude (and temporal v	S_{eLsp} , S_{eLth}	-	3.894	0.195
scaling factor for muonic production as a function of elevation, latitude (and temporal var	S_{eLsl}	-	2.062	0.103
correction factor for shielding of a sample of arbitrary orientation by surrounding topogra	S_T	-	0.989	0.00989
correction factor for geometry effects on spallogenic production	S_{shape}	-	1	0.03
correction factor for snow shielding for spallogenic production	S_{snow}	-	1	0.01
effective fast neutron attenuation coefficient	$\Lambda_{f,e}$	g cm^{-2}	160	
estimated ^{36}Cl concentration from inheritance at t_{exp}=0	$N_{inher}(0)$	atoms ^{36}Cl g^{-1}		
measured ^{36}Cl concentration in sample	N_{meas}	atoms ^{36}Cl g^{-1}	1.06E+06	4.63E+04
exposure duration (independently determined or estimated)	t_{expo}	a	14419	1296.686834
formation age of rock (independently determined or estimated) for radiogenic correction	t_{form}	a	200000000	1000
erosion rate	**ε**	mm ka^{-1}	0	0

bulk rock:

CaO [wt-%]	K2O [wt-%]	TiO2 [wt-%]	Fe2O3 [wt-%]	Cl [ppm]	SiO2 [wt-%]	Na2O [wt-%]	MgO [wt-%]	Al2O3 [wt-%]	MnO [wt-%]	P2O5 [wt-%]	CO2 [wt-%]	H2O [wt-%]
33.969	0.07	0.02	0.16	0.00	0.62	0.01	0.78	0.39	0.00	0.00		0.52

target fraction:

53.16	0.07	0.02	0.16	21.76	0.62	0.01	0.78	0.39	0.00	0.00		0.52
1.68	0.01	0.01	0.01	0.67								

Li [ppm]	B [ppm]	Sm [ppm]	Gd [ppm]	Th [ppm]	U [ppm]
2.25	4.7	0.13	0.12	0.24	0.38
2.25	4.7	0.1278	0.1161	0.2433	0.3825

Cr [ppm]	Be [ppm]	N [ppm]	F [ppm]	S [ppm]	Sc [ppm]	Co [ppm]	Ni [ppm]	Se [ppm]	Br [ppm]	Rb [ppm]	Sr [ppm]	Zr [ppm]	Mo [ppm]	Ru [ppm]	Te [ppm]	I [ppm]	Cs [ppm]	Ba [ppm]
3.52	0.05				0.36	0.31	2.56			3.74	140.92	4.15	0.00				0.20	6.40
3.5241	0.0508	0	0	0	0.36	0.3128	2.5575	0	0	3.7437	140.9176	4.1494	0	0	0	0	0.1954	6.4031

2- Output A: exposure age of sample (only for uneroded surface)

decay constant for ^{36}Cl	λ_{36}	a^{-1}	2.30E-06	1.51998E-08
scaled total sample specific ^{36}Cl production rate without radiogenic	P_{total}	atoms ^{36}Cl g^{-1} a	75.0	5.8
time factor radiogenic	t_i		434216	2865.8
calculated concentration of radiogenically produced ^{36}Cl atoms for estimated age	N_i	atoms ^{36}Cl g^{-1}	422.6	21.3
estimated ^{36}Cl concentration from inheritance at time of sampling	$N_{inher}(t)$	atoms ^{36}Cl g^{-1}	0.0	
measured ^{36}Cl concentration in sample corrected from radiogenic component and inheritance	$N_{meas-inher}$	atoms ^{36}Cl g^{-1}	1.06E+06	46349.5
exposure age of sample	**t**	**a**	14419	1296

3- Output B: eroding surface

calculated ^{36}Cl concentration for an eroding sample	$N_{calc,total}$	atoms ^{36}Cl g^{-1}	1.06E+06	
difference measured/calculated ^{36}Cl concentration in eroding sample	$\Delta N_{meas-calc}$		0.00%	
erosion rate	ε	cm a^{-1}	0	0
time factor with erosion for spallation reaction	$t_{cosm,s}$		14182	1254
time factor with erosion for capture of epithermal neutrons	$t_{cosm,eth}$		14182	1254
time factor with erosion for capture of thermal neutrons	$t_{cosm,th}$		14182	1254
time factor with erosion for capture of slow negative muons	$t_{cosm,sl}$		14182	1254
depth reference factor for spallogenic reaction	d_s		0.975	
depth reference factor for capture of epithermal neutrons	d_{eth}		0.887	
depth reference factor for capture of thermal neutrons	d_{th}		0.925	
depth reference factor for capture of slow negative muons	d_{sl}		0.997	
production rate coefficient corrected for sample thickness for spallogenic reaction	J_{Cs}		20.53	
production rate coefficient corrected for sample thickness for capture of epithermal neutrons	J_{Ceth}		1.03	
production rate coefficient corrected for sample thickness for capture of thermal neutrons	J_{Cth}		-4.56	
production rate coefficient corrected for sample thickness for capture of slow negative muons	J_{Csl}		2.77	
production rate coefficient for spallogenic reaction	J_s		20.54	
production rate coefficient for capture of epithermal neutrons	J_{eth}		1.03	
production rate coefficient for capture of thermal neutrons	J_{th}		-4.57	
production rate coefficient for capture of slow negative muons	J_{sl}		2.77	

4- Output C: calculated ^{36}Cl contributions from all production mechanism

time factor cosmogenic without erosion	t_{cosm}		14182	1254
calculated ^{36}Cl concentration for given time + radiogenic	$N_{calc,total}$	atoms ^{36}Cl g^{-1}	1.06E+06	124722
difference measured/calculated ^{36}Cl concentration	$\Delta N_{meas-calc}$		0.00%	
contribution from each production mechanism:				
number of atoms ^{36}Cl per g by spallation of Ca	$N_{s,Ca}$	atoms ^{36}Cl g^{-1}	850280	79.90%
number of atoms ^{36}Cl per g by spallation of K	$N_{s,K}$	atoms ^{36}Cl g^{-1}	4779	0.45%
number of atoms ^{36}Cl per g by spallation of Ti	$N_{s,Ti}$	atoms ^{36}Cl g^{-1}	79	0.01%
number of atoms ^{36}Cl per g by spallation of Fe	$N_{s,Fe}$	atoms ^{36}Cl g^{-1}	114	0.01%
number of atoms ^{36}Cl per g by spallation of target elements	N_s	atoms ^{36}Cl g^{-1}	855251	80.37%
number of atoms ^{36}Cl per g by capture of thermal neutrons	N_{th}	atoms ^{36}Cl g^{-1}	48691	4.58%
number of atoms ^{36}Cl per g by capture of epithermal neutrons	N_{eth}	atoms ^{36}Cl g^{-1}	19113	1.80%
number of atoms ^{36}Cl per g by capture of thermal and epithermal neutrons	N_n	atoms ^{36}Cl g^{-1}	67804	6.37%
number of atoms ^{36}Cl per g by capture of slow negative muons	N_{sl}	atoms ^{36}Cl g^{-1}	140715	13.22%
number of atoms ^{36}Cl per g by radiogenic production	N_i	atoms ^{36}Cl g^{-1}	423	0.04%
				100.00%

5- elemental parameters

			Ca	K	Ti	Fe	Cl	O, rock	Si	Na	Mg	Al	Mn	P	C	H	O, water	Li	B	Sm	Gd	Th	U	Cr	Be	N	F	S	Sc	Co	Ni	Se	Br	Rb	Sr	Zr	Mo	Ru	Te	I	Cs	Ba
element concentration [wt-ppm] **bulk rock**		ppm	385457	606	114	1125	0	162612	2895	104	4679	2084	22	0	0	582	4649	2.25	4.7	0.1	0.1	0.2433	0.3825	3.5241	0.0508	0	0	0	0.36	0.3128	2.5575	0	0	3.7437	140.9176	4.1494	0	0	0	0	0.1954	6.4031
element concentration dissolved sample [wt-ppm] in **target fraction**		ppm	380119	606	114	1125	22	160484	2895	104	4679	2084	22	0	0	582	4649	2.25	4.7	0.1278	0.1161	0.2433	0.3825	3.5241	0.0508	0	0	0	0.36	0.3128	2.5575	0	0	3.7437	140.9176	4.1494	0	0	0	0	0.1954	6.4031
atomic mass of element k (Reference: http://www.ciaaw.org/atomic-weights.htm)	A_k	g mol^{-1}	40.078	39.0983	47.867	55.845	35.453	15.999	28.085	22.98977	24.305	26.981538	54.938043	30.973761	12.01	1.008	15.999	6.941	10.811	150.36	157.25	232.0377	238.02891	51.9961	9.012182	14.0067	18.998403	32.065	44.95591	58.9332	58.6934	78.96	79.904	85.4678	87.62	91.224	95.94	101.07	127.6	126.90447	132.90545	137.327
avoqadro			6.02E+23																																							
atomic concentration of element k in **bulk rock**	N_k	atoms g^{-1}	1.25E+22	5.79E+21	9.33E+18	1.43E+18	1.21E+19	0.00E+00	6.12E+21	6.21E+19	2.72E+18	1.16E+20	4.65E+19	2.38E+17	0.00E+00	0.00E+00	1.29E+20	1.75E+20	1.95E+17	2.62E+17	5.12E+14	4.45E+14	6.31E+14	9.68E+14	4.08E+16	3.39E+15	0.00E+00	0.00E+00	0.00E+00	4.82E+15	3.20E+15	2.62E+16	0.00E+00	0.00E+00	2.64E+16	9.69E+17	2.74E+16	0.00E+00	0.00E+00	0.00E+00	0.00E+00	8.85E+14	2.81E+16
atomic concentration of element k in **target fraction**	N_{Cl}	atoms g^{-1}					#########																																				
dilute resonance integral for absorption of epithermal neutrons by element k	$I_{0,k}$	E^{-04} cm^2		0.233	1	3.1	1.36	13.83	0.0002693	0.082	0.311	0.038	0.17	13.4	0.079	0.0018	0	0.0002693	0	343	1400	390	83.3	277	1.6																	
average log decrement of energy loss per collision for element k	x_k	-		0.049	0.05	0.041	0.035	0.055	0.12	0.07	0.084	0.08	0.072	0.036	0.06321	0.1577605	1	0.12	0.264	0.174	0.013	0.013	0.008594	0.008379	0.038																	
neutron scattering cross section of element k	$\sigma_{n,s,k}$	E^{-24} cm^2		2.93	2.04	4.09	11.35	15.8	3.76	2.04	3.038	3.414	1.41	2.06	3.134	4.74	20.5	3.76	0.95	4.27	38	172	13.55	9.08	3.38																	
thermal neutron absorption cross section of element k	$\sigma_{n,a,k}$	E^{-24} cm^2		0.43	2.1	6.41	2.56	33.14	0.0002	0.171	0.517	0.0666	0.231	13.36	0.165	0.0035	0.33		70.5	767	9640	41560	7.34	2.68	3.1																	
proportion of muons stopped in element i that are captured by the nucleus	$f_{sl,k}$			0.864	0.83		0.906		0.223	0.671	0.432	0.538	0.582			0.09																											
average neutron yield per captured muon	Y_{sl}			0.75	1.25		1.125		0.8	0.86	1	0.6	1.26			0.76																											

6- unscaled sample specific ^{36}Cl production rate by spallation of target elements

spallation production rate for Ca, SLHL	PR_{Ca}	atoms ^{36}Cl (g C	42	3	Braucher et al. 2011
mass concentration of Ca in **target fraction**	C_{Ca}	g Ca (g rock)$^{-1}$	0.380	0.007	
result unscaled ^{36}Cl production by spallation of ^{40}Ca	$\mathbf{P_{s,Ca}}$	atoms ^{36}Cl (g C	15.566	0.802	
spallation production rate for K, SLHL	PR_K	atoms ^{36}Cl (g K	148.1	7.8	Schimmelpfennig et al., 2014, St scaling
mass concentration of K in **target fraction**	C_K	g K (g rock)$^{-1}$	0.001	0.000	
result unscaled ^{36}Cl production by spallation of ^{39}K	$\mathbf{P_{s,K}}$	atoms ^{36}Cl (g K	0.087	0.013	
spallation production rate for Ti, SLHL	PR_{Ti}	atoms ^{36}Cl (g T	13	3	Fink et al., 2002
mass concentration of Ti in **target fraction**	C_{Ti}	g Ti (g rock)$^{-1}$	0.000	0.000	
result unscaled ^{36}Cl production by spallation of Ti	$\mathbf{P_{s,Ti}}$	atoms ^{36}Cl (g Ti	0.001	0.001	
spallation production rate for Fe, SLHL	PR_{Fe}	atoms ^{36}Cl (g F	1.9	0.266	Stone et al., 2005
mass concentration of Fe in **target fraction**	C_{Fe}	g Fe (g rock)$^{-1}$	0.001	0.000	
result unscaled ^{36}Cl production by spallation of Fe	$\mathbf{P_{s,Fe}}$	atoms ^{36}Cl (g Fe	0.002	0.000	
result unscaled sample specific ^{36}Cl production rate by spallation of target elements	$\mathbf{P_s}$	atoms ^{36}Cl (g)$^{-1}$	15.657	0.802	

7- unscaled sample specific ^{36}Cl production rate by capture of epithermal neutrons

					Ca	K	Ti	Fe	Cl	O, rock	Si	Na	Mg	Al	Mn	P	C	H	O, water	Li	B	Sm	Gd	Th	U	Cr	Be	N	F	S	Sc	Co	Ni	Se	Br	Rb	Sr	Zr	Mo	Ru	Te	I	Cs	Ba
effective macroscopic resonance integral for absorption of epithermal neutrons	I_{eff}	cm^2 g^{-1}	0.0015		1.35E-03	9.33E-06	4.45E-06	1.65E-05	0.00E+00	1.65E-06	5.09E-06	8.46E-07	4.41E-06	7.91E-06	3.18E-06		0.00E+00	0.00E+00		0.00E+00	8.98E-05	7.17E-07	1.73E-07			6.53E-08																		
fraction of epithermal neutrons absorbed by ^{35}Cl (**target fraction**)	f_{eth}	-	0.0034																																								
neutron macroscopic scattering cross section in subsurface	Σ_{sl}	cm^2 g^{-1}	0.0440		1.70E-02	1.90E-05	5.87E-06	1.38E-04	0.00E+00	2.30E-02	1.27E-04	8.27E-06	3.96E-04	6.56E-05	4.89E-07	0.00E+00	0.00E+00	2.64E-03	6.58E-04	1.85E-07	1.12E-06	1.95E-08	7.65E-08	8.56E-09	8.79E-09	1.38E-07	0.00E+00	0.00E+00	0.00E+00	0.00E+00	0.00E+00	0.00E+00	0.00E+00	0.00E+00	0.00E+00	0.00E+00	0.00E+00	0.00E+00	0.00E+00	0.00E+00	0.00E+00	0.00E+00	0.00E+00	0.00E+00
scattering rate parameter	B		6.36E-03		8.32E-04	9.52E-07	2.41E-07	4.82E-06	0.00E+00	2.76E-03	8.87E-06	6.94E-07	3.17E-05	4.72E-06	1.76E-08	0.00E+00	0.00E+00	2.64E-03	7.90E-05	4.90E-08	1.95E-07	2.53E-10	9.94E-10	7.35E-11	7.36E-11	5.24E-09	0.00E+00	0.00E+00	0.00E+00	0.00E+00	0.00E+00	0.00E+00	0.00E+00	0.00E+00	0.00E+00	0.00E+00	0.00E+00	0.00E+00	0.00E+00	0.00E+00	0.00E+00	0.00E+00	0.00E+00	0.00E+00	0.00E+00
mean macroscopic log decrement of energy loss per collision in subsurface	X_{sl}		0.144																																								
macroscopic absorption and moderation cross section for epithermal neutrons	Σ_{eth}	cm^2 g^{-1}	0.007																																								
attenuation length for absorption and moderation of epithermal neutron flux	Λ_{eth}	g cm^{-2}	151.986																																								
	$A_a * N_k$	atoms mol^{-1}	3.37E+23		2.32E+23	3.65E+20	6.87E+19	6.78E+20	0.00E+00	9.79E+22	1.74E+21	6.26E+19	2.82E+21	1.26E+21	1.31E+19		0.00E+00	1.30E+20		1.35E+18	2.83E+18	7.70E+16	6.99E+16			2.12E+18																		
average atomic weight in subsurface	A_{ss}	g mol^{-1}	27.044																																								
production rate of epithermal neutrons from fast neutrons in atmosphere at land/atm interface	$P_n(0)$	n cm^{-2} a^{-1}	696	185	Marrero et al. 2016, St scaling																																							
Ratio of epithermal neutron production in subsurface to that in atmosphere	R_{eth}	-	1.37																																								
epithermal neutron diffusion coefficient in subsurface	D_{eth}	g cm^{-2}	7.76																																								
apparent fast neutron attenuation coefficient	Λ_f	g cm^{-2}	160																																								
epithermal neutron flux at land/atmosphere interface that would be observed in ss if interface was	ϕ_{*eth}	n cm^{-2} a^{-1}	151442																																								
average neutron yield per stopped negative muon	Y_s		0.504		0.441	0.001		0.002		0.051	0.003	0.000	0.003	0.003			0.000																												
slow negative muon stopping rate at land surface SLHL	$\Psi_s(0)$	μ g^{-1} a^{-1}	190																																								
fast muon flux at land surface SLHL	$\phi_{s(0)}$	μ cm^{-2} a^{-1}	7.90E+05																																								
total muon induced neutron production at land surface	P_{*sl}	μ cm^{-2} a^{-1}	100.361																																								
ratio of muon production rate to epithermal neutron production rate	R_e	-	0.056																																								
macroscopic neutron scattering cross section of atmosphere	$\Sigma_{sl,a}$	cm^2 g^{-1}	0.3773																																								
thermal neutron diffusion coefficient in atmosphere	D_a	g cm^{-2}	0.926																																								
macroscopic absorption and moderation cross section for epithermal neutrons in atmosphere	$\Sigma_{eth,a}$	cm^2 g^{-1}	0.0548																																								

epithermal neutron diffusion length in atmosphere	$L_{eth,a}$	g cm^{-2}	4.015	
epithermal neutron flux at land/atmosphere interface that would be observed in atm if interface we	$\phi^*_{eth,a}$	n cm^{-2} a^{-1}	12709	
difference between hypothetical equilibrium epithermal neutron fluxes in atmosphere and subsurf	$\Delta\phi^*_{eth}$	n cm^{-2} a^{-1}	-138733	
adjusted difference between hypothetical equilibrium epithermal neutron fluxes in atmosphere an	$\Delta\phi^{**}_{eth,a}$	n cm^{-2} a^{-1}	149925	
epithermal neutron diffusion length in subsurface	L_{eth}	g cm^{-2}	33.916	
difference between phi_star_eth and actual epithermal neutron flux at land surface	$(\Gamma.\Delta\phi)^*_{eth}$	-	-85471	
slow muon attenuation length	Λ_μ	g cm^{-2}	1510	
epithermal neutron flux (concentration)	$\phi_{eth,total}$	n cm^{-2} a^{-1}	74458	
result unscaled sample specific ^{36}Cl production rate by capture of epithermal neutrons	**P_{eth}**	**atoms ^{36}Cl g^{-1} a^{-1}**	**0.351**	0.10523

8- unscaled sample specific ^{36}Cl production rate by capture of thermal neutrons				
macroscopic thermal neutron absorption cross section for ss **(bulk rock)**	Σ_{th}	cm^2 g^{-1}	0.003	
fraction of thermal neutrons absorbed by elements that produce ^{36}Cl **(target fraction)**	f_{th}	-	0.0043	
attenuation length for absorption of thermal neutron flux	Λ_{th}	g cm^{-2}	3.49E+02	
resonance escape probability of the atmosphere	$p(E_{th})_a$	-	0.56	
resonance escape probability of a neutron from the epithermal energy range in subsurface	$p(E_{th})$	-	0.791	
ratio of thermal neutron production in subsurface to that in atmosphere	R_{th}	-	1.412	
thermal neutron diffusion coefficient in subsurface	D_{th}	g cm^{-2}	7.76	
thermal neutron flux at land/atmosphere interface that would be observed in ss if interface was no	ϕ^*_{th}	n cm^{-2} a^{-1}	3.07E+05	
ratio of muon production rate to thermal neutron production rate	R'_μ	-	0.040	
portion of difference between phi_star_eth and actual flux due to epithermal flux profile	$(Im.\Delta\phi)^*_{eth}$	-	114616.6	
	$R_{th,a}$	-	1	
macroscopic thermal neutron cross section of atmosphere	$\Sigma_{th,a}$	cm^2 g^{-1}	0.060241	
thermal neutron flux at land/atmosphere interface that would be observed in atmosphere if interfa	$\phi^*_{th,a}$	n cm^{-2} a^{-1}	6478	
difference in equilibrium thermal neutron fluxes between atmosphere and subsurface	$\Delta\phi^*_{th,a}$	n cm^{-2} a^{-1}	3.01E+05	
difference in equilibrium epithermal neutron fluxes between atmosphere and surface	$\Delta\phi^*_{eth,a}$	n cm^{-2} a^{-1}	138732.7	
parameter governing epithermal neutron flux near the land/atm interface	$(\Gamma.\Delta\phi)^*_{eth,a}$	-	53261.625	
portion of difference between phi_star_eth,a and actual flux due to epithermal flux profile	$(Im.\Delta\phi)^*_{eth,a}$		583739.9	
difference between (Im.sphi)_star,eth and (Im.sphi)_star,eth,a	$\Delta(Im.\Delta\phi)^*_{eth}$		4.69E+05	
thermal neutron diffusion length in atmosphere	$L_{th,a}$	g cm^{-2}	3.921	
difference between hypothetical equilibrium thermal neutron fluxes in atmosphere and subsurface	$\Delta\phi^*_{th}$	n cm^{-2} a^{-1}	-3.01E+05	
thermal neutron diffusion length in subsurface	L_{th}	g cm^{-2}	52.036	
portion of difference between phi_star_th and actual flux due to thermal flux profile	$(Im.\Delta\phi)^*_{th}$		-353013.6	
thermal neutron flux (concentration)	$\phi_{th,total}$	n cm^{-2} a^{-1}	7.28E+04	
result unscaled sample specific ^{36}Cl production rate by capture of thermal neutrons	**P_{th}**	**atoms ^{36}Cl g^{-1} a^{-1}**	**0.892**	0.268

| | | | |

Chlorine-36 exposure age and erosion rate determination: Please follow the instructions on the first worksheet

modifications regarding muonic 36Cl production

Sample name GAR01.18

1- Input

(and output for eroding surfaces)

	symbol	units	calculations	Uncertainties
element concentration in bulk rock: maior element as oxides [wt-%] and trace elements [wt-ppm]				
element concentration in target fraction: major element as oxides [wt-%] and Cl in [wt-ppm]				
uncertainty target element concentration in target fraction (oxides in [wt-%] and Cl in [wt-ppm])				
depth reference: top of sample		cm	0	
sample thickness		cm	3	
bulk rock density	rho	g cm^{-3}	2.716778327	
mass depth reference: center of sample	z	g cm^{-2}	4.075167491	
mass thickness	z_s	g cm^{-2}	8.150334981	
scaling factor for nucleonic production as a function of elevation, latitude (and temporal v	S_{eLsp} , S_{eLth}	-	6.153	0.308
scaling factor for muonic production as a function of elevation, latitude (and temporal var	$S_{eLμ}$	-	2.679	0.134
correction factor for shielding of a sample of arbitrary orientation by surrounding topogra	S_T	-	0.96052	0.0096052
correction factor for geometry effects on spallogenic production	S_{shape}	-	1	0.03
correction factor for snow shielding for spallogenic production	S_{snow}	-	1	0.01
effective fast neutron attenuation coefficient	$\Lambda_{f,e}$	g cm^{-2}	160	
estimated ^{36}Cl concentration from inheritance at t_{exp}=0	$N_{inher}(0)$	atoms ^{36}Cl g^{-1}		
measured ^{36}Cl concentration in sample	N_{meas}	atoms ^{36}Cl g^{-1}	1.73E+06	4.49E+05
exposure duration (independently determined or estimated)	t_{expo}	a	9873	3205.717673
formation age of rock (independently determined or estimated) for radiogenic correction	t_{form}	a	200000000	1000
erosion rate	**ε**	mm ka^{-1}	0	0

bulk rock:	CaO [wt-%]	K2O [wt-%]	TiO2 [wt-%]	Fe2O3 [wt-%]	Cl [ppm]	SiO2 [wt-%]	Na2O [wt-%]	MgO [wt-%]	Al2O3 [wt-%]	MnO [wt-%]	P2O5 [wt-%]	CO2 [wt-%]	H2O [wt-%]
	28.980	0.07	0.03	0.27	175.00	1.46	0.05	21.26	0.89	0.01	0.00		0.5
target fraction:													
	29.58	0.07	0.03	0.27	284.85	1.46	0.05	21.26	0.89	0.01	0.00		0.50
	0.14	0.01	0.01	0.01	82.22								

	Li [ppm]	B [ppm]	Sm [ppm]	Gd [ppm]	Th [ppm]	U [ppm]
	0.81536223	2.9556881	0.23	0.26	0.04	1.44
	0.81536223	2.9556881	0.2321517	0.260462934	0.0396357	1.4382084
	0.81536223	2.9556881	0.2321517	0.260462934	0.0396357	1.4382084

	Cr [ppm]	Be [ppm]	N [ppm]	F [ppm]	S [ppm]	Sc [ppm]	Co [ppm]	Ni [ppm]	Se [ppm]	Br [ppm]	Rb [ppm]	Sr [ppm]	Zr [ppm]	Mo [ppm]	Ru [ppm]	Te [ppm]	I [ppm]	Cs [ppm]	Ba [ppm]
	1.51	0.03				0.58	0.35	0.75			0.39	97.56	0.20	0.14				2.61	2.33
	1.5061552	0.0283112				0.58	0.35	0.75			0.39	97.56	0.20	0.14				2.61	2.33

2- Output A: exposure age of sample (only for uneroded surface)

decay constant for ^{36}Cl	λ_{36}	a^{-1}	2.30E-06	1.51998E-08
scaled total sample specific ^{36}Cl production rate without radiogenic	P_{total}	atoms ^{36}Cl g^{-1} a	167.5	27.8
time factor radiogenic	t_i		434216	2865.8
calculated concentration of radiogenically produced ^{36}Cl atoms for estimated age	N_i	atoms ^{36}Cl g^{-1}	94634.1	4772.7
estimated ^{36}Cl concentration from inheritance at time of sampling	$N_{inher}(t)$	atoms ^{36}Cl g^{-1}	0.0	
measured ^{36}Cl concentration in sample corrected from radiogenic component and inheritance	$N_{meas-inher}$	atoms ^{36}Cl g^{-1}	1.64E+06	449255.3
exposure age of sample	**t**	**a**	9873	3205

3- Output B: eroding surface

calculated ^{36}Cl concentration for an eroding sample	$N_{calc,total}$	atoms ^{36}Cl g^{-1}	1.73E+06
difference measured/calculated ^{36}Cl concentration in eroding sample	$\Delta N_{meas-calc}$		0.00%
erosion rate	ε	cm a^{-1}	0
time factor with erosion for spallation reaction	$t_{cosm,s}$		9762
time factor with erosion for capture of epithermal neutrons	$t_{cosm,eth}$		9762
time factor with erosion for capture of thermal neutrons	$t_{cosm,th}$		9762
time factor with erosion for capture of slow negative muons	$t_{cosm,\mu}$		9762
depth reference factor for spallogenic reaction	d_s		0.975
depth reference factor for capture of epithermal neutrons	d_{eth}		0.876
depth reference factor for capture of thermal neutrons	d_{th}		0.933
depth reference factor for capture of slow negative muons	d_μ		0.997
production rate coefficient corrected for sample thickness for spallogenic reaction	$J_{Cl,s}$		89.57
production rate coefficient corrected for sample thickness for capture of epithermal neutrons	$J_{Cl,eth}$		8.67
production rate coefficient corrected for sample thickness for capture of thermal neutrons	$J_{Cl,th}$		-75.04
production rate coefficient corrected for sample thickness for capture of slow negative muons	$J_{Cl,\mu}$		3.44
production rate coefficient for spallogenic reaction	J_s		89.66
production rate coefficient for capture of epithermal neutrons	J_{eth}		8.67
production rate coefficient for capture of thermal neutrons	J_{th}		-75.12
production rate coefficient for capture of slow negative muons	J_μ		3.45

4- Output C: calculated ^{36}Cl contributions from all production mechanism

time factor cosmogenic without erosion	t_{cosm}		9762	3134
calculated ^{36}Cl concentration for given time + radiogenic	$N_{calc,total}$	atoms ^{36}Cl g^{-1}	1.73E+06	591007
difference measured/calculated ^{36}Cl concentration	$\Delta N_{meas-calc}$		0.00%	
contribution from each production mechanism:				
number of atoms ^{36}Cl per g by spallation of Ca	$N_{s,Ca}$	atoms ^{36}Cl g^{-1}	499606	28.88%
number of atoms ^{36}Cl per g by spallation of K	$N_{s,K}$	atoms ^{36}Cl g^{-1}	4840	0.28%
number of atoms ^{36}Cl per g by spallation of Ti	$N_{s,Ti}$	atoms ^{36}Cl g^{-1}	132	0.01%
number of atoms ^{36}Cl per g by spallation of Fe	$N_{s,Fe}$	atoms ^{36}Cl g^{-1}	202	0.01%
number of atoms ^{36}Cl per g by spallation of target elements	N_s	atoms ^{36}Cl g^{-1}	504781	29.18%
number of atoms ^{36}Cl per g by capture of thermal neutrons	N_{th}	atoms ^{36}Cl g^{-1}	821036	47.46%
number of atoms ^{36}Cl per g by capture of epithermal neutrons	N_{eth}	atoms ^{36}Cl g^{-1}	239089	13.82%
number of atoms ^{36}Cl per g by capture of thermal and epithermal neutrons	N_n	atoms ^{36}Cl g^{-1}	1060125	61.29%
number of atoms ^{36}Cl per g by capture of slow negative muons	N_μ	atoms ^{36}Cl g^{-1}	70266	4.06%
number of atoms ^{36}Cl per g by radiogenic production	N_i	atoms ^{36}Cl g^{-1}	94634	5.47%
				100.00%

5- elemental parameters

			Ca	K	Ti	Fe	Cl	O, rock	Si	Na	Mg	Al	Mn	P	C	H	O, water	Li	B	Sm	Gd	Th	U	Cr	Be	N	F	S	Sc	Co	Ni	Se	Br	Rb	Sr	Zr	Mo	Ru	Te	I	Cs	Ba
element concentration [wt-ppm] **bulk rock**		ppm	207207	581	180	1887	175	180172	6818	371	128198	4708	77	0	0	560	4470	0.81536223	3.0	0.2	0.3	0.0396357	1.4382084	1.5061552	0.0283112	0	0	0	0.5775482	0.3510587	0.7530776	0	0	0.3850322	97.560355	0.2038406	0.1358937	0	0	0	2.6102916	2.3328419
element concentration dissolved sample [wt-ppm] in **target fraction**		ppm	211487	581	180	1887	285	181878	6818	371	128198	4708	77	0	0	560	4470	0.81536223	2.9556881	0.2321517	0.260462934	0.0396357	1.4382084	1.5061552	0.0283112	0	0	0	0.5775482	0.3510587	0.7530776	0	0	0.3850322	97.560355	0.2038406	0.1358937	0	0	0	2.6102916	2.3328419
atomic mass of element k (Reference: http://www.ciaaw.org/atomic-weights.htm)	A_k	g mol^{-1}	40.078	39.0983	47.867	55.845	35.453	15.999	28.085	22.98977	24.305	26.981538	54.938043	30.973761	12.01	1.008	15.999	6.941	10.811	150.36	157.25	232.0377	238.02891	51.9961	9.012182	14.0067	18.998403	32.065	44.95591	58.9332	58.6934	78.96	79.904	85.4678	87.62	91.224	95.94	101.07	127.6	126.90447	132.90545	137.327
avoqadro			6.02E+23																																							
atomic concentration of element k in **bulk rock**	N_k	atoms g^{-1}	3.11E+21	8.95E+18	2.26E+18	2.04E+19	2.97E+18	6.78E+21	1.46E+20	9.72E+18	3.18E+21	1.05E+20	8.48E+17	0.00E+00	0.00E+00	1.23E+20	1.68E+20	7.07E+16	1.65E+17	9.30E+14	9.97E+14	1.03E+14	3.64E+15	1.74E+16	1.89E+15	0.00E+00	0.00E+00	0.00E+00	7.74E+15	3.59E+15	7.73E+15	0.00E+00	0.00E+00	2.71E+15	6.71E+17	1.35E+15	8.53E+14	0.00E+00	0.00E+00	0.00E+00	1.18E+16	1.02E+16
atomic concentration of element k in **target fraction**	N_{Cl}	atoms g^{-1}					########																																			
dilute resonance integral for absorption of epithermal neutrons by element k	$I_{0,k}$	E^{-24} cm^2	0.233	1	3.1	1.36	13.83	0.0002693	0.082	0.311	0.038	0.17	13.4	0.079	0.0018	0	0.0002693	0	343	1400	390	83.3	277	1.6																	
average log decrement of energy loss per collision for element k	x_k	-	0.049	0.05	0.041	0.035	0.055	0.12	0.07	0.084	0.08	0.072	0.036	0.06321	0.15776047	1	0.12	0.264	0.174	0.013	0.013	0.008594	0.008379	0.038																	
neutron scattering cross section of element k	$\sigma_{scat,k}$	E^{-24} cm^2	2.93	2.04	4.09	11.35	15.8	3.76	2.04	3.038	3.414	1.41	2.06	3.134	4.74	20.5	3.76	0.95	4.27	38	172	13.55	9.08	3.38																	
thermal neutron absorption cross section of element k	$\sigma_{a,k}$	E^{-24} cm^2	0.43	2.1	6.41	2.56	33.14	0.0002	0.171	0.517	0.0666	0.231	13.36	0.165	0.0035	0.33		70.5	767	9640	41560	7.34	2.68	3.1																	
proportion of muons stopped in element i that are captured by the nucleus	$f_{th,k}$		0.864	0.83		0.906		0.223	0.671	0.432	0.538	0.582			0.09																											
average neutron yield per captured muon	Y_k		0.75	1.25		1.125		0.8	0.86	1	0.6	1.26			0.76																											

6- unscaled sample specific ^{36}Cl production rate by spallation of target elements

spallation production rate for Ca, SLHL	PR_{Ca}	atoms ^{36}Cl (g C	42		Braucher et al. 2011
mass concentration of Ca in **target fraction**	C_{Ca}	g Ca (g rock)$^{-1}$	0.211	0.001	
result unscaled ^{36}Cl production by spallation of ^{40}Ca	$\mathbf{P_{s,Ca}}$	atoms ^{36}Cl (g C	8.659	0.414	
spallation production rate for K, SLHL	PR_K	atoms ^{36}Cl (g K	148.1	7.8	Schimmelpfennig et al., 2014, St scaling
mass concentration of K in **target fraction**	C_K	g K (g rock)$^{-1}$	0.001	0.000	
result unscaled ^{36}Cl production by spallation of ^{39}K	$\mathbf{P_{s,K}}$	atoms ^{36}Cl (g K	0.084	0.013	
spallation production rate for Ti, SLHL	PR_{Ti}	atoms ^{36}Cl (g T	13		Fink et al., 2002
mass concentration of Ti in **target fraction**	C_{Ti}	g Ti (g rock)$^{-1}$	0.000	0.000	
result unscaled ^{36}Cl production by spallation of Ti	$\mathbf{P_{s,Ti}}$	atoms ^{36}Cl (g Ti	0.002	0.001	
spallation production rate for Fe, SLHL	PR_{Fe}	atoms ^{36}Cl (g F	1.9	0.288	Stone et al., 2005
mass concentration of Fe in **target fraction**	C_{Fe}	g Fe (g rock)$^{-1}$	0.002	0.000	
result unscaled ^{36}Cl production by spallation of Fe	$\mathbf{P_{s,Fe}}$	atoms ^{36}Cl (g Fe	0.003	0.000	
result unscaled sample specific ^{36}Cl production rate by spallation of target elements	$\mathbf{P_s}$	atoms ^{36}Cl (g)$^{-1}$	8.749	0.415	

7- unscaled sample specific ^{36}Cl production rate by capture of epithermal neutrons

effective macroscopic resonance integral for absorption of epithermal neutrons	I_{eff}	cm^2 g^{-1}	0.0010		
fraction of epithermal neutrons absorbed by ^{35}Cl (**target fraction**)	f_{eth}	-	0.0646		
neutron macroscopic scattering cross section in subsurface	Σ_{scl}	cm^2 g^{-1}	0.0494		
scattering rate parameter	B		7.02E-03		
mean macroscopic log decrement of energy loss per collision in subsurface	X_{sk}		0.142		
macroscopic absorption and moderation cross section for epithermal neutrons	Σ_{ath}	cm^2 g^{-1}	0.007		
attenuation length for absorption and moderation of epithermal neutron flux	Λ_{eth}	g cm^{-2}	139.552		
	$A_s * N_k$	atoms mol^{-1}	3.20E+23		
average atomic weight in subsurface	A_{sk}	g mol^{-1}	23.391		
production rate of epithermal neutrons from fast neutrons in atmosphere at land/atm interface	$P_n(0)$	n cm^{-2} a^{-1}	696	185	Marrero et al. 2016, St scaling
Ratio of epithermal neutron production in subsurface to that in atmosphere	R_{eth}	-	1.27		
epithermal neutron diffusion coefficient in subsurface	D_{eth}	g cm^{-2}	6.94		
apparent fast neutron attenuation coefficient	Λ_f	g cm^{-2}	160		
epithermal neutron flux at land/atmosphere interface that would be observed in ss if interface was	ϕ_{eth}	n cm^{-2} a^{-1}	128217		
average neutron yield per stopped negative muon	Y_μ		0.406		
slow negative muon stopping rate at land surface SLHL	$\Psi_\mu(0)$	μ g^{-1} a^{-1}	190		
fast muon flux at land surface SLHL	$\phi_{\mu 0}$	μ cm^{-2} a^{-1}	7.90E+05		
total muon induced neutron production at land surface	$P_{n\mu}$	μ cm^{-2} a^{-1}	81.752		
ratio of muon production rate to epithermal neutron production rate	R_μ	-	0.040		
macroscopic neutron scattering cross section of atmosphere	$\Sigma_{scl,a}$	cm^2 g^{-1}	0.3773		
thermal neutron diffusion coefficient in atmosphere	D_a	g cm^{-2}	0.926		
macroscopic absorption and moderation cross section for epithermal neutrons in atmosphere	$\Sigma_{ath,a}$	cm^2 g^{-1}	0.0548		

epithermal neutron diffusion length in atmosphere	$L_{eth,a}$	g cm^{-2}	4.015		
epithermal neutron flux at land/atmosphere interface that would be observed in atm if interface wa	$\phi^*_{eth,a}$	n cm^{-2} a^{-1}	12709		
difference between hypothetical equilibrium epithermal neutron fluxes in atmosphere and subsurf	$\Delta\phi^*_{eth}$	n cm^{-2} a^{-1}	-115508		
adjusted difference between hypothetical equilibrium epithermal neutron fluxes in atmosphere an	$\Delta\phi^{**}_{eth,a}$	n cm^{-2} a^{-1}	126523		
epithermal neutron diffusion length in subsurface	L_{eth}	g cm^{-2}	30.685		
difference between phi_star_eth and actual epithermal neutron flux at land surface	$(F.\Delta\phi)^*_{eth}$	-	-70316		
slow muon attenuation length	Λ_μ	g cm^{-2}	1510		
epithermal neutron flux (concentration)	$\phi_{eth,total}$	n cm^{-2} a^{-1}	65422		
result unscaled sample specific ^{36}Cl production rate by capture of epithermal neutrons	**P_{eth}**	**atoms ^{36}Cl g^{-1} a^{-1}**	**4.156**	1.24665	

| **8- unscaled sample specific ^{36}Cl production rate by capture of thermal neutrons** | | | | |

Chlorine-36 exposure age and erosion rate determination: Please follow the instructions on the first worksheet

modifications regarding muonic 36Cl production

Sample name GAR02.18

1- Input

(and output for eroding surfaces)

	symbol	units	calculations	Uncertainties
element concentration in bulk rock: major element as oxides [wt-%] and trace elements [wt-ppm]				
element concentration in target fraction: major element as oxides [wt-%] and Cl in [wt-pom]				
uncertainty target element concentration in target fraction (oxides in [wt-%] and Cl in [wt-ppm])				
depth reference: top of sample		cm	0	
sample thickness		cm	2.5	
bulk rock density	rho	g cm^{-3}	2.674384026	
mass depth reference: center of sample	z	g cm^{-2}	3.342980033	
mass thickness	z_s	g cm^{-2}	6.685960065	
scaling factor for nucleonic production as a function of elevation, latitude (and temporal v	$S_{el,e}$, $S_{el,n}$	-	6.027	0.301
scaling factor for muonic production as a function of elevation, latitude (and temporal var	$S_{el,\mu}$	-	2.647	0.132
correction factor for shielding of a sample of arbitrary orientation by surrounding topogra	S_T	-	0.930692821	0.009306928
correction factor for geometry effects on spallogenic production	S_{shape}	-	1	0.03
correction factor for snow shielding for spallogenic production	S_{snow}	-	1	0.01
effective fast neutron attenuation coefficient	$\Lambda_{f,e}$	g cm^{-2}	160	
estimated ^{36}Cl concentration from inheritance at t_{expo}=0	$N_{inher}(0)$	atoms ^{36}Cl g^{-1}		
measured ^{36}Cl concentration in sample	N_{meas}	atoms ^{36}Cl g^{-1}	1.62E+06	1.62E+05
exposure duration (independently determined or estimated)	t_{expo}	a	17103	2463.826093
formation age of rock (independently determined or estimated) for radiogenic correction	t_{form}	a	200000000	1000
erosion rate	ε	mm ka^{-1}	0	0

CaO [wt-%]	K2O [wt-%]	TiO2 [wt-%]	Fe2O3 [wt-%]	Cl [ppm]
bulk rock:				
36.600	0.12	0.03	0.25	76.00
target fraction:				
33.90	0.12	0.03	0.25	90.46
8.10	0.01	0.01	0.01	10.91

SiO2 [wt-%]	Na2O [wt-%]	MgO [wt-%]	Al2O3 [wt-%]	MnO [wt-%]	P2O5 [wt-%]	CO2 [wt-%]	H2O [wt-%]
1.33	0.00	14.73	0.65	0.03	0.00		0.5
1.33	0.00	14.73	0.65	0.03	0.00		0.50

Li [ppm]	B [ppm]	Sm [ppm]	Gd [ppm]	Th [ppm]	U [ppm]
0.15780103	1.4765668	0.30	0.35	0.03	0.16
0.15780103	1.4765668	0.2986948	0.34941657	0.0338145	0.1634368

Cr [ppm]	Be [ppm]	N [ppm]	F [ppm]	S [ppm]	Sc [ppm]	Co [ppm]	Ni [ppm]	Se [ppm]	Br [ppm]	Rb [ppm]	Sr [ppm]	Zr [ppm]	Mo [ppm]	Ru [ppm]	Te [ppm]	I [ppm]	Cs [ppm]	Ba [ppm]
2.44	0.02				0.60	0.51	0.87			0.25	57.37	0.11	0.05				0.04	4.62
2.4402802	0.022543				0.60	0.51	0.87			0.25	57.37	0.11	0.05				0.04	4.62

2- Output A: exposure age of sample (only for uneroded surface)

decay constant for ^{36}Cl	λ_{36}	a^{-1}	2.30E-06	1.51998E-08
scaled total sample specific ^{36}Cl production rate without radiogenic	P_{total}	atoms ^{36}Cl g^{-1} a	96.3	9.6
time factor radiogenic	t_r		434216	2865.8
calculated concentration of radiogenically produced ^{36}Cl atoms for estimated age	N_r	atoms ^{36}Cl g^{-1}	2508.9	126.5
estimated ^{36}Cl concentration from inheritance at time of sampling	$N_{inher}(t)$	atoms ^{36}Cl g^{-1}	0.0	
measured ^{36}Cl concentration in sample corrected from radiogenic component and inheritance	$N_{meas-r-inher}$	atoms ^{36}Cl g^{-1}	1.62E+06	161500.8
exposure age of sample	**t**	**a**	17103	2463.8

3- Output B: eroding surface

calculated ^{36}Cl concentration for an eroding sample	$N_{calc,total}$	atoms ^{36}Cl g^{-1}	1.62E+06	
difference measured/calculated ^{36}Cl concentration in eroding sample	$\Delta N_{meas-calc}$		0.00%	
erosion rate	ε	cm a^{-1}	0	0
time factor with erosion for spallation reaction	$t_{coem,s}$		16771	2369
time factor with erosion for capture of epithermal neutrons	$t_{coem,eth}$		16771	2369
time factor with erosion for capture of thermal neutrons	$t_{coem,th}$		16771	2369
time factor with erosion for capture of slow negative muons	$t_{coem,\mu}$		16771	2369
depth reference factor for spallogenic reaction	d_s		0.979	
depth reference factor for capture of epithermal neutrons	d_{eth}		0.900	
depth reference factor for capture of thermal neutrons	d_{th}		0.943	
depth reference factor for capture of slow negative muons	d_μ		0.998	
production rate coefficient corrected for sample thickness for spallogenic reaction	$J_{Q,s}$		33.87	
production rate coefficient corrected for sample thickness for capture of epithermal neutrons	$J_{Q,eth}$		3.09	
production rate coefficient corrected for sample thickness for capture of thermal neutrons	$J_{Q,th}$		-22.23	
production rate coefficient corrected for sample thickness for capture of slow negative muons	$J_{Q,\mu}$		2.19	
production rate coefficient for spallogenic reaction	J_s		33.89	
production rate coefficient for capture of epithermal neutrons	J_{eth}		3.09	
production rate coefficient for capture of thermal neutrons	J_{th}		-22.25	
production rate coefficient for capture of slow negative muons	J_μ		2.19	

4- Output C: calculated ^{36}Cl contributions from all production mechanism

time factor cosmogenic without erosion	t_{coem}		16771	2369
calculated ^{36}Cl concentration for given time + radiogenic	$N_{calc,total}$	atoms ^{36}Cl g^{-1}	1.62E+06	279316
difference measured/calculated ^{36}Cl concentration	$\Delta N_{meas-calc}$		0.00%	
contribution from each production mechanism:				
number of atoms ^{36}Cl per g by spallation of Ca	$N_{s,Ca}$	atoms ^{36}Cl g^{-1}	937951	57.98%
number of atoms ^{36}Cl per g by spallation of K	$N_{s,K}$	atoms ^{36}Cl g^{-1}	13590	0.84%
number of atoms ^{36}Cl per g by spallation of Ti	$N_{s,Ti}$	atoms ^{36}Cl g^{-1}	216	0.01%
number of atoms ^{36}Cl per g by spallation of Fe	$N_{s,Fe}$	atoms ^{36}Cl g^{-1}	306	0.02%
number of atoms ^{36}Cl per g by spallation of target elements	N_s	atoms ^{36}Cl g^{-1}	952062	58.85%
number of atoms ^{36}Cl per g by capture of thermal neutrons	N_{th}	atoms ^{36}Cl g^{-1}	397854	24.59%
number of atoms ^{36}Cl per g by capture of epithermal neutrons	N_{eth}	atoms ^{36}Cl g^{-1}	126149	7.80%
number of atoms ^{36}Cl per g by capture of thermal and epithermal neutrons	N_{th}	atoms ^{36}Cl g^{-1}	524003	32.39%
number of atoms ^{36}Cl per g by capture of slow negative muons	N_μ	atoms ^{36}Cl g^{-1}	139240	8.61%
number of atoms ^{36}Cl per g by radiogenic production	N_r	atoms ^{36}Cl g^{-1}	2509	0.16%
				100.00%

5- elemental parameters

			Ca	K	Ti	Fe	Cl	O, rock	Si	Na	Mg	Al	Mn	P	C	H	O, water	Li	B	Sm	Gd	Th	U	Cr	Be	N	F	S	Sc	Co	Ni	Se	Br	Rb	Sr	Zr	Mo	Ru	Te	I	Cs	Ba
element concentration [wt-ppm] **bulk rock**		ppm	261690	996	180	1748	76	174083	6211	0	88822	3439	232	0	0	560	4470	0.15780103	1.5	0.3	0.3	0.0338145	0.1634368	2.4402802	0.022543	0	0	0	0.6030254	0.5128534	0.8679057	0	0	0.247973	57.371946	0.1070793	0.0507218	0	0	0	0.0394503	4.6213159
element concentration dissolved sample [wt-ppm] in **target fraction**		ppm	242402	996	180	1748	90	166394	6211	0	88822	3439	232	0	0	560	4470	0.15780103	1.4765668	0.2986948	0.34941657	0.0338145	0.1634368	2.4402802	0.022543	0	0	0	0.6030254	0.5128534	0.8679057	0	0	0.247973	57.371946	0.1070793	0.0507218	0	0	0	0.0394503	4.6213159
atomic mass of element k (Reference: http://www.ciaaw.org/atomic-weights.htm)	A_k	g mol^{-1}	40.078	39.0983	47.867	55.845	35.453	15.999	28.085	22.98977	24.305	26.981538	54.938043	30.973761	12.01	1.008	15.999	6.941	10.811	150.36	157.25	232.0377	238.02891	51.9961	9.012182	14.0067	18.998403	32.065	44.95591	58.9332	58.6934	78.96	79.904	85.4678	87.62	91.224	95.94	101.07	127.6	126.90447	132.90545	137.327
avogadro			6.02E+23																																							
atomic concentration of element k in **bulk rock**	N_k	atoms g^{-1}	1.32E+22	3.93E+21	1.53E+19	2.26E+18	1.88E+19	1.29E+18	6.55E+21	1.33E+20	0.00E+00	2.20E+21	7.67E+19	2.55E+18	0.00E+00	0.00E+00	1.25E+20	1.68E+20	1.37E+16	8.22E+16	1.20E+15	1.34E+15	8.78E+13	4.13E+14	2.83E+16	1.51E+15	0.00E+00	0.00E+00	0.00E+00	8.08E+15	5.24E+15	8.90E+15	0.00E+00	0.00E+00	1.75E+15	3.94E+17	7.07E+14	3.18E+14	0.00E+00	0.00E+00	0.00E+00	1.79E+14	2.03E+16
atomic concentration of element k in **target fraction**	N_{Cl}	atoms g^{-1}					#########																																				
dilute resonance integral for absorption of epithermal neutrons by element k	$I_{0,k}$	E^{-24} cm^2		0.233	1	3.1	1.36	13.83	0.0002693	0.082	0.311	0.038	0.17	13.4	0.079	0.0018	0	0.0002693	0	343	1400	390	83.3	277	1.6																	
average log decrement of energy loss per collision for element k	x_k	-		0.049	0.05	0.041	0.035	0.055	0.12	0.07	0.084	0.08	0.072	0.036	0.06321	0.15776047	1	0.12	0.264	0.174	0.013	0.013	0.008594	0.006379	0.038																	
neutron scattering cross section of element k	$\sigma_{sc,k}$	E^{-24} cm^2		2.93	2.04	4.09	11.35	15.8	3.76	2.04	3.038	3.414	1.41	2.06	3.134	4.74	20.5	3.76	0.95	4.27	38	172	13.55	9.08	3.38																	
thermal neutron absorption cross section of element k	$\sigma_{a,k}$	E^{-24} cm^2		0.43	2.1	6.41	2.56	33.14	0.0002	0.171	0.517	0.0666	0.231	13.36	0.165	0.0035	0.33		70.5	767	9640	41560	7.34	2.68	3.1																	
proportion of muons stopped in element i that are captured by the nucleus	f_{cik}			0.864	0.83		0.906		0.223	0.671	0.432	0.538	0.582			0.09																											
average neutron yield per captured muon	Y_n			0.75	1.25		1.125		0.8	0.86	1	0.6	1.26			0.76																											

6- unscaled sample specific ^{36}Cl production rate by spallation of target elements

spallation production rate for Ca, SLHL	PR_{Ca}	atoms ^{36}Cl (g C	42	2	Braucher et al. 2011
mass concentration of Ca in **target fraction**	C_{Ca}	g Ca (g rock)$^{-1}$	0.242	0.001	
result unscaled ^{36}Cl production by spallation of ^{40}Ca	$\mathbf{P_{s,Ca}}$	atoms ^{36}Cl (g C	**9.970**	0.477	
spallation production rate for K, SLHL	PR_K	atoms ^{36}Cl (g K	148.1	7.8	Schimmelpfennig et al., 2014, St scaling
mass concentration of K in **target fraction**	C_K	g K (g rock)$^{-1}$	0.001	0.000	
result unscaled ^{36}Cl production by spallation of ^{39}K	$\mathbf{P_{s,K}}$	atoms ^{36}Cl (g K	**0.144**	0.014	
spallation production rate for Ti, SLHL	PR_{Ti}	atoms ^{36}Cl (g T	13	3	Fink et al., 2002
mass concentration of Ti in **target fraction**	C_{Ti}	g Ti (g rock)$^{-1}$	0.000	0.000	
result unscaled ^{36}Cl production by spallation of Ti	$\mathbf{P_{s,Ti}}$	atoms ^{36}Cl (g T	**0.002**	0.001	
spallation production rate for Fe, SLHL	PR_{Fe}	atoms ^{36}Cl (g F	1.9	0.288	Stone et al., 2005
mass concentration of Fe in **target fraction**	C_{Fe}	g Fe (g rock)$^{-1}$	0.002	0.000	
result unscaled ^{36}Cl production by spallation of Fe	$\mathbf{P_{s,Fe}}$	atoms ^{36}Cl (g F	**0.003**	0.000	
result unscaled sample specific ^{36}Cl production rate by spallation of target elements	$\mathbf{P_s}$	atoms ^{36}Cl (g)$^{-1}$	**10.120**	0.477	

7- unscaled sample specific ^{36}Cl production rate by capture of epithermal neutrons

| | | | | | | | | | | | | | | | | | | |

total muon induced neutron production at land surface	$P_{n,0}$	μ cm^{-2} a^{-1}	87.887	
ratio of muon production rate to epithermal neutron production rate	R_μ	-	0.043	
macroscopic neutron scattering cross section of atmosphere	$\sum_{sc,a}$	cm^2 g^{-1}	0.3773	
thermal neutron diffusion coefficient in atmosphere	D_a	q cm^2	0.926	
macroscopic absorption and moderation cross section for epithermal neutrons in atmosphere	$\sum_{eth,a}$	cm^2 g^{-1}	0.0548	
epithermal neutron diffusion length in atmosphere	$L_{eth,a}$	g cm^{-2}	4.015	
epithermal neutron flux at land/atmosphere interface that would be observed in atm if interface w	$\phi^*_{eth,a}$	n cm^{-2} a^{-1}	12709	
difference between hypothetical equilibrium epithermal neutron fluxes in atmosphere and subsur	$\Delta\phi^*_{eth}$	n cm^{-2} a^{-1}	-122630	
adjusted difference between hypothetical equilibrium epithermal neutron fluxes in atmosphere ar	$\Delta\phi^{**}_{eth,a}$	n cm^{-2} a^{-1}	133706	
epithermal neutron diffusion length in subsurface	L_{eth}	g cm^{-2}	31.737	
difference between phi_star_eth and actual epithermal neutron flux at land surface	$(F,\Delta\phi)^*_{eth}$	-	-74939	
slow muon attenuation length	Λ_μ	q cm^{-2}	1510	
epithermal neutron flux (concentration)	$\phi_{eth,total}$	n cm^{-2} a^{-1}	67118	
result unscaled sample specific ^{36}Cl production rate by capture of epithermal neutrons	**P_{eth}**	**atoms ^{36}Cl g^{-1} a^{-1}**	**1.343**	0.40305

8- unscaled sample specific ^{36}Cl production rate by capture of thermal neutrons

| | | | |

Chlorine-36 exposure age and erosion rate determination: Please follow the instructions on the first worksheet

modifications regarding muonic 36Cl production

1- Input

(and output for eroding surfaces)

	symbol	units	calculation	Uncertaintie	CaO [wt-%]	K2O [wt-%]	TiO2 [wt-%]	Fe2O3 [wt-%	Cl [ppm]	SiO2 [wt-%	Na2O [wt-%	MgO [wt-%]	Al2O3 [wt-%	MnO [wt-%]	P2O5 [wt-%	CO2 [wt-%]	H2O [wt-%]	Li [ppm]	B [ppm]	Sm [ppm]	Gd [ppm]	Th [ppm]	U [ppm]	Cr [ppm]	Be [ppm]	N [ppm]	F [ppm]	S [ppm]	Sc [ppm]	Co [ppm]	Ni [ppm]	Se [ppm]	Br [ppm]	Rb [ppm]	Sr [ppm]	Zr [ppm]	Mo [ppm]	Ru [ppm]	Te [ppm]	I [ppm]	Cs [ppm]	Ba [ppm]
element concentration in bulk rock: major element as oxides [wt-%] and trace elements [wt-ppm]					**bulk rock:**																																				
					42.780	0.15	0.03	0.24	67.00	1.43	0.04	9.25	0.67	0.02	0.00		0.5	0.227214	1.0584868	0.25	0.30	0.03	0.24	1.32	0.03				0.67	0.35	1.19			0.20	89.50	0.06	0.05				0.60	2.51
element concentration in target fraction: major element as oxides [wt-%] and Cl in [wt-ppm]					**target fraction:**																																			
uncertainty target element concentration in target fraction (oxides in [wt-%] and Cl in [wt-ppm])					**43.38**	**0.15**	**0.03**	**0.24**	**46.02**	**1.43**	**0.04**	**9.25**	**0.67**	**0.02**	**0.00**		**0.50**	**0.22721445**	**1.0584868**	**0.2493817**	**0.304799871**	**0.0332509**	**0.2382981**	**1.3189522**	**0.0277091**				0.67	0.35	1.19			0.20	89.50	0.06	0.05				0.60	2.51
					0.28	0.01	0.01	0.01	3.72																																
depth reference: top of sample		cm	**0**																																					
sample thickness		cm	**3**																																					
bulk rock density	rho	g cm^{-3}	**2.7064385**																																					
mass depth reference: center of sample	z	g cm^{-2}	4.0596578																																					
mass thickness	z_s	g cm^{-2}	8.1193155																																					
scaling factor for nucleonic production as a function of elevation, latitude (and temporal vi	$S_{sl,ti}$, $S_{sl,ti}$	-	**6.014**	0.301																																				
scaling factor for muonic production as a function of elevation, latitude (and temporal vari	$S_{sl,ti}$	-	**2.644**	0.132																																				
correction factor for shielding of a sample of arbitrary orientation by surrounding topogra	S_T	-	**0.953776**	0.0095378																																				
correction factor for geometry effects on spallogenic production	S_{shape}	-	**1**	0.03																																				
correction factor for snow shielding for spallogenic production	S_{snow}	-	**1**	0.01																																				
effective fast neutron attenuation coefficient	$\Lambda_{f,a}$	g cm^{-2}	**160**																																					
estimated ^{36}Cl concentration from inheritance at t_{expo}=0	$N_{inher}(0)$	atoms ^{36}Cl g^{-1}																																						
measured ^{36}Cl concentration in sample	N_{meas}	atoms ^{36}Cl g^{-1}	**1.32E+06**	**8.86E+04**																																				
exposure duration (independently determined or estimated)	t_{expo}	a	**13363**	1485.3736																																				
formation age of rock (independently determined or estimated) for radiogenic correction	t_{form}	a	**200000000**	1000																																				
erosion rate	**ε**	mm ka^{-1}	**0**	0																																				

2- Output A: exposure age of sample (only for uneroded surface)

decay constant for ^{36}Cl	λ_{36}	a^{-1}	2.30E-06	1.52E-08
scaled total sample specific ^{36}Cl production rate without radiogenic	P_{total}	atoms ^{36}Cl g^{-1} a	100.0	7.9
time factor radiogenic	t_t		434216	2865.8
calculated concentration of radiogenically produced ^{36}Cl atoms for estimated age	N_t	atoms ^{36}Cl g^{-1}	1270.9	64.1
estimated ^{36}Cl concentration from inheritance at time of sampling	$N_{inher}(t)$	atoms ^{36}Cl g^{-1}	0.0	
measured ^{36}Cl concentration in sample corrected from radiogenic component and inheritance	$N_{meas-i-inher}$	atoms ^{36}Cl g^{-1}	1.32E+06	88556.0
exposure age of sample	**t**	**a**	**13363**	1000

3- Output B: eroding surface

calculated ^{36}Cl concentration for an eroding sample	$N_{calc,total}$	atoms ^{36}Cl g^{-1}	**1.32E+06**	
difference measured/calculated ^{36}Cl concentration in eroding sample	$\Delta N_{meas-calc}$		**0.00%**	
erosion rate	ε	cm a^{-1}	0	0
time factor with erosion for spallation reaction	$t_{coem,s}$		13159	1363
time factor with erosion for capture of epithermal neutrons	$t_{coem,eth}$		13159	1363
time factor with erosion for capture of thermal neutrons	$t_{coem,th}$		13159	1363
time factor with erosion for capture of slow negative muons	$t_{coem,sl}$		13159	1363
depth reference factor for spallogenic reaction	d_s		0.975	
depth reference factor for capture of epithermal neutrons	d_{eth}		0.883	
depth reference factor for capture of thermal neutrons	d_{th}		0.929	
depth reference factor for capture of slow negative muons	d_{sl}		0.997	
production rate coefficient corrected for sample thickness for spallogenic reaction	$J_{O,s}$		24.28	
production rate coefficient corrected for sample thickness for capture of epithermal neutrons	$J_{O,eth}$		1.77	
production rate coefficient corrected for sample thickness for capture of thermal neutrons	$J_{O,th}$		-10.65	
production rate coefficient corrected for sample thickness for capture of slow negative muons	$J_{O,sl}$		2.11	
production rate coefficient for spallogenic reaction	J_s		24.29	
production rate coefficient for capture of epithermal neutrons	J_{eth}		1.77	
production rate coefficient for capture of thermal neutrons	J_{th}		-10.66	
production rate coefficient for capture of slow negative muons	J_{sl}		2.11	

4- Output C: calculated ^{36}Cl contributions from all production mechanism

time factor cosmogenic without erosion	t_{coem}		13159	1363
calculated ^{36}Cl concentration for given time + radiogenic	$N_{calc,total}$	atoms ^{36}Cl g^{-1}	**1.32E+06**	171226
difference measured/calculated ^{36}Cl concentration	$\Delta N_{meas-calc}$		**0.00%**	
contribution from each production mechanism:				
number of atoms ^{36}Cl per g by spallation of Ca	$N_{s,Ca}$	atoms ^{36}Cl g^{-1}	958845	**72.78%**
number of atoms ^{36}Cl per g by spallation of K	$N_{s,K}$	atoms ^{36}Cl g^{-1}	13571	**1.03%**
number of atoms ^{36}Cl per g by spallation of Ti	$N_{s,Ti}$	atoms ^{36}Cl g^{-1}	172	**0.01%**
number of atoms ^{36}Cl per g by spallation of Fe	$N_{s,Fe}$	atoms ^{36}Cl g^{-1}	235	**0.02%**
number of atoms ^{36}Cl per g by spallation of target elements	N_s	atoms ^{36}Cl g^{-1}	972823	**73.84%**
number of atoms ^{36}Cl per g by capture of thermal neutrons	N_{th}	atoms ^{36}Cl g^{-1}	157478	**11.95%**
number of atoms ^{36}Cl per g by capture of epithermal neutrons	N_{eth}	atoms ^{36}Cl g^{-1}	53713	**4.08%**
number of atoms ^{36}Cl per g by capture of thermal and epithermal neutrons	N_n	atoms ^{36}Cl g^{-1}	211191	**16.03%**
number of atoms ^{36}Cl per g by capture of slow negative muons	N_{sl}	atoms ^{36}Cl g^{-1}	132239	**10.04%**
number of atoms ^{36}Cl per g by radiogenic production	N_r	atoms ^{36}Cl g^{-1}	1271	**0.10%**
				100.00%

5- elemental parameters

			Ca	K	Ti	Fe	Cl	O, rock	Si	Na	Mg	Al	Mn	P	C	H	O, water	Li	B	Sm	Gd	Th	U	Cr	Be	N	F	S	Sc	Co	Ni	Se	Br	Rb	Sr	Zr	Mo	Ru	Te	I	Cs	Ba
element concentration [wt-ppm] **bulk rock**		ppm	305877	1245	180	1678	67	170669	6678	297	55778	3544	155	0	0	560	4470	0.22721445	1.1	0.2	0.3	0.0332509	0.2382981	1.3189522	0.0277091	0	0	0	0	0.6650179	0.3546762	1.1914904	0	0	0.1995054	89.500326	0.0554182	0.0498763	0	0	0	0.5985161	2.5104426
element concentration dissolved sample [wt-ppm] in **target fraction**		ppm	310169	1245	180	1678	46	172380	6678	297	55778	3544	155	0	0	560	4470	0.22721445	1.0584868	0.2493817	0.304799871	0.0332509	0.2382981	1.3189522	0.0277091	0	0	0	0	0.6650179	0.3546762	1.1914904	0	0	0.1995054	89.500326	0.0554182	0.0498763	0	0	0	0.5985161	2.5104426
atomic mass of element k (Reference: http://www.ciaaw.org/atomic-weights.htm)	A_k	g mol^{-1}	40.078	39.0983	47.867	55.845	35.453	15.999	28.085	22.98977	24.305	26.981538	54.938043	30.973761	12.01	1.008	15.999	6.941	10.811	150.36	157.25	232.0377	238.02891	51.9961	9.012182	14.0067	18.998403	32.065	44.95591	58.9332	58.6934	78.96	79.904	85.4678	87.62	91.224	95.94	101.07	127.6	126.90447	132.90545	137.327
avogadro		6.02E+23																																								
atomic concentration of element k in **bulk rock**	N_k	atoms g^{-1}	1.30E+22	4.60E+21	1.92E+19	2.26E+18	1.81E+19	1.14E+18	6.42E+21	1.43E+20	7.77E+18	1.38E+21	7.91E+19	1.70E+18	0.00E+00	0.00E+00	1.24E+20	1.68E+20	1.97E+16	5.90E+16	9.99E+14	1.17E+15	8.63E+13	6.03E+14	1.53E+16	1.85E+15	0.00E+00	0.00E+00	0.00E+00	8.91E+15	3.62E+15	1.22E+16	0.00E+00	0.00E+00	1.41E+15	6.15E+17	3.66E+14	3.13E+14	0.00E+00	0.00E+00	0.00E+00	2.71E+15	1.10E+16
atomic concentration of element k in **target fraction**	N_{Ct}	atoms g^{-1}						#########																																			
dilute resonance integral for absorption of epithermal neutrons by element k	$I_{0,k}$	E^{-24} cm^2	0.233	1	3.1	1.36	13.83	0.0002693	0.082	0.311	0.038	0.17	13.4	0.079	0.0018	0	0.0002693	0	343	1400	390	83.3	277	1.6																		
average log decrement of energy loss per collision for element k	x_k	-	0.049	0.05	0.041	0.035	0.055	0.12	0.07	0.084	0.08	0.072	0.036	0.06321	0.1577605	1	0.12	0.264	0.174	0.013	0.013	0.008594	0.008379	0.038																		
neutron scattering cross section of element k	$\sigma_{sc,k}$	E^{-24} cm^2	2.93	2.04	4.09	11.35	15.8	3.76	2.04	3.038	3.414	1.41	2.06	3.134	4.74	20.5	3.76	0.95	4.27	38	172	13.55	9.08	3.38																		
thermal neutron absorption cross section of element k	$\sigma_{a,k}$	E^{-24} cm^2	0.43	2.1	6.41	2.56	33.14	0.0002	0.171	0.517	0.0666	0.231	13.36	0.165	0.0035	0.33		70.5	767	9640	41560	7.34	2.68	3.1																		
proportion of muons stopped in element i that are captured by the nucleus	f_{ck}		0.864	0.83		0.906		0.223	0.671	0.432	0.538	0.582			0.09																												
average neutron yield per captured muon	Y_n		0.75	1.25		1.125		0.8	0.86	1	0.6	1.26			0.76																												

6- unscaled sample specific ^{36}Cl production rate by spallation of target elements

spallation production rate for Ca, SLHL	PR_{Ca}	atoms ^{36}Cl (g C	**42**	3	Braucher et al. 2011
mass concentration of Ca in **target fraction**	C_{Ca}	g Ca (g rock)$^{-1}$	0.310	0.002	
result unscaled ^{36}Cl production by spallation of ^{40}Ca	**$P_{s,Ca}$**	atoms ^{36}Cl (g C	**12.701**	0.610	
spallation production rate for K, SLHL	PR_K	atoms ^{36}Cl (g K	**148.1**	7.4	Schimmelpfennig et al., 2014, St scaling
mass concentration of K in **target fraction**	C_K	g K (g rock)$^{-1}$	0.001	0.000	
result unscaled ^{36}Cl production by spallation of ^{39}K	**$P_{s,K}$**	atoms ^{36}Cl (g K	**0.180**	0.015	
spallation production rate for Ti, SLHL	PR_{Ti}	atoms ^{36}Cl (g Ti	**13**	3	Fink et al., 2002
mass concentration of Ti in **target fraction**	C_{Ti}	g Ti (g rock)$^{-1}$	0.000	0.000	
result unscaled ^{36}Cl production by spallation of Ti	**$P_{s,Ti}$**	atoms ^{36}Cl (g Ti	**0.002**	0.001	
spallation production rate for Fe, SLHL	PR_{Fe}	atoms ^{36}Cl (g Fe	**1.9**	0.285	Stone et al., 2005
mass concentration of Fe in **target fraction**	C_{Fe}	g Fe (g rock)$^{-1}$	0.002	0.000	
result unscaled ^{36}Cl production by spallation of Fe	**$P_{s,Fe}$**	atoms ^{36}Cl (g Fe	**0.003**	0.000	
result unscaled sample specific ^{36}Cl production rate by spallation of target elements	**P_s**	atoms ^{36}Cl (g)$^{-1}$	**12.886**	0.610	

7- unscaled sample specific ^{36}Cl production rate by capture of epithermal neutrons

					Ca	K	Ti	Fe	Cl	O, rock	Si	Na	Mg	Al	Mn	P	C	H	O, water	Li	B	Sm	Gd	Th	U	Cr	Be	N	F	S	Sc	Co	Ni	Se	Br	Rb	Sr	Zr	Mo	Ru	Te	I	Cs	Ba
effective macroscopic resonance integral for absorption of epithermal neutrons	I_{eff}	cm^2 g^{-1}	**0.0013**		1.07E-03	1.92E-05	7.02E-06	2.46E-05	1.57E-05	1.73E-06	1.17E-05	2.42E-06	5.25E-05	1.34E-05	2.27E-05		0.00E+00	0.00E+00		0.00E+00	2.02E-05	1.40E-06	4.55E-07			2.44E-08																		
fraction of epithermal neutrons absorbed by ^{36}Cl (**target fraction**)	f_{eth}	-	0.0086																																								
neutron macroscopic scattering cross section in subsurface	Σ_{sc}	cm^2 g^{-1}	0.0462		1.35E-02	3.91E-05	9.26E-06	2.05E-04	1.80E-05	2.42E-02	2.92E-04	2.36E-05	4.72E-03	1.12E-04	3.50E-06	0.00E+00	0.00E+00	2.53E-03	6.33E-04	1.87E-08	2.52E-07	3.80E-08	2.01E-07	1.17E-09	5.47E-09	5.16E-08	0.00E+00	0.00E+00	0.00E+00	0.00E+00	0.00E+00	0.00E+00	0.00E+00	0.00E+00	0.00E+00	0.00E+00	0.00E+00	0.00E+00	0.00E+00	0.00E+00	0.00E+00	0.00E+00	0.00E+00	0.00E+00
scattering rate parameter	B		6.58E-03		6.60E-04	1.96E-06	3.80E-07	7.19E-06	9.89E-07	2.90E-03	2.04E-05	1.98E-06	3.77E-04	8.03E-06	1.26E-07	0.00E+00	0.00E+00	2.53E-03	7.59E-05	4.94E-09	4.38E-08	4.93E-10	2.61E-09	1.00E-11	4.59E-11	1.96E-09	0.00E+00	0.00E+00	0.00E+00	0.00E+00	0.00E+00	0.00E+00	0.00E+00	0.00E+00	0.00E+00	0.00E+00	0.00E+00	0.00E+00	0.00E+00	0.00E+00	0.00E+00	0.00E+00	0.00E+00	0.00E+00
mean macroscopic log decrement of energy loss per collision in subsurface	x_{ss}		0.143																																								
macroscopic absorption and moderation cross section for epithermal neutrons	Σ_{eth}	cm^2 g^{-1}	0.007																																								
attenuation length for absorption and moderation of epithermal neutron flux	Λ_{eth}	g cm^{-2}	147.823																																								
	A_k* N_K	atoms mol^{-1}	3.29E+23		1.84E+23	7.50E+20	1.08E+20	1.01E+21	4.03E+19	1.03E+23	4.02E+21	1.79E+20	3.36E+22	2.13E+21	9.32E+19		0.00E+00	1.24E+20		1.37E+17	6.37E+17	1.50E+17	1.84E+17			7.94E+17																		
average atomic weight in subsurface	A_{ss}	g mol^{-1}	25.374																																								
production rate of epithermal neutrons from fast neutrons in atmosphere at land/atm interface	$P_f(0)$	n cm^{-2} a^{-1}	**696**	185	Marrero et al. 2016, St scaling																																							
Ratio of epithermal neutron production in subsurface to that in atmosphere	R_{eth}	-	1.32																																								
epithermal neutron diffusion coefficient in subsurface	D_{eth}	g cm^{-2}	7.41																																								
apparent fast neutron attenuation coefficient	Λ_f	g cm^{-2}	**160**																																								
epithermal neutron flux at land/atmosphere interface that would be observed in ss if interface was	ϕ_{*eth}	n cm^{-2} a^{-1}	142185																																								

| | | |

Chlorine-36 exposure age and erosion rate determination: Please follow the instructions on the first worksheet

modifications regarding muonic 36Cl production

Sample name GAR04.18

1- Input

(and output for eroding surfaces)

	symbol	units	calculations	Uncertainties
element concentration in bulk rock: maior element as oxides [wt-%] and trace elements [wt-ppm]				
element concentration in target fraction: major element as oxides [wt-%] and Cl in [wt-ppm]				
uncertainty target element concentration in target fraction (oxides in [wt-%] and Cl in [wt-ppm])				
depth reference: top of sample		cm	0	
sample thickness		cm	3.5	
bulk rock density	rho	g cm^{-3}	2.64123145	
mass depth reference: center of sample	z	g cm^{-2}	4.62215503	
mass thickness	z_s	g cm^{-2}	9.24431006	
scaling factor for nucleonic production as a function of elevation, latitude (and temporal v	$S_{St/A}$, $S_{St/K}$	-	5.967	0.293
scaling factor for muonic production as a function of elevation, latitude (and temporal var	$S_{St/\mu}$	-	2.606	0.130
correction factor for shielding of a sample of arbitrary orientation by surrounding topogra	S_T	-	0.92669584	0.009266958
correction factor for geometry effects on spallogenic production	S_{shape}	-	1	0.03
correction factor for snow shielding for spallogenic production	S_{snow}	-	1	0.01
effective fast neutron attenuation coefficient	$\Lambda_{f,e}$	g cm^{-2}	160	
estimated ^{36}Cl concentration from inheritance at t_{exp}=0	$N_{inher}(0)$	atoms ^{36}Cl g^{-1}		
measured ^{36}Cl concentration in sample	N_{meas}	atoms ^{36}Cl g^{-1}	1.53E+06	1.45E+05
exposure duration (independently determined or estimated)	t_{expo}	a	15925	2214.918784
formation age of rock (independently determined or estimated) for radiogenic correction	t_{form}	a	200000000	1000
erosion rate	**ε**	mm ka^{-1}	0	0

bulk rock:	CaO [wt-%]	K2O [wt-%]	TiO2 [wt-%]	Fe2O3 [wt-%]	Cl [ppm]	SiO2 [wt-%]	Na2O [wt-%]	MgO [wt-%]	Al2O3 [wt-%]	MnO [wt-%]	P2O5 [wt-%]	CO2 [wt-%]	H2O [wt-%]
	37.560	0.13	0.02	0.21	84.00	1.42	0.05	13.93	0.66	0.03	0.00		0.5
target fraction:													
	36.39	0.13	0.02	0.21	87.79	1.42	0.05	13.93	0.66	0.03	0.00		0.50
	0.14	0.01	0.01	0.01	9.96								

	Li [ppm]	B [ppm]	Sm [ppm]	Gd [ppm]	Th [ppm]	U [ppm]	Cr [ppm]	Be [ppm]	N [ppm]	F [ppm]	S [ppm]	Sc [ppm]	Co [ppm]	Ni [ppm]	Se [ppm]	Br [ppm]	Rb [ppm]	Sr [ppm]	Zr [ppm]	Mo [ppm]	Ru [ppm]	Te [ppm]	I [ppm]	Cs [ppm]	Ba [ppm]
	0.15879556	0.7885021	0.20	0.24	0.05	0.19	1.48	0.03				0.66	0.42	0.57			0.20	63.96	0.06	0.04				1.54	4.20
	0.15879556	0.7885021	0.2026012	0.240931201	0.0492814	0.1916498	1.4784415	0.0273785				0.66	0.42	0.57			0.20	63.96	0.06	0.04				1.54	4.20

2- Output A: exposure age of sample (only for uneroded surface)

decay constant for ^{36}Cl	λ_{36}	a^{-1}	2.30E-06	1.51998E-08
scaled total sample specific ^{36}Cl production rate without radiogenic	P_{total}	atoms ^{36}Cl g^{-1} a	97.4	9.5
time factor radiogenic	t_i		434216	2865.8
calculated concentration of radiogenically produced ^{36}Cl atoms for estimated age	N_i	atoms ^{36}Cl g^{-1}	2819.5	142.2
estimated ^{36}Cl concentration from inheritance at time of sampling	$N_{inher}(t)$	atoms ^{36}Cl g^{-1}	0.0	
measured ^{36}Cl concentration in sample corrected from radiogenic component and inheritance	$N_{meas-r-inher}$	atoms ^{36}Cl g^{-1}	1.52E+06	145033.9
exposure age of sample	**t**	**a**	15929	2288

3- Output B: eroding surface

calculated ^{36}Cl concentration for an eroding sample	$N_{calc,total}$	atoms ^{36}Cl g^{-1}	1.53E+06	
difference measured/calculated ^{36}Cl concentration in eroding sample	$\Delta N_{meas-calc}$		0.00%	
erosion rate	ε	cm a^{-1}	0	0
time factor with erosion for spallation reaction	$t_{cosm,s}$		15640	2135
time factor with erosion for capture of epithermal neutrons	$t_{cosm,eth}$		15640	2135
time factor with erosion for capture of thermal neutrons	$t_{cosm,th}$		15640	2135
time factor with erosion for capture of slow negative muons	$t_{cosm,\mu}$		15640	2135
depth reference factor for spallogenic reaction	d_s		0.972	
depth reference factor for capture of epithermal neutrons	d_{eth}		0.864	
depth reference factor for capture of thermal neutrons	d_{th}		0.922	
depth reference factor for capture of slow negative muons	d_μ		0.997	
production rate coefficient corrected for sample thickness for spallogenic reaction	$J_{Cl,s}$		34.08	
production rate coefficient corrected for sample thickness for capture of epithermal neutrons	$J_{Cl,eth}$		2.97	
production rate coefficient corrected for sample thickness for capture of thermal neutrons	$J_{Cl,th}$		-21.70	
production rate coefficient corrected for sample thickness for capture of slow negative muons	$J_{Cl,\mu}$		2.26	
production rate coefficient for spallogenic reaction	J_s		34.11	
production rate coefficient for capture of epithermal neutrons	J_{eth}		2.98	
production rate coefficient for capture of thermal neutrons	J_{th}		-21.73	
production rate coefficient for capture of slow negative muons	J_μ		2.26	

4- Output C: calculated ^{36}Cl contributions from all production mechanism

time factor cosmogenic without erosion	t_{cosm}		15640	2135
calculated ^{36}Cl concentration for given time + radiogenic	$N_{calc,total}$	atoms ^{36}Cl g^{-1}	1.53E+06	255832
difference measured/calculated ^{36}Cl concentration	$\Delta N_{meas-calc}$		0.00%	
contribution from each production mechanism:				
number of atoms ^{36}Cl per g by spallation of Ca	$N_{s,Ca}$	atoms ^{36}Cl g^{-1}	902816	**59.15%**
number of atoms ^{36}Cl per g by spallation of K	$N_{s,K}$	atoms ^{36}Cl g^{-1}	13204	**0.87%**
number of atoms ^{36}Cl per g by spallation of Ti	$N_{s,Ti}$	atoms ^{36}Cl g^{-1}	129	**0.01%**
number of atoms ^{36}Cl per g by spallation of Fe	$N_{s,Fe}$	atoms ^{36}Cl g^{-1}	230	**0.02%**
number of atoms ^{36}Cl per g by spallation of target elements	N_s	atoms ^{36}Cl g^{-1}	916379	**60.04%**
number of atoms ^{36}Cl per g by capture of thermal neutrons	N_{th}	atoms ^{36}Cl g^{-1}	361782	**23.70%**
number of atoms ^{36}Cl per g by capture of epithermal neutrons	N_{eth}	atoms ^{36}Cl g^{-1}	113467	**7.43%**
number of atoms ^{36}Cl per g by capture of thermal and epithermal neutrons	N_n	atoms ^{36}Cl g^{-1}	475249	**31.14%**
number of atoms ^{36}Cl per g by capture of slow negative muons	N_μ	atoms ^{36}Cl g^{-1}	131907	**8.64%**
number of atoms ^{36}Cl per g by radiogenic production	N_r	atoms ^{36}Cl g^{-1}	2819	**0.18%**
				100.00%

5- elemental parameters

			Ca	K	Ti	Fe	Cl	O, rock	Si	Na	Mg	Al	Mn	P	C	H	O, water	Li	B	Sm	Gd	Th	U	Cr	Be	N	F	S	Sc	Co	Ni	Se	Br	Rb	Sr	Zr	Mo	Ru	Te	I	Cs	Ba
element concentration [wt-ppm] **bulk rock**		ppm	268554	1079	120	1468	84	174155	6631	371	83998	3491	232	0	0	560	4470	0.15879556	0.8	0.2	0.2	0.0492814	0.1916498	1.4784415	0.0273785	0	0	0	0.6625608	0.4216296	0.5749495	0	0	0.1971255	63.956282	0.0602328	0.0438057	0	0	0	1.5386743	4.1998689
element concentration dissolved sample [wt-ppm] in **target fraction**		ppm	260156	1079	120	1468	88	170808	6631	371	83998	3491	232	0	0	560	4470	0.15879556	0.7885021	0.2026012	0.240931201	0.0492814	0.1916498	1.4784415	0.0273785	0	0	0	0.6625608	0.4216296	0.5749495	0	0	0.1971255	63.956282	0.0602328	0.0438057	0	0	0	1.5386743	4.1998689
atomic mass of element k (Reference: http://www.ciaaw.org/atomic-weights.htm)	A_k	g mol^{-1}	40.078	39.0983	47.867	55.845	35.453	15.999	28.085	22.98977	24.305	26.981538	54.938043	30.973761	12.01	1.008	15.999	6.941	10.811	150.36	157.25	232.0377	238.02891	51.9961	9.012182	14.0067	18.998403	32.065	44.95591	58.9332	58.6934	78.96	79.904	85.4678	87.62	91.224	95.94	101.07	127.6	126.90447	132.90545	137.327
avoqadro			6.02E+23																																							
atomic concentration of element k in **bulk rock**	N_k	atoms g^{-1}	1.32E+22	4.04E+21	1.66E+19	1.51E+18	1.58E+19	1.43E+18	6.56E+21	1.42E+20	9.72E+18	2.08E+21	7.79E+19	2.55E+18	0.00E+00	0.00E+00	1.27E+20	1.68E+20	1.38E+16	4.39E+16	8.11E+14	9.23E+14	1.28E+14	4.85E+14	1.71E+16	1.83E+15	0.00E+00	0.00E+00	0.00E+00	8.88E+15	4.31E+15	5.90E+15	0.00E+00	0.00E+00	1.39E+15	4.40E+17	3.98E+14	2.75E+14	0.00E+00	0.00E+00	0.00E+00	6.97E+15	1.84E+16
atomic concentration of element k in **target fraction**	N_{Cl}	atoms g^{-1}						#########																																			
dilute resonance integral for absorption of epithermal neutrons by element k	$I_{0,k}$	E^{-04} cm^2		0.233	1	3.1	1.36	13.83	0.0002693	0.082	0.311	0.038	0.17	13.4	0.079	0.0018	0	0.0002693	0	343	1400	390	83.3	277	1.6																	
average log decrement of energy loss per collision for element k	x_k	-		0.049	0.05	0.041	0.035	0.055	0.12	0.07	0.084	0.08	0.072	0.036	0.06321	0.1577655	1	0.12	0.264	0.174	0.013	0.013	0.008594	0.008379	0.038																	
neutron scattering cross section of element k	$\sigma_{scat,k}$	E^{-24} cm^2		2.93	2.04	4.09	11.35	15.8	3.76	2.04	3.038	3.414	1.41	2.66	3.134	4.74	20.5	3.76	0.95	4.27	38	172	13.55	9.08	3.38																	
thermal neutron absorption cross section of element k	$\sigma_{a,k}$	E^{-24} cm^2		0.43	2.1	6.41	2.56	33.14	0.0002	0.171	0.517	0.0666	0.231	13.36	0.165	0.0035	0.33		70.5	767	9640	41560	7.34	2.68	3.1																	
proportion of muons stopped in element i that are captured by the nucleus	f_{cik}			0.864	0.83		0.906		0.223	0.671	0.432	0.538	0.582			0.09																											
average neutron yield per captured muon	Y_k			0.75	1.25		1.125		0.8	0.86	1	0.6	1.26			0.76																											

6- unscaled sample specific ^{36}Cl production rate by spallation of target elements

spallation production rate for Ca, SLHL	PR_{Ca}	atoms ^{36}Cl (g C	42		Braucher et al. 2011
mass concentration of Ca in **target fraction**	C_{Ca}	g Ca (g rock)$^{-1}$	0.260	0.001	
result unscaled ^{36}Cl production by spallation of ^{40}Ca	$\mathbf{P_{s,Ca}}$	atoms ^{36}Cl (g C	**10.615**	0.507	
spallation production rate for K, SLHL	PR_K	atoms ^{36}Cl (g K	148.1	7.1	Schimmelpfennig et al., 2014, St scaling
mass concentration of K in **target fraction**	C_K	g K (g rock)$^{-1}$	0.001	0.000	
result unscaled ^{36}Cl production by spallation of ^{39}K	$\mathbf{P_{s,K}}$	atoms ^{36}Cl (g K	**0.155**	0.014	
spallation production rate for Ti, SLHL	PR_{Ti}	atoms ^{36}Cl (g T	13		Fink et al., 2002
mass concentration of Ti in **target fraction**	C_{Ti}	g Ti (g rock)$^{-1}$	0.000	0.000	
result unscaled ^{36}Cl production by spallation of Ti	$\mathbf{P_{s,Ti}}$	atoms ^{36}Cl (g Ti	**0.002**	0.001	
spallation production rate for Fe, SLHL	PR_{Fe}	atoms ^{36}Cl (g F	1.9	0.285	Stone et al., 2005
mass concentration of Fe in **target fraction**	C_{Fe}	g Fe (g rock)$^{-1}$	0.001	0.000	
result unscaled ^{36}Cl production by spallation of Fe	$\mathbf{P_{s,Fe}}$	atoms ^{36}Cl (g Fe	**0.003**	0.000	
result unscaled sample specific ^{36}Cl production rate by spallation of target elements	$\mathbf{P_s}$	atoms ^{36}Cl (g)$^{-1}$	**10.775**	0.507	

7- unscaled sample specific ^{36}Cl production rate by capture of epithermal neutrons

						Ca	K	Ti	Fe	Cl	O, rock	Si	Na	Mg	Al	Mn	P	C	O, water	Li	B	Sm	Gd	Th	U	Cr	Be	N	F	S	Sc	Co	Ni	Se	Br	Rb	Sr	Zr	Mo	Ru	Te	I	Cs	Ba
effective macroscopic resonance integral for absorption of epithermal neutrons	I_{eff}	cm^2 g^{-1}	0.0012	9.40E-04	1.66E-05	4.68E-06	2.15E-05	1.97E-05	1.77E-06	1.17E-05	3.02E-06	7.91E-05	1.32E-05	3.41E-05		0.00E+00	0.00E+00		0.00E+00	1.51E-05	1.14E-06	3.60E-07			2.74E-08																		
fraction of epithermal neutrons absorbed by ^{35}Cl (**target fraction**)	f_{eth}	-	0.0177																																							
neutron macroscopic scattering cross section in subsurface	Σ_{scl}	cm^2 g^{-1}	0.0475	1.18E-02	3.39E-05	6.17E-06	1.80E-04	2.25E-05	2.46E-02	2.90E-04	2.95E-05	7.11E-03	1.10E-04	5.24E-06	0.00E+00	0.00E+00	2.59E-03	6.33E-04	1.31E-08	1.88E-07	3.08E-08	1.59E-07	1.73E-09	4.40E-09	5.79E-08	0.00E+00	0.00E+00	0.00E+00	0.00E+00	0.00E+00	0.00E+00	0.00E+00	0.00E+00	0.00E+00	0.00E+00	0.00E+00	0.00E+00	0.00E+00	0.00E+00	0.00E+00	0.00E+00	0.00E+00	0.00E+00
scattering rate parameter	B		6.82E-03	5.79E-04	1.70E-06	2.53E-07	6.29E-06	1.24E-06	2.96E-03	2.03E-05	2.48E-06	5.68E-04	7.91E-06	1.89E-07	0.00E+00	0.00E+00	2.59E-03	7.59E-05	3.46E-09	3.26E-08	4.01E-10	2.06E-09	1.49E-11	3.69E-11	2.20E-09	0.00E+00	0.00E+00	0.00E+00	0.00E+00	0.00E+00	0.00E+00	0.00E+00	0.00E+00	0.00E+00	0.00E+00	0.00E+00	0.00E+00	0.00E+00	0.00E+00	0.00E+00	0.00E+00	0.00E+00	0.00E+00
mean macroscopic log decrement of energy loss per collision in subsurface	X_{ss}		0.144																																							
macroscopic absorption and moderation cross section for epithermal neutrons	Σ_{eth}	cm^2 g^{-1}	0.007																																							
attenuation length for absorption and moderation of epithermal neutron flux	Λ_{eth}	g cm^{-2}	143.206																																							
	$A_k * N_k$	atoms mol^{-1}	3.25E+23	1.62E+23	6.50E+20	7.23E+19	8.84E+20	5.06E+19	1.05E+23	3.99E+21	2.23E+20	5.06E+22	2.10E+21	1.40E+20		0.00E+00	1.28E+20		9.56E+16	4.75E+17	1.22E+17	1.45E+17			8.90E+17																		
average atomic weight in subsurface	A_{ss}	g mol^{-1}	24.589																																							
production rate of epithermal neutrons from fast neutrons in atmosphere at land/atm interface	$P_n(0)$	n cm^{-2} a^{-1}	696	185	Marrero et al. 2016, St scaling																																							
Ratio of epithermal neutron production in subsurface to that in atmosphere	R_{eth}	-	1.30																																							
epithermal neutron diffusion coefficient in subsurface	D_{eth}	g cm^{-2}	7.22																																							
apparent fast neutron attenuation coefficient	Λ_f	g cm^{-2}	160																																							
epithermal neutron flux at land/atmosphere interface that would be observed in ss if interface was	ϕ^*_{eth}	n cm^{-2} a^{-1}	135254																																							
average neutron yield per stopped negative muon	Y_μ		0.442	0.319	0.002		0.003		0.057	0.007	0.000	0.049	0.005			0.000																											
slow negative muon stopping rate at land surface SLHL	$\Psi_\mu(0)$	μ g^{-1} a^{-1}	190																																							
fast muon flux at land surface SLHL	$\phi_{\mu 0}$	μ cm^{-2} a^{-1}	7.90E+05																																							
total muon induced neutron production at land surface	$P_{n\mu 0}$	μ cm^{-2} a^{-1}	88.571																																							
ratio of muon production rate to epithermal neutron production rate	R_μ	-	0.043																																							
macroscopic neutron scattering cross section of atmosphere	$\Sigma_{scl,a}$	cm^2 g^{-1}	0.3773																																							
thermal neutron diffusion coefficient in atmosphere	D_a	g cm^{-2}	0.926																																							
macroscopic absorption and moderation cross section for epithermal neutrons in atmosphere	$\Sigma_{ath,a}$	cm^2 g^{-1}	0.0548																																							

epithermal neutron diffusion length in atmosphere	$L_{eth,a}$	g cm^{-2}	4.015	
epithermal neutron flux at land/atmosphere interface that would be observed in atm if interface we	$\phi^*_{eth,a}$	n cm^{-2} a^{-1}	12709	
difference between hypothetical equilibrium epithermal neutron fluxes in atmosphere and subsurf	$\Delta\phi^*_{eth}$	n cm^{-2} a^{-1}	-122545	
adjusted difference between hypothetical equilibrium epithermal neutron fluxes in atmosphere an	$\Delta\phi^{**}_{eth,a}$	n cm^{-2} a^{-1}	133623	
epithermal neutron diffusion length in subsurface	L_{eth}	g cm^{-2}	31.708	
difference between phi_star_eth and actual epithermal neutron flux at land surface	$(F.\Delta\phi)^*_{eth}$	-	-74833	
slow muon attenuation length	Λ_μ	g cm^{-2}	1510	
epithermal neutron flux (concentration)	$\phi_{eth,total}$	n cm^{-2} a^{-1}	68918	
result unscaled sample specific ^{36}Cl production rate by capture of epithermal neutrons	**P_{eth}**	**atoms ^{36}Cl g^{-1} a^{-1}**	**1.339**	0.40161

| **8- unscaled sample specific ^{36}Cl production rate by capture of thermal neutrons** | | | |

Chlorine-36 exposure age and erosion rate determination: Please follow the instructions on the first worksheet

modifications regarding muonic 36Cl production

Sample name SOR01.18

1- Input

(and output for eroding surfaces)

	symbol	units	calculations	Uncertainties
element concentration in bulk rock: maior element as oxides [wt-%] and trace elements [wt-ppm]				
element concentration in target fraction: major element as oxides [wt-%] and Cl in [wt-ppm]				
uncertainty target element concentration in target fraction (oxides in [wt-%] and Cl in [wt-ppm])				
depth reference: top of sample		cm	0	
sample thickness		cm	2.5	
bulk rock density	rho	g cm^{-3}	2.69587747	
mass depth reference: center of sample	z	g cm^{-2}	3.36984683	
mass thickness	z_s	g cm^{-2}	6.73969367	
scaling factor for nucleonic production as a function of elevation, latitude (and temporal v	S_{eLin} , S_{eLin}	-	5.017	0.251
scaling factor for muonic production as a function of elevation, latitude (and temporal var	$S_{\mu(z)}$	-	2.382	0.119
correction factor for shielding of a sample of arbitrary orientation by surrounding topogra	S_T	-	0.99038747	0.009903875
correction factor for geometry effects on spallogenic production	S_{shape}	-	1	0.03
correction factor for snow shielding for spallogenic production	S_{snow}	-	1	0.01
effective fast neutron attenuation coefficient	$\Lambda_{f,e}$	g cm^{-2}	160	
estimated ^{36}Cl concentration from inheritance at t_{exp}=0	$N_{inher}(0)$	atoms ^{36}Cl g^{-1}		
measured ^{36}Cl concentration in sample	N_{meas}	atoms ^{36}Cl g^{-1}	1.35E+06	1.61E+05
exposure duration (independently determined or estimated)	t_{expo}	a	14830	2629.483875
formation age of rock (independently determined or estimated) for radiogenic correction	t_{form}	a	200000000	1000
erosion rate	ε	mm ka^{-1}	0	0

bulk rock:	CaO [wt-%]	K2O [wt-%]	TiO2 [wt-%]	Fe2O3 [wt-%]	Cl [ppm]	SiO2 [wt-%]	Na2O [wt-%]	MgO [wt-%]	Al2O3 [wt-%]	MnO [wt-%]	P2O5 [wt-%]	CO2 [wt-%]	H2O [wt-%]	Li [ppm]	B [ppm]	Sm [ppm]	Gd [ppm]	Th [ppm]	U [ppm]	Cr [ppm]	Be [ppm]	N [ppm]	F [ppm]	S [ppm]	Sc [ppm]	Co [ppm]	Ni [ppm]	Se [ppm]	Br [ppm]	Rb [ppm]	Sr [ppm]	Zr [ppm]	Mo [ppm]	Ru [ppm]	Te [ppm]	I [ppm]	Cs [ppm]	Ba [ppm]
39.510	0.00	0.01	0.06	105.00	0.11	0.02	22.62	0.12	0.02	0.00		0.5	0.7197619	2.1260659	0.09	0.11	0.02	1.18	2.15	0.02				0.43	0.17	0.84			0.28	77.24	0.08	0.08				0.70	2.40
target fraction:																																					
29.58	0.00	0.01	0.06	123.93	0.11	0.02	22.62	0.12	0.02	0.00		0.50	0.7197619	2.1260659	0.0885861	0.110732601	0.0166099	1.1848388	2.1482125	0.0166099				0.43	0.17	0.84			0.28	77.24	0.08	0.08				0.70	2.40
0.11	0.01	0.01	0.01	17.66																																	

2- Output A: exposure age of sample (only for uneroded surface)

decay constant for ^{36}Cl	λ_{36}	a^{-1}	2.30E-06	1.51998E-08
scaled total sample specific ^{36}Cl production rate without radiogenic	P_{total}	atoms ^{36}Cl g^{-1} a	90.2	11.1
time factor radiogenic	t_i		434216	2865.8
calculated concentration of radiogenically produced ^{36}Cl atoms for estimated age	N_i	atoms ^{36}Cl g^{-1}	36359.1	1833.7
estimated ^{36}Cl concentration from inheritance at time of sampling	$N_{inher}(t)$	atoms ^{36}Cl g^{-1}	0.0	
measured ^{36}Cl concentration in sample corrected from radiogenic component and inheritance	$N_{meas-inher}$	atoms ^{36}Cl g^{-1}	1.31E+06	160699.1
exposure age of sample	**t**	**a**	14830	2629

3- Output B: eroding surface

calculated ^{36}Cl concentration for an eroding sample	$N_{calc,total}$	atoms ^{36}Cl g^{-1}	1.35E+06
difference measured/calculated ^{36}Cl concentration in eroding sample	$\Delta N_{meas-calc}$		0.00%
erosion rate	ε	cm a^{-1}	0
time factor with erosion for spallation reaction	$t_{cosm,s}$		14580
time factor with erosion for capture of epithermal neutrons	$t_{cosm,eth}$		14580
time factor with erosion for capture of thermal neutrons	$t_{cosm,th}$		14580
time factor with erosion for capture of slow negative muons	$t_{cosm,\mu}$		14580
depth reference factor for spallogenic reaction	d_s		0.979
depth reference factor for capture of epithermal neutrons	d_{eth}		0.896
depth reference factor for capture of thermal neutrons	d_{th}		0.946
depth reference factor for capture of slow negative muons	d_μ		0.998
production rate coefficient corrected for sample thickness for spallogenic reaction	$J_{O,s}$		46.65
production rate coefficient corrected for sample thickness for capture of epithermal neutrons	$J_{O,eth}$		3.67
production rate coefficient corrected for sample thickness for capture of thermal neutrons	$J_{O,th}$		-35.20
production rate coefficient corrected for sample thickness for capture of slow negative muons	$J_{O,\mu}$		2.47
production rate coefficient for spallogenic reaction	J_s		46.68
production rate coefficient for capture of epithermal neutrons	J_{eth}		3.67
production rate coefficient for capture of thermal neutrons	J_{th}		-35.23
production rate coefficient for capture of slow negative muons	J_μ		2.47

4- Output C: calculated ^{36}Cl contributions from all production mechanism

time factor cosmogenic without erosion	t_{cosm}		14580	2532
calculated ^{36}Cl concentration for given time + radiogenic	$N_{calc,total}$	atoms ^{36}Cl g^{-1}	1.35E+06	280056
difference measured/calculated ^{36}Cl concentration	$\Delta N_{meas-calc}$		0.00%	
contribution from each production mechanism:				
number of atoms ^{36}Cl per g by spallation of Ca	$N_{s,Ca}$	atoms ^{36}Cl g^{-1}	630227	46.66%
number of atoms ^{36}Cl per g by spallation of K	$N_{s,K}$	atoms ^{36}Cl g^{-1}	0	0.00%
number of atoms ^{36}Cl per g by spallation of Ti	$N_{s,Ti}$	atoms ^{36}Cl g^{-1}	55	0.00%
number of atoms ^{36}Cl per g by spallation of Fe	$N_{s,Fe}$	atoms ^{36}Cl g^{-1}	57	0.00%
number of atoms ^{36}Cl per g by spallation of target elements	N_s	atoms ^{36}Cl g^{-1}	630339	46.67%
number of atoms ^{36}Cl per g by capture of thermal neutrons	N_{th}	atoms ^{36}Cl g^{-1}	456610	33.80%
number of atoms ^{36}Cl per g by capture of epithermal neutrons	N_{eth}	atoms ^{36}Cl g^{-1}	129439	9.58%
number of atoms ^{36}Cl per g by capture of thermal and epithermal neutrons	N_n	atoms ^{36}Cl g^{-1}	586050	43.39%
number of atoms ^{36}Cl per g by capture of slow negative muons	N_μ	atoms ^{36}Cl g^{-1}	98022	7.26%
number of atoms ^{36}Cl per g by radiogenic production	N_i	atoms ^{36}Cl g^{-1}	36359	2.69%
				100.00%

5- elemental parameters

			Ca	K	Ti	Fe	Cl	O, rock	Si	Na	Mg	Al	Mn	P	C	H	O, water	Li	B	Sm	Gd	Th	U	Cr	Be	N	F	S	Sc	Co	Ni	Se	Br	Rb	Sr	Zr	Mo	Ru	Te	I	Cs	Ba
element concentration [wt-ppm] **bulk rock**		ppm	218147	0	60	419	105	178224	514	148	136399	635	155	0	0	560	4470	0.7197619	2.1	0.1	0.1	0.0166099	1.1848388	2.1482125	0.0166099	0	0	0	0.4263205	0.1660989	0.8415678	0	0	0.2823681	77.235989	0.0775128	0.0775128	0	0	0	0.703152	2.4028974
element concentration dissolved sample [wt-ppm] in **taroet fraction**		ppm	211514	0	60	419	124	175580	514	148	136399	635	155	0	0	560	4470	0.7197619	2.1260659	0.0885861	0.110732601	0.0166099	1.1848388	2.1482125	0.0166099	0	0	0	0.4263205	0.1660989	0.8415678	0	0	0.2823681	77.235989	0.0775128	0.0775128	0	0	0	0.703152	2.4028974
atomic mass of element k (Reference: http://www.ciaaw.org/atomic-weights.html)	A_k	g mol^{-1}	40.078	39.0983	47.867	55.845	35.453	15.999	28.085	22.98977	24.305	26.981538	54.938043	30.973761	12.01	1.008	15.999	6.941	10.811	150.36	157.25	232.0377	238.02891	51.9961	9.012182	14.0067	18.998403	32.065	44.95591	58.9332	58.6934	78.96	79.904	85.4678	87.62	91.224	95.94	101.07	127.6	126.90447	132.90545	137.327
avoqadro			6.02E+23																																						
atomic concentration of element k in **bulk rock**	N_k	atoms g^{-1}	3.28E+21	0.00E+00	7.55E+17	4.52E+18	1.78E+18	6.71E+21	1.10E+19	3.89E+18	3.38E+21	1.42E+19	1.70E+18	0.00E+00	0.00E+00	1.24E+20	1.68E+20	6.24E+16	1.18E+17	3.55E+14	4.24E+14	4.31E+13	3.00E+15	2.49E+16	1.11E+15	0.00E+00	0.00E+00	0.00E+00	5.71E+15	1.70E+15	8.63E+15	0.00E+00	0.00E+00	1.99E+15	5.31E+17	5.12E+14	4.87E+14	0.00E+00	0.00E+00	0.00E+00	3.19E+15	1.05E+16
atomic concentration of element k in **target fraction**	N_{Ci}	atoms g^{-1}	1.37E+22				#########																																		
dilute resonance integral for absorption of epithermal neutrons by element k	$I_{k,k}$	E^{-04} cm^2	0.233	1	3.1	1.36	13.83	0.0002693	0.082	0.311	0.038	0.17	13.4	0.079	0.0018	0	0.0002693	0	343	1400	390	83.3	277	1.6																	
average log decrement of energy loss per collision for element k	x_k	-	0.049	0.05	0.041	0.035	0.055	0.12	0.07	0.084	0.08	0.072	0.036	0.06321	0.15776047	1	0.12	0.264	0.174	0.013	0.013	0.008594	0.008379	0.038																	
neutron scattering cross section of element k	$\sigma_{n,s,k}$	E^{-24} cm^2	2.93	2.04	4.09	11.35	15.8	3.76	2.04	3.038	3.414	1.41	2.06	3.134	4.74	20.5	3.76	0.95	4.27	38	172	13.55	9.08	3.38																	
thermal neutron absorption cross section of element k	$\sigma_{a,k}$	E^{-24} cm^2	0.43	2.1	6.41	2.56	33.14	0.0002	0.171	0.517	0.0666	0.231	13.36	0.165	0.0035	0.33		70.5	767	9640	41560	7.34	2.68	3.1																	
proportion of muons stopped in element i that are captured by the nucleus	$f_{k,k}$		0.864	0.83		0.906		0.223	0.671	0.432	0.538	0.582			0.09																											
average neutron yield per captured muon	Y_k		0.75	1.25		1.125		0.8	0.86	1	0.6	1.26			0.76																											

6- unscaled sample specific ^{36}Cl production rate by spallation of target elements

spallation production rate for Ca, SLHL	PR_{Ca}	atoms ^{36}Cl (g C	42	3	Braucher et al. 2011
mass concentration of Ca in **target fraction**	C_{Ca}	g Ca (g rock)$^{-1}$	0.212	0.001	
result unscaled ^{36}Cl production by spallation of ^{40}Ca	$\mathbf{P_{s,Ca}}$	atoms ^{36}Cl (g C	8.698	0.415	
spallation production rate for K, SLHL	PR_K	atoms ^{36}Cl (g K	148.1	7.8	Schimmelpfennig et al., 2014, St scaling
mass concentration of K in **target fraction**	C_K	g K (g rock)$^{-1}$	0.000	0.000	
result unscaled ^{36}Cl production by spallation of ^{39}K	$\mathbf{P_{s,K}}$	atoms ^{36}Cl (g K	0.000	0.012	
spallation production rate for Ti, SLHL	PR_{Ti}	atoms ^{36}Cl (g T	13	1	Fink et al., 2002
mass concentration of Ti in **target fraction**	C_{Ti}	g Ti (g rock)$^{-1}$	0.000	0.000	
result unscaled ^{36}Cl production by spallation of Ti	$\mathbf{P_{s,Ti}}$	atoms ^{36}Cl (g Ti	0.001	0.001	
spallation production rate for Fe, SLHL	PR_{Fe}	atoms ^{36}Cl (g F	1.9	0.288	Stone et al., 2005
mass concentration of Fe in **target fraction**	C_{Fe}	g Fe (g rock)$^{-1}$	0.000	0.000	
result unscaled ^{36}Cl production by spallation of Fe	$\mathbf{P_{s,Fe}}$	atoms ^{36}Cl (g Fe	0.001	0.000	
result unscaled sample specific ^{36}Cl production rate by spallation of target elements	$\mathbf{P_s}$	atoms ^{36}Cl (g)$^{-1}$	8.700	0.416	

7- unscaled sample specific ^{36}Cl production rate by capture of epithermal neutrons

						Ca	K	Ti	Fe	Cl	O, rock	Si	Na	Mg	Al	Mn	P	C	H	O, water	Li	B	Sm	Gd	Th	U	Cr	Be	N	F	S	Sc	Co	Ni	Se	Br	Rb	Sr	Zr	Mo	Ru	Te	I	Cs	Ba
effective macroscopic resonance integral for absorption of epithermal neutrons	I_{eff}	cm^2 g^{-1}	0.0010			7.64E-04	0.00E+00	2.34E-06	6.15E-06	2.47E-05	1.81E-06	9.03E-07	1.21E-06	1.28E-04	2.41E-06	2.27E-05		0.00E+00	0.00E+00		0.00E+00	4.06E-05	4.97E-07	1.65E-07		3.98E-08																			
fraction of epithermal neutrons absorbed by ^{35}Cl (**target fraction**)	f_{eth}	-	0.0292																																								
neutron macroscopic scattering cross section in subsurface	Σ_{sn}	cm^2 g^{-1}	0.0497			9.60E-03	0.00E+00	3.09E-06	5.13E-05	2.82E-05	2.52E-02	2.25E-05	1.18E-05	1.15E-02	2.00E-05	3.50E-06	0.00E+00	0.00E+00	2.54E-03	6.33E-04	5.93E-08	5.06E-07	1.35E-08	7.29E-08	5.84E-10	2.72E-08	8.41E-08	0.00E+00	0.00E+00	0.00E+00	0.00E+00	0.00E+00	0.00E+00	0.00E+00	0.00E+00	0.00E+00	0.00E+00	0.00E+00	0.00E+00	0.00E+00	0.00E+00	0.00E+00	0.00E+00	0.00E+00
scattering rate parameter	B		7.05E-03			4.71E-04	0.00E+00	1.27E-07	1.80E-06	1.55E-06	3.03E-03	1.57E-06	9.92E-07	9.23E-04	1.44E-06	1.26E-07	0.00E+00	0.00E+00	2.54E-03	7.59E-05	1.57E-08	8.80E-08	1.75E-10	9.48E-10	5.02E-12	2.28E-10	3.20E-09	0.00E+00	0.00E+00	0.00E+00	0.00E+00	0.00E+00	0.00E+00	0.00E+00	0.00E+00	0.00E+00	0.00E+00	0.00E+00	0.00E+00	0.00E+00	0.00E+00	0.00E+00	0.00E+00	0.00E+00
mean macroscopic log decrement of energy loss per collision in subsurface	X_{ss}		0.142																																								
macroscopic absorption and moderation cross section for epithermal neutrons	Σ_{eth}	cm^2 g^{-1}	0.007																																								
attenuation length for absorption and moderation of epithermal neutron flux	Λ_{eth}	g cm^{-2}	139.140																																								
	$A_a * N_k$	atoms mol^{-1}	3.22E+23			1.31E+23	0.00E+00	3.61E+19	2.53E+20	6.32E+19	1.07E+23	3.09E+20	8.94E+19	8.21E+22	3.82E+20	9.32E+19		0.00E+00	1.25E+20		4.33E+17	1.28E+18	5.33E+16	6.67E+16		1.29E+18																			
average atomic weight in subsurface	A_{ss}	g mol^{-1}	23.523																																								
production rate of epithermal neutrons from fast neutrons in atmosphere at land/atm interface	$P_n(0)$	n cm^{-2} a^{-1}	696	185	Marrero et al. 2016, St scaling																																							
Ratio of epithermal neutron production in subsurface to that in atmosphere	R_{eth}	-	1.27																																								
epithermal neutron diffusion coefficient in subsurface	D_{eth}	g cm^{-2}	6.91																																								
apparent fast neutron attenuation coefficient	Λ_f	g cm^{-2}	160																																								
epithermal neutron flux at land/atmosphere interface that would be observed in ss if interface was	ϕ_{*eth}	n cm^{-2} a^{-1}	128157																																								
average neutron yield per stopped negative muon	Y_μ		0.404			0.262	0.000		0.001		0.059	0.001	0.000	0.081	0.001			0.000																											
slow negative muon stopping rate at land surface SLHL	$\Psi_\mu(0)$	g^{-1} a^{-1}	190																																								
fast muon flux at land surface SLHL	$\phi_{\mu 0}$	cm^{-2} a^{-1}	7.90E+05																																								
total muon induced neutron production at land surface	$P_{n\mu 0}$	cm^{-2} a^{-1}	81.377																																								
ratio of muon production rate to epithermal neutron production rate	R_μ	-	0.044																																								
macroscopic neutron scattering cross section of atmosphere	$\Sigma_{sn,a}$	cm^2 g^{-1}	0.3773																																								
thermal neutron diffusion coefficient in atmosphere	D_a	g cm^{-2}	0.926																																								
macroscopic absorption and moderation cross section for epithermal neutrons in atmosphere	$\Sigma_{ath,a}$	cm^2 g^{-1}	0.0548																																								

| | | |

Chlorine-36 exposure age and erosion rate determination: Please follow the instructions on the first worksheet

modifications regarding muonic 36Cl production

Sample name VEG01.18

1- Input

(and output for eroding surfaces)

	symbol	units	calculations	Uncertainties
element concentration in bulk rock: maior element as oxides [wt-%] and trace elements [wt-ppm]				
element concentration in target fraction: major element as oxides [wt-%] and Cl in [wt-ppm]				
uncertainty target element concentration in target fraction (oxides in [wt-%] and Cl in [wt-ppm])				
depth reference: top of sample		cm	0	
sample thickness		cm	3	
bulk rock density	rho	g cm^{-3}	2.702803712	
mass depth reference: center of sample	z	g cm^{-2}	4.054205568	
mass thickness	z_s	g cm^{-2}	8.108411136	
scaling factor for nucleonic production as a function of elevation, latitude (and temporal v	$S_{St,N}$, $S_{St,\mu}$	-	5.107	0.255
scaling factor for muonic production as a function of elevation, latitude (and temporal var	$S_{St,\mu}$	-	2.406	0.120
correction factor for shielding of a sample of arbitrary orientation by surrounding topogra	S_T	-	0.996917269	0.009969173
correction factor for geometry effects on spallogenic production	S_{shape}	-	1	0.03
correction factor for snow shielding for spallogenic production	S_{snow}	-	1	0.01
effective fast neutron attenuation coefficient	$\Lambda_{f,e}$	g cm^{-2}	160	
estimated ^{36}Cl concentration from inheritance at t_{exp}=0	$N_{inher}(0)$	atoms ^{36}Cl g^{-1}		
measured ^{36}Cl concentration in sample	N_{meas}	atoms ^{36}Cl g^{-1}	1.26E+06	1.45E+05
exposure duration (independently determined or estimated)	t_{expo}	a	13588	2361.983476
formation age of rock (independently determined or estimated) for radiogenic correction	t_{form}	a	200000000	1000
erosion rate	ε	mm ka^{-1}	0	0

bulk rock:	CaO [wt-%]	K2O [wt-%]	TiO2 [wt-%]	Fe2O3 [wt-%]	Cl [ppm]
	30.450	0.00	0.00	0.07	116.00
target fraction:					
	29.38	0.00	0.00	0.07	124.03
	0.61	0.01	0.01	0.01	17.12

	SiO2 [wt-%]	Na2O [wt-%]	MgO [wt-%]	Al2O3 [wt-%]	MnO [wt-%]	P2O5 [wt-%]	CO2 [wt-%]	H2O [wt-%]
	0.16	0.03	22.65	0.14	0.01	0.00		0.5
	0.16	0.03	22.65	0.14	0.01	0.00		0.50

	Li [ppm]	B [ppm]	Sm [ppm]	Gd [ppm]	Th [ppm]	U [ppm]
	0.55049839	2.45319	0.09	0.12	0.01	0.88
	0.55049839	2.45319	0.0855143	0.11758218	0.0106893	0.8765217

	Cr [ppm]	Be [ppm]	N [ppm]	F [ppm]	S [ppm]	Sc [ppm]	Co [ppm]	Ni [ppm]	Se [ppm]	Br [ppm]	Rb [ppm]	Sr [ppm]	Zr [ppm]	Mo [ppm]	Ru [ppm]	Te [ppm]	I [ppm]	Cs [ppm]	Ba [ppm]
	1.98	0.02				0.44	0.10	0.36			0.18	73.06	0.08	0.05				0.04	1.65
	1.9775185	0.0213786				0.44	0.10	0.36			0.18	73.06	0.08	0.05				0.04	1.65

2- Output A: exposure age of sample (only for uneroded surface)

decay constant for ^{36}Cl	λ_{36}	a^{-1}	2.30E-06	1.51998E-08
scaled total sample specific ^{36}Cl production rate without radiogenic	P_{total}	atoms ^{36}Cl g^{-1} a	92.5	11.5
time factor radiogenic	t_i		434216	2865.8
calculated concentration of radiogenically produced ^{36}Cl atoms for estimated age	N_i	atoms ^{36}Cl g^{-1}	26897.3	1356.5
estimated ^{36}Cl concentration from inheritance at time of sampling	$N_{inher}(t)$	atoms ^{36}Cl g^{-1}	0.0	
measured ^{36}Cl concentration in sample corrected from radiogenic component and inheritance	$N_{meas-r-inher}$	atoms ^{36}Cl g^{-1}	1.24E+06	144827.7
exposure age of sample	**t**	**a**	13588	2361

3- Output B: eroding surface

calculated ^{36}Cl concentration for an eroding sample	$N_{calc,total}$	atoms ^{36}Cl g^{-1}	1.26E+06
difference measured/calculated ^{36}Cl concentration in eroding sample	$\Delta N_{meas-calc}$		0.00%
erosion rate	ε	cm a^{-1}	0
time factor with erosion for spallation reaction	$t_{cosm,s}$		13378
time factor with erosion for capture of epithermal neutrons	$t_{cosm,eth}$		13378
time factor with erosion for capture of thermal neutrons	$t_{cosm,th}$		13378
time factor with erosion for capture of slow negative muons	$t_{cosm,\mu}$		13378
depth reference factor for spallogenic reaction	d_s		0.975
depth reference factor for capture of epithermal neutrons	d_{eth}		0.876
depth reference factor for capture of thermal neutrons	d_{th}		0.935
depth reference factor for capture of slow negative muons	d_μ		0.997
production rate coefficient corrected for sample thickness for spallogenic reaction	J_{Cs}		46.50
production rate coefficient corrected for sample thickness for capture of epithermal neutrons	J_{Ceth}		3.68
production rate coefficient corrected for sample thickness for capture of thermal neutrons	J_{Cth}		-35.10
production rate coefficient corrected for sample thickness for capture of slow negative muons	$J_{C\mu}$		2.44
production rate coefficient for spallogenic reaction	J_s		46.54
production rate coefficient for capture of epithermal neutrons	J_{eth}		3.68
production rate coefficient for capture of thermal neutrons	J_{th}		-35.14
production rate coefficient for capture of slow negative muons	J_μ		2.45

4- Output C: calculated ^{36}Cl contributions from all production mechanism

time factor cosmogenic without erosion	t_{cosm}		13378	2289
calculated ^{36}Cl concentration for given time + radiogenic	$N_{calc,total}$	atoms ^{36}Cl g^{-1}	1.26E+06	262148
difference measured/calculated ^{36}Cl concentration	$\Delta N_{meas-calc}$		0.00%	
contribution from each production mechanism:				
number of atoms ^{36}Cl per g by spallation of Ca	$N_{s,Ca}$	atoms ^{36}Cl g^{-1}	586029	46.35%
number of atoms ^{36}Cl per g by spallation of K	$N_{s,K}$	atoms ^{36}Cl g^{-1}	0	0.00%
number of atoms ^{36}Cl per g by spallation of Ti	$N_{s,Ti}$	atoms ^{36}Cl g^{-1}	0	0.00%
number of atoms ^{36}Cl per g by spallation of Fe	$N_{s,Fe}$	atoms ^{36}Cl g^{-1}	62	0.00%
number of atoms ^{36}Cl per g by spallation of target elements	N_s	atoms ^{36}Cl g^{-1}	586091	46.35%
number of atoms ^{36}Cl per g by capture of thermal neutrons	N_{th}	atoms ^{36}Cl g^{-1}	437082	34.57%
number of atoms ^{36}Cl per g by capture of epithermal neutrons	N_{eth}	atoms ^{36}Cl g^{-1}	123411	9.76%
number of atoms ^{36}Cl per g by capture of thermal and epithermal neutrons	N_n	atoms ^{36}Cl g^{-1}	560492	44.33%
number of atoms ^{36}Cl per g by capture of slow negative muons	N_μ	atoms ^{36}Cl g^{-1}	90975	7.19%
number of atoms ^{36}Cl per g by radiogenic production	N_i	atoms ^{36}Cl g^{-1}	26897	2.13%
				100.00%

5- elemental parameters

			Ca	K	Ti	Fe	Cl	O, rock	Si	Na	Mg	Al	Mn	P	C	H	O, water	Li	B	Sm	Gd	Th	U	Cr	Be	N	F	S	Sc	Co	Ni	Se	Br	Rb	Sr	Zr	Mo	Ru	Te	I	Cs	Ba
element concentration [wt-ppm] **bulk rock**		ppm	217718	0	0	489	116	178526	747	223	136580	741	77	0	0	560	4470	0.55049839	2.5	0.1	0.1	0.0106893	0.8765217	1.9775185	0.0213786	0	0	0	0.4382609	0.1015482	0.3634358	0	0	0.1817179	73.061291	0.0801697	0.0534464	0	0	0	0.0427572	1.6514952
element concentration dissolved sample [wt-ppm] in **target fraction**		ppm	210102	0	0	489	124	175491	747	223	136580	741	77	0	0	560	4470	0.55049839	2.45319	0.0855143	0.11758218	0.0106893	0.8765217	1.9775185	0.0213786	0	0	0	0.4382609	0.1015482	0.3634358	0	0	0.1817179	73.061291	0.0801697	0.0534464	0	0	0	0.0427572	1.6514952
atomic mass of element k (Reference: http://www.ciaaw.org/atomic-weights.html)	A_k	g mol^{-1}	40.078	39.0983	47.867	55.845	35.453	15.999	28.085	22.98977	24.305	26.981538	54.938043	30.973761	12.01	1.008	15.999	6.941	10.811	150.36	157.25	232.0377	238.02891	51.9961	9.012182	14.0067	18.998403	32.065	44.95591	58.9332	58.6934	78.96	79.904	85.4678	87.62	91.224	95.94	101.07	127.6	126.90447	132.90545	137.327
avoqadro			6.02E+23																																								
atomic concentration of element k in **bulk rock**	N_k	atoms g^{-1}	1.37E+22	3.27E+21	0.00E+00	0.00E+00	5.28E+18	1.97E+18	6.72E+21	1.60E+19	5.83E+18	3.38E+21	1.65E+19	8.48E+17	0.00E+00	0.00E+00	1.24E+20	1.68E+20	4.78E+16	1.37E+17	3.42E+14	4.50E+14	2.77E+13	2.22E+15	2.29E+16	1.43E+15	0.00E+00	0.00E+00	0.00E+00	5.87E+15	1.04E+15	3.73E+15	0.00E+00	0.00E+00	1.28E+15	5.02E+17	5.29E+14	3.35E+14	0.00E+00	0.00E+00	0.00E+00	1.94E+14	7.24E+15
atomic concentration of element k in **target fraction**	N_{Cl}	atoms g^{-1}					########																																				
dilute resonance integral for absorption of epithermal neutrons by element k	$I_{k,k}$	E^{-04} cm^2		0.233	1	3.1	1.36	13.83	0.0002693	0.082	0.311	0.038	0.17	13.4	0.079	0.0018	0	0.0002693	0	343	1400	390	83.3	277	1.6																	
average log decrement of energy loss per collision for element k	x_k	-		0.049	0.05	0.041	0.035	0.055	0.12	0.07	0.084	0.08	0.072	0.036	0.06321	0.1577605	1	0.12	0.264	0.174	0.013	0.013	0.008594	0.008379	0.038																	
neutron scattering cross section of element k	$\sigma_{n,s,k}$	E^{-24} cm^2		2.93	2.04	4.09	11.35	15.8	3.76	2.04	3.038	3.414	1.41	2.66	3.134	4.74	20.5	3.76	0.95	4.27	38	172	13.55	9.08	3.38																	
thermal neutron absorption cross section of element k	$\sigma_{a,k}$	E^{-24} cm^2		0.43	2.1	6.41	2.56	33.14	0.0002	0.171	0.517	0.0666	0.231	13.36	0.165	0.0035	0.33		70.5	767	9640	41560	7.34	2.68	3.1																	
proportion of muons stopped in element i that are captured by the nucleus	f_{cik}			0.864	0.83		0.906		0.223	0.671	0.432	0.538	0.582			0.09																											
average neutron yield per captured muon	Y_k			0.75	1.25		1.125		0.8	0.86	1	0.6	1.26			0.76																											

6- unscaled sample specific ^{36}Cl production rate by spallation of target elements

spallation production rate for Ca, SLHL	PR_{Ca}	atoms ^{36}Cl (g C	42		Braucher et al. 2011
mass concentration of Ca in **target fraction**	C_{Ca}	g Ca (g rock)$^{-1}$	0.210	0.001	
result unscaled ^{36}Cl production by spallation of ^{40}Ca	$\mathbf{P_{s,Ca}}$	atoms ^{36}Cl (g C	8.604	0.411	
spallation production rate for K, SLHL	PR_K	atoms ^{36}Cl (g K	148.1	7.1	Schimmelpfennig et al., 2014, St scaling
mass concentration of K in **target fraction**	C_K	g K (g rock)$^{-1}$	0.000	0.000	
result unscaled ^{36}Cl production by spallation of ^{39}K	$\mathbf{P_{s,K}}$	atoms ^{36}Cl (g K	0.000	0.012	
spallation production rate for Ti, SLHL	PR_{Ti}	atoms ^{36}Cl (g T	13		Fink et al., 2002
mass concentration of Ti in **target fraction**	C_{Ti}	g Ti (g rock)$^{-1}$	0.000	0.000	
result unscaled ^{36}Cl production by spallation of Ti	$\mathbf{P_{s,Ti}}$	atoms ^{36}Cl (g Ti	0.000	0.001	
spallation production rate for Fe, SLHL	PR_{Fe}	atoms ^{36}Cl (g F	1.9	0.285	Stone et al., 2005
mass concentration of Fe in **target fraction**	C_{Fe}	g Fe (g rock)$^{-1}$	0.000	0.000	
result unscaled ^{36}Cl production by spallation of Fe	$\mathbf{P_{s,Fe}}$	atoms ^{36}Cl (g Fe	0.001	0.000	
result unscaled sample specific ^{36}Cl production rate by spallation of target elements	$\mathbf{P_s}$	atoms ^{36}Cl (g)$^{-1}$	8.604	0.411	

7- unscaled sample specific ^{36}Cl production rate by capture of epithermal neutrons

						Ca	K	Ti	Fe	Cl	O, rock	Si	Na	Mg	Al	Mn	P	C	H	O, water	Li	B	Sm	Gd	Th	U	Cr	Be	N	F	S	Sc	Co	Ni	Se	Br	Rb	Sr	Zr	Mo	Ru	Te	I	Cs	Ba
effective macroscopic resonance integral for absorption of epithermal neutrons	I_{eff}	cm^2 g^{-1}	0.0010	7.62E-04	0.00E+00	0.00E+00	7.18E-06	2.73E-05	1.81E-06	1.31E-06	1.81E-06	1.29E-04	2.81E-06	1.14E-05		0.00E+00	0.00E+00		0.00E+00	4.69E-05	4.79E-07	1.76E-07			3.66E-08																			
fraction of epithermal neutrons absorbed by ^{36}Cl (**target fraction**)	f_{eth}	-	0.0294																																								
neutron macroscopic scattering cross section in subsurface	Σ_{sn}	cm^2 g^{-1}	0.0497	9.59E-03	0.00E+00	0.00E+00	5.99E-05	3.11E-05	2.53E-02	3.27E-05	1.77E-05	1.16E-02	2.33E-05	1.75E-06	0.00E+00	0.00E+00	0.00E+00	2.54E-03	6.33E-04	4.54E-08	5.83E-07	1.30E-08	7.74E-08	3.76E-10	2.01E-08	7.74E-08	0.00E+00	0.00E+00	0.00E+00	0.00E+00	0.00E+00	0.00E+00	0.00E+00	0.00E+00	0.00E+00	0.00E+00	0.00E+00	0.00E+00	0.00E+00	0.00E+00	0.00E+00	0.00E+00	0.00E+00	0.00E+00
scattering rate parameter	B		7.05E-03	4.70E-04	0.00E+00	0.00E+00	2.10E-06	1.71E-06	3.03E-03	2.29E-06	1.49E-06	9.24E-04	1.68E-06	6.29E-08	0.00E+00	0.00E+00	2.54E-03	7.59E-05	1.20E-08	1.02E-07	1.69E-10	1.01E-09	3.23E-12	1.69E-10	2.94E-09	0.00E+00	0.00E+00	0.00E+00	0.00E+00	0.00E+00	0.00E+00	0.00E+00	0.00E+00	0.00E+00	0.00E+00	0.00E+00	0.00E+00	0.00E+00	0.00E+00	0.00E+00	0.00E+00	0.00E+00	0.00E+00	0.00E+00
mean macroscopic log decrement of energy loss per collision in subsurface	X_{sk}		0.142																																								
macroscopic absorption and moderation cross section for epithermal neutrons	Σ_{eth}	cm^2 g^{-1}	0.007																																								
attenuation length for absorption and moderation of epithermal neutron flux	Λ_{eth}	g cm^{-2}	139.141																																								
	$A_k * N_k$	atoms mol^{-1}	3.22E+23	1.31E+23	0.00E+00	0.00E+00	2.95E+20	6.99E+19	1.08E+23	4.50E+20	1.34E+20	8.22E+22	4.46E+20	4.66E+19		0.00E+00	1.25E+20		3.32E+17	1.48E+18	5.15E+16	7.08E+16			1.19E+18																			
average atomic weight in subsurface	A_{sa}	g mol^{-1}	23.511																																								
production rate of epithermal neutrons from fast neutrons in atmosphere at land/atm interface	$P_n(0)$	n cm^{-2} a^{-1}	696	185 Marrero et al. 2016, St scaling																																								
Ratio of epithermal neutron production in subsurface to that in atmosphere	R_{eth}	-	1.27																																								
epithermal neutron diffusion coefficient in subsurface	D_{eth}	g cm^{-2}	6.90																																								
apparent fast neutron attenuation coefficient	Λ_f	g cm^{-2}	160																																								
epithermal neutron flux at land/atmosphere interface that would be observed in ss if interface was	ϕ^*_{eth}	n cm^{-2} a^{-1}	128118																																								
average neutron yield per stopped negative muon	Y_μ		0.404	0.261	0.000		0.001		0.059	0.001	0.000	0.081	0.001			0.000																												
slow negative muon stopping rate at land surface SLHL	$\Psi_\mu(0)$	μ g^{-1} a^{-1}	190																																								
fast muon flux at land surface SLHL	$\phi_{\mu 0}$	μ cm^{-2} a^{-1}	7.90E+05																																								
total muon induced neutron production at land surface	$P_{n\mu 0}$	μ cm^{-2} a^{-1}	81.371																																								
ratio of muon production rate to epithermal neutron production rate	R_μ	-	0.043																																								
macroscopic neutron scattering cross section of atmosphere	$\Sigma_{sn,a}$	cm^2 g^{-1}	0.3773																																								
thermal neutron diffusion coefficient in atmosphere	D_a	g cm^{-2}	0.926																																								
macroscopic absorption and moderation cross section for epithermal neutrons in atmosphere	$\Sigma_{ath,a}$	cm^2 g^{-1}	0.0548																																								

epithermal neutron diffusion length in atmosphere	$L_{eth,a}$	g cm^{-2}	4.015	
epithermal neutron flux at land/atmosphere interface that would be observed in atm if interface wa	$\phi^*_{eth,a}$	n cm^{-2} a^{-1}	12709	
difference between hypothetical equilibrium epithermal neutron fluxes in atmosphere and subsurf	$\Delta\phi^*_{eth}$	n cm^{-2} a^{-1}	-115409	
adjusted difference between hypothetical equilibrium epithermal neutron fluxes in atmosphere an	$\Delta\phi^{**}_{eth,a}$	n cm^{-2} a^{-1}	126412	
epithermal neutron diffusion length in subsurface	L_{eth}	g cm^{-2}	30.536	
difference between phi_star_eth and actual epithermal neutron flux at land surface	$(F.\Delta\phi)^*_{eth}$	-	-70244	
slow muon attenuation length	Λ_{sl}	g cm^{-2}	1510	
epithermal neutron flux (concentration)	$\phi_{eth,total}$	n cm^{-2} a^{-1}	65541	
result unscaled sample specific ^{36}Cl production rate by capture of epithermal neutrons	**P_{eth}**	**atoms ^{36}Cl g^{-1} a^{-1}**	**1.817**	0.54507

| **8- unscaled sample specific ^{36}Cl production rate by capture of thermal neutrons** | | | |

Chlorine-36 exposure age and erosion rate determination: Please follow the instructions on the first worksheet

modifications regarding muonic 36Cl production

Sample name: CRU01.18

1- Input

(and output for eroding surfaces)

	symbol	units	calculations	Uncertainties
element concentration in bulk rock: major element as oxides [wt-%] and trace elements [wt-ppm]				
element concentration in target fraction: major element as oxides [wt-%] and Cl in [wt-pm]				
uncertainty target element concentration in target fraction (oxides in [wt-%] and Cl in [wt-ppm])				
depth reference: top of sample		cm	0	
sample thickness		cm	3.5	
bulk rock density	rho	g cm^{-3}	2.772557516	
mass depth reference: center of sample	z	g cm^{-2}	4.851976182	
mass thickness	z_s	g cm^{-2}	9.703952363	
scaling factor for nucleonic production as a function of elevation, latitude (and temporal v	$S_{el,e}$, $S_{el,n}$	-	5.304	0.265
scaling factor for muonic production as a function of elevation, latitude (and temporal var	$S_{el,\mu}$	-	2.459	0.123
correction factor for shielding of a sample of arbitrary orientation by surrounding topogra	S_T	-	0.953070497	0.009530705
correction factor for geometry effects on spallogenic production	S_{shape}	-	1	0.03
correction factor for snow shielding for spallogenic production	S_{snow}	-	1	0.01
effective fast neutron attenuation coefficient	$\Lambda_{f,e}$	g cm^{-2}	160	
estimated ^{36}Cl concentration from inheritance at t_{expo}=0	$N_{inher}(0)$	atoms ^{36}Cl g^{-1}		
measured ^{36}Cl concentration in sample	N_{meas}	atoms ^{36}Cl g^{-1}	6.98E+05	4.66E+04
exposure duration (independently determined or estimated)	t_{expo}	a	9766	1132.639081
formation age of rock (independently determined or estimated) for radiogenic correction	t_{form}	a	200000000	1000
erosion rate	ε	mm ka^{-1}	0	0

	CaO [wt-%]	K2O [wt-%]	TiO2 [wt-%]	Fe2O3 [wt-%	Cl [ppm]
bulk rock:					
3ĝ.710	0.02	0.01	0.08	59.00	
target fraction:					
	29.67	0.02	0.01	0.08	49.36
	0.17	0.01	0.01	0.01	3.92

	SiO2 [wt-%]	Na2O [wt-%]	MgO [wt-%]	Al2O3 [wt-%]	MnO [wt-%]	P2O5 [wt-%]	CO2 [wt-%]	H2O [wt-%]
	0.39	0.02	21.70	0.24	0.01	0.00		0.5
	0.39	0.02	21.70	0.24	0.01	0.00		0.50

	Li [ppm]	B [ppm]	Sm [ppm]	Gd [ppm]	Th [ppm]	U [ppm]
	1.57861196	3.2517183	0.07	0.08	0.05	4.04
	1.57861196	3.2517183	0.0667019	0.077818899	0.0500264	4.0410243

	Cr [ppm]	Be [ppm]	N [ppm]	F [ppm]	S [ppm]	Sc [ppm]	Co [ppm]	Ni [ppm]	Se [ppm]	Br [ppm]	Rb [ppm]	Sr [ppm]	Zr [ppm]	Mo [ppm]	Ru [ppm]	Te [ppm]	I [ppm]	Cs [ppm]	Ba [ppm]
	2.07	0.02				0.44	0.17	1.56			0.40	105.44	0.22	0.44				0.21	3.59
	2.0733178	0.022234				0.44	0.17	1.56			0.40	105.44	0.22	0.44				0.21	3.59

2- Output A: exposure age of sample (only for uneroded surface)

decay constant for ^{36}Cl	λ_{36}	a^{-1}	2.30E-06	1.51998E-08
scaled total sample specific ^{36}Cl production rate without radiogenic	P_{total}	atoms ^{36}Cl g^{-1} a	67.4	6.0
time factor radiogenic	t_r		434216	2865.8
calculated concentration of radiogenically produced ^{36}Cl atoms for estimated age	N_r	atoms ^{36}Cl g^{-1}	47629.4	2402.1
estimated ^{36}Cl concentration from inheritance at time of sampling	$N_{inher}(t)$	atoms ^{36}Cl g^{-1}	0.0	
measured ^{36}Cl concentration in sample corrected from radiogenic component and inheritance	$N_{meas-r-inher}$	atoms ^{36}Cl g^{-1}	6.51E+05	46684.0
exposure age of sample	**t**	**a**	9765	1132.6

3- Output B: eroding surface

calculated ^{36}Cl concentration for an eroding sample	$N_{calc,total}$	atoms ^{36}Cl g^{-1}	6.98E+05	
difference measured/calculated ^{36}Cl concentration in eroding sample	$\Delta N_{meas-calc}$		0.00%	
erosion rate	ε	cm a^{-1}	0	0
time factor with erosion for spallation reaction	$t_{coem,s}$		9657	1107
time factor with erosion for capture of epithermal neutrons	$t_{coem,eth}$		9657	1107
time factor with erosion for capture of thermal neutrons	$t_{coem,th}$		9657	1107
time factor with erosion for capture of slow negative muons	$t_{coem,\mu}$		9657	1107
depth reference factor for spallogenic reaction	d_s		0.970	
depth reference factor for capture of epithermal neutrons	d_{eth}		0.855	
depth reference factor for capture of thermal neutrons	d_{th}		0.923	
depth reference factor for capture of slow negative muons	d_μ		0.997	
production rate coefficient corrected for sample thickness for spallogenic reaction	$J_{Q,s}$		23.78	
production rate coefficient corrected for sample thickness for capture of epithermal neutrons	$J_{Q,eth}$		1.51	
production rate coefficient corrected for sample thickness for capture of thermal neutrons	$J_{Q,th}$		-13.88	
production rate coefficient corrected for sample thickness for capture of slow negative muons	$J_{Q,\mu}$		1.77	
production rate coefficient for spallogenic reaction	J_s		23.81	
production rate coefficient for capture of epithermal neutrons	J_{eth}		1.51	
production rate coefficient for capture of thermal neutrons	J_{th}		-13.90	
production rate coefficient for capture of slow negative muons	J_μ		1.77	

4- Output C: calculated ^{36}Cl contributions from all production mechanism

time factor cosmogenic without erosion	t_{coem}		9657	1107
calculated ^{36}Cl concentration for given time + radiogenic	$N_{calc,total}$	atoms ^{36}Cl g^{-1}	6.98E+05	94669
difference measured/calculated ^{36}Cl concentration	$\Delta N_{meas-calc}$		0.00%	
contribution from each production mechanism:				
number of atoms ^{36}Cl per g by spallation of Ca	$N_{s,Ca}$	atoms ^{36}Cl g^{-1}	421949	60.42%
number of atoms ^{36}Cl per g by spallation of K	$N_{s,K}$	atoms ^{36}Cl g^{-1}	1164	0.17%
number of atoms ^{36}Cl per g by spallation of Ti	$N_{s,Ti}$	atoms ^{36}Cl g^{-1}	37	0.01%
number of atoms ^{36}Cl per g by spallation of Fe	$N_{s,Fe}$	atoms ^{36}Cl g^{-1}	50	0.01%
number of atoms ^{36}Cl per g by spallation of target elements	N_s	atoms ^{36}Cl g^{-1}	423201	60.60%
number of atoms ^{36}Cl per g by capture of thermal neutrons	N_{th}	atoms ^{36}Cl g^{-1}	126238	18.08%
number of atoms ^{36}Cl per g by capture of epithermal neutrons	N_{eth}	atoms ^{36}Cl g^{-1}	36092	5.17%
number of atoms ^{36}Cl per g by capture of thermal and epithermal neutrons	N_n	atoms ^{36}Cl g^{-1}	162330	23.25%
number of atoms ^{36}Cl per g by capture of slow negative muons	N_μ	atoms ^{36}Cl g^{-1}	65150	9.33%
number of atoms ^{36}Cl per g by radiogenic production	N_r	atoms ^{36}Cl g^{-1}	47629	6.82%
				100.00%

5- elemental parameters

				Ca	K	Ti	Fe	Cl	O, rock	Si	Na	Mg	Al	Mn	P	C	H	O, water	Li	B	Sm	Gd	Th	U	Cr	Be	N	F	S	Sc	Co	Ni	Se	Br	Rb	Sr	Zr	Mo	Ru	Te	I	Cs	Ba
element concentration [wt-ppm] **bulk rock**		ppm		219577	166	60	559	59	177271	1821	148	130851	1270	77	0	0	560	4470	1.57861196	3.3	0.1	0.1	0.0500264	4.0410243	2.0733178	0.022234				0.4446794	0.1667548	1.556378	0	0	0.4002115	105.44461	0.2167812	0.4391209	0	0	0	0.2112227	3.5852279
element concentration dissolved sample [wt-ppm] in **target fraction**		ppm		212116	166	60	559	49	174297	1821	148	130851	1270	77	0	0	560	4470	1.57861196	3.2517183	0.0667019	0.077818899	0.0500264	4.0410243	2.0733178	0.022234	0	0	0	0.4446794	0.1667548	1.556378	0	0	0.4002115	105.44461	0.2167812	0.4391209	0	0	0	0.2112227	3.5852279
atomic mass of element k (Reference: http://www.ciaaw.org/atomic-weights.htm)	A_k	g mol^{-1}		40.078	39.0983	47.867	55.845	35.453	15.999	28.085	22.98977	24.305	26.981538	54.938043	30.973761	12.01	1.008	15.999	6.941	10.811	150.36	157.25	232.0377	238.02891	51.9961	9.012182	14.0067	18.998403	32.065	44.95591	58.9332	58.6934	78.96	79.904	85.4678	87.62	91.224	95.94	101.07	127.6	126.90447	132.90545	137.327
avogadro			6.02E+23																																								
atomic concentration of element k in **bulk rock**	N_k	atoms g^{-1}	1.36E+22	3.30E+21	2.56E+18	7.55E+17	6.03E+18	1.00E+18	6.67E+21	3.91E+19	3.89E+18	3.24E+21	2.83E+19	8.48E+17	0.00E+00	0.00E+00	1.21E+20	1.68E+20	1.37E+17	1.81E+17	2.67E+14	2.98E+14	1.30E+14	1.02E+16	2.40E+16	1.49E+15	0.00E+00	0.00E+00	0.00E+00	5.96E+15	1.70E+15	1.60E+16	0.00E+00	0.00E+00	2.82E+15	7.25E+17	1.43E+15	2.76E+15	0.00E+00	0.00E+00	0.00E+00	9.57E+14	1.57E+16
atomic concentration of element k in **target fraction**	N_{Cl}	atoms g^{-1}						#########																																				
dilute resonance integral for absorption of epithermal neutrons by element k	$I_{0,k}$	E^{-24} cm^2		0.233	1	3.1	1.36	13.83	0.0002693	0.082	0.311	0.038	0.17	13.4	0.079	0.0018	0	0.0002693	0	343	1400	390	83.3	277	1.6																		
average log decrement of energy loss per collision for element k	x_k	-		0.049	0.05	0.041	0.035	0.055	0.12	0.07	0.084	0.08	0.072	0.036	0.06321	0.157760047	1	0.12	0.264	0.174	0.013	0.013	0.008594	0.008379	0.038																		
neutron scattering cross section of element k	$\sigma_{sct,k}$	E^{-24} cm^2		2.93	2.04	4.09	11.35	15.8	3.76	2.04	3.038	3.414	1.41	2.06	3.134	4.74	20.5	3.76	0.95	4.27	38	172	13.55	9.08	3.38																		
thermal neutron absorption cross section of element k	$\sigma_{a,k}$	E^{-24} cm^2		0.43	2.1	6.41	2.56	33.14	0.0002	0.171	0.517	0.0666	0.231	13.36	0.165	0.0035	0.33		70.5	767	9640	41560	7.34	2.68	3.1																		
proportion of muons stopped in element i that are captured by the nucleus	f_{cik}			0.864	0.83		0.906		0.223	0.671	0.432	0.538	0.582			0.09																												
average neutron yield per captured muon	Y_n			0.75	1.25		1.125		0.8	0.86	1	0.6	1.26			0.76																												

6- unscaled sample specific ^{36}Cl production rate by spallation of target elements

spallation production rate for Ca, SLHL	PR_{Ca}	atoms ^{36}Cl (g C	42	2	Braucher et al. 2011
mass concentration of Ca in **target fraction**	C_{Ca}	g Ca (g rock)$^{-1}$	0.212	0.001	
result unscaled ^{36}Cl production by spallation of ^{40}Ca	$\mathbf{P_{s,Ca}}$	atoms ^{36}Cl (g C	8.643	0.415	
spallation production rate for K, SLHL	PR_K	atoms ^{36}Cl (g K	148.1	7.8	Schimmelpfennig et al., 2014, St scaling
mass concentration of K in **target fraction**	C_K	g K (g rock)$^{-1}$	0.000	0.000	
result unscaled ^{36}Cl production by spallation of ^{39}K	$\mathbf{P_{s,K}}$	atoms ^{36}Cl (g K	0.024	0.012	
spallation production rate for Ti, SLHL	PR_{Ti}	atoms ^{36}Cl (g T	13	3	Fink et al., 2002
mass concentration of Ti in **target fraction**	C_{Ti}	g Ti (g rock)$^{-1}$	0.000	0.000	
result unscaled ^{36}Cl production by spallation of Ti	$\mathbf{P_{s,Ti}}$	atoms ^{36}Cl (g T	0.001	0.001	
spallation production rate for Fe, SLHL	PR_{Fe}	atoms ^{36}Cl (g F	1.9	0.388	Stone et al., 2005
mass concentration of Fe in **target fraction**	C_{Fe}	g Fe (g rock)$^{-1}$	0.001	0.000	
result unscaled ^{36}Cl production by spallation of Fe	$\mathbf{P_{s,Fe}}$	atoms ^{36}Cl (g F	0.001	0.000	
result unscaled sample specific ^{36}Cl production rate by spallation of target elements	$\mathbf{P_s}$	atoms ^{36}Cl (g)$^{-1}$	8.668	0.415	

7- unscaled sample specific ^{36}Cl production rate by capture of epithermal neutrons

						Ca	K	Ti	Fe	Cl	O, rock	Si	Na	Mg	Al	Mn	P	C	H	O, water	Li	B	Sm	Gd	Th	U	Cr	Be	N	F	S	Sc	Co	Ni	Se	Br	Rb	Sr	Zr	Mo	Ru	Te	I	Cs	Ba
effective macroscopic resonance integral for absorption of epithermal neutrons	I_{eff}	cm^2 g^{-1}	0.0010			7.69E-04	2.56E-06	2.34E-06	8.20E-06	1.39E-05	1.80E-06	3.20E-06	1.21E-06	1.23E-04	4.82E-06	1.14E-05		0.00E+00	0.00E+00		0.00E+00	6.21E-05	3.74E-07	1.16E-07		3.84E-08																		
fraction of epithermal neutrons absorbed by ^{35}Cl **(target fraction)**	f_{eth}	-	0.0116																																								
neutron macroscopic scattering cross section in subsurface	Σ_{scl}	cm^2 g^{-1}	0.0492			9.67E-03	5.22E-06	3.09E-06	6.84E-05	1.58E-05	2.51E-02	7.97E-05	1.18E-05	1.11E-02	4.00E-05	1.75E-06	0.00E+00	0.00E+00	2.47E-03	6.33E-04	1.30E-07	7.73E-07	1.02E-08	5.13E-08	1.76E-09	9.28E-08	8.12E-08	0.00E+00	0.00E+00	0.00E+00	0.00E+00	0.00E+00	0.00E+00	0.00E+00	0.00E+00	0.00E+00	0.00E+00	0.00E+00	0.00E+00	0.00E+00	0.00E+00	0.00E+00	0.00E+00	0.00E+00	0.00E+00
scattering rate parameter	B		6.93E-03			4.74E-04	2.61E-07	1.27E-07	2.40E-06	8.71E-07	3.01E-03	5.58E-06	9.92E-07	8.85E-04	2.88E-06	6.29E-08	0.00E+00	0.00E+00	2.47E-03	7.59E-05	3.43E-08	1.35E-07	1.32E-10	6.66E-10	1.51E-11	7.78E-10	3.08E-09																		
mean macroscopic log decrement of energy loss per collision in subsurface	X_{ss}		0.141																																								
macroscopic absorption and moderation cross section for epithermal neutrons	Σ_{eth}	cm^2 g^{-1}	0.007																																								
attenuation length for absorption and moderation of epithermal neutron flux	Λ_{eth}	g cm^{-2}	141.402																																								
	$A_k * N_K$	atoms mol^{-1}	3.20E+23			1.32E+23	1.00E+20	3.61E+19	3.37E+20	3.55E+19	1.07E+23	1.10E+21	8.94E+19	7.88E+22	7.65E+20	4.66E+19		0.00E+00	1.22E+20		9.51E+17	1.96E+18	4.02E+16	4.69E+16		1.25E+18																		
average atomic weight in subsurface	A_{ss}	g mol^{-1}	23.584																																								
production rate of epithermal neutrons from fast neutrons in atmosphere at land/atm interface	$P_n(0)$	n cm^{-2} a^{-1}	696	185	Marrero et al. 2016, St scaling																																							
Ratio of epithermal neutron production in subsurface to that in atmosphere	R_{eth}	-	1.28																																								
epithermal neutron diffusion coefficient in subsurface	D_{eth}	g cm^{-2}	6.98																																								
apparent fast neutron attenuation coefficient	Λ_f	g cm^{-2}	160																																								
epithermal neutron flux at land/atmosphere interface that would be observed in ss if interface wa	ϕ^*_{eth}	n cm^{-2} a^{-1}	130544																																								
average neutron yield per stopped negative muon	Y_n		0.407			0.265	0.000		0.001		0.059	0.002	0.000	0.078	0.002			0.000																											
slow negative muon stopping rate at land surface SLHL	$\Psi_\mu(0)$	μ g^{-1} a^{-1}	190																																								
fast muon flux at land surface SLHL	$\phi_{\mu f0}$	μ cm^{-2} a^{-1}	7.90E+05																																								

total muon induced neutron production at land surface	$P_{n\mu 0}$	μ cm^{-2} a^{-1}	81.967	
ratio of muon production rate to epithermal neutron production rate	R_μ	-	0.043	
macroscopic neutron scattering cross section of atmosphere	$\Sigma_{sc,a}$	cm^2 g^{-1}	0.3773	
thermal neutron diffusion coefficient in atmosphere	D_a	g cm^{-2}	0.926	
macroscopic absorption and moderation cross section for epithermal neutrons in atmosphere	$\Sigma_{eth,a}$	cm^2 g^{-1}	0.0548	
epithermal neutron diffusion length in atmosphere	$L_{eth,a}$	g cm^{-2}	4.015	
epithermal neutron flux at land/atmosphere interface that would be observed in atm if interface w	$\phi^*_{eth,a}$	n cm^{-2} a^{-1}	12709	
difference between hypothetical equilibrium epithermal neutron fluxes in atmosphere and subsur	$\Delta\phi^*_{eth}$	n cm^{-2} a^{-1}	-117835	
adjusted difference between hypothetical equilibrium epithermal neutron fluxes in atmosphere ar	$\Delta\phi^{**}_{eth,a}$	n cm^{-2} a^{-1}	128858	
epithermal neutron diffusion length in subsurface	L_{eth}	g cm^{-2}	30.966	
difference between phi_star_eth and actual epithermal neutron flux at land surface	$(F,\Delta\phi)^*_{eth}$	-	-71924	
slow muon attenuation length	Λ_μ	g cm^{-2}	1510	
epithermal neutron flux (concentration)	$\phi_{eth,total}$	n cm^{-2} a^{-1}	67365	
result unscaled sample specific ^{36}Cl production rate by capture of epithermal neutrons	$\mathbf{P_{eth}}$	**atoms ^{36}Cl g^{-1} a^{-1}**	**0.742**	0.22263

| **8- unscaled sample specific ^{36}Cl production rate by capture of thermal neutrons** | | | |

Chlorine-36 exposure age and erosion rate determination: Please follow the instructions on the first worksheet

modifications regarding muonic 36Cl production

Sample name PIC01.18

1- Input

(and output for eroding surfaces)

	symbol	units	calculations	Uncertainties
element concentration in bulk rock: maior element as oxides [wt-%] and trace elements [wt-ppm]				
element concentration in target fraction: major element as oxides [wt-%] and Cl in [wt-ppm]				
uncertainty target element concentration in target fraction (oxides in [wt-%] and Cl in [wt-ppm])				
depth reference: top of sample		cm	0	
sample thickness		cm	2.5	
bulk rock density	rho	g cm^{-3}	2.76556468	
mass depth reference: center of sample	z	g cm^{-2}	3.45695585	
mass thickness	z_s	g cm^{-2}	6.9139117	
scaling factor for nucleonic production as a function of elevation, latitude (and temporal v	$S_{St/A}$, $S_{St/N}$	-	4.599	0.230
scaling factor for muonic production as a function of elevation, latitude (and temporal var	$S_{St/\mu}$	-	2.266	0.113
correction factor for shielding of a sample of arbitrary orientation by surrounding topogra	S_T	-	0.99586758	0.009958676
correction factor for geometry effects on spallogenic production	S_{shape}	-	1	0.03
correction factor for snow shielding for spallogenic production	S_{snow}	-	1	0.01
effective fast neutron attenuation coefficient	$\Lambda_{f,e}$	g cm^{-2}	160	
estimated ^{36}Cl concentration from inheritance at t_{exp}=0	$N_{inher}(0)$	atoms ^{36}Cl g^{-1}		
measured ^{36}Cl concentration in sample	N_{meas}	atoms ^{36}Cl g^{-1}	1.36E+06	1.41E+05
exposure duration (independently determined or estimated)	t_{expo}	a	17960	2835.644435
formation age of rock (independently determined or estimated) for radiogenic correction	t_{form}	a	200000000	1000
erosion rate	ε	mm ka^{-1}	0	0

	CaO [wt-%]	K2O [wt-%]	TiO2 [wt-%]	Fe2O3 [wt-%]	Cl [ppm]	SiO2 [wt-%]	Na2O [wt-%]	MgO [wt-%]	Al2O3 [wt-%]	MnO [wt-%]	P2O5 [wt-%]	CO2 [wt-%]	H2O [wt-%]
bulk rock:													
	30.160	0.02	0.01	0.06	96.00	0.46	0.04	22.36	0.40	0.01	0.00		0.5
target fraction:													
	29.48	0.02	0.01	0.06	97.73	0.46	0.04	22.36	0.40	0.01	0.00		0.50
	0.15	0.01	0.01	0.01	12.16								

	Li [ppm]	B [ppm]	Sm [ppm]	Gd [ppm]	Th [ppm]	U [ppm]
	0.83987577	2.1728399	0.09	0.12	0.03	1.45
	0.83987577	2.1728399	0.0921154	0.124626727	0.0270928	1.4521723

	Cr [ppm]	Be [ppm]	N [ppm]	F [ppm]	S [ppm]	Sc [ppm]	Co [ppm]	Ni [ppm]	Se [ppm]	Br [ppm]	Rb [ppm]	Sr [ppm]	Zr [ppm]	Mo [ppm]	Ru [ppm]	Te [ppm]	I [ppm]	Cs [ppm]	Ba [ppm]
	1.12	0.03				0.45	0.07	0.34			0.55	100.19	0.07	0.08				1.12	1.45
	1.1216405	0.0325113				0.45	0.0704412	0.3413689	0	0	0.5472739	100.18905	0.0650226	0.0758597	0	0	0	1.1216405	1.4467537

2- Output A: exposure age of sample (only for uneroded surface)

decay constant for ^{36}Cl	λ_{36}	a^{-1}	2.30E-06	1.51998E-08
scaled total sample specific ^{36}Cl production rate without radiogenic	P_{total}	atoms ^{36}Cl g^{-1} a	75.5	8.5
time factor radiogenic	t_i		434216	2865.8
calculated concentration of radiogenically produced ^{36}Cl atoms for estimated age	N_i	atoms ^{36}Cl g^{-1}	35426.9	1786.7
estimated ^{36}Cl concentration from inheritance at time of sampling	$N_{inher}(t)$	atoms ^{36}Cl g^{-1}	0.0	
measured ^{36}Cl concentration in sample corrected from radiogenic component and inheritance	$N_{meas-inher}$	atoms ^{36}Cl g^{-1}	1.33E+06	141308.7
exposure age of sample	**t**	**a**	17960	2835

3- Output B: eroding surface

calculated ^{36}Cl concentration for an eroding sample	$N_{calc,total}$	atoms ^{36}Cl g^{-1}	1.36E+06
difference measured/calculated ^{36}Cl concentration in eroding sample	$\Delta N_{meas-calc}$		0.00%
erosion rate	ε	cm a^{-1}	0
time factor with erosion for spallation reaction	$t_{cosm,s}$		17594
time factor with erosion for capture of epithermal neutrons	$t_{cosm,eth}$		17594
time factor with erosion for capture of thermal neutrons	$t_{cosm,th}$		17594
time factor with erosion for capture of slow negative muons	$t_{cosm,\mu}$		17594
depth reference factor for spallogenic reaction	d_s		0.979
depth reference factor for capture of epithermal neutrons	d_{eth}		0.893
depth reference factor for capture of thermal neutrons	d_{th}		0.944
depth reference factor for capture of slow negative muons	d_μ		0.998
production rate coefficient corrected for sample thickness for spallogenic reaction	$J_{Cl,s}$		38.84
production rate coefficient corrected for sample thickness for capture of epithermal neutrons	$J_{Cl,eth}$		2.92
production rate coefficient corrected for sample thickness for capture of thermal neutrons	$J_{Cl,th}$		-28.01
production rate coefficient corrected for sample thickness for capture of slow negative muons	$J_{Cl,\mu}$		2.32
production rate coefficient for spallogenic reaction	J_s		38.87
production rate coefficient for capture of epithermal neutrons	J_{eth}		2.92
production rate coefficient for capture of thermal neutrons	J_{th}		-28.03
production rate coefficient for capture of slow negative muons	J_μ		2.32

4- Output C: calculated ^{36}Cl contributions from all production mechanism

time factor cosmogenic without erosion	t_{cosm}		17594	2721
calculated ^{36}Cl concentration for given time + radiogenic	$N_{calc,total}$	atoms ^{36}Cl g^{-1}	1.36E+06	253684
difference measured/calculated ^{36}Cl concentration	$\Delta N_{meas-calc}$		0.00%	
contribution from each production mechanism:				
number of atoms ^{36}Cl per g by spallation of Ca	$N_{s,Ca}$	atoms ^{36}Cl g^{-1}	698064	51.21%
number of atoms ^{36}Cl per g by spallation of K	$N_{s,K}$	atoms ^{36}Cl g^{-1}	1939	0.14%
number of atoms ^{36}Cl per g by spallation of Ti	$N_{s,Ti}$	atoms ^{36}Cl g^{-1}	62	0.00%
number of atoms ^{36}Cl per g by spallation of Fe	$N_{s,Fe}$	atoms ^{36}Cl g^{-1}	63	0.00%
number of atoms ^{36}Cl per g by spallation of target elements	N_s	atoms ^{36}Cl g^{-1}	700127	51.36%
number of atoms ^{36}Cl per g by capture of thermal neutrons	N_{th}	atoms ^{36}Cl g^{-1}	401132	29.43%
number of atoms ^{36}Cl per g by capture of epithermal neutrons	N_{eth}	atoms ^{36}Cl g^{-1}	114307	8.39%
number of atoms ^{36}Cl per g by capture of thermal and epithermal neutrons	N_n	atoms ^{36}Cl g^{-1}	515439	37.81%
number of atoms ^{36}Cl per g by capture of slow negative muons	N_μ	atoms ^{36}Cl g^{-1}	112201	8.23%
number of atoms ^{36}Cl per g by radiogenic production	N_r	atoms ^{36}Cl g^{-1}	35427	2.60%
				100.00%

5- elemental parameters

			Ca	K	Ti	Fe	Cl	O, rock	Si	Na	Mg	Al	Mn	P	C	H	O, water	Li	B	Sm	Gd	Th	U	Cr	Be	N	F	S	Sc	Co	Ni	Se	Br	Rb	Sr	Zr	Mo	Ru	Te	I	Cs	Ba
element concentration [wt-ppm] **bulk rock**		ppm	215644	166	60	419	96	179441	2148	297	134831	2116	77	0	0	560	4470	0.83987577	2.2	0.1	0.1	0.0270928	1.4521723	1.1216405	0.0325113				0.4497399	0.0704412	0.3413689			0.5472739	100.18905	0.0650226	0.0758597				1.1216405	1.4467537
element concentration dissolved sample [wt-ppm] in **target fraction**		ppm	210759	166	60	419	98	177494	2148	297	134831	2116	77	0	0	560	4470	0.83987577	2.1728399	0.0921154	0.124626727	0.0270928	1.4521723	1.1216405	0.0325113	0	0	0	0.4497399	0.0704412	0.3413689	0	0	0.5472739	100.18905	0.0650226	0.0758597	0	0	0	1.1216405	1.4467537
atomic mass of element k (Reference: http://www.ciaaw.org/atomic-weights.htm)	A_k	g mol^{-1}	40.078	39.0983	47.867	55.845	35.453	15.999	28.085	22.98977	24.305	26.981538	54.938043	30.973761	12.01	1.008	15.999	6.941	10.811	150.36	157.25	232.0377	238.02891	51.9961	9.012182	14.0067	18.998403	32.065	44.95591	58.9332	58.6934	78.96	79.904	85.4678	87.62	91.224	95.94	101.07	127.6	126.90447	132.90545	137.327
avoqadro			6.02E+23																																							
atomic concentration of element k in **bulk rock**	N_k	atoms g^{-1}	3.24E+21	2.56E+18	7.55E+17	4.52E+18	1.63E+18	6.75E+21	4.61E+19	7.77E+18	3.34E+21	4.72E+19	8.48E+17	0.00E+00	0.00E+00	1.21E+20	1.68E+20	7.29E+16	1.21E+17	3.69E+14	4.77E+14	7.03E+13	3.67E+15	1.30E+16	2.17E+15	0.00E+00	0.00E+00	0.00E+00	6.02E+15	7.20E+14	3.50E+15	0.00E+00	0.00E+00	3.86E+15	6.89E+17	4.29E+14	4.76E+14	0.00E+00	0.00E+00	0.00E+00	5.08E+15	6.34E+15
atomic concentration of element k in **target fraction**	N_{Cl}	atoms g^{-1}					########																																				
dilute resonance integral for absorption of epithermal neutrons by element k	$I_{0,k}$	E^{-04} cm^2	0.233	1	3.1	1.36	13.83	0.0002693	0.082	0.311	0.038	0.17	13.4	0.079	0.0018	0	0.0002693	0	343	1400	390	83.3	277	1.6																	
average log decrement of energy loss per collision for element k	x_k	-	0.049	0.05	0.041	0.035	0.055	0.12	0.07	0.084	0.08	0.072	0.036	0.06321	0.15776047	1	0.12	0.264	0.174	0.013	0.013	0.008594	0.008379	0.038																	
neutron scattering cross section of element k	$\sigma_{s,e,k}$	E^{-24} cm^2	2.93	2.04	4.09	11.35	15.8	3.76	2.04	3.038	3.414	1.41	2.06	3.134	4.74	20.5	3.76	0.95	4.27	38	172	13.55	9.08	3.38																	
thermal neutron absorption cross section of element k	$\sigma_{a,k}$	E^{-24} cm^2	0.43	2.1	6.41	2.56	33.14	0.0002	0.171	0.517	0.0666	0.231	13.36	0.165	0.0035	0.33		70.5	767	9640	41560	7.34	2.68	3.1																	
proportion of muons stopped in element i that are captured by the nucleus	f_{cik}		0.864	0.83		0.906		0.223	0.671	0.432	0.538	0.582			0.09																												
average neutron yield per captured muon	Y_k		0.75	1.25		1.125		0.8	0.86	1	0.6	1.26			0.76																												

6- unscaled sample specific ^{36}Cl production rate by spallation of target elements

spallation production rate for Ca, SLHL	PR_{Ca}	atoms ^{36}Cl (g C	42		Braucher et al. 2011
mass concentration of Ca in **target fraction**	C_{Ca}	g Ca (g rock)$^{-1}$	0.211	0.001	
result unscaled ^{36}Cl production by spallation of ^{40}Ca	$\mathbf{P_{s,Ca}}$	atoms ^{36}Cl (g C	8.663	0.414	
spallation production rate for K, SLHL	PR_K	atoms ^{36}Cl (g K	148.1	7.8	Schimmelpfennig et al., 2014, St scaling
mass concentration of K in **target fraction**	C_K	g K (g rock)$^{-1}$	0.000	0.000	
result unscaled ^{36}Cl production by spallation of ^{39}K	$\mathbf{P_{s,K}}$	atoms ^{36}Cl (g K	0.024	0.012	
spallation production rate for Ti, SLHL	PR_{Ti}	atoms ^{36}Cl (g T	13		Fink et al., 2002
mass concentration of Ti in **target fraction**	C_{Ti}	g Ti (g rock)$^{-1}$	0.000	0.000	
result unscaled ^{36}Cl production by spallation of Ti	$\mathbf{P_{s,Ti}}$	atoms ^{36}Cl (g Ti	0.001	0.001	
spallation production rate for Fe, SLHL	PR_{Fe}	atoms ^{36}Cl (g F	1.9	0.285	Stone et al., 2005
mass concentration of Fe in **target fraction**	C_{Fe}	g Fe (g rock)$^{-1}$	0.000	0.000	
result unscaled ^{36}Cl production by spallation of Fe	$\mathbf{P_{s,Fe}}$	atoms ^{36}Cl (g Fe	0.001	0.000	
result unscaled sample specific ^{36}Cl production rate by spallation of target elements	$\mathbf{P_s}$	atoms ^{36}Cl (g)$^{-1}$	8.688	0.414	

7- unscaled sample specific ^{36}Cl production rate by capture of epithermal neutrons

						Ca	K	Ti	Fe	Cl	O, rock	Si	Na	Mg	Al	Mn	P	C	H	O, water	Li	B	Sm	Gd	Th	U	Cr	Be	N	F	S	Sc	Co	Ni	Se	Br	Rb	Sr	Zr	Mo	Ru	Te	I	Cs	Ba
effective macroscopic resonance integral for absorption of epithermal neutrons	I_{eff}	cm^2 g^{-1}	0.0010			7.55E-04	2.56E-06	2.34E-06	6.15E-06	2.26E-05	1.82E-06	3.78E-06	2.42E-06	1.27E-04	8.03E-06	1.14E-05		0.00E+00	0.00E+00		0.00E+00	4.15E-05	5.16E-07	1.86E-07		2.08E-08																		
fraction of epithermal neutrons absorbed by ^{35}Cl (**target fraction**)	f_{eth}	-	0.0233																																								
neutron macroscopic scattering cross section in subsurface	Σ_{ss}	cm^2 g^{-1}	0.0497			9.49E-03	5.22E-06	3.09E-06	5.13E-05	2.58E-05	2.54E-02	9.40E-05	2.36E-05	1.14E-02	6.66E-05	1.75E-06	0.00E+00	0.00E+00	2.48E-03	6.33E-04	6.92E-08	5.17E-07	1.40E-08	8.21E-08	9.53E-10	3.34E-08	4.39E-08	0.00E+00	0.00E+00	0.00E+00	0.00E+00	0.00E+00	0.00E+00	0.00E+00	0.00E+00	0.00E+00	0.00E+00	0.00E+00	0.00E+00	0.00E+00	0.00E+00	0.00E+00	0.00E+00	0.00E+00	0.00E+00
scattering rate parameter	B		7.00E-03			4.65E-04	2.61E-07	1.27E-07	1.80E-06	1.42E-06	3.05E-03	6.58E-06	1.98E-06	9.12E-04	4.79E-06	6.29E-08	0.00E+00	0.00E+00	2.48E-03	7.59E-05	1.83E-08	8.99E-08	1.82E-10	1.07E-09	8.19E-12	2.80E-10	1.67E-09	0.00E+00	0.00E+00	0.00E+00	0.00E+00	0.00E+00	0.00E+00	0.00E+00	0.00E+00	0.00E+00	0.00E+00	0.00E+00	0.00E+00	0.00E+00	0.00E+00	0.00E+00	0.00E+00	0.00E+00	0.00E+00
mean macroscopic log decrement of energy loss per collision in subsurface	X_{ss}		0.141																																								
macroscopic absorption and moderation cross section for epithermal neutrons	Σ_{eth}	cm^2 g^{-1}	0.007																																								
attenuation length for absorption and moderation of epithermal neutron flux	Λ_{eth}	g cm^{-2}	140.163																																								
	$A_k * N_k$	atoms mol^{-1}	3.22E+23			1.30E+23	1.00E+20	3.61E+19	2.53E+20	5.78E+19	1.08E+23	1.29E+21	1.79E+20	8.12E+22	1.27E+21	4.66E+19		0.00E+00	1.22E+20		5.06E+17	1.31E+18	5.55E+16	7.51E+16		6.75E+17																		
average atomic weight in subsurface	A_{ss}	g mol^{-1}	23.476																																								
production rate of epithermal neutrons from fast neutrons in atmosphere at land/atm interface	$P_n(0)$	n cm^{-2} a^{-1}	696	185	Marrero et al. 2016, St scaling																																							
Ratio of epithermal neutron production in subsurface to that in atmosphere	R_{eth}	-	1.27																																								
epithermal neutron diffusion coefficient in subsurface	D_{eth}	g cm^{-2}	6.91																																								
apparent fast neutron attenuation coefficient	Λ_f	g cm^{-2}	160																																								
epithermal neutron flux at land/atmosphere interface that would be observed in ss if interface was	ϕ_{eth}	n cm^{-2} a^{-1}	129007																																								
average neutron yield per stopped negative muon	Y_μ		0.404			0.259	0.000		0.001		0.059	0.002	0.000	0.080	0.003			0.000																											
slow negative muon stopping rate at land surface SLHL	$\Psi_\mu(0)$	μ g^{-1} a^{-1}	190																																								
fast muon flux at land surface SLHL	$\phi_{\mu 0}$	μ cm^{-2} a^{-1}	7.90E+05																																								
total muon induced neutron production at land surface	$P_{n\mu 0}$	μ cm^{-2} a^{-1}	81.423																																								
ratio of muon production rate to epithermal neutron production rate	R_μ	-	0.045																																								
macroscopic neutron scattering cross section of atmosphere	$\Sigma_{eth,a}$	cm^2 g^{-1}	0.3773																																								
thermal neutron diffusion coefficient in atmosphere	D_a	g cm^{-2}	0.926																																								
macroscopic absorption and moderation cross section for epithermal neutrons in atmosphere	$\Sigma_{eth,a}$	cm^2 g^{-1}	0.0548																																								

epithermal neutron diffusion length in atmosphere	$L_{eth,a}$	g cm^{-2}	4.015	
epithermal neutron flux at land/atmosphere interface that would be observed in atm if interface we	$\phi^*_{eth,a}$	n cm^{-2} a^{-1}	12709	
difference between hypothetical equilibrium epithermal neutron fluxes in atmosphere and subsurf	$\Delta\phi^*_{eth}$	n cm^{-2} a^{-1}	-116297	
adjusted difference between hypothetical equilibrium epithermal neutron fluxes in atmosphere an	$\Delta\phi^{**}_{eth,a}$	n cm^{-2} a^{-1}	127302	
epithermal neutron diffusion length in subsurface	L_{eth}	g cm^{-2}	30.668	
difference between phi_star_eth and actual epithermal neutron flux at land surface	$(F.\Delta\phi)^*_{eth}$	-	-70897	
slow muon attenuation length	Λ_μ	g cm^{-2}	1510	
epithermal neutron flux (concentration)	$\phi_{eth,total}$	n cm^{-2} a^{-1}	65089	
result unscaled sample specific ^{36}Cl production rate by capture of epithermal neutrons	**P_{eth}**	**atoms ^{36}Cl g^{-1} a^{-1}**	**1.421**	0.42645

| **8- unscaled sample specific ^{36}Cl production rate by capture of thermal neutrons** | | | |

Chlorine-36 exposure age and erosion rate determination: Please follow the instructions on the first worksheet

modifications regarding muonic 36Cl production

Sample name SEL01.18

1- Input

(and output for eroding surfaces)

	symbol	units	calculations	Uncertainties
element concentration in bulk rock: maior element as oxides [wt-%] and trace elements [wt-ppm]				
element concentration in target fraction: major element as oxides [wt-%] and Cl in [wt-ppm]				
uncertainty target element concentration in target fraction (oxides in [wt-%] and Cl in [wt-ppm])				
depth reference: top of sample		cm	0	
sample thickness		cm	2.5	
bulk rock density	rho	g cm^{-3}	2.710054209	
mass depth reference: center of sample	z	g cm^{-2}	3.387567761	
mass thickness	z_s	g cm^{-2}	6.775135523	
scaling factor for nucleonic production as a function of elevation, latitude (and temporal v	S_{eLin} , S_{eLsc}	-	5.848	0.292
scaling factor for muonic production as a function of elevation, latitude (and temporal var	$S_{\mu(z)}$	-	2.602	0.130
correction factor for shielding of a sample of arbitrary orientation by surrounding topogra	S_T	-	0.959243575	0.009592436
correction factor for geometry effects on spallogenic production	S_{shape}	-	1	0.03
correction factor for snow shielding for spallogenic production	S_{snow}	-	1	0.01
effective fast neutron attenuation coefficient	$\Lambda_{f,e}$	g cm^{-2}	160	
estimated ^{36}Cl concentration from inheritance at t_{exp}=0	$N_{inher}(0)$	atoms ^{36}Cl g^{-1}		
measured ^{36}Cl concentration in sample	N_{meas}	atoms ^{36}Cl g^{-1}	1.95E+06	3.04E+05
exposure duration (independently determined or estimated)	t_{expo}	a	15762	3443.58782
formation age of rock (independently determined or estimated) for radiogenic correction	t_{form}	a	200000000	1000
erosion rate	ε	mm ka^{-1}	0	0

bulk rock:	CaO [wt-%]	K2O [wt-%]	TiO2 [wt-%]	Fe2O3 [wt-%]	Cl [ppm]
29.230	0.07	0.02	0.26	148.00	
target fraction:					
29.53	0.07	0.02	0.26	183.19	
0.14	0.01	0.01	0.01	33.20	

	SiO2 [wt-%]	Na2O [wt-%]	MgO [wt-%]	Al2O3 [wt-%]	MnO [wt-%]	P2O5 [wt-%]	CO2 [wt-%]	H2O [wt-%]
	0.90	0.03	21.53	0.54	0.03	0.00		0.5
	0.90	0.03	21.53	0.54	0.03	0.00		0.50

	Li [ppm]	B [ppm]	Sm [ppm]	Gd [ppm]	Th [ppm]	U [ppm]
	0.77641915	2.0931841	0.14	0.16	0.06	1.30
	0.77641915	2.0931841	0.136398	0.162628335	0.0577068	1.2957806

	Cr [ppm]	Be [ppm]	N [ppm]	F [ppm]	S [ppm]	Sc [ppm]	Co [ppm]	Ni [ppm]	Se [ppm]	Br [ppm]	Rb [ppm]	Sr [ppm]	Zr [ppm]	Mo [ppm]	Ru [ppm]	Te [ppm]	I [ppm]	Cs [ppm]	Ba [ppm]
	2.23	0.05				0.56	0.35	0.86			0.38	97.68	0.08	0.42				0.41	1.99
	2.2348281	0.0472147				0.56	0.35	0.86			0.38	97.68	0.08	0.42				0.41	1.99

2- Output A: exposure age of sample (only for uneroded surface)

decay constant for ^{36}Cl	λ_{36}	a^{-1}	2.30E-06	1.51998E-08
scaled total sample specific ^{36}Cl production rate without radiogenic	P_{total}	atoms ^{36}Cl g^{-1} a	122.4	17.4
time factor radiogenic	t_i		434216	2865.6
calculated concentration of radiogenically produced ^{36}Cl atoms for estimated age	N_i	atoms ^{36}Cl g^{-1}	56911.9	2870.3
estimated ^{36}Cl concentration from inheritance at time of sampling	$N_{inher}(t)$	atoms ^{36}Cl g^{-1}	0.0	
measured ^{36}Cl concentration in sample corrected from radiogenic component and inheritance	$N_{meas-i-inher}$	atoms ^{36}Cl g^{-1}	1.89E+06	303754.3
exposure age of sample	**t**	**a**	15762	3443

3- Output B: eroding surface

calculated ^{36}Cl concentration for an eroding sample	$N_{calc,total}$	atoms ^{36}Cl g^{-1}	1.95E+06
difference measured/calculated ^{36}Cl concentration in eroding sample	$\Delta N_{meas-calc}$		0.00%
erosion rate	ε	cm a^{-1}	0
time factor with erosion for spallation reaction	$t_{cosm,s}$		15479
time factor with erosion for capture of epithermal neutrons	$t_{cosm,eth}$		15479
time factor with erosion for capture of thermal neutrons	$t_{cosm,th}$		15479
time factor with erosion for capture of slow negative muons	$t_{cosm,\mu}$		15479
depth reference factor for spallogenic reaction	d_s		0.979
depth reference factor for capture of epithermal neutrons	d_{eth}		0.896
depth reference factor for capture of thermal neutrons	d_{th}		0.945
depth reference factor for capture of slow negative muons	d_μ		0.998
production rate coefficient corrected for sample thickness for spallogenic reaction	J_{Cs}		62.75
production rate coefficient corrected for sample thickness for capture of epithermal neutrons	J_{Ceth}		5.55
production rate coefficient corrected for sample thickness for capture of thermal neutrons	J_{Cth}		-50.12
production rate coefficient corrected for sample thickness for capture of slow negative muons	$J_{C\mu}$		2.77
production rate coefficient for spallogenic reaction	J_s		62.80
production rate coefficient for capture of epithermal neutrons	J_{eth}		5.55
production rate coefficient for capture of thermal neutrons	J_{th}		-50.16
production rate coefficient for capture of slow negative muons	J_μ		2.77

4- Output C: calculated ^{36}Cl contributions from all production mechanism

time factor cosmogenic without erosion	t_{cosm}		15479	3321
calculated ^{36}Cl concentration for given time + radiogenic	$N_{calc,total}$	atoms ^{36}Cl g^{-1}	1.95E+06	487995
difference measured/calculated ^{36}Cl concentration	$\Delta N_{meas-calc}$		0.00%	
contribution from each production mechanism:				
number of atoms ^{36}Cl per g by spallation of Ca	$N_{s,Ca}$	atoms ^{36}Cl g^{-1}	753869	38.63%
number of atoms ^{36}Cl per g by spallation of K	$N_{s,K}$	atoms ^{36}Cl g^{-1}	7315	0.37%
number of atoms ^{36}Cl per g by spallation of Ti	$N_{s,Ti}$	atoms ^{36}Cl g^{-1}	133	0.01%
number of atoms ^{36}Cl per g by spallation of Fe	$N_{s,Fe}$	atoms ^{36}Cl g^{-1}	294	0.02%
number of atoms ^{36}Cl per g by spallation of target elements	N_s	atoms ^{36}Cl g^{-1}	761610	39.03%
number of atoms ^{36}Cl per g by capture of thermal neutrons	N_{th}	atoms ^{36}Cl g^{-1}	793875	40.68%
number of atoms ^{36}Cl per g by capture of epithermal neutrons	N_{eth}	atoms ^{36}Cl g^{-1}	229742	11.77%
number of atoms ^{36}Cl per g by capture of thermal and epithermal neutrons	N_n	atoms ^{36}Cl g^{-1}	1023617	52.45%
number of atoms ^{36}Cl per g by capture of slow negative muons	N_μ	atoms ^{36}Cl g^{-1}	109368	5.60%
number of atoms ^{36}Cl per g by radiogenic production	N_i	atoms ^{36}Cl g^{-1}	56912	2.92%
				100.00%

5- elemental parameters

			Ca	K	Ti	Fe	Cl	O, rock	Si	Na	Mg	Al	Mn	P	C	H	O, water	Li	B	Sm	Gd	Th	U	Cr	Be	N	F	S	Sc	Co	Ni	Se	Br	Rb	Sr	Zr	Mo	Ru	Te	I	Cs	Ba
element concentration [wt-ppm] **bulk rock**		ppm	208995	581	120	1817	148	177247	4203	223	129826	2857	232	0	0	560	4470	0.77641915	2.1	0.1	0.2	0.0577068	1.2957806	2.2348281	0.0472147	0	0	0	0.556084	0.351487	0.8551103	0	0	0.3829635	97.681923	0.0786911	0.4249321	0	0	0	0.4091939	1.9882625
element concentration dissolved sample [wt-ppm] in **target fraction**		ppm	211130	581	120	1817	183	178098	4203	223	129826	2857	232	0	0	560	4470	0.77641915	2.0931841	0.136398	0.162628335	0.0577068	1.2957806	2.2348281	0.0472147	0	0	0	0.556084	0.351487	0.8551103	0	0	0.3829635	97.681923	0.0786911	0.4249321	0	0	0	0.4091939	1.9882625
atomic mass of element k (Reference: http://www.ciaaw.org/atomic-weights.htm)	A_k	g mol^{-1}	40.078	39.0983	47.867	55.845	35.453	15.999	28.085	22.98977	24.305	26.981538	54.938043	30.973761	12.01	1.008	15.999	6.941	10.811	150.36	157.25	232.0377	238.02891	51.9961	9.012182	14.0067	18.998403	32.065	44.95591	58.9332	58.6934	78.96	79.904	85.4678	87.62	91.224	95.94	101.07	127.6	126.90447	132.90545	137.327
avoqadro			6.02E+23																																							
atomic concentration of element k in **bulk rock**	N_k	atoms g^{-1}	1.35E+22	3.14E+21	8.95E+18	1.51E+18	1.96E+19	2.51E+18	6.67E+21	9.01E+19	5.83E+18	3.22E+21	6.38E+19	2.55E+18	0.00E+00	0.00E+00	1.23E+20	1.68E+20	6.74E+16	1.17E+17	5.46E+14	6.23E+14	1.50E+14	3.28E+15	2.59E+16	3.15E+15	0.00E+00	0.00E+00	0.00E+00	7.45E+15	3.59E+15	8.77E+15	0.00E+00	0.00E+00	2.70E+15	6.71E+17	5.19E+14	2.67E+15	0.00E+00	0.00E+00	0.00E+00	1.85E+15	8.72E+15
atomic concentration of element k in **target fraction**	N_{Cl}	atoms g^{-1}						#########																																			
dilute resonance integral for absorption of epithermal neutrons by element k	$I_{0,k}$	E^{-04} cm^2		0.233	1	3.1	1.36	13.83	0.0002693	0.082	0.311	0.038	0.17	13.4	0.079	0.0018	0	0.0002693	0	343	1400	390	83.3	277	1.6																	
average log decrement of energy loss per collision for element k	x_k	-		0.049	0.05	0.041	0.035	0.055	0.12	0.07	0.084	0.08	0.072	0.036	0.06321	0.15776047	1	0.12	0.264	0.174	0.013	0.013	0.008594	0.008379	0.038																	
neutron scattering cross section of element k	$\sigma_{sc,k}$	E^{-24} cm^2		2.93	2.04	4.09	11.35	15.8	3.76	2.04	3.036	3.414	1.41	2.06	3.134	4.74	20.5	3.76	0.95	4.27	38	172	13.55	9.08	3.38																	
thermal neutron absorption cross section of element k	$\sigma_{a,k}$	E^{-24} cm^2		0.43	2.1	6.41	2.56	33.14	0.0002	0.171	0.517	0.0666	0.231	13.36	0.165	0.0035	0.33		70.5	767	9640	41560	7.34	2.68	3.1																	
proportion of muons stopped in element i that are captured by the nucleus	f_{cik}			0.864	0.83		0.906		0.223	0.671	0.432	0.538	0.582			0.09																											
average neutron yield per captured muon	Y_k			0.75	1.25		1.125		0.8	0.86	1	0.6	1.26			0.76																											

6- unscaled sample specific ^{36}Cl production rate by spallation of target elements

spallation production rate for Ca, SLHL	PR_{Ca}	atoms ^{36}Cl (g C	42	3	Braucher et al. 2011
mass concentration of Ca in **target fraction**	C_{Ca}	q Ca (q rock)$^{-1}$	0.211	0.001	
result unscaled ^{36}Cl production by spallation of ^{40}Ca	$\mathbf{P_{s,Ca}}$	atoms ^{36}Cl (q C	8.682	0.415	
spallation production rate for K, SLHL	PR_K	atoms ^{36}Cl (g K	148.1	7.8	Schimmelpfennig et al., 2014, St scaling
mass concentration of K in **target fraction**	C_K	q K (q rock)$^{-1}$	0.001	0.000	
result unscaled ^{36}Cl production by spallation of ^{39}K	$\mathbf{P_{s,K}}$	atoms ^{36}Cl (q K	0.084	0.013	
spallation production rate for Ti, SLHL	PR_{Ti}	atoms ^{36}Cl (g T	13	3	Fink et al., 2002
mass concentration of Ti in **target fraction**	C_{Ti}	q Ti (q rock)$^{-1}$	0.000	0.000	
result unscaled ^{36}Cl production by spallation of Ti	$\mathbf{P_{s,Ti}}$	atoms ^{36}Cl (q Ti	0.002	0.001	
spallation production rate for Fe, SLHL	PR_{Fe}	atoms ^{36}Cl (g F	1.9	0.286	Stone et al., 2005
mass concentration of Fe in **target fraction**	C_{Fe}	q Fe (q rock)$^{-1}$	0.002	0.000	
result unscaled ^{36}Cl production by spallation of Fe	$\mathbf{P_{s,Fe}}$	atoms ^{36}Cl (q Fe	0.003	0.000	
result unscaled sample specific ^{36}Cl production rate by spallation of target elements	$\mathbf{P_s}$	atoms ^{36}Cl (g)$^{-1}$	8.771	0.416	

7- unscaled sample specific ^{36}Cl production rate by capture of epithermal neutrons

						Ca	K	Ti	Fe	Cl	O, rock	Si	Na	Mg	Al	Mn	P	C	H	O, water	Li	B	Sm	Gd	Th	U	Cr	Be	N	F	S	Sc	Co	Ni	Se	Br	Rb	Sr	Zr	Mo	Ru	Te	I	Cs	Ba
effective macroscopic resonance integral for absorption of epithermal neutrons	I_{eff}	cm^2 g^{-1}	0.0010	7.32E-04	8.95E-06	4.68E-06	2.67E-05	3.48E-05	1.80E-06	7.39E-06	1.81E-06	1.22E-04	1.08E-05	3.41E-05		0.00E+00	0.00E+00		0.00E+00	4.00E-05	7.65E-07	2.43E-07			4.14E-08																			
fraction of epithermal neutrons absorbed by ^{35}Cl (**target fraction**)	f_{eth}	-	0.0419																																								
neutron macroscopic scattering cross section in subsurface	Σ_{scl}	cm^2 g^{-1}	0.0490	9.20E-03	1.83E-05	6.17E-06	2.22E-04	3.97E-05	2.51E-02	1.84E-04	1.77E-05	1.10E-02	8.99E-05	5.24E-06	0.00E+00	0.00E+00	2.53E-03	6.33E-04	6.40E-08	4.98E-07	2.08E-08	1.07E-07	2.03E-09	2.98E-08	8.75E-08	0.00E+00	0.00E+00	0.00E+00	0.00E+00	0.00E+00	0.00E+00	0.00E+00	0.00E+00	0.00E+00	0.00E+00	0.00E+00	0.00E+00	0.00E+00	0.00E+00	0.00E+00	0.00E+00	0.00E+00	0.00E+00
scattering rate parameter	B		6.98E-03	4.51E-04	9.13E-07	2.53E-07	7.79E-06	2.18E-06	3.01E-03	1.29E-05	1.49E-06	8.79E-04	6.47E-06	1.89E-07	0.00E+00	0.00E+00	2.53E-03	7.59E-05	1.69E-08	8.66E-08	2.70E-10	1.39E-09	1.74E-11	2.49E-10	3.32E-09	0.00E+00	0.00E+00	0.00E+00	0.00E+00	0.00E+00	0.00E+00	0.00E+00	0.00E+00	0.00E+00	0.00E+00	0.00E+00	0.00E+00	0.00E+00	0.00E+00	0.00E+00	0.00E+00	0.00E+00	0.00E+00
mean macroscopic log decrement of energy loss per collision in subsurface	X_{sk}		0.142																																								
macroscopic absorption and moderation cross section for epithermal neutrons	Σ_{ath}	cm^2 g^{-1}	0.007																																								
attenuation length for absorption and moderation of epithermal neutron flux	Λ_{eth}	q cm^{-2}	140.405																																								
	$A_k * N_k$	atoms mol^{-1}	3.17E+23	1.26E+23	3.50E+20	7.23E+19	1.09E+21	8.91E+19	1.07E+23	2.53E+21	1.34E+20	7.82E+22	1.72E+21	1.40E+20		0.00E+00	1.24E+20		4.68E+17	1.26E+18	8.21E+16	9.79E+16			1.35E+18																			
average atomic weight in subsurface	A_{ss}	g mol^{-1}	23.456																																								
production rate of epithermal neutrons from fast neutrons in atmosphere at land/atm interface	$P_n(0)$	n cm^{-2} a^{-1}	696	185	Marrero et al. 2016, St scaling																																							
Ratio of epithermal neutron production in subsurface to that in atmosphere	R_{eth}	-	1.27																																								
epithermal neutron diffusion coefficient in subsurface	D_{eth}	q cm^{-2}	7.00																																								
apparent fast neutron attenuation coefficient	Λ_f	q cm^{-2}	160																																								
epithermal neutron flux at land/atmosphere interface that would be observed in ss if interface was	ϕ_{eth}	n cm^{-2} a^{-1}	129253																																								
average neutron yield per stopped negative muon	Y_μ		0.406	0.255	0.001		0.003		0.060	0.005	0.000	0.078	0.004			0.000																												
slow negative muon stopping rate at land surface SLHL	$\Psi_\mu(0)$	μ g^{-1} a^{-1}	190																																								
fast muon flux at land surface SLHL	$\phi_{\mu 0}$	μ cm^{-2} a^{-1}	7.90E+05																																								
total muon induced neutron production at land surface	$P_{n\mu 0}$	μ cm^{-2} a^{-1}	81.715																																								
ratio of muon production rate to epithermal neutron production rate	R_μ	-	0.041																																								
macroscopic neutron scattering cross section of atmosphere	$\Sigma_{scl,a}$	cm^2 g^{-1}	0.3773																																								
thermal neutron diffusion coefficient in atmosphere	D_a	q cm^{-2}	0.926																																								
macroscopic absorption and moderation cross section for epithermal neutrons in atmosphere	$\Sigma_{ath,a}$	cm^2 g^{-2}	0.0548																																								

epithermal neutron diffusion length in atmosphere	$L_{eth,a}$	g cm^{-2}	4.015	
epithermal neutron flux at land/atmosphere interface that would be observed in atm if interface we	$\phi^*_{eth,a}$	n cm^{-2} a^{-1}	12709	
difference between hypothetical equilibrium epithermal neutron fluxes in atmosphere and subsurf	$\Delta\phi^*_{eth}$	n cm^{-2} a^{-1}	-116544	
adjusted difference between hypothetical equilibrium epithermal neutron fluxes in atmosphere an	$\Delta\phi^{**}_{eth,a}$	n cm^{-2} a^{-1}	127572	
epithermal neutron diffusion length in subsurface	L_{eth}	g cm^{-2}	30.901	
difference between phi_star_eth and actual epithermal neutron flux at land surface	$(\Gamma.\Delta\phi)^*_{eth}$	-	-71004	
slow muon attenuation length	Λ_μ	g cm^{-2}	1510	
epithermal neutron flux (concentration)	$\phi_{eth,total}$	n cm^{-2} a^{-1}	64886	
result unscaled sample specific ^{36}Cl production rate by capture of epithermal neutrons	**P_{eth}**	**atoms ^{36}Cl g^{-1} a^{-1}**	**2.651**	0.79531

| **8- unscaled sample specific ^{36}Cl production rate by capture of thermal neutrons** | | | |

Chlorine-36 exposure age and erosion rate determination: Please follow the instructions on the first worksheet

modifications regarding muonic 36Cl production

Sample name SEL02.18

1- Input

(and output for eroding surfaces)

	symbol	units	calculations	Uncertainties
element concentration in bulk rock: maior element as oxides [wt-%] and trace elements [wt-ppm]				
element concentration in target fraction: major element as oxides [wt-%] and Cl in [wt-ppm]				
uncertainty target element concentration in target fraction (oxides in [wt-%] and Cl in [wt-ppm])				
depth reference: top of sample		cm	0	
sample thickness		cm	3	
bulk rock density	rho	g cm^{-3}	2.739391024	
mass depth reference: center of sample	z	g cm^{-2}	4.109086536	
mass thickness	z_s	g cm^{-2}	8.218173072	
scaling factor for nucleonic production as a function of elevation, latitude (and temporal v	$S_{St/A}$, $S_{St/N}$	-	5.783	0.289
scaling factor for muonic production as a function of elevation, latitude (and temporal var	$S_{St/\mu}$	-	2.585	0.129
correction factor for shielding of a sample of arbitrary orientation by surrounding topogra	S_T	-	0.962265105	0.009622651
correction factor for geometry effects on spallogenic production	S_{shape}	-	1	0.03
correction factor for snow shielding for spallogenic production	S_{snow}	-	1	0.01
effective fast neutron attenuation coefficient	$\Lambda_{f,e}$	g cm^{-2}	160	
estimated ^{36}Cl concentration from inheritance at t_{expo}=0	$N_{inher}(0)$	atoms ^{36}Cl g^{-1}		
measured ^{36}Cl concentration in sample	N_{meas}	atoms ^{36}Cl g^{-1}	1.59E+06	1.98E+05
exposure duration (independently determined or estimated)	t_{expo}	a	16396	2805.382144
formation age of rock (independently determined or estimated) for radiogenic correction	t_{form}	a	200000000	1000
erosion rate	ε	mm ka^{-1}	0	0

	CaO [wt-%]	K2O [wt-%]	TiO2 [wt-%]	Fe2O3 [wt-%]	Cl [ppm]
bulk rock:	30.000	0.02	0.01	0.12	138.00
target fraction:	29.67	0.02	0.01	0.12	128.01
	0.11	0.01	0.01	0.01	18.92

	SiO2 [wt-%]	Na2O [wt-%]	MgO [wt-%]	Al2O3 [wt-%]	MnO [wt-%]	P2O5 [wt-%]	CO2 [wt-%]	H2O [wt-%]
bulk rock:	0.38	0.02	22.16	0.29	0.02	0.00		0.5
target fraction:	0.38	0.02	22.16	0.29	0.02	0.00		0.50

	Li [ppm]	B [ppm]	Sm [ppm]	Gd [ppm]	Th [ppm]	U [ppm]
bulk rock:	0.74991763	2.2553078	0.08	0.10	0.04	1.04
target fraction:	0.74991763	2.2553078	0.0833242	0.099989017	0.0388846	1.0387748

	Cr [ppm]	Be [ppm]	N [ppm]	F [ppm]	S [ppm]	Sc [ppm]	Co [ppm]	Ni [ppm]	Se [ppm]	Br [ppm]	Rb [ppm]	Sr [ppm]	Zr [ppm]	Mo [ppm]	Ru [ppm]	Te [ppm]	I [ppm]	Cs [ppm]	Ba [ppm]
bulk rock:	1.48	0.03				0.49	0.19	0.56			0.19	87.82	0.09	0.11				0.12	3.95
target fraction:	1.4831704	0.0277747				0.49	0.19	0.56			0.19	87.82	0.09	0.11				0.12	3.95

2- Output A: exposure age of sample (only for uneroded surface)

decay constant for ^{36}Cl	λ_{36}	a^{-1}	2.30E-06	1.51998E-08
scaled total sample specific ^{36}Cl production rate without radiogenic	P_{total}	atoms ^{36}Cl g^{-1} a	102.8	12.9
time factor radiogenic	t_i		4.34216	2865.8
calculated concentration of radiogenically produced ^{36}Cl atoms for estimated age	N_i	atoms ^{36}Cl g^{-1}	32718.2	1650.1
estimated ^{36}Cl concentration from inheritance at time of sampling	$N_{inher}(t)$	atoms ^{36}Cl g^{-1}	0.0	
measured ^{36}Cl concentration in sample corrected from radiogenic component and inheritance	$N_{meas-r-inher}$	atoms ^{36}Cl g^{-1}	1.55E+06	197660.5
exposure age of sample	**t**	**a**	15396	2805

3- Output B: eroding surface

calculated ^{36}Cl concentration for an eroding sample	$N_{calc,total}$	atoms ^{36}Cl g^{-1}	1.59E+06
difference measured/calculated ^{36}Cl concentration in eroding sample	$\Delta N_{meas-calc}$		0.00%
erosion rate	ε	cm a^{-1}	0
time factor with erosion for spallation reaction	$t_{cosm,x}$		15126
time factor with erosion for capture of epithermal neutrons	$t_{cosm,eth}$		15126
time factor with erosion for capture of thermal neutrons	$t_{cosm,th}$		15126
time factor with erosion for capture of slow negative muons	$t_{cosm,\mu}$		15126
depth reference factor for spallogenic reaction	d_x		0.975
depth reference factor for capture of epithermal neutrons	d_{eth}		0.875
depth reference factor for capture of thermal neutrons	d_{th}		0.934
depth reference factor for capture of slow negative muons	d_μ		0.997
production rate coefficient corrected for sample thickness for spallogenic reaction	$J_{Cl,x}$		47.51
production rate coefficient corrected for sample thickness for capture of epithermal neutrons	$J_{Cl,eth}$		3.86
production rate coefficient corrected for sample thickness for capture of thermal neutrons	$J_{Cl,th}$		-35.94
production rate coefficient corrected for sample thickness for capture of slow negative muons	$J_{Cl,\mu}$		2.36
production rate coefficient for spallogenic reaction	J_x		47.55
production rate coefficient for capture of epithermal neutrons	J_{eth}		3.86
production rate coefficient for capture of thermal neutrons	J_{th}		-35.97
production rate coefficient for capture of slow negative muons	J_μ		2.36

4- Output C: calculated ^{36}Cl contributions from all production mechanism

time factor cosmogenic without erosion	t_{cosm}		15126	2708
calculated ^{36}Cl concentration for given time + radiogenic	$N_{calc,total}$	atoms ^{36}Cl g^{-1}	1.59E+06	340224
difference measured/calculated ^{36}Cl concentration	$\Delta N_{meas-calc}$		0.00%	
contribution from each production mechanism:				
number of atoms ^{36}Cl per g by spallation of Ca	$N_{x,Ca}$	atoms ^{36}Cl g^{-1}	731011	46.06%
number of atoms ^{36}Cl per g by spallation of K	$N_{x,K}$	atoms ^{36}Cl g^{-1}	2017	0.13%
number of atoms ^{36}Cl per g by spallation of Ti	$N_{x,Ti}$	atoms ^{36}Cl g^{-1}	64	0.00%
number of atoms ^{36}Cl per g by spallation of Fe	$N_{x,Fe}$	atoms ^{36}Cl g^{-1}	131	0.01%
number of atoms ^{36}Cl per g by spallation of target elements	N_x	atoms ^{36}Cl g^{-1}	733223	46.20%
number of atoms ^{36}Cl per g by capture of thermal neutrons	N_{th}	atoms ^{36}Cl g^{-1}	555620	35.01%
number of atoms ^{36}Cl per g by capture of epithermal neutrons	N_{eth}	atoms ^{36}Cl g^{-1}	158186	9.97%
number of atoms ^{36}Cl per g by capture of thermal and epithermal neutrons	N_n	atoms ^{36}Cl g^{-1}	713806	44.95%
number of atoms ^{36}Cl per g by capture of slow negative muons	N_μ	atoms ^{36}Cl g^{-1}	107266	6.76%
number of atoms ^{36}Cl per g by radiogenic production	N_i	atoms ^{36}Cl g^{-1}	32718	2.06%
				100.00%

5- elemental parameters

			Ca	K	Ti	Fe	Cl	O, rock	Si	Na	Mg	Al	Mn	P	C	H	O, water	Li	B	Sm	Gd	Th	U	Cr	Be	N	F	S	Sc	Co	Ni	Se	Br	Rb	Sr	Zr	Mo	Ru	Te	I	Cs	Ba
element concentration [wt-ppm] **bulk rock**		ppm	214500	166	60	839	138	177399	1775	148	133625	1534	155	0	0	560	4470	0.74991763	2.3	0.1	0.1	0.0388846	1.0387748	1.4831704	0.0277747	0	0	0	0.4943901	0.1944231	0.5610495	0	0	0.1888681	87.823687	0.0944341	0.105544	0	0	0	0.1166539	3.9495662
element concentration in **target fraction**		ppm	212121	166	60	839	128	176450	1775	148	133625	1534	155	0	0	560	4470	0.74991763	2.2553078	0.0833242	0.099989017	0.0388846	1.0387748	1.4831704	0.0277747	0	0	0	0.4943901	0.1944231	0.5610495	0	0	0.1888681	87.823687	0.0944341	0.105544	0	0	0	0.1166539	3.9495662
atomic mass of element k (Reference: http://www.ciaaw.org/atomic-weights.htm)	A_k	g mol^{-1}	40.078	39.0983	47.867	55.845	35.453	15.999	28.085	22.98977	24.305	26.981538	54.938043	30.973761	12.01	1.008	15.999	6.941	10.811	150.36	157.25	232.0377	238.02891	51.9961	9.012182	14.0067	18.998403	32.065	44.95591	58.9332	58.6934	78.96	79.904	85.4678	87.62	91.224	95.94	101.07	127.6	126.90447	132.90545	137.327
avoqadro			6.02E+23																																							
atomic concentration of element k in **bulk rock**	N_k	atoms g^{-1}	1.36E+22	3.22E+21	2.56E+18	7.55E+17	9.05E+18	2.34E+18	6.68E+21	3.81E+19	3.89E+18	3.31E+21	3.42E+19	1.70E+18	0.00E+00	0.00E+00	1.22E+20	1.68E+20	6.51E+16	1.26E+17	3.34E+14	3.83E+14	1.01E+14	2.63E+15	1.72E+16	1.86E+15	0.00E+00	0.00E+00	0.00E+00	6.62E+15	1.99E+15	5.76E+15	0.00E+00	0.00E+00	1.33E+15	6.04E+17	6.23E+14	6.62E+14	0.00E+00	0.00E+00	0.00E+00	5.29E+14	1.73E+16
atomic concentration of element k in **target fraction**	N_{Cl}	atoms g^{-1}						#########																																			
dilute resonance integral for absorption of epithermal neutrons by element k	$I_{0,k}$	E^{-24} cm^2		0.233	1	3.1	1.36	13.83	0.0002693	0.082	0.311	0.038	0.17	13.4	0.079	0.0018	0	0.0002693	0	343	1400	390	83.3	277	1.6																	
average log decrement of energy loss per collision for element k	x_k	-		0.049	0.05	0.041	0.035	0.055	0.12	0.07	0.084	0.08	0.072	0.036	0.06321	0.1577605	1	0.12	0.264	0.174	0.013	0.013	0.008594	0.008379	0.038																	
neutron scattering cross section of element k	$\sigma_{n,s,k}$	E^{-24} cm^2		2.93	2.04	4.09	11.35	15.8	3.76	2.04	3.038	3.414	1.41	2.06	3.134	4.74	20.5	3.76	0.95	4.27	38	172	13.55	9.08	3.38																	
thermal neutron absorption cross section of element k	$\sigma_{a,k}$	E^{-24} cm^2		0.43	2.1	6.41	2.56	33.14	0.0002	0.171	0.517	0.0666	0.231	13.36	0.165	0.0035	0.33		70.5	767	9640	41560	7.34	2.68	3.1																	
proportion of muons stopped in element i that are captured by the nucleus	f_{cik}			0.864	0.83		0.906		0.223	0.671	0.432	0.538	0.582			0.09																											
average neutron yield per captured muon	Y_k			0.75	1.25		1.125		0.8	0.86	1	0.6	1.26			0.76																											

6- unscaled sample specific ^{36}Cl production rate by spallation of target elements

spallation production rate for Ca, SLHL	PR_{Ca}	atoms ^{36}Cl (g Ca)$^{-1}$	42	3 Braucher et al. 2011
mass concentration of Ca in **target fraction**	C_{Ca}	g Ca (g rock)$^{-1}$	0.212	0.001
result unscaled ^{36}Cl production by spallation of ^{40}Ca	$\mathbf{P_{x,Ca}}$	atoms ^{36}Cl (g Ca	8.683	0.415
spallation production rate for K, SLHL	PR_K	atoms ^{36}Cl (g K	148.1	7.8 Schimmelpfennig et al., 2014, St scaling
mass concentration of K in **target fraction**	C_K	g K (g rock)$^{-1}$	0.000	0.000
result unscaled ^{36}Cl production by spallation of ^{39}K	$\mathbf{P_{x,K}}$	atoms ^{36}Cl (g K	0.024	0.012
spallation production rate for Ti, SLHL	PR_{Ti}	atoms ^{36}Cl (g T	13	1 Fink et al., 2002
mass concentration of Ti in **target fraction**	C_{Ti}	g Ti (g rock)$^{-1}$	0.000	0.000
result unscaled ^{36}Cl production by spallation of Ti	$\mathbf{P_{x,Ti}}$	atoms ^{36}Cl (g Ti	0.001	0.001
spallation production rate for Fe, SLHL	PR_{Fe}	atoms ^{36}Cl (g F	1.9	0.288 Stone et al., 2005
mass concentration of Fe in **target fraction**	C_{Fe}	g Fe (g rock)$^{-1}$	0.001	0.000
result unscaled ^{36}Cl production by spallation of Fe	$\mathbf{P_{x,Fe}}$	atoms ^{36}Cl (g Fe	0.002	0.000
result unscaled sample specific ^{36}Cl production rate by spallation of target elements	$\mathbf{P_x}$	atoms ^{36}Cl (g)$^{-1}$	8.709	0.415

7- unscaled sample specific ^{36}Cl production rate by capture of epithermal neutrons

					Ca	K	Ti	Fe	Cl	O, rock	Si	Na	Mg	Al	Mn	P	C	H	O, water	Li	B	Sm	Gd	Th	U	Cr	Be	N	F	S	Sc	Co	Ni	Se	Br	Rb	Sr	Zr	Mo	Ru	Te	I	Cs	Ba
effective macroscopic resonance integral for absorption of epithermal neutrons	I_{eff}	cm^2 g^{-1}	0.0010		7.51E-04	2.56E-06	2.34E-06	1.23E-05	3.24E-05	1.80E-06	3.12E-06	1.21E-06	1.26E-04	5.82E-06	2.27E-05		0.00E+00	0.00E+00		0.00E+00	4.31E-05	4.67E-07	1.49E-07		2.75E-08																			
fraction of epithermal neutrons absorbed by ^{35}Cl (**target fraction**)	f_{eth}	-	0.0299																																								
neutron macroscopic scattering cross section in subsurface	Σ_{sn}	cm^2 g^{-1}	0.0493		9.44E-03	5.22E-06	3.09E-06	1.03E-04	3.70E-05	2.51E-02	7.76E-05	1.18E-05	1.13E-02	4.83E-05	3.50E-06	0.00E+00	0.00E+00	2.50E-03	6.33E-04	6.18E-08	5.36E-07	1.27E-08	6.59E-08	1.37E-09	2.39E-08	5.81E-08	0.00E+00	0.00E+00	0.00E+00	0.00E+00	0.00E+00	0.00E+00	0.00E+00	0.00E+00	0.00E+00	0.00E+00	0.00E+00	0.00E+00	0.00E+00	0.00E+00	0.00E+00	0.00E+00	0.00E+00	0.00E+00
scattering rate parameter	B		6.97E-03		4.63E-04	2.61E-07	1.27E-07	3.59E-06	2.04E-06	3.01E-03	5.43E-06	9.92E-07	9.04E-04	3.48E-06	1.26E-07	0.00E+00	0.00E+00	2.50E-03	7.59E-05	1.63E-08	9.33E-08	1.65E-10	8.56E-10	1.18E-11	2.00E-10	2.21E-09	0.00E+00	0.00E+00	0.00E+00	0.00E+00	0.00E+00	0.00E+00	0.00E+00	0.00E+00	0.00E+00	0.00E+00	0.00E+00	0.00E+00	0.00E+00	0.00E+00	0.00E+00	0.00E+00	0.00E+00	0.00E+00
mean macroscopic log decrement of energy loss per collision in subsurface	X_{ss}		0.142																																							
macroscopic absorption and moderation cross section for epithermal neutrons	Σ_{eth}	cm^2 g^{-1}	0.007																																							
attenuation length for absorption and moderation of epithermal neutron flux	Λ_{eth}	g cm^{-2}	140.540																																							
	$A_k * N_k$	atoms mol^{-1}	3.19E+23		1.29E+23	1.00E+20	3.61E+19	5.05E+20	8.31E+19	1.07E+23	1.07E+21	8.94E+19	8.05E+22	9.24E+20	9.32E+19		0.00E+00	1.23E+20		4.52E+17	1.36E+18	5.02E+16	6.02E+16		8.93E+17																			
average atomic weight in subsurface	A_{ss}	g mol^{-1}	23.501																																							
production rate of epithermal neutrons from fast neutrons in atmosphere at land/atm interface	$P_n(0)$	n cm^{-2} a^{-1}	696	185 Marrero et al. 2016, St scaling																																							
Ratio of epithermal neutron production in subsurface to that in atmosphere	R_{eth}	-	1.27																																							
epithermal neutron diffusion coefficient in subsurface	D_{eth}	g cm^{-2}	6.96																																							
apparent fast neutron attenuation coefficient	Λ_f	g cm^{-2}	160																																							
epithermal neutron flux at land/atmosphere interface that would be observed in ss if interface was	$\phi_{*,eth}$	n cm^{-2} a^{-1}	129478																																							
average neutron yield per stopped negative muon	Y_μ		0.405		0.260	0.000		0.001		0.059	0.002	0.000	0.080	0.002			0.000																											
slow negative muon stopping rate at land surface SLHL	$\Psi_\mu(0)$	μ g^{-1} a^{-1}	190																																							
fast muon flux at land surface SLHL	$\phi_{\mu 0}$	μ cm^{-2} a^{-1}	7.90E+05																																							
total muon induced neutron production at land surface	$P_{n\mu 0}$	μ cm^{-2} a^{-1}	81.506																																							
ratio of muon production rate to epithermal neutron production rate	R_μ	-	0.041																																							
macroscopic neutron scattering cross section of atmosphere	$\Sigma_{sn,a}$	cm^2 g^{-1}	0.3773																																							
thermal neutron diffusion coefficient in atmosphere	D_a	g cm^{-2}	0.926																																							
macroscopic absorption and moderation cross section for epithermal neutrons in atmosphere	$\Sigma_{ath,a}$	cm^2 g^{-1}	0.0548																																							

epithermal neutron diffusion length in atmosphere	$L_{eth,a}$	g cm^{-2}	4.015	
epithermal neutron flux at land/atmosphere interface that would be observed in atm if interface we	$\phi^*_{eth,a}$	n cm^{-2} a^{-1}	12709	
difference between hypothetical equilibrium epithermal neutron fluxes in atmosphere and subsurf	$\Delta\phi^*_{eth}$	n cm^{-2} a^{-1}	-116769	
adjusted difference between hypothetical equilibrium epithermal neutron fluxes in atmosphere an	$\Delta\phi^{**}_{eth,a}$	n cm^{-2} a^{-1}	127788	
epithermal neutron diffusion length in subsurface	L_{eth}	g cm^{-2}	30.833	
difference between phi_star_eth and actual epithermal neutron flux at land surface	$(F.\Delta\phi)^*_{eth}$	-	-71186	
slow muon attenuation length	Λ_μ	g cm^{-2}	1510	
epithermal neutron flux (concentration)	$\phi_{eth,total}$	n cm^{-2} a^{-1}	65939	
result unscaled sample specific ^{36}Cl production rate by capture of epithermal neutrons	$\mathbf{P_{eth}}$	**atoms ^{36}Cl g^{-1}**	**1.884**	0.56530

| **8- unscaled sample specific ^{36}Cl production rate by capture of thermal neutrons** | | | |

Appendix 4

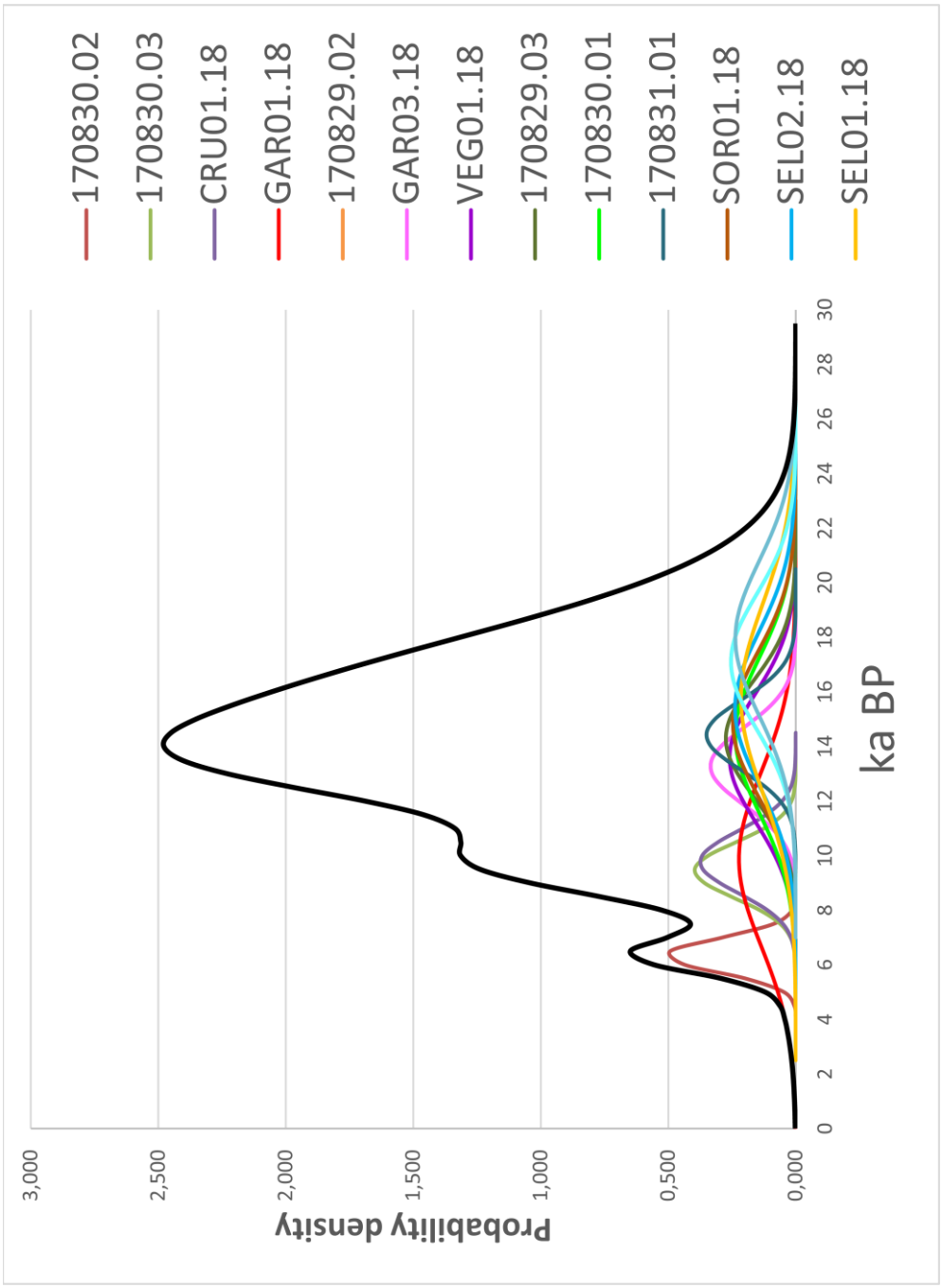

Probability density plot of ^{36}Cl surface exposure ages.